Volume 2, Issue 2, June 2022

CHEMICAL SYNTHESIS

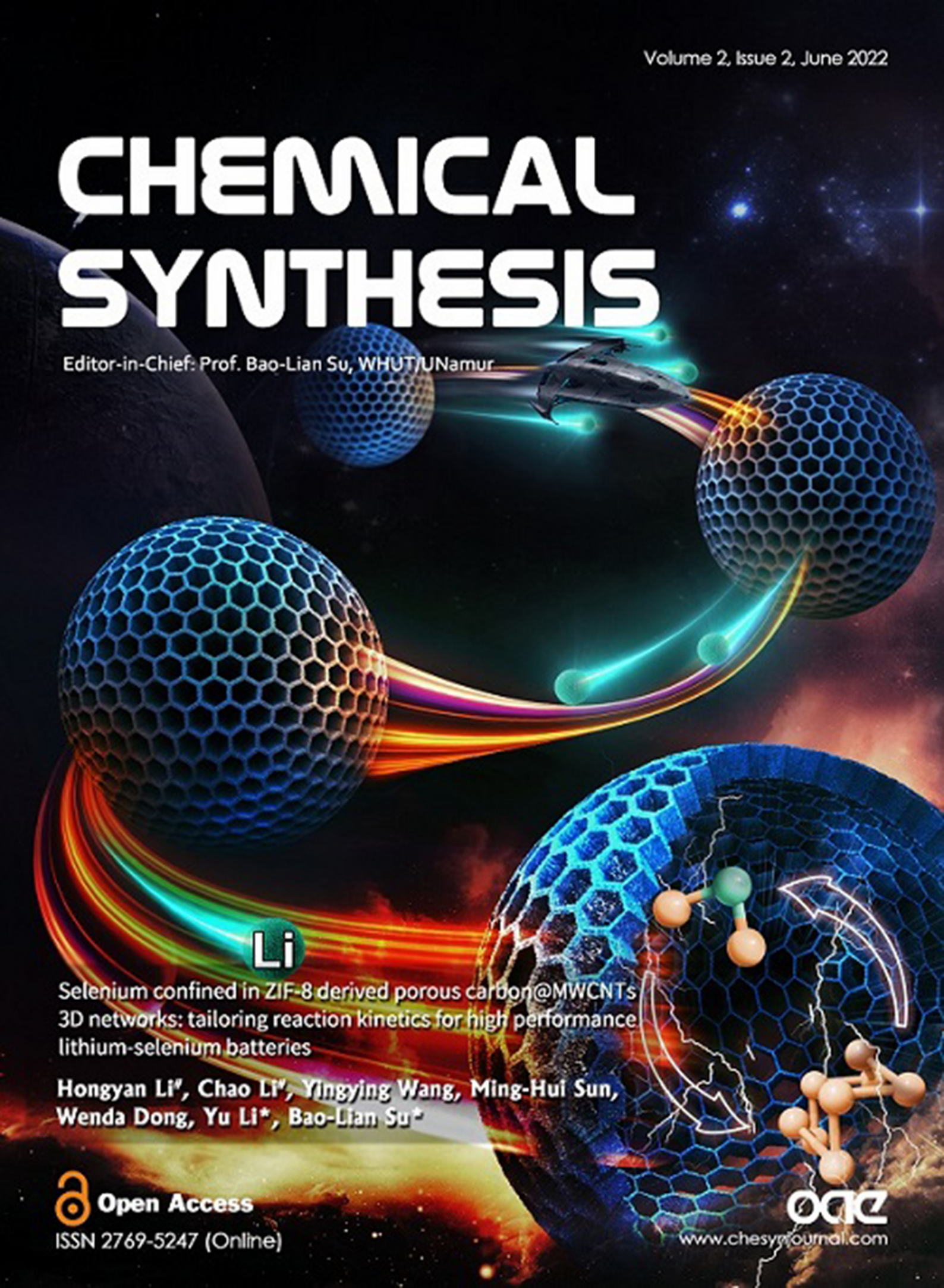

Selenium confined in ZIF-8 derived porous carbon@MWCNTs 3D networks: tailoring reaction kinetics for high performance lithium-selenium batteries

Hongyan Li#, Chao Li#, Yingying Wang, Ming-Hui Sun, Wenda Dong, Yu Li*, Bao-Lian Su*

Open Access
ISSN 2769-5247 (Online)
www.chesynjournal.com

EDITORIAL BOARD

GENERAL INFORMATION

About the Journal

Chemical Synthesis (*CS*) is an international peer-reviewed, open access, online journal. *Chemical Synthesis* is an open access peer-reviewed journal publishing original research involving all areas of the chemical sciences. The journal aims to be the premier resource of seminal and insightful research and showcases for researchers in both academia and industry, providing a platform of inspiration for the future of chemistry. *Chemical Synthesis* intends to serve as the preeminent international chemistry journal and has the ambition to be among the first choices of chemists for publication of their discoveries.

The scope of the journal focuses on the breadth of the chemical synthetic sciences, covering fields from synthetic methodologies, property studies by theoretical calculations or instrumental approaches at molecular and/or nano levels of the obtained products (materials) to the applications in catalysis, energy conversion and storage, biomedicals, pharmaceuticals, environment protection and remediation, etc.

Information for Authors

Manuscripts should be prepared in accordance with Author Instructions.
Please check www.chesynjournal.com/pages/view/author_instructions for details.
All manuscripts should be submitted online at https://oaemesas.com/login?JournalId=cs.

Copyright

Permissions

For information on how to request permissions to reproduce articles/information from this journal, please visit www.chesynjournal.com.

Disclaimer

The information and opinions presented in the journal reflect the views of the authors and not of the journal or its Editorial Board or the Publisher. Publication does not constitute endorsement by the journal. Neither the *CS* nor its publishers nor anyone else involved in creating, producing or delivering the *CS* or the materials contained therein, assumes any liability or responsibility for the accuracy, completeness, or usefulness of any information provided in the *CS*, nor shall they be liable for any direct, indirect, incidental, special, consequential or punitive damages arising out of the use of the *CS*. The *CS*, nor its publishers, nor any other party involved in the preparation of material contained in the *CS* represents or warrants that the information contained herein is in every respect accurate or complete, and they are not responsible for any errors or omissions or for the results obtained from the use of such material. Readers are encouraged to confirm the information contained herein with other sources.

Publisher

OAE Publishing Inc.
245 E Main Street st112, Alhambra, CA 91801, USA
Website: www.oaepublish.com

Contacts

E-mail: editorialoffice@chesynjournal.com
Website: www.chesynjournal.com

Chemical Synthesis

CONTENTS

Volume 2 / Issue 2 / June 2022

Li *et al. Chem Synth* 2022;2:8
DOI: 10.20517/cs.2022.04

Chemical Synthesis

Research Article

Open Access

Check for updates

Selenium confined in ZIF-8 derived porous carbon@MWCNTs 3D networks: tailoring reaction kinetics for high performance lithium-selenium batteries

Hongyan Li[1,2,#], Chao Li[1,2,#], Yingying Wang[1,2], Ming-Hui Sun[1,2], Wenda Dong[3], Yu Li[3,*], Bao-Lian Su[1,2,3,*]

[1]Laboratory of Inorganic Materials Chemistry (CMI), University of Namur, Namur B-5000, Belgium.
[2]Namur Institute of Structured Matter (NISM), University of Namur, Namur B-5000, Belgium.
[3]State Key Laboratory of Advanced Technology for Materials Synthesis and Processing, Wuhan University of Technology, Wuhan 430074, Hubei, China.
[#]Authors contributed equally.

***Correspondence to:** Prof. Bao-Lian Su, Laboratory of Inorganic Materials Chemistry (CMI), University of Namur, Rue de Bruxelles 61, Namur B-5000, Belgium. E-mail: bao-lian.su@unamur.be/baoliansu@whut.edu.cn; Prof. Yu Li, State Key Laboratory of Advanced Technology for Materials Synthesis and Processing, Wuhan University of Technology, 122 Luoshi Road, Wuhan 430074, Hubei, China. E-mail: yu.li@whut.edu.cn

How to cite this article: Li H, Li C, Wang Y, Sun MH, Dong W, Li Y, Su BL. Selenium confined in ZIF-8 derived porous carbon@MWCNTs 3D networks: tailoring reaction kinetics for high performance lithium-selenium batteries. *Chem Synth* 2022;2:8. https://dx.doi.org/10.20517/cs.2022.04

Received: 15 Feb 2022 **First Decision:** 22 Mar 2022 **Revised:** 17 Apr 2022 **Accepted:** 22 Apr 2022 **Published:** 28 Apr 2022

Academic Editor: Xiangdong Yao **Copy Editor:** Jia-Xin Zhang **Production Editor:** Jia-Xin Zhang

Abstract

Lithium-selenium battery is nowadays a highly competing technology to the commercial Li-ion battery because it has a high volumetric capacity of 3253 mAh cm^{-3} and gravimetric capacity of 675 mAh g^{-1}. However, the practical application of lithium-selenium (Li-Se) batteries is impeded by the shuttle effect of the soluble polyselenides during the cycling process. Herein, we report the in situ growth and pyrolysis of the metal-organic framework zeolitic imidazolate framework-8 (ZIF-8) on three-dimensional (3D) interconnected highly conductive multiwalled carbon nanotubes (MWCNTs). The obtained composites are used to anchor Se for advanced Li-Se batteries. Compared with the isolated ZIF-8 derived microporous carbon, our synthesized ZIF-8 derived porous carbon@MWCNTs (ZIF-8-C@MWCNTs) 3D highly conductive networks facilitate lithium ion diffusion and electron transportation. The particle size of ZIF-8 crystals has an important impact on the battery performance. By adjusting the particle size of ZIF-8, the electrochemical reaction kinetics in ZIF-8-C@MWCNTs 3D networks can be tuned. The optimized particle size of ZIF-8 around 300-500 nm coated on MWCNTs composite achieves an excellent initial

discharge capacity of 756 mAh g^{-1} and a stabilized capacity of 468 mAh g^{-1} at 0.2 C after 200 cycles. Combining the 3D MWCNTs with the appropriate size of ZIF-8 derived microporous carbon particles could highly improve the performance of the Li-Se battery. This work provides significant guidance for further structural design and host particle size selection for high-performance Li-Se batteries.

Keywords: Metal-organic framework (MOF), carbon nanotubes, lithium-selenium battery, in situ growth, zeolitic imidazolate framework-8 (ZIF-8), crystal size

INTRODUCTION

With the increase of global energy demand, the design of advanced energy materials for energy storage applications including smart power grids, commercial electronics, and electric cars has attracted considerable attention[1]. Elemental sulfur, when employed as a positive electrode material in a Li-S battery, has a high theoretical specific capacity of 1672 mAh g^{-1} and a theoretical energy density of 2600 Wh kg^{-1}[2]. Moreover, sulfur has other advantages, such as high natural abundance, competitive cost, and minimum environmental impact[3]. Hence, it is one of the most promising positive electrode materials for next-generation energy storage systems. Although the concept of Li-S batteries has been known for years and attracts intensive research interest, several key issues in Li-S batteries, such as the shuttle effect and the inherent electric insulation property of sulfur, lead to quick capacity fading, low active-material utilization, and poor positive electrode conductivity, severely hindering their commercial application[4,5].

Selenium, another element from the same main group, has been considered as a competitive candidate, which owns a similar reaction mechanism and comparable volumetric capacity (3253 mAh cm^{-3}) compared with sulfur but with much improved electric conductivity (1×10^{-3} S m^{-1})[6]. However, the shuttle effect generated by the soluble intermediates polyselenides (Li_2Se_n, $n \geq 4$) still exists in Li-Se batteries and leads to quick capacity decay, poor cycle performance, and low coulombic efficiency[7]. Besides, the pure selenium positive electrode is subject to volume expansion, and the lithium ion and electrical conductivity are still not efficient enough[8,9]. To address these drawbacks, the widely used effective approach is the confinement of selenium in porous carbon matrix materials. The carbon systems containing microporous, mesoporous, and even hierarchically porous structures with diverse morphologies and architectures, such as spheres[10], 1D nanotubes[11], 2D graphene[12], 3D hierarchical structures[13-15], hollow nanostructures[16], core-shell structures[17,18], *etc.*, lead to the efficiency improvement in the performance of Li-Se batteries. After the first utilization of the typical ordered mesoporous carbon CMK-3 to Li-S batteries, achieving good cycling stability with 80% of the theoretical capacity of sulfur, CMK-3 was used to confine selenium by Yang *et al.*[19] and delivered a high reversible discharge capacity[19,20].

More recently, metal-organic frameworks (MOFs) have attracted increasing attention in battery research area owing to their high surface area, uniform pore size, chemical composition, and structural diversity[21-24]. Among them, zeolitic imidazolate frameworks (ZIFs), which are based on metal imidazolates, are widely investigated because of their tunable pore sizes, apparent thermal stability, and chemical functionality. Generally, ZIF-8 can be synthesized by green, fast, and massive methods in aqueous or methanol solution, or by more environmentally friendly solid-state mechanochemistry methods at room temperature[25-27]. ZIF-8 has a pore aperture of 0.34 nm in diameter, providing the possibility to adsorb small gas molecules and store the adsorbed materials in the cavity (1.11 nm). Zhou *et al.*[28] first used ZIF-8 nanocrystals as the host with 30 wt.% sulfur loading, achieving long cycle capabilities in a Li-S battery. They further proved that the particle size of MOF significantly influences the final battery performance, because hosts mainly affect the internal Li^+/e^- transport. However, the poor conductivity of MOFs leads to low capacity and rate capability, so it is ineffective to directly confine selenium inside the pores with a high amount. The pyrolysis of ZIF-8

can precisely maintain the particle size, morphology, and structure, but with much improved conductivity, which has recently attracted much attention[29-33]. Zheng *et al.*[11] reported nitrogen-doped graphene particle analogs with a high nitrogen content from the pyrolysis of a nitrogen-containing zeolitic imidazolate framework as lithium anode materials. This idea was further extended to sodium anode batteries[17]. The ZIF-8 derived high-level N-doped graphene analogous particles obtained by pyrolysis as an anode material exhibited excellent electrochemical performance for lithium and sodium batteries. The porous carbon host from ZIF-8 pyrolysis used for lithium-selenium batteries by Liu *et al.*[34] showed that the interconnected microporous carbon polyhedrons (1.1 nm) would have a large surface area and pore volume to effectively confine Se and withstand volume variation. Besides, the dissolution of polyselenides in electrolytes would be suppressed at the same time. Li *et al.*[35] used NH_3 to enlarge the microporous structure to create a hierarchically mesoporous structure. The obtained sulfur- and ZIF-8 derived porous carbon composites resulted in twice higher capacity retention than that of MOF-C made by direct pyrolysis of MOFs. However, the conductivity of MOF-derived porous carbon is still not high enough due to relatively low graphitic crystallinity, together with the aggregation, which will lead to sluggish lithium ion transport and insufficient contact with dissolved polyselenides[36-38]. In addition, the poor flexibility of microporous carbon materials derived from the pyrolysis of MOFs limits its future application in highly efficient flexible electronic devices. Carbon nanotubes (CNTs) have been widely applied in the energy area because of their one-dimensional electronic conductivity, great surface area, and mechanical properties[39]. It is possible to build fast three-dimensional electron transportation pathways with multiwalled CNTs (MWCNTs) entanglement[40]. ZIF decorated on MWCNT-derived materials has proven to be a feasible approach to achieving high-efficiency supercapacitors[41] and can be used as anode materials[42,43]. The 3D MIL-68 (Al)@MWCNTs obtained by in situ pyrolyzing MIL-68 particles on the surface of MWCNTs have recently been reported to achieve excellent performance in a Li-Se battery[44].

Herein, we report 3D structured microporous carbon/MWCNT composite materials for selenium confinement through in situ formations of ZIF-8-coated MWCNTs by feasible solvothermal reaction and their pyrolysis for lithium-selenium batteries. Such ZIF-8 derived porous carbon@MWCNTs 3D networks can effectively accelerate electrons transport, provide the pathways for Li^+ transfer, and enhance the adsorption of the polyselenides, which will further improve the reaction kinetics. The ZIF-8 derived microporous carbon particle sizes are tuned from 30 nm to 1.5 μm with a modulator. The rich micropores serve the sites for Se loading and possess strong adsorption to polyselenides. The pyrolyzed ZIF-8 with particle size around 300 nm-500 nm coated on MWCNT composites retained the best specific capacity of 468 mAh g^{-1} at 0.2 C after 200 cycles. The unique 3D structure with the tunable size of pyrolyzed ZIF-8 particles can confine the soluble polyselenides, accelerate Li^+ transfer, promote the conductivity of positive electrode materials, and optimize the electrochemical reaction kinetics, thereby leading to an excellent electrochemical property. This work reveals enormous advantages for the MWCNTs in tandem with the tunable ZIF-8 derived microporous carbon particles and explores their optimal combination. The achieved outstanding property is one step closer to having a potential commercial application of the Li-Se battery.

EXPERIMENTAL

Preparation of ZIF-8

Typically, a solution of $Zn(NO_3)_2 \cdot 6H_2O$ (470 mg) in 50 mL of methanol was rapidly poured into a solution of 2-methylimidazole (Hmim, 810 mg) in 50 mL of methanol under stirring. The mixture slowly turned turbid after 30 min, and then was kept stirring for another 2 h. Finally, the white ZIF-8 nanocrystals were separated from the milky dispersion by centrifugation and washing with fresh methanol three times. The nanocrystals were dried at 40 °C in vacuum. It is worth noting that the dried ZIF-8 will not be redispersible in methanol again.

Preparation of ZIF-8@MWCNTs

Before synthesis, MWCNTs were pretreated with strong acid to decorate oxygen-containing functional groups at the surface to facilitate the growth of ZIF-8 crystals on the surface of MWCNTs. Then, 30 mg of modified MWCNTs were added into the solution of Hmim (810 mg) in 50 mL of methanol with strong ultrasound, following the exact same procedure as for ZIF-8. Finally, a grey black powder was obtained compared to the white crystals of ZIF-8. The obtained composite was denoted as ZIF-8@MWCNTs-1. Different weight percentages of 1-methylimidazole as a modulator, namely 50 wt.%, 70 wt.%, 90 wt.%, and 100 wt.%, compared to the weight of ligand 2-methylimidazole were added to give ZIF-8@MWCNTs-2, ZIF-8@MWCNTs-3, ZIF-8@MWCNTs-4, and ZIF-8@MWCNTs-5, respectively.

Preparation of ZIF-8 derived porous carbon (ZIF-8-C) and ZIF-8 derived porous carbon coated MWCNTs (ZIF-8-C@MWCNTs)

The as-synthesized ZIF-8 and ZIF-8@MWCNTs-X (X = 1-5) were calcined at 800 °C with a heating rate of 5 °C min^{-1} for 4 h in an argon atmosphere. To completely remove the zinc species, the acquired black powder was immersed in 4 M HCl aqueous solution at room temperature for 12 h. After washing three times with deionized water to pH equal to 7, the products dried in a vacuum oven overnight were labeled as ZIF-8-C, ZIF-8-C@MWCNTs-1, ZIF-8-C@MWCNTs-2, ZIF-8-C@MWCNTs-3, ZIF-8-C@MWCNTs-4, and ZIF-8-C@MWCNTs-5, respectively.

Se confinement in ZIF-8-C and ZIF-8-C@MWCNTs-X (X = 1-5)

The selenium confined porous carbon composites were synthesized by two-step melt-diffusion procedures. With a weight ratio of 2:1, bulk Se (Sigma-Aldrich) and ZIF-8-C or ZIF-8-C@MWCNTs-X (X = 1-5) materials were then thoroughly mixed by ball milling. The mixtures were heated up to 260 °C and maintained for 16 h in a tube furnace full of flowing Ar, followed by 300 °C for 2 h to obtain the composites. The final products were labeled as Se@ZIF-8-C, Se@ZIF-8-C@MWCNTs-1, Se@ZIF-8-C@MWCNTs-2, Se@ZIF-8-C@MWCNTs-3, Se@ZIF-8-C@MWCNTs-4, and Se@ZIF-8-C@MWCNTs-5, respectively.

Materials characterization

X-ray diffraction (XRD) patterns were obtained on a Bruker D8 system with Cu Kα radiation (λ = 0.15405 nm) at 40 mA and 30 kV. Scanning electron microscopy (SEM) observation was carried out using a JEOL 7500 F field-emission SEM. Transmission electron microscopy (TEM) images of the samples were recorded on carbon-coated copper grids by using a TECNAI 10 at an acceleration voltage of 100 kV. Nitrogen adsorption-desorption isotherms were obtained using an ASAP 2420 surface area and porosity analyzer at 77 K. The specific surface area was calculated by the Brunauer-Emmett-Teller (BET) method. The pore size distribution was calculated using the Barrett-Joyner-Halenda (BJH) method for mesopores and nonlocal density functional theory (NLDFT) for the micropores analysis method. Thermogravimetric analysis (TGA) was carried out using a thermal analyzer (Setaram Labsys Evo) under a flow of nitrogen with a temperature ramp of 5 °C min^{-1}. X-ray photoelectron spectroscopy (XPS) characterization was carried out in a ThermoFisher ESCALAB 250 Xi instrument with a monochromatic Al Kα X-ray source (1486.6 eV).

Electrochemical measurements

The electrochemical measurements were carried out at room temperature using CR2032 coin-type cells. The working electrode was prepared by mixing with active material, Super-P carbon (Timcal), and sodium alginate (SA, Sigma-Aldrich) at the weight ratio of 8:1:1 in distilled water. The resulting slurry was coated onto aluminum foil and dried in vacuum at 60 °C overnight. The coin-type cells were assembled in an Ar-filled glovebox with moisture and oxygen concentrations lower than 1 ppm, using lithium metal as the counter/reference electrode, glass fiber membrane as the separator, and 1 M lithium bis(trifluoromethanesulfonyl)imide (LiTFSI) (Solvay) in a mixture of dioxolane (DOL, Sigma-Aldrich), and dimethoxygethane (DME, Sigma-Aldrich) (1:1 in volume) with 1% $LiNO_3$ (Sigma-Aldrich) additive as the

electrolyte. The galvanostatic discharge and charge experiments were performed on a battery tester (LAND) with a voltage window of 1.75 V-2.6 V *vs.* Li^+/Li at different current densities of 0.1 C, 0.2 C, 0.5 C, 1 C, 2 C, and 5 C (1 C = 675 mA g^{-1}). Cyclic voltammetry (CV) was performed using an electrochemical workstation Princeton VersaSTAT 3 at a voltage of 1.75 V -2.6 V with a scan rate of 0.1 mV s^{-1}. Electrochemical impedance spectroscopy (EIS) measurement was also conducted using Princeton VersaSTAT 3 with a frequency range between 100 kHz and 10 mHz.

RESULTS AND DISCUSSION

Compared to the preparation of ZIF-8@MWCNTs by two-step method including filtering the metal salts with MWCNTs followed by adding of 2-methylimidazole (Hmim) reported in the literature[45,46], our novel method is notably much simpler, but it can also tune the ZIF-8 crystal size grown on MWCNTs. Figure 1A and B schematically illustrates the preparation process of Se@ZIF-8-C@MWCNTs and the tunable crystal sizes of the ZIF-8 in the ZIF-8-C@MWCNTs 3D network composites. Our present work demonstrates that ZIF-8 with variable crystal sizes can directly grow on the surface of MWCNTs via a simple mixing reaction in methanol at room temperature. The ZIF-8 as a reference sample was synthesized by simple mixing of zinc salts and 2-methylimidazole in the methanol at room temperature. The ZIF-8@MWCNTs composites were synthesized by in situ growth of ZIF-8 crystals on oxidized MWCNTs with the different weight ratio of modulator (1-methylimidazole). The modulator was used to tune the size of ZIF-8 crystals. The higher the amount of modulator, the larger the crystal size. ZIF-8 with different crystal sizes grown on MWCNTs were obtained [Figure 1B]. When the ZIF-8 crystal size is small, it grows along the single nanotube where only one nanotube is across the ZIF-8 crystal. As the crystal size increases, multiple CNTs pass through the ZIF-8 crystals. The ZIF-8 derived porous carbons (ZIF-8-C) and ZIF-8 derived porous carbon on 3D multiwalled carbon nanotubes (ZIF-8-C@MWCNTs) were obtained by the pyrolysis of ZIF-8 crystals at 800 °C in argon, followed by acid washing to remove the metal. Finally, the selenium was confined inside the pores of the composites at 260 °C [Figure 1C].

The successful synthesis of ZIF-8@MWCNTs was confirmed by X-ray powder diffraction [Figure 2A]. The two broad peaks at 26° and 43.5° (2θ) in the XRD pattern of MWCNTs correspond to the (002) and (100) Bragg reflection planes with low crystallinity[47]. In terms of ZIF-8, the diffraction peaks at 7.3°, 10.3°, 12.7°, and 18° (2θ), representing the crystal structures of ZIF-8 are observed, being consistent with its typical crystalline structure (CCDC # 602542)[48,49]. After the addition of MWCNTs, the peaks of ZIF-8 appear at the same positions, which proved the successful synthesis of the ZIF-8@MWCNTs composites. Due to the high intensity of the ZIF-8, the broad peaks belonging to MWCNTs are indistinguishable. Supplementary Figure 1 demonstrates that there is no effect on the formation of ZIF-8 crystalline structure by adding MWCNTs in the synthesis, and that the peak intensity of ZIF-8@MWCNTs composite increases with increasing the amount of modulator (1-methylimidazole) as the crystal size of ZIF-8 in situ grown on MWCNTs gradually increased. Following the high-temperature pyrolysis at 800 °C, the 3D network composites made of ZIF-8 derived porous carbon and MWCNTs were obtained. The XRD pattern of ZIF-8-C indicates the carbon derived from ZIF-8 is in an amorphous state. After the encapsulation of selenium in ZIF-8-C@MWCNTs composites, the characteristic peaks of selenium at 23.5° and 29.5° (2θ) almost disappear from Se@ZIF-8-C@MWCNTs-1 as a representative sample, indicating that the selenium is in the amorphous phase[50].

The confinement condition of selenium inside ZIF-8-C@MWCNTs-X (X = 1-5) composites can also be confirmed by the N_2 adsorption-desorption isotherms [Figure 2B and Supplementary Figure 2]. The adsorption-desorption isotherms of ZIF-8-C and the ZIF-8-C@MWCNTs-X (X = 1-5) composites display typical Type I curves with hysteresis at a high relative pressure of 0.8-1.0, showing the microporous characteristics with the presence of interparticular large pore size of these materials. The pore size

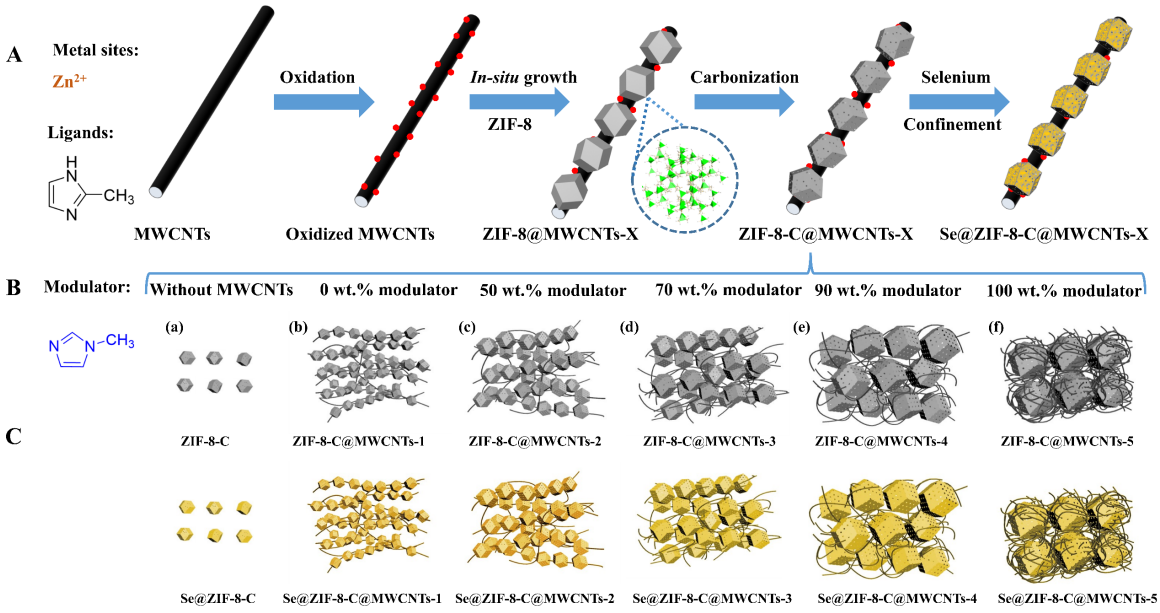

Figure 1. (A) Schematic synthesis routes of ZIF-8-C@MWCNTs-X, (B) tuning of the size of ZIF-8 for a series of ZIF-8-C@MWCNTs-X (X = 1-5) and (C) synthesis the final selenium-confined composites of Se@ZIF-8-C, Se@ZIF-8-C@MWCNTs-1, Se@ZIF-8-C@MWCNTs-2, Se@ZIF-8-C@MWCNTs-3, Se@ZIF-8-C@MWCNTs-4, and Se@ZIF-8-C@MWCNTs-5, respectively.

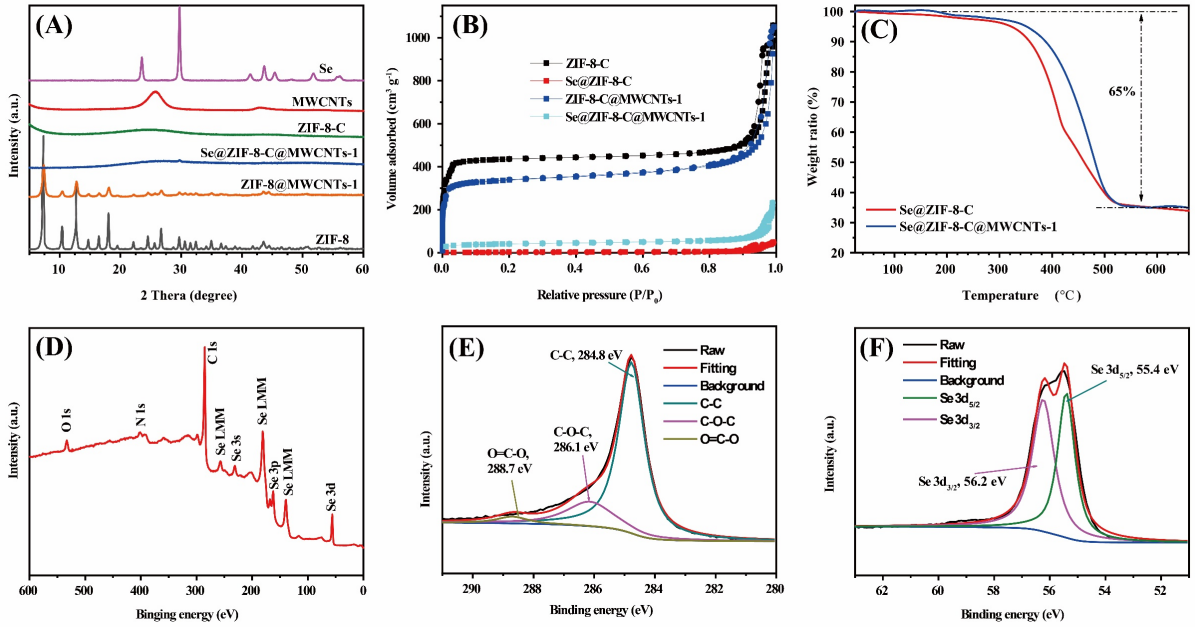

Figure 2. (A) XRD patterns of ZIF-8, MWCNTs, ZIF-8@MWCNTs-1, ZIF-8-C, Se@ZIF-8-C@MWCNTs-1, and selenium. (B) Nitrogen adsorption and desorption isotherms of ZIF-8-C, Se@ZIF-8-C, ZIF-8-C@MWCNTs-1 and Se@ZIF-8-C@MWCNTs-1. (C) TGA curves of Se@ZIF-8-C and Se@ZIF-8-C@MWCNTs-1 under nitrogen with a rate of 5 °C min^{-1}. XPS spectrum of Se@ZIF-8-C@MWCNTs-1: (D) Survey scan; (E) C1s; and (F) Se3d.

distribution curves show the presence of two kinds of micropores, 1.0 nm and 1.5 nm, in all the as-prepared materials [Supplementary Figure 2]. The hysteresis at the very high relative pressure over 0.8 [Supplementary Figure 2A and B] is due to the intergranular porosity coming from the aggregation of ZIF-8

derived porous carbon particles. The calculated BET surface areas and pore volumes are listed in Supplementary Table 1. The pore volume and surface area decrease with increasing the amount of modulator, and then increase back to 1.32 $cm^3 g^{-1}$ and 1283 $m^2 g^{-1}$, respectively. After selenium loading, the micropores disappear, indicating that the pores were filled with selenium [Figure 2B].

The exact weight ratio of selenium in Se@ZIF-8-C and Se@ZIF-8-C@MWCNTs-X (X = 1-5) composites were measured by TGA. The TG curves of Se@ZIF-8-C and Se@ZIF-8-C@MWCNTs-1 as representative samples are shown in Figure 2C. The series of Se@ZIF-8-C@MWCNTs-X are given in Supplementary Figure 3. In Figure 2C, a weight loss is observed at around 200 °C, because of the small amount of selenium residue at the surface of ZIF-8-C@MWCNTs-1. The main weight loss starts from 300 °C to 500 °C, which is responsible for the encapsulated selenium. The selenium weight ratio of Se@ZIF-8-C and Se@ZIF-8-C@MWCNTs-X (X = 1-5) are around 65%. The high Se loading proportion in the Se@host composites is due to the high surface area and high pore volume of all the host materials. XPS was also applied to investigate the elemental composition and ratio and the electronic state of the specific elements. The survey scan of the Se@ZIF-8-C@MWCNTs-1 [Figure 2D] gives the peaks located at 533, 402.6, 284 and 55.3 eV corresponding to O1s, N1s, C1s, and Se3d, respectively. The existence of O1s peak with very low intensity may be due to the physically adsorbed moisture/oxygen[51]. The peak of N1s is originally from the ligands of 2-methylimidazole. The weight ratio of selenium from the survey scan is 63.5%, which is consistent with the data from TGA. The peak of high-resolution C1s spectrum could be deconvoluted into three components at 284.8 eV, 286.1 eV, and 288.7 eV, related to C-C, C-O, and C=O, respectively [Figure 2E]. The high-resolution Se3d spectrum in Figure 2F can be deconvoluted into two contributions of 55.4 and 56.2 eV, corresponding to $Se3d_{5/2}$ and $Se3d_{3/2}$, respectively, due to spin-orbit coupling[52].

The morphologies of ZIF-8-C and ZIF-8-C@MWCNTs-X (X = 1-5) were examined by TEM and SEM, as shown in Figures 3 and 4, respectively. The particle sizes of pure ZIF-8-C are quite uniform, around 50 nm ± 10 nm. After adding oxidized MWCNTs into the methanol solution, the ZIF-8 particles clearly grew along the surface of MWCNTs, and the ZIF-8 crystal size was largely reduced to around 20 nm-30 nm. This indicates that the surface functionalization of MWCNTs by strong acid treatment favors the interaction between ZIF-8 crystals and MWCNTs, leading to the growth of ZIF-8 crystals at the surface of MWCNTs. It is interesting to note that almost all the ZIF-8 crystals grew along the MWCNTs. Increasing the amount of 1-methylimidazole as a modulator, the crystal size of ZIF-8 starts to increase. The interconnected CNT network and the ZIF-8 crystals on its surface form a sponge structure with a large number of pores inside. After the pyrolysis process, the particle sizes are 50 nm for ZIF-8-C [Figure 3A and D], 20nm-30 nm for ZIF-8-C@MWCNTs-1 [Figure 3B and E], 100 nm-150 nm for ZIF-8-C@MWCNTs-2 [Figure 3C and F], 300 nm-500 nm for ZIF-8-C@MWCNTs-3 [Figure 3G and J], 500 nm-800 nm for ZIF-8-C@MWCNTs-4 [Figure 3H and K], and 800 nm to 1.5 μm for ZIF-8-C@MWCNTs-5 [Figure 3I and L]. It clearly shows that the ZIF-8-C particles are embedded in multiple CNTs networks. Figure 4 further proves the presence of ZIF-8-C with very homogenous particle size in ZIF-8-C@MWCNTs-X (X = 1-5) composites. The SEM and TEM images of Se@ZIF-8-C are shown in Supplementary Figure 4. After confining Se into ZIF-8-C, the morphology of the obtained Se@ZIF-8-C remains unchanged. The uniform dispersion of carbon, selenium, and nitrogen was confirmed by energy-dispersive X-ray spectroscopy (EDX) element analysis mapping. The accurate weight loading of selenium inside ZIF-8-C@MWCNTs-1 is 64 wt.% by EDX element analysis, which is in agreement with the data from XPS and TGA. The other EDX mapping data of other composites are shown in Supplementary Figure 5, indicating that the C, Se, and N elements are well dispersed[53].

Coin cells were assembled with lithium metal as anode and mixtures of Se@ZIF-8-C or Se@ZIF-8-C@MWCNTs-X, conductive carbon, and sodium alginate with a weight ratio of 8:1:1 as a positive electrode

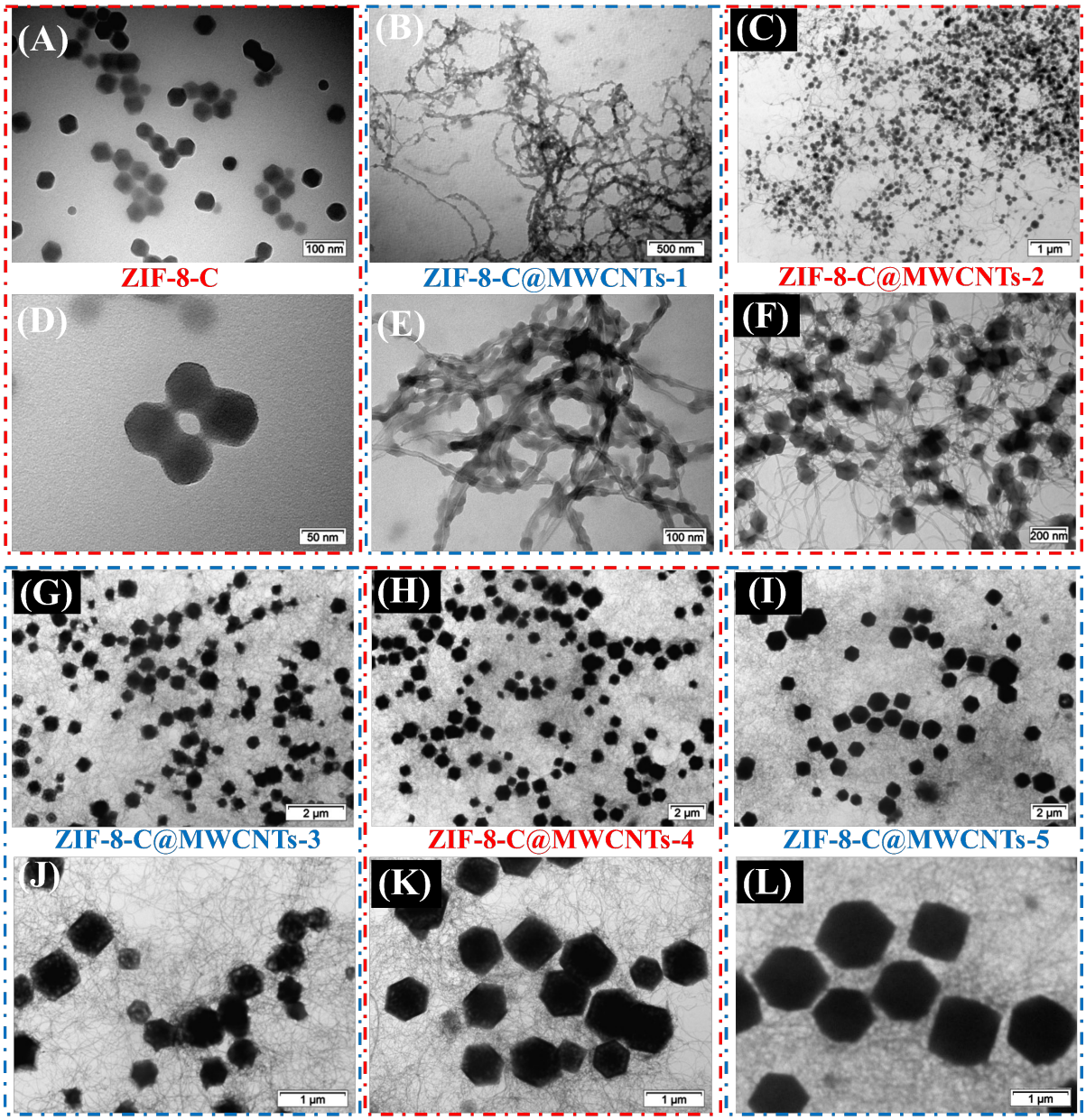

Figure 3. TEM images of: ZIF-8-C (A,D); ZIF-8-C@MWCNTs-1 (B,E); ZIF-8-C@MWCNTs-2 (C,F); ZIF-8-C@MWCNTs-3 (G,J); ZIF-8-C@MWCNTs-4 (H,K); and ZIF-8-C@MWCNTs-5 (I,L).

to evaluate the battery performance. The electrolyte was composed of 1 M LiTFSI DOL: DME with a volume ratio of 1:1, accompanied with 1% $LiNO_3$. From 50 to 80 μL of electrolyte were added to every cell, and glass fiber was used as the separator in our case. The typical battery voltage used was in the range of 1.75 V-2.6 V to avoid excessive $LiNO_3$ decomposition for sustainable protection as $LiNO_3$ can react with metallic lithium anode to form a passivation layer on lithium anode, at the same time getting a higher coulombic efficiency. To explore the electrochemical reaction during the discharge-charge process, CV analyses of Se@ZIF-8-C@MWCNTs-3, as representative samples of Se@ZIF-8-C@MWCNTs-X, are presented in Figure 5A. The CV curve shows two obvious reduction peaks at 2.14 V and 1.93 V at the first cycle, relevant to the stepwise electrochemical reaction from selenium to lithium polyselenides (Li_2Se_n, $n \geq$

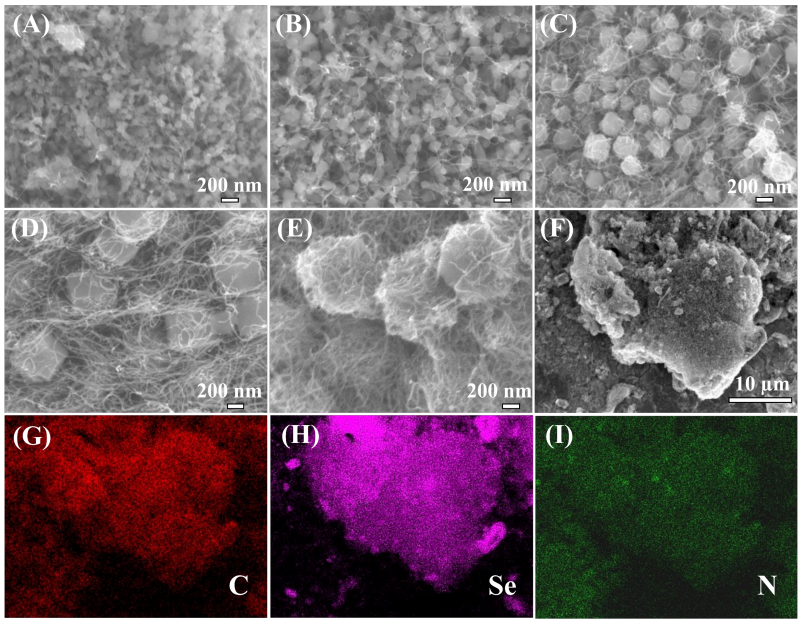

Figure 4. SEM images of: (A) ZIF-8-C@MWCNTs-1; (B) ZIF-8-C@MWCNTs-2; (C) ZIF-8-C@MWCNTs-3; (D) ZIF-8-C@MWCNTs-4; (E) ZIF-8-C@MWCNTs-5; and (F) Se@ZIF-8-C@MWCNTs-1. EDX mapping images of Se@ZIF-8-C@MWCNTs-1: (G) C; (H) Se; and (I) N.

4), finally to Li_2Se[54,55]. There is another small reduction peak observed at 2.26 V, which is due to the irreversible transformation of cyclic Se_8 into higher-order linear Se_n[51]. Two oxidation peaks corresponding to the reaction from Li_2Se to Se with the intermediate Li_2Se_n appear at 2.17 and 2.26 V, respectively. The following cycles show similar peaks to the first cycle, but the reduction/oxidation peaks shift to a lower overpotential position due to the formation of the solid electrolyte interphase (SEI) layer on the surface of positive electrode and the activation of Se electrode[56]. Moreover, the absence of a small reduction peak at 2.26 V in the following cycles is due to the irreversible transformation of cyclic Se_8 into higher-order linear Se_n. After that, the CV curves overlap well, demonstrating the improvement of the reversibility with cycling.

The cycling performance of Se@ZIF-8-C, Se@ZIF-8-C@MWCNTs-1, and Se@ZIF-8-C@MWCNTs-3 were carried out at 0.2 C (1 C = 675 mA g^{-1}) [Figure 5B]. The initial discharge/charge capacities of Se@ZIF-8-C and Se@ZIF-8-C@MWCNTs-1 are 294/613 and 422/578 mAh g^{-1}, respectively. The initial coulombic efficiencies of Se@ZIF-8-C and Se@ZIF-8-C@MWCNTs-1 are 48% and 76%, respectively. The low coulombic efficiencies can be attributed to the irreversible formation process of SEI in the first cycle and electrolyte decomposition[57]. After the first few cycles, the coulombic efficiencies of Se@ZIF-8-C@MWCNTs-1 quickly climbed to more than 95% and stabilized. However, Se@ZIF-8-C electrodes needed more cycles to be stabilized because of their sluggish utilization of selenium by inefficient ionic and electron mobility. After 200 cycles, the capacity of Se@ZIF-8-C@MWCNTs-1 electrode is stabilized at 216 mAh g^{-1}, while the capacity of Se@ZIF-8-C is sharply reduced to 150 mAh g^{-1}. This reflects that the electrochemical reaction was accelerated by introducing interconnected MWCNTs to the system. By optimizing the composition of MWCNTs and ZIF-8-C particles, the battery can achieve further improved performance. As shown in Figure 5B, Se@ZIF-8-C@MWCNTs-3 exhibits a high initial capacity of 756 mAh g^{-1} and remains at 468 mAh g^{-1} after 200 cycles. The detailed discharge/charge curves of the Se@ZIF-8-C@MWCNTs-3 electrode at the 1st, 50th, 100th, 150th, and 200th cycles are shown in Figure 5C. The discharge curves show two typical platforms, which are consistent with the cyclic voltammetry measurements containing two reduction peaks.

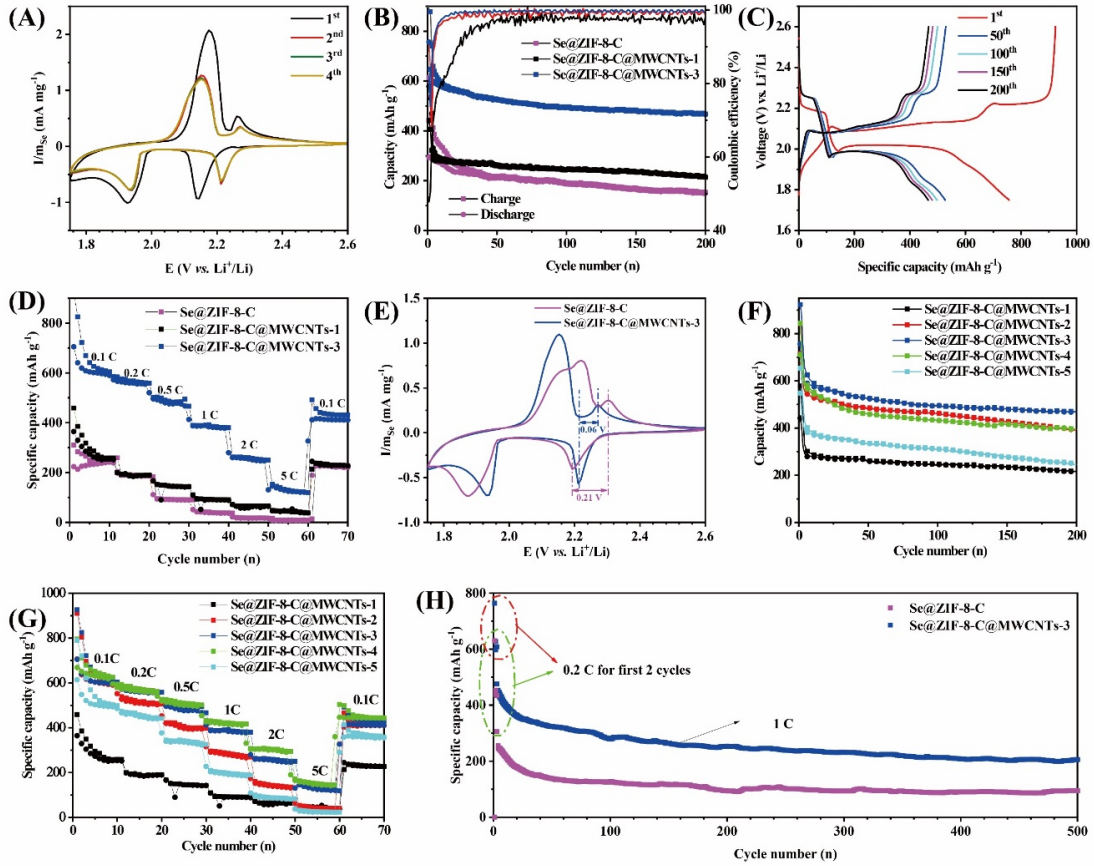

Figure 5. (A) Se mass-normalized CV curves of Se@ZIF-8-C@MWCNTs-3 at first four cycles. (B) The cycling performance and corresponding coulombic efficiency of Se@ZIF-8-C, Se@ZIF-8-C@MWCNTs-1, and Se@ZIF-8-C@MWCNTs-3. (C) The charge and discharge curves at different cycles of Se@ZIF-8-C@MWCNTs-3. (D) Rate capability of Se@ZIF-8-C, Se@ZIF-8-C@MWCNTs-1, and Se@ZIF-8-C@MWCNTs-3. (E) CV curves of Se@ZIF-8-C and Se@ZIF-8-C@MWCNT-3 in the fourth cycle. (F) The cycling performance and (G) rate capability of Se @ZIF-8-C@MWCNTs-1, Se@ZIF-8-C@MWCNTs-2, Se@ZIF-8-C@MWCNTs-3, Se@ZIF-8-C@MWCNTs-4, and Se@ZIF-8-C@MWCNTs-5. (H) Cycling performance of Se@ZIF-8-C and Se@ZIF-8-C@MWCNTs-3 at a high current density of 1 C.

Figure 5D shows the rate performance of Se@ZIF-8-C, Se@ZIF-8-C@MWCNTs-1, and Se@ZIF-8-C@MWCNTs-3 at current densities of 0.1, 0.2, 0.5, 1, 2, and 5 C. The capacity decreased with the increase of current densities due to the electrolyte polarization and the limitation of the ions transfer and transformation. The capacities of Se@ZIF-8-C@MWCNTs-1 are around 250, 192, 150, 100, 60 and 45 mAh g^{-1} at the current densities of 0.1, 0.2, 0.5, 1, 2, and 5 C, respectively. When back to 0.1 C, a capacity of 220 mAh g^{-1} is observed, showing excellent capacity recovery, indicating the stable structure of Se@ZIF-8-C@MWCNTs in high current density cycling. The rate performance of their counterpart Se@ZIF-8-C showed lower rate capacities of 220, 180, 100, 40, 20 and 10 mAh g^{-1} at the current densities of 0.1, 0.2, 0.5, 1, 2, and 5 C, respectively. Se@ZIF-8-C@MWCNTs-3 present an improved capacity at different current densities than those of Se@ZIF-8-C@MWCNTs-1 and Se@ZIF-8-C, showing its superior performance. The improved performance of Se@ZIF-8-C@MWCNTs compared to Se@ZIF-8-C confirms the ability of the 3D composite with microporous carbon and interconnected CNTs networks. The encapsulation of selenium inside the porous carbon of ZIF-8-C possesses more reaction sites, and the presence of MWCNTs is beneficial to fast electron mobility, which facilitates the electrochemical kinetics of selenium species. Moreover, the 3D structure further firmly fixes the ZIF-8 in the specific position, proves the interconnected

pathways for Li^+ transfer, and enhances the adsorption of the polyselenides by its surface polar bonds. The CV measurements for comparison of Se@ZIF-8-C and Se@ZIF-8-C@MWCNTs-3 were performed under the same operating conditions as the battery with a voltage of 1.75-2.6 V. The CV curves of Se@ZIF-8-C and Se@ZIF-8-C@MWCNTs-3 at the fourth cycle are shown in Figure 5E. The higher current density and lower overpotential of Se@ZIF-8-C@MWCNTs-3 (0.06 V) than that of Se@ZIF-8-C (0.21 V) indicate that Se@ZIF-8-C@MWCNTs achieves accelerated electrochemical kinetics.

To explore the optimal combination of ZIF-8 derived porous carbon particles and MWCNTs, cells with a series of Se@ZIF-8-C@MWCNTs-X (X = 1-5) positive electrodes were assembled and further tested. As shown in Figure 5F, the batteries exhibit very high initial discharge capacities of 715, 756, 710, and 547 mAh g^{-1} for Se@ZIF-8-C@MWCNTs-2, Se@ZIF-8-C@MWCNTs-3, Se@ZIF-8-C@MWCNTs-4, and Se@ZIF-8-C@MWCNTs-5, respectively. The higher value than the theoretical one (675 mAh g^{-1}) is due to the additional capacity contribution from the formation of SEI layer. The Se@ZIF-8-C@MWCNTs-X (X = 2-5) positive electrodes achieve much better performance than that of Se@ZIF-8-C@MWCNTs-1 and have a trend of increase first and then decrease with the increase of the particle size of the ZIF-8 derived porous carbons. At a ZIF-8 derived porous carbon particle size of 300 nm-500 nm, the Se@ZIF-8-C@MWCNTs-3 positive electrode reaches the best electrochemical performance. With the cycles running, the Se@ZIF-8-C@MWCNTs-2, Se@ZIF-8-C@MWCNTs-4, and Se@ZIF-8-C@MWCNTs-5 have relatively faster decay than Se@ZIF-8-C@MWCNTs-3 and stabilize at 392, 396, and 246 mAh g^{-1} after 200 cycles, respectively. The capacity performance results of all the different fabricated positive electrodes are summarized in Table 1. Se@ZIF-8-C@MWCNTs-3, with the highest discharge of 468 mAh g^{-1} after 200 cycles, shows the best cycling performance. This can be attributed to the appropriate particle size of ZIF-8 derived microporous carbon, ensuring the full utilization of Se and adsorption of polyselenides. To confirm the capacity contributed by Se rather than MWCNTs, the CV measurement and cycle capacity of pure-MWCNTs were conducted at 1.75 V-2.6 V. The results are shown in Supplementary Figure 6. A reduction peak at the voltage of 1.82 V is shown in Supplementary Figure 6A, which is due to the decomposition of electrolyte at low voltage and SEI layer formation during the first cycle. After that, the formed SEI separates the electrolyte and MWCNTs host material and the decomposition of electrolyte is greatly decreased. In Supplementary Figure 6B, the discharge capacity of cells with pure-MWCNTs is 156 mAh g^{-1} at the first cycle, which rapidly drops to 26.7 mAh g^{-1} and stabilizes at 8 mAh g^{-1}. This indicates that the capacity achievement in the battery with Se@ZIF-8-C@MWCNTs is contributed by active Se after the first cycle.

The rate performance of Se@ZIF-8-C@MWCNTs-X (X = 1-5) was tested at different current densities [Figure 5G], as listed in Table 2. The Se@ZIF-8-C@MWCNTs-2 exhibits the capacity of 600 mAh g^{-1}, 520 mAh g^{-1}, 405 mAh g^{-1}, 285 mAh g^{-1}, 143 mAh g^{-1}, and 50 mAh g^{-1} at the current densities of 0.1 C, 0.2 C, 0.5 C, 1 C, 2 C, and 5 C, respectively, showing a largely improved performance compared with that of Se@ZIF-8-C@MWCNTs-1. As the size of ZIF-8 derived porous carbon increases, the capacity of Se@ZIF-8-C@MWCNTs-3 (675 mAh g^{-1}, 584 mAh g^{-1}, 496 mAh g^{-1}, 391 mAh g^{-1}, 260 mAh g^{-1}, and 145 mAh g^{-1}) and Se@ZIF-8-C@MWCNTs-4 (660 mAh g^{-1}, 582 mAh g^{-1}, 517 mAh g^{-1}, 426 mAh g^{-1}, 306 mAh g^{-1}, and 156 mAh g^{-1}) have further significant improvement at current densities of 0.1 C-5 C with high recoverability. The rate performance of Se@ZIF-8-C@MWCNTs-4 shows the same best performance as Se@ZIF-8-C@MWCNTs-3, whereas Se@ZIF-8-C@MWCNTs-5, with the largest ZIF-8 derived porous carbon particles, has a relatively reduced capacity of 564 mAh g^{-1}, 467 mAh g^{-1}, 343 mAh g^{-1}, 205 mAh g^{-1}, 99 mAh g^{-1}, and 30 mAh g^{-1} at the currents of 0.1 C, 0.2 C, 0.5 C, 1 C, 2 C, and 5 C, respectively. With the increase of ZIF-8 derived porous carbon particle size, the performance increases as the passage of multiple CNTs through the carbon particles ensures its good stability and high electronic/ionic conductivity. Conversely, because of the lack of the channels inside the big size of the ZIF-8 derived porous carbon particles, it is not

Table 1. The cycle performance at 0.2 C and rate capacity of Se@ZIF-8-C and Se@ZIF-8-C@MWCNTs-X (X = 1-5)

Samples	Initial discharge capacity (mAh g^{-1})	2nd cycle discharge capacity (mAh g^{-1})	200th cycle discharge capacity (mAh g^{-1})	Discharge capacity at 5 C (mAh g^{-1})
Se@ZIF-8-C	294	296	150	10
Se@ZIF-8-C@MWCNTs-1	442	405	216	45
Se@ZIF-8-C@MWCNTs-2	715	606	392	50
Se@ZIF-8-C@MWCNTs-3	756	647	468	145
Se@ZIF-8-C@MWCNTs-4	710	647	396	156
Se@ZIF-8-C@MWCNTs-5	547	455	246	30

Table 2. The rate capacity (mAh g^{-1}) at different current densities of Se@ZIF-8-C and Se@ZIF-8-C@MWCNTs-X (X = 1-5)

Samples	0.1 C	0.2 C	0.5 C	1 C	2 C	5 C
Se@ZIF-8-C	220	180	100	40	20	10
Se@ZIF-8-C@MWCNTs-1	250	192	150	100	60	45
Se@ZIF-8-C@MWCNTs-2	600	520	405	284	143	50
Se@ZIF-8-C@MWCNTs-3	675	584	496	391	260	145
Se@ZIF-8-C@MWCNTs-4	660	582	517	426	306	156
Se@ZIF-8-C@MWCNTs-5	564	467	343	205	99	30

beneficial to the ions transfer, leading to the electrochemical reaction kinetics drop. Thus, the optimal size of ZIF-8 derived carbon porous material at 300-500 nm achieves the best performance in the Li-Se battery. The cycling performance of Se@ZIF-8-C and Se@ZIF-8-C@MWCNTs-3 at a high current density of 1 C was conducted, as shown in Figure 5H. The capacity of Se@ZIF-8-C@MWCNTs-3 reaches 206 mAh g^{-1} after 500 cycles, which is much higher than that of Se@ZIF-8-C at only 95 mAh g^{-1}. Therefore, the advantages of the composites of optimized ZIF-8-C size combined with the interconnected MWCNTs are fully demonstrated when compared with Se@ZIF-8-C at the high current density with a long cycle operation.

Figure 6A-C schematically illustrates the mechanism of electrochemical performances of Se@ZIF-8-C, ZIF-8-C@MWCNTs-1, and Se@ZIF-8-C@MWCNTs-5. The combination of ZIF-8 derived microporous carbon particles with highly conductive MWCNTs is beneficial for fast electron transportation in the electrode. It is observed that the particle size has a huge influence on the final electrochemical performances due to the following dilemmas: (A) the soluble polyselenides can easily escape from the micropores of ZIF-8-C if the particle size is too small; and (B) the selenium is not easily fully utilized inside micropores of ZIF-8-C if the particle size is too large. There exists a balance, where the suitable size of ZIF-8-C helps to achieve the best battery performance.

The EIS analysis was carried out at open circuit potential, and the results are shown in Figure 6D and E. For the fresh battery, the curves are composed of a semicircle at high frequency followed by a straight line at low frequency. The start point of the semicircle is R_s, which is assigned to the ohmic resistance of the coin cells[58], while the semicircle in the EIS is related to interface resistance between electrode and electrolyte, which is also called charge transfer impedance (R_{ct})[59]. The relevant equivalent circuit model is inserted in the image. The chi-square values (χ^2) between calculated result and measured data is within 10^{-4}. The

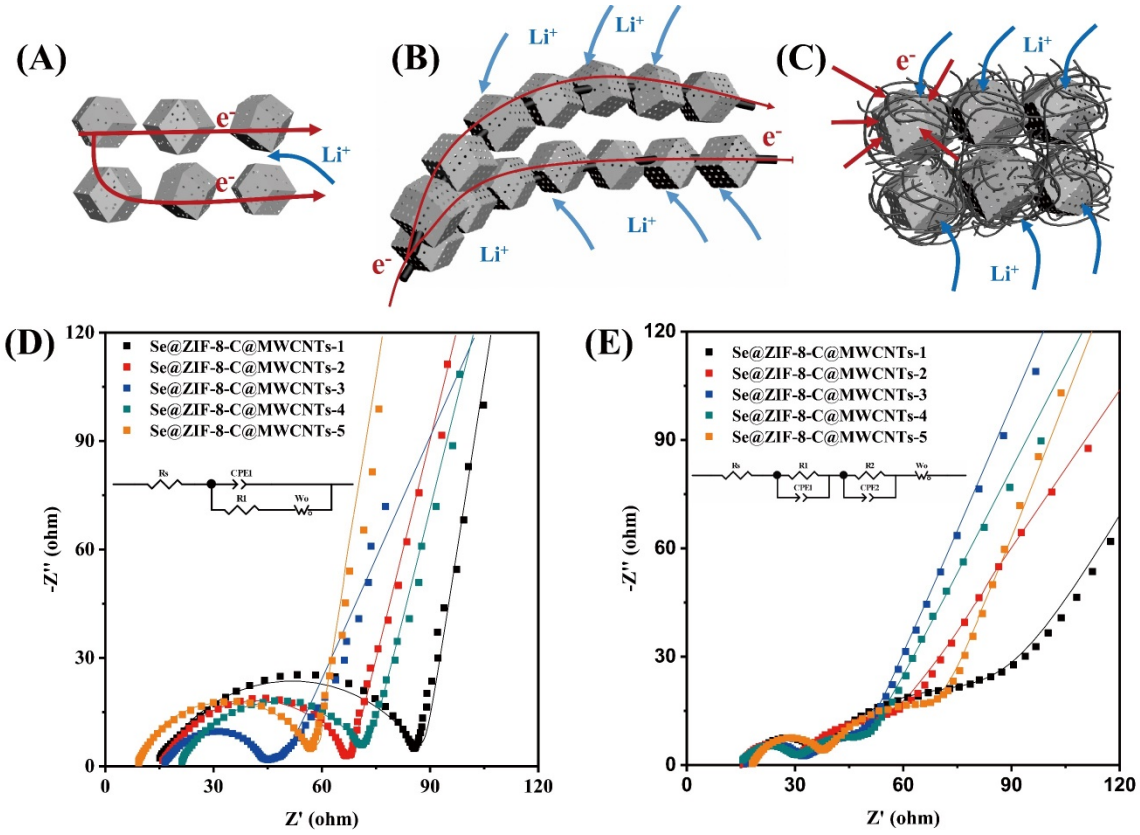

Figure 6. Schematic mechanism of the electrodes for lithium ion and electron movement: (A) Se@ZIF-8-C; (B) ZIF-8-C@MWCNTs-1; and (C) Se@ZIF-8-C@MWCNTs-5. Nyquist plots of Se@ZIF-8-C@MWCNTs-X (X = 1-5) electrode measured when fresh (D) and after 100 cycles with 0.2 C (E).

interface resistance has a huge influence on lithium ion and electron transportation. The interface resistance of Se@ZIF-8-C@MWCNTs-3 is 27 Ω, being much lower than all other electrodes. The clear second semicircle appears at the 100th cycle for the generation of the SEI layer[60]. The interface resistance (R_{SEI}) of Se@ZIF-8-C@MWCNTs-3 shows a similar tendency that proves the structural stability of the electrode. With the increase of ZIF-8 particle size, more carbon nanotubes pass through it, which improves the electrons transfer. However, a too big particle size of ZIF-8 is not beneficial to the transfer of ions. Thus, at the middle size of ZIF-8, Se@ZIF-8-C@MWCNTs-3 achieves the best reaction kinetics.

To better illustrate the relationship between ZIF-8 derived porous carbon particle size and the battery performance, the specific discharge capacity and impedance of the Se@ZIF-8-C@MWCNTs-X (X = 1-5) positive electrodes as a function of the particle size of the internal ZIF-8 derived porous carbon are summarized in Figure 7. With the increase of ZIF-8 derived porous carbon particle size, the number of CNTs that pass through the particles increases. That is favorable for the tight connection of particles with MWCNTs in the composites and rapid electronic conductivity of the positive electrode, leading to the improved capacity and stability of the battery. With the further increase of the ZIF-8 derived porous carbon particle size, the electrolyte and ion transfer are inhibited because of the increased depth of the micropores in the center of the particles, resulting in decrease in the capacity. Thus, the battery achieves the best performance when the ZIF-8 derived porous carbon particle and MWCNTs have an optimal combination. The optimal particle size of ZIF-8 derived porous carbon material at 300 nm-500 nm achieves the best performance in the Li-Se battery owing to the optimal reaction kinetics. The lowest EIS value of Se@ZIF-8-

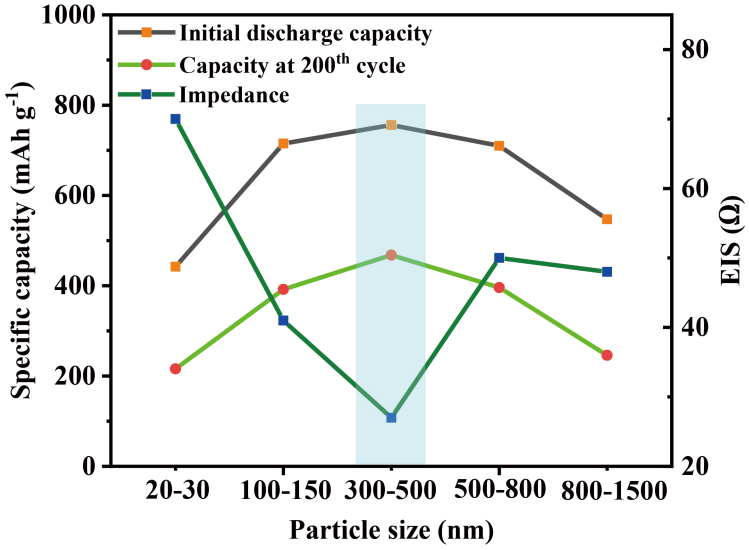

Figure 7. Summary of the specific capacity and impedance of the Se@ZIF-8-C@MWCNTs-X (X = 1-5) positive electrodes according to the particle size of the internal ZIF-8 derived porous carbon.

C@MWCNTs-3 from the impedance test again confirms the accelerated charge transfer.

CONCLUSIONS

Series of microporous carbon particles derived from ZIF-8 strung by MWCNTs were obtained by in situ solvothermal reaction. The Se@ZIF-8-C@MWCNTs-X (X = 1-5) can benefit from the large microporosity of the ZIF-8 and much improved conductivity of MWCNTs for fast electron transportation. Besides, the interconnected 3D MWCNTs network formed fluffy structures can accelerate ions transfer and enhance adsorption of the polyselenides, which will further improve the electrochemical reaction and maintain the good stability of the battery. Importantly, the crystal size of ZIF-8 derived microporous carbon particles on the MWCNTs has a significant influence on the battery performance. The ZIF-8-C with particle size around 300-500 nm coated on MWCNTs, which gives Se@ZIF-8-C@MWCNTs-3 composite, possesses the highest conductivity and fast Li^+ transfer, thereby achieving the best performance with a capacity of 468 mAh g^{-1} at 0.2 C after 200 cycles. The strategy developed in this work provides the facile way to obtain the connection of MOFs to MWCNTs to alleviate the inefficient electron transportation. The particle size of ZIF-8 derived microporous carbon should be thoroughly considered. In perspective, this strategy can be applied to the penetration of other MOFs by the conductive network to improve reaction kinetics for advanced Li-Se or Li-S batteries.

DECLARATIONS

Authors' contributions

Conceived the idea of the project: Su BL, Li Y

Made substantial contributions to conception and design of the study and performed data analysis and interpretation and wrote the draft of manuscript: Li H, Li C

Performed data acquisition, as well as provided administrative, technical, and material support: Wang Y, Sun MH, Dong W

Discussed and revised the manuscript: Li Y, Su BL
Finalized the manuscript: Su BL

Availability of data and materials
Not applicable.

Financial support and sponsorship
This work was supported by National Natural Science Foundation of China (U1663225), Changjiang Scholars and Innovative Research Team in University (IRT_15R52), Program for introducing Talents of Discipline to Universities-National Plan 111 (Grant No: B20002), National Key R&D Program of China (2016YFA0202602). H.Y. Li and C. Li thank the financial support from the China Scholarship Council (CSC) and a scholarship from the Laboratory of Inorganic Materials Chemistry, Université de Namur.

Conflicts of interest
All authors declared that there are no conflicts of interest.

Ethical approval and consent to participate
Not applicable.

Consent for publication
Not applicable.

REFERENCES
1. Peng H, Huang J, Cheng X, Zhang Q. Lithium-sulfur batteries: review on high-loading and high-energy lithium-sulfur batteries (Adv. Energy Mater. 24/2017). *Adv Energy Mater* 2017;7:1770141. DOI
2. Zhao M, Chen X, Li XY, Li BQ, Huang JQ. An organodiselenide comediator to facilitate sulfur redox kinetics in lithium-sulfur batteries. *Adv Mater* 2021;33:e2007298. DOI PubMed
3. Zhang Y, Liu X, Wu L, et al. A flexible, hierarchically porous PANI/MnO_2 network with fast channels and an extraordinary chemical process for stable fast-charging lithium-sulfur batteries. *J Mater Chem A* 2020;8:2741-51. DOI
4. Wang X, Tan Y, Liu Z, et al. New insight into the confinement effect of microporous carbon in Li/Se battery chemistry: a cathode with enhanced conductivity. *Small* 2020;16:e2000266. DOI PubMed
5. Lin S, Chen Y, Wang Y, et al. Three-dimensional ordered porous nanostructures for lithium-selenium battery cathodes that confer superior energy-storage performance. *ACS Appl Mater Interfaces* 2021;13:9955-64. DOI PubMed
6. Yang CP, Yin YX, Guo YG. Elemental selenium for electrochemical energy storage. *J Phys Chem Lett* 2015;6:256-66. DOI PubMed
7. Xiang H, Deng N, Zhao H, et al. A review on electronically conducting polymers for lithium-sulfur battery and lithium-selenium battery: progress and prospects. *Journal of Energy Chemistry* 2021;58:523-56. DOI
8. Kim S, Cho M, Lee Y. High-performance Li-Se battery enabled via a one - piece cathode design. *Adv Energy Mater* 2019;10:1903477. DOI
9. Jin J, Tian X, Srikanth N, Kong LB, Zhou K. Advances and challenges of nanostructured electrodes for Li-Se batteries. *J Mater Chem A* 2017;5:10110-26. DOI
10. Li Z, Yuan L, Yi Z, Liu Y, Huang Y. Confined selenium within porous carbon nanospheres as cathode for advanced Li-Se batteries. *Nano Energy* 2014;9:229-36. DOI
11. Zheng F, Yang Y, Chen Q. High lithium anodic performance of highly nitrogen-doped porous carbon prepared from a metal-organic framework. *Nat Commun* 2014;5:5261. DOI PubMed
12. Youn HC, Jeong JH, Roh KC, Kim KB. Graphene-selenium hybrid microballs as cathode materials for high-performance lithium-selenium secondary battery applications. *Sci Rep* 2016;6:30865. DOI PubMed PMC
13. He J, Chen Y, Lv W, et al. Three-dimensional hierarchical graphene-CNT@Se: a highly efficient freestanding cathode for Li-Se batteries. *ACS Energy Lett* 2016;1:16-20. DOI
14. Chen LH, Li Y, Su BL. Hierarchy in materials for maximized efficiency. *Natl Sci Rev* 2020;7:1626-30. DOI PubMed PMC
15. Wu L, Li Y, Fu Z, Su BL. Hierarchically structured porous materials: synthesis strategies and applications in energy storage. *Natl Sci*

Rev 2020;7:1667-701. DOI PubMed PMC
16. Fan S, Zhang Y, Li S, Lan T, Xu J. Hollow selenium encapsulated into 3D graphene hydrogels for lithium-selenium batteries with high rate performance and cycling stability. *RSC Adv* 2017;7:21281-6. DOI
17. Fan JM, Chen JJ, Zhang Q, et al. An Amorphous carbon nitride composite derived from ZIF-8 as anode material for sodium-ion batteries. *ChemSusChem* 2015;8:1856-61. DOI PubMed
18. Song JP, Wu L, Dong WD, et al. MOF-derived nitrogen-doped core-shell hierarchical porous carbon confining selenium for advanced lithium-selenium batteries. *Nanoscale* 2019;11:6970-81. DOI PubMed
19. Yang CP, Xin S, Yin YX, Ye H, Zhang J, Guo YG. An advanced selenium-carbon cathode for rechargeable lithium-selenium batteries. *Angew Chem Int Ed Engl* 2013;52:8363-7. DOI PubMed
20. Ji X, Lee KT, Nazar LF. A highly ordered nanostructured carbon-sulphur cathode for lithium-sulphur batteries. *Nat Mater* 2009;8:500-6. DOI PubMed
21. Zhao Y, Song Z, Li X, et al. Metal organic frameworks for energy storage and conversion. *Energy Storage Materials* 2016;2:35-62. DOI
22. Wang L, Han Y, Feng X, Zhou J, Qi P, Wang B. Metal-organic frameworks for energy storage: Batteries and supercapacitors. *Coordination Chemistry Reviews* 2016;307:361-81. DOI
23. Liu X, Sun T, Hu J, Wang S. Composites of metal-organic frameworks and carbon-based materials: preparations, functionalities and applications. *J Mater Chem A* 2016;4:3584-616. DOI
24. Xu J, Lawson T, Fan H, Su D, Wang G. Updated metal compounds (MOFs, S, OH, N, C) used as cathode materials for lithium-sulfur batteries. *Adv Energy Mater* 2018;8:1702607. DOI
25. Pan Y, Liu Y, Zeng G, Zhao L, Lai Z. Rapid synthesis of zeolitic imidazolate framework-8 (ZIF-8) nanocrystals in an aqueous system. *Chem Commun (Camb)* 2011;47:2071-3. DOI PubMed
26. Cravillon J, Münzer S, Lohmeier S, Feldhoff A, Huber K, Wiebcke M. Rapid room-temperature synthesis and characterization of nanocrystals of a prototypical zeolitic imidazolate framework. *Chem Mater* 2009;21:1410-2. DOI
27. Stolar T, Užarević K. Mechanochemistry: an efficient and versatile toolbox for synthesis, transformation, and functionalization of porous metal-organic frameworks. *CrystEngComm* 2020;22:4511-25. DOI
28. Zhou J, Li R, Fan X, et al. Rational design of a metal-organic framework host for sulfur storage in fast, long-cycle Li-S batteries. *Energy Environ Sci* 2014;7:2715. DOI
29. Tang J, Yamauchi Y. Carbon materials: MOF morphologies in control. *Nat Chem* 2016;8:638-9. DOI PubMed
30. Dang S, Zhu Q, Xu Q. Nanomaterials derived from metal-organic frameworks. *Nat Rev Mater* 2018;3:17075. DOI
31. Lim S, Suh K, Kim Y, et al. Porous carbon materials with a controllable surface area synthesized from metal-organic frameworks. *Chem Commun (Camb)* 2012;48:7447-9. DOI PubMed
32. Chaikittisilp W, Ariga K, Yamauchi Y. A new family of carbon materials: synthesis of MOF-derived nanoporous carbons and their promising applications. *J Mater Chem A* 2013;1:14-9. DOI
33. Wu HB, Lou XWD. Metal-organic frameworks and their derived materials for electrochemical energy storage and conversion: promises and challenges. *Sci Adv* 2017;3:eaap9252. DOI PubMed PMC
34. Liu Y, Si L, Zhou X, et al. A selenium-confined microporous carbon cathode for ultrastable lithium-selenium batteries. *J Mater Chem A* 2014;2:17735-9. DOI
35. Li X, Sun Q, Liu J, Xiao B, Li R, Sun X. Tunable porous structure of metal organic framework derived carbon and the application in lithium-sulfur batteries. *Journal of Power Sources* 2016;302:174-9. DOI
36. Kim D, Kim DW, Hong WG, Coskun A. Graphene/ZIF-8 composites with tunable hierarchical porosity and electrical conductivity. *J Mater Chem A* 2016;4:7710-7. DOI
37. Chen K, Sun Z, Fang R, Shi Y, Cheng H, Li F. Metal-organic frameworks (MOFs)-derived nitrogen-doped porous carbon anchored on graphene with multifunctional effects for lithium-sulfur batteries. *Adv Funct Mater* 2018;28:1707592. DOI
38. Park S, Park J, Kang YC. Selenium-infiltrated metal-organic framework-derived porous carbon nanofibers comprising interconnected bimodal pores for Li-Se batteries with high capacity and rate performance. *J Mater Chem A* 2018;6:1028-36. DOI
39. Yu W, Dong W, Li C, et al. Interwoven scaffolded porous titanium oxide nanocubes/carbon nanotubes framework for high-performance sodium-ion battery. *Journal of Energy Chemistry* 2021;59:38-46. DOI
40. Yuan L, Yuan H, Qiu X, Chen L, Zhu W. Improvement of cycle property of sulfur-coated multi-walled carbon nanotubes composite cathode for lithium/sulfur batteries. *Journal of Power Sources* 2009;189:1141-6. DOI
41. Lu C, Wang D, Zhao J, Han S, Chen W. A continuous carbon nitride polyhedron assembly for high-performance flexible supercapacitors. *Adv Funct Mater* 2017;27:1606219. DOI
42. Huang G, Zhang F, Du X, Qin Y, Yin D, Wang L. Metal organic frameworks route to in situ insertion of multiwalled carbon nanotubes in Co_3O_4 polyhedra as anode materials for lithium-ion batteries. *ACS Nano* 2015;9:1592-9. DOI PubMed
43. Wu R, Wang DP, Rui X, et al. In-situ formation of hollow hybrids composed of cobalt sulfides embedded within porous carbon polyhedra/carbon nanotubes for high-performance lithium-ion batteries. *Adv Mater* 2015;27:3038-44. DOI PubMed
44. Li C, Wang Y, Li H, et al. Weaving 3D highly conductive hierarchically interconnected nanoporous web by threading MOF crystals onto multi walled carbon nanotubes for high performance Li-Se battery. *Journal of Energy Chemistry* 2021;59:396-404. DOI
45. Mao Y, Li G, Guo Y, et al. Foldable interpenetrated metal-organic frameworks/carbon nanotubes thin film for lithium-sulfur batteries. *Nat Commun* 2017;8:14628. DOI PubMed PMC

46. Zhang H, Zhao W, Zou M, et al. 3D, mutually embedded MOF@Carbon nanotube hybrid networks for high-performance lithium-sulfur batteries. *Adv Energy Mater* 2018;8:1800013. DOI
47. Zhu J, Jiang Z. Electrochemical photocatalytic degradation of eriochrome black T dye using synthesized TiO_2@CNTs nanofibers. *Int J Electrochem Sci* 2021;16:210318. DOI PubMed
48. Kulkarni G, Velhal N, Phadtare V, Puri V. Enhanced electromagnetic interference shielding effectiveness of chemical vapor deposited MWCNTs in X-band region. *J Mater Sci: Mater Electron* 2017;28:7212-20. DOI
49. Chen M, Lu Q, Li Y, Chu M, Cao X. ZnO@ZIF-8 core-shell heterostructures with improved photocatalytic activity. *CrystEngComm* 2021;23:4327-35. DOI
50. Dong W, Chen H, Xia F, et al. Selenium clusters in Zn-glutamate MOF derived nitrogen-doped hierarchically radial-structured microporous carbon for advanced rechargeable Na-Se batteries. *J Mater Chem A* 2018;6:22790-7. DOI
51. Balakumar K, Kalaiselvi N. Selenium containing tube-in-tube carbon: a one dimensional carbon frame work for selenium cathode in Li-Se battery. *Carbon* 2017;112:79-90. DOI
52. Liu T, Dai C, Jia M, et al. Selenium embedded in metal-organic framework derived hollow hierarchical porous carbon spheres for advanced lithium-selenium batteries. *ACS Appl Mater Interfaces* 2016;8:16063-70. DOI PubMed
53. Dong W, Li C, Wang C, et al. Phase conversion accelerating "Zn-Escape" effect in ZnSe-CFs heterostructure for high performance Sodium-Ion half/full batteries. *Small*. DOI
54. Dong W, Wang D, Li X, et al. Bronze TiO_2 as a cathode host for lithium-sulfur batteries. *Journal of Energy Chemistry* 2020;48:259-66. DOI
55. Han K, Liu Z, Shen J, Lin Y, Dai F, Ye H. A free-standing and ultralong-life lithium-selenium battery cathode enabled by 3D mesoporous carbon/graphene hierarchical architecture. *Adv Funct Mater* 2015;25:455-63. DOI
56. Qiu R, Fei R, Zhang T, et al. Biomass-derived, 3D interconnected N-doped carbon foam as a host matrix for Li/Na/K-selenium batteries. *Electrochimica Acta* 2020;356:136832. DOI
57. Li H, Dong W, Li C, et al. Three-dimensional ordered hierarchically porous carbon materials for high performance Li-Se battery. *Journal of Energy Chemistry* 2022;68:624-36. DOI
58. Xiao L, Li E, Yi J, et al. Enhancing the performance of nanostructured ZnO as an anode material for lithium-ion batteries by polydopamine-derived carbon coating and confined crystallization. *Journal of Alloys and Compounds* 2018;764:545-54. DOI
59. Dong WD, Yu WB, Xia FJ, et al. Melamine-based polymer networks enabled N, O, S Co-doped defect-rich hierarchically porous carbon nanobelts for stable and long-cycle Li-ion and Li-Se batteries. *J Colloid Interface Sci* 2021;582:60-9. DOI PubMed
60. Li Y, Dong B, Zerrin T, et al. State-of-health prediction for lithium-ion batteries via electrochemical impedance spectroscopy and artificial neural networks. *Energy Storage* 2020:2. DOI

Bao-Lian Su

Bao-Lian Su created the Laboratory of Inorganic Materials Chemistry (CMI) at the University of Namur, Belgium in 1995. He is currently Full Professor of Chemistry, Member of the European Academy of Sciences, Member of the Royal Academy of Belgium, Fellow of the Royal of Society of Chemistry, UK and Life Member of Clare Hall College, University of Cambridge. He is also a strategy scientist at Wuhan University of Technology, China. He is the Editor-in-Chief of the *Chemical Synthesis*, Section Editor of the National Science Review and the Managing Editor of the NANO. His current research fields include the synthesis, the property study and the molecular engineering of organized, hierarchically porous and bio-organisms for artificial photosynthesis, (photo) Catalysis, Energy Conversion and Storage, Biotechnology, Cell therapy and Biomedical applications.

Yu Li

Yu Li received his B.S. from Xi'an Jiaotong University in 1999 and received his M.S. from Liaoning Shihua University in 2002. He obtained his Ph.D. from Zhejiang University in 2005. He worked in EMAT at the University of Antwerp with Prof. G. Vantendeloo in 2005 and then in CMI at the University of Namur with Prof. Bao-Lian Su in 2006. Currently, he is a full-time Professor at Wuhan University of Technology. His research interests include nanomaterials design and synthesis, hierarchically porous materials synthesis, and their applications in the fundamental aspects of energy and environment.

Hongyan Li

Hongyan Li received her ME degree in 2017 from Ocean University of China. She is a PhD candidate at the University of Namur, Inorganic Materials Chemistry (CMI). Her research interests mainly focus on Lithium-selenium battery, Lithium-ion battery and Dye-Sensitized Solar Cells.

Li *et al. Chem Synth* 2022;2:9
DOI: 10.20517/cs.2022.05

Chemical Synthesis

Review

Open Access

Nanostructured heterogeneous photocatalyst materials for green synthesis of valuable chemicals

Yaru Li[1,2,3], Dongsheng Zhang[2,4], Wei Qiao[4], Hongwei Xiang[1,2], Flemming Besenbacher[5], Yongwang Li[1,2], Ren Su[2,4,*]

[1]State Key Laboratory of Coal Conversion, Institute of Coal Chemistry, Chinese Academy of Science, Taiyuan 030001, Shanxi, China.
[2]SynCat@Beijing, Synfuels China Technology Co. Ltd., Beijing 101407, China.
[3]University of Chinese Academy of Sciences, Beijing 100049, China.
[4]Key Laboratory of Advanced Carbon Materials and Wearable Energy Technologies of Jiangsu Province, Soochow Institute for Energy and Materials InnovationS (SIEMIS), Soochow University, Suzhou 215006, Jiangsu, China.
[5]Interdisciplinary Nanoscience Center (iNANO), Aarhus University, Aarhus C DK-8000, Denmark.

***Correspondence to:** Prof. Ren Su, Key Laboratory of Advanced Carbon Materials and Wearable Energy Technologies of Jiangsu Province, Soochow Institute for Energy and Materials InnovationS (SIEMIS), Soochow University, Moxie Road 688, Gusu District, Suzhou 215006, Jiangsu, China. E-mail: suren@suda.edu.cn

How to cite this article: Li Y, Zhang D, Qiao W, Xiang H, Besenbacher F, Li Y, Su R. Nanostructured heterogeneous photocatalyst materials for green synthesis of valuable chemicals. *Chem Synth* 2022;2:9. https://dx.doi.org/10.20517/cs.2022.05

Received: 9 Mar 2022 **First decision:** 31 Mar 2022 **Revised:** 23 Apr 2022 **Accepted:** 27 Apr 2022 **Published:** 27 Apr 2022

Academic Editor: Bao-Lian Su **Copy Editor:** Jia-Xin Zhang **Production Editor:** Jia-Xin Zhang

Abstract

The photocatalytic process employing nanostructured semiconductor materials has attracted great attention in energy production, CO_2 reduction, and water/air purification for decades. Recently, applying heterogeneous photocatalyst for the synthesis of valuable chemicals is gradually emerging and considered as a promising process for the conversion of cheap resources (i.e., biomass derivatives, polyols, and aromatic hydrocarbons). Compared with traditional thermal catalytic approaches, the photocatalytic process provides a mild reaction condition and flexible platform (photocatalyst) that allows precise tweaking of reaction intermediates and reaction pathways, thus resulting in fine control of the selective synthesis of specialized chemicals that are challenging for thermal catalysis. In this review, we summarize recent achievements in photocatalytic synthesis of various industrial important chemicals via photo-oxidative and photo-reductive processes. The selective oxidation of alcohols and aromatics, epoxidation of alkenes, hydrogenation of gaseous molecules and hydrocarbons, and coupling reactions by means of various photocatalysts including metal oxides, supported plasmonic metal nanostructures, conjugated organic polymers, anchored homogeneous catalysts, and dye-sensitized heterostructures are discussed from a material perspective. In addition, fundamental understandings of reaction mechanisms and rational design of nanostructured photocatalysts for enhancing efficiency, selectivity, and stability are discussed in detail.

Keywords: Photocatalysis, chemical synthesis, green chemistry, reaction mechanisms, material design

INTRODUCTION

Heterogeneous catalysis is paramount in modern society, and different types of catalysts have been designed and utilized in various industrial applications, e.g., ammonia synthesis[1,2], Fischer-Tropsch synthesis[3], oil desulfurization[4], and fuel cells[5]. As a branch of heterogeneous catalysis, photocatalysis has received great attention over the last decades in water splitting, CO_2 reduction, and water/air purification from both fundamental and application perspectives[6-11]. To drive these reactions using solar energy, various semiconductor-based materials, including metal oxides, nitrides, and sulfides[12-20], organic polymers[21,22], perovskites[23,24], and metal-organic frameworks (MOF)[25-28], with moderate bandgaps have been developed. These materials have been further engineered by means of constructing heterojunctions (i.e., semiconductor interfaces and loading of metal cocatalysts) to improve their photocatalytic performance in terms of efficiency and stability[29-36]. The boom in photocatalyst materials also leads to the exploration of employing a photocatalytic approach for synthetic applications[37-42] that may have an instantaneous impact.

The synthetic paths via photocatalysis exhibit several intrinsic advances compared with conventional thermal-catalytic approaches. While traditional catalysts accelerate reactions by means of forming instable surface adsorbed intermediate species with lower activation energy, the photocatalytic processes involve the excitation of the catalyst and the reactants to higher energy states that overcome the activation energy barriers. Therefore, corrosion-resistant reactors for harsh reaction conditions (i.e., high temperatures and pressures and strong oxidants and reductants) can be simplified for photocatalytic synthesis (i.e., ammonia synthesis, Fischer-Tropsch synthesis, and selective oxidation and hydrogenation reactions)[43-46]. However, researchers should be aware that specialized reactors with optimized light transmittance and mass transportation are required for heterogeneous photocatalysis. In fact, the photon energy is ~1.7-3 eV in the visible light region, which is sufficient to drive most catalytic reactions. Owing to the mild reaction conditions and tunable band positions of the semiconductor photocatalysts, some challenging redox reactions that require precise control of the redox potentials can be realized by photocatalytic approaches with high conversion and selectivity (i.e., epoxidation reactions and coupling reactions)[47-49]. This results in a significant reduction in energy consumption for separation processes (i.e., distillation, filtration, and sublimation), which is desirable for economic and environmental purposes. Nevertheless, a longer lifetime of the photocatalyst materials is expected due to such mild reaction conditions, which is essential for noble metal-supported systems, delicate surface engineered materials, and anchored homogeneous catalysts.

Employing homogeneous photocatalyst materials for the synthesis of value-added chemicals has been investigated for decades and received significant achievements. Metal complex redox catalysts (i.e., $[Ru(bpz)_3](PF_6)_2$ and fac-$Ir(ppy)_3$) and conjugated soluble dye molecules (i.e., Eosin Y and fluorescein) are frequently used in homogeneous photocatalysts due to their strong light absorbance in the visible light region, excellent solubility, and long excited-state lifetimes[50-53]. By controlling the reaction conditions and the chelating ligands of the redox complexes, a variety of important reactions including carbonyl (C-C) coupling, imino-pinacol (C-N) coupling, C-O coupling, cycloaddition, and alkylation and arylation of alkanes can be realized with high selectivity and stereo-regularity[54-65]. However, homogeneous photocatalytic systems are facing challenges in the cost of expensive metal complex catalysts, the instability of the polymeric catalysts, and the separation of products.

Several in-depth reviews summarize recent progress in utilizing heterogeneous photocatalyst for the synthesis of valuable chemicals from different perspectives, targeting specific reactions (i.e., partial

oxidation, C-C coupling, and biomass products conversion), materials (i.e., TiO_2, polyoxometalate, and supported plasmonic metal nanoparticles), and reactor design[45,46,66-74]. Miyabe and Kohtani[68] emphasized recent developments of TiO_2-based photocatalysts in heterogeneous photocatalytic reductive and oxidative organic synthesis. Bloh *et al.*[69] summarized recent developments in heterogeneous photoredox catalysis with a special focus on materials optimization. This review addresses advances in photocatalytic synthesis from an application-orientated perspective, presenting the development in the design of nanostructured photocatalyst materials by covering up-to-date and classical works. We categorize the photocatalytic reactions into oxidative and reductive reactions, which are further subdivided into alcohol oxidation, epoxidation, oxidation of aromatics oxidative coupling, hydrogenation reactions, and reductive coupling [Scheme 1]. The design strategies, selection rules, advantages, and limitations of various nanostructured photocatalyst materials, including metal oxides, supported plasmonic metal nanostructures, organic polymers, anchored homogeneous catalysts, and dye-sensitized heterostructures, are also summarized. For oxidation reactions, the optimization of oxidation power of the photocatalyst is presented for the controlled synthesis of target products to avoid overoxidation. Correspondingly, the manipulation of photogenerated hydrogen atoms for selective reduction reactions by controlling the surface properties of the photocatalyst is discussed. In addition, fundamental understandings of reaction mechanisms for the rational design of nanostructured photocatalysts are presented. Moreover, this review presents the recent design and development of continuous reactors for scaling-up of photocatalytic processes.

NANOSIZED PHOTOCATALYSTS FOR OXIDATION REACTIONS

Alcohol oxidation

Monohydric alcohols

Monohydric and polyhydric alcohols are widely used as hole scavengers in photocatalytic hydrogen production (i.e., methanol, ethanol, glycerol, and triethanolamine)[75-77]. Bahruji *et al.*[76] showed that monohydric alcohols dissociate via the decarbonylation oxidation process when Pd nanoparticle (NP)-modified TiO_2 is used as the photocatalyst under deaerated conditions, resulting in the formation of H_2, CO_2, and corresponding hydrocarbons, as demonstrated in Equations (1) and (2):

$$RCH_2OH + H_2O \xrightarrow{Pd/TiO_2,\ hv} CO_2 + RH + 2H_2 \quad \text{Eq. (1)}$$

$$RR'CHOH + H_2O \xrightarrow{Pd/TiO_2,\ hv} CO_2 + RH + R'H + H_2 \quad \text{Eq. (2)}$$

It is proposed that the alcohol decarbonylation process takes place on the Pd NP surface with CO as the reaction intermediate, which is further oxidized to CO_2 by the photogenerated oxygen species on the TiO_2 surface. To further enhance the activity and extend the reaction into visible light region, plasmonic metal NPs have been loaded onto various semiconductor photocatalysts (i.e., TiO_2 and g-C_3N_4) to serve as both promoter and light absorber[78,79].

Beyond the evolution of gaseous H_2, the liquid phase products may also be influenced by the identity of the metal promoter and the microstructure of the semiconductor during photocatalytic alcohol oxidation under anaerobic conditions. Ruberu *et al.*[80] revealed that the semiconductor-metal heterostructures dictate photocatalytic dehydrogenation and hydrogenolysis of benzyl alcohol. As demonstrated in Figure 1A, while CdS-Pt favors dehydrogenation of benzyl alcohol to generate benzaldehyde and H_2, $CdS_{0.4}Se_{0.6}$-Pd favors further hydrogenolysis of the generated benzaldehyde by the photogenerated H_2, resulting in the formation of toluene. A mechanistic study using labeled benzyl alcohol reveals that the adsorption of photogenerated

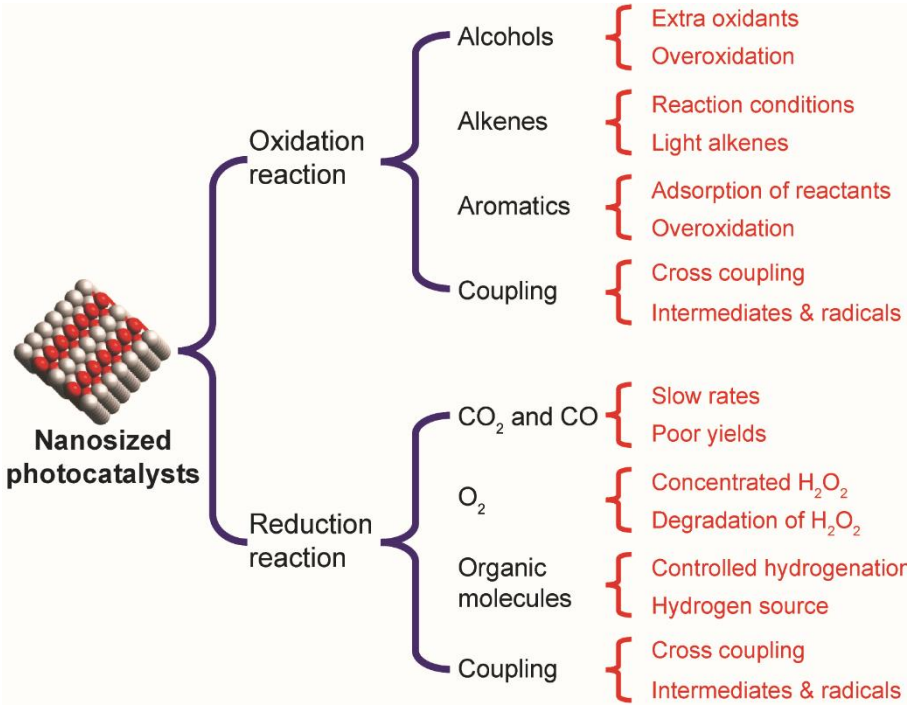

Scheme 1. Categories of heterogeneous photocatalytic synthetic reactions discussed in this review and their major challenges.

hydrogen atoms is stronger on the Pd surface than on the Pt surface, thus resulting in the consecutive hydrogenolysis benzaldehyde. Such a design strategy is useful for synthetic chemistry via photocatalytic hydrogen transfer reactions.

Lu *et al.*[81] showed that modulation of TiO_2 microstructure and polymorph can alter the oxidation kinetics and pathway of photocatalytic ethanol reforming under deaerated conditions in water solution. While ethanol is oxidized to acetaldehyde and acetic acid over Pt-modified Degussa P25®, the value-added coupling product (2,3-butanediol) is selectively formed on rutile TiO_2. The conversion of ethanol and selectivity to 2,3-butanediol can be further enhanced by employing Pt-modified rutile nanotubes with filled channels, as shown in Figure 1B. Such configuration prevents the deep oxidation of photogenerated α-hydroxyethyl radicals (CH_3•CHOH) within the pores and thus facilitates the desorption of CH_3•CHOH, which undergoes a coupling reaction to form 2,3-butanediol in the solution. Later, the same group reported that absolute ethanol can be directly converted to 1,1-diethoxyethane and H_2 using Pt-TiO_2 nanotubes and nanorods under deaerated conditions following Equations (3) and (4)[82]:

$$CH_3CH_2OH \xrightarrow{hv,\ Pt/TiO_2} CH_3CHO + H_2 \quad \text{Eq. (3)}$$

$$CH_3CHO + 2CH_3CH_2OH \rightarrow CH_3CH(OCH_2CH_3)_2 + H_2O \quad \text{Eq. (4)}$$

Interestingly, although almost the same photocatalyst materials were used in both studies[81,82], the liquid phase products are completely different. Therefore, we suppose that the different reaction mechanisms originate from the presence of water, which dictates the conversion of ethanol to undergo either dehydrogenation or dehydration process.

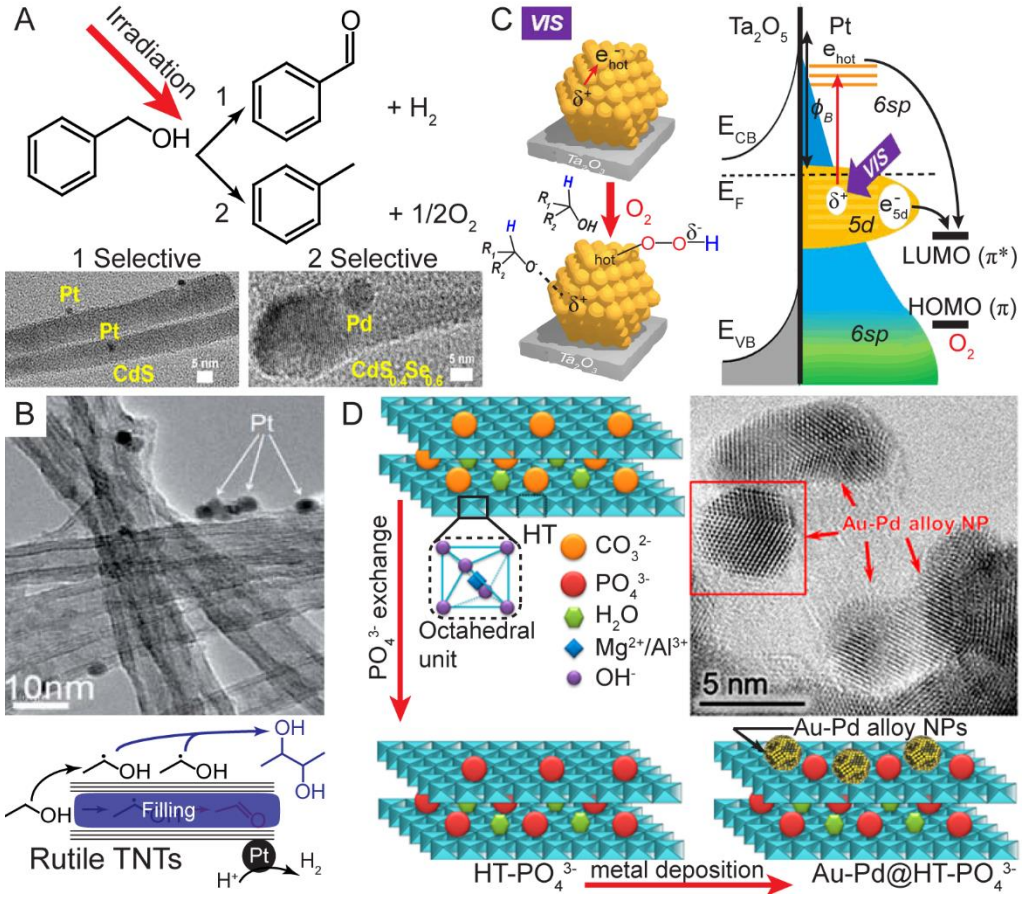

Figure 1. (A) Selective oxidation of benzyl alcohol to benzaldehyde and toluene using Pt/CdS and Pd/$CdS_{0.4}Se_{0.6}$ photocatalyst, respectively. This figure is used with permission from the American Chemistry Society[80]. (B) Selective photoconversion of ethanol to butanediol using rutile TiO_2 nanotubes with filled channels. This figure is used with permission from the Royal Society of Chemistry[81]. (C) Schematic demonstration of aerobic alcohol oxidation using a Pt/Ta_2O_5 photocatalyst under visible light irradiation. (D) Au-Pd NPs functionalized HT-PO_4^{3-} for selective photocatalytic esterification of alcohols. This figure is used with permission from the American Chemistry Society[87,91]. NPs: Nanoparticles.

Recently, more attention has been focused on the oxidation half-reaction, where the alcohols may convert to various value-added products in liquid phase under aerobic conditions. Photocatalytic oxidation of alcohols into aldehydes or ketones has been realized under aerobic conditions using TiO_2-based photocatalysts[83]; however, low efficiency and poor selectivity are the main challenges that need to be solved. Generally, loading Au, Ag, or Pt NPs on semiconductor photocatalysts can promote visible light absorption via interband transition of d band electrons and produce hot electrons (e_{hot}^-)[84], which are injected into the conduction band (CB) of the semiconductor. e_{hot}^-, together with the positive charges (holes, δ^+) formed on the semiconductor, are consequently consumed by surface adsorbed O_2 and alcohol molecules to complete the aerobic oxidation cycle. e_{hot}^- should not be confused with the CB electrons (e_{CB}^-) generated by semiconductor photocatalysts, as it refers to the surface localized vibrational electrons generated by plasmonic metal nanoparticles under irradiation. To further enhance the charge separation efficiency, Li *et al.*[85] deposited Au NPs on BiOCl with oxygen vacancies. The photogenerated e_{hot}^- can therefore be trapped at the vacancy states, thus prolonging the lifetime of the δ^+ on the Au surface. However, researchers should be aware that, since the injection of e_{hot}^- into the semiconductor needs to overcome the Schottky barrier at the metal-semiconductor interface[86], the efficiency of these systems is still low in general. To further increase the efficiency, Sakamoto *et al.*[87] proposed depositing noble metal NPs on large bandgap

semiconductors to create sufficient high work function (ϕ_B) and thus avoid electron transferring across the metal/semiconductor interface. Here, Pt NPs are supported on Ta_2O_5 (E_g ~4.0 eV) to absorb visible light. The photogenerated e_{hot} and δ^+ will be confined on the Pt surface to react with molecular O_2 and alcohols, as demonstrated in Figure 1C. A series of high-performance systems have been developed with this design principle (i.e., Au/Al_2O_3 and Pt/SiO_2) for the oxidation of various alcohols (i.e., isopropanol and benzyl alcohols) into corresponding aldehydes or ketones. Similarly, the confinement of e_{hot}^- on the metal surface can also be realized by employing engineered alloy NPs or simply metal clusters[88,89]. However, researchers should be aware that such a process is a photo-induced thermal catalytic reaction rather than a classical photocatalytic reaction.

Beyond aldehydes and ketones, alcohols can also be converted to other products via photocatalytic oxidation process. Han *et al.*[90] showed that Au-Ag alloy NPs supported on TiO_2 can efficiently oxidize methanol into methyl formate selectively under low oxygen pressure and UV irradiation. Here, methanol gradually dissociates into methoxy (CH_3O•) or formaldehyde (CH_2O) on TiO_2 surface. The generated formaldehyde then undergoes dehydration with another methanol molecule to generate methyl formate. The presence of metal NPs promotes oxygen dissociation to consume the surface-adsorbed H atoms into water. The optimum conversion and selectivity to methyl formate are achieved when the Au-Ag alloy with a 1:1 ratio is loaded onto TiO_2. However, this reaction takes place in gas phase, and the concentration of O_2 (< 0.5%) needs to be carefully controlled to avoid CO_2 formation. To overcome these drawbacks, Xiao *et al.*[91] employed Au-Pd alloy NPs supported on phosphate-modified hydrotalcite (HT-PO_4^{3-}) to convert a series of aliphatic alcohols into corresponding esters in O_2 under neutral conditions. As presented in Figure 1D, phosphate anions are introduced into the calcined HT ($[Mg_6Al_2(OH)_{16}]CO_3 \cdot mH_2O$) via ion exchange, which is then loaded onto Au-Pd alloy NPs. Such structure couples the basic sites of the HT support and the photocatalytic properties of the alloy NPs, which promotes the dehydrogenation of alcohols into ketones and thus the consecutive esterification of the generated ketones with alcohols via under dehydration.

Polyhydric alcohols

Catalytic conversion of polyols (i.e., diols, triols, sugars, cyclitols, and celluloses) to high-value chemicals (i.e., polyurethanes, polyesters, and polycarbonates) is of potential importance in the chemical industry and has also attracted increasing attention in photocatalysis. Employing glycerol and other polyols as hole scavengers for photocatalytic hydrogen production under deaerated conditions is the most direct application[92,93], but the conversion efficiency is relatively low. To help the design of high performance photocatalyst, Lercher's group investigated photocatalytic reforming of a series polyols in water solution over the Rh-TiO_2 system based on global kinetic analysis[94,95]. The polyol conversion takes place via three possible pathways: oxidative C-C bond cleavage from direct hole transfer to chemisorbed oxygenates on terminal Ti(IV)-OH groups, oxidation to corresponding aldoses or ketoses initiated by indirect hole trapping at surface lattice oxygen sites, and light-driven dehydration (minor). Jin *et al.*[96] further revealed the reaction mechanism of polyol conversion using ethylene glycol (EG) at molecular level on pristine TiO_2 and metal NPs decorated TiO_2 by coupling *in situ* surface science techniques with vibrational spectroscopies. As shown in Figure 2A and B, *in situ* scanning tunneling microscopy (STM) images suggest that EG molecules are adsorbed on the five-coordinated Ti (Ti5c) of rutile TiO_2 (110) surface and photocatalytically converted into two parts of formaldehyde and surface-adsorbed hydrogen atoms (H_{ads}) via oxidative C-C bond cleavage. The active sites remain on the TiO_2 surface even after loading Au nanoclusters on rutile TiO_2 (110), as shown in Figure 2C and D. *In situ* IR-MS spectroscopy suggests that the desorption of H_{ads} to H_2 is the rate-determining step (RDS), which can be promoted by metal NPs (Au, Pd, and Pt) due to the low free adsorption energy of H_{ads} on metal surface, thus improving the dissociation of EG. Chong *et al.*[97] confirmed that the selectivity and efficiency in polyol conversion can be tuned by

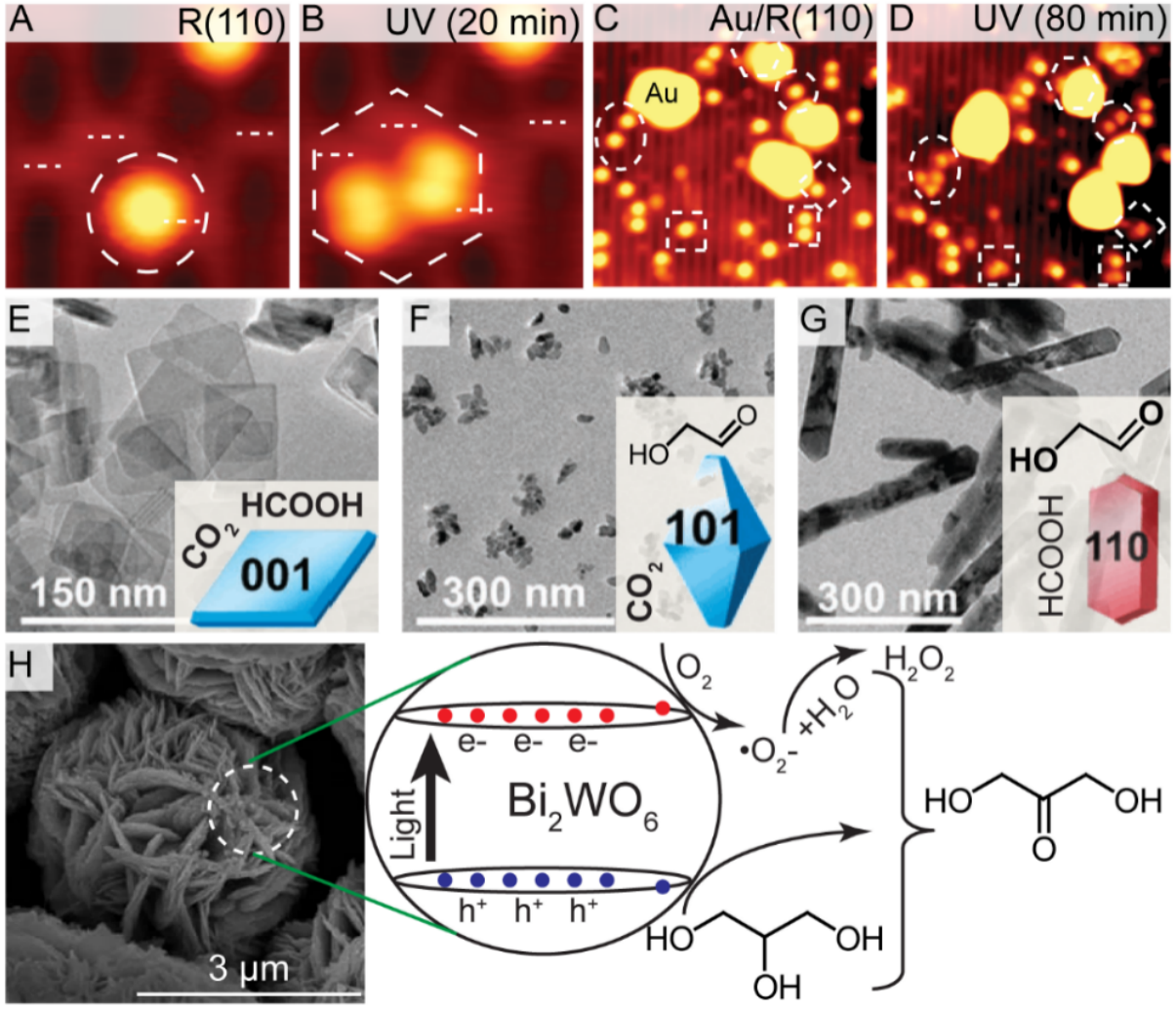

Figure 2. (A,B) *In situ* STM images (2.7 × 2.7 nm) of EG adsorbed on pristine rutile (110) before and after irradiation. (C,D) *In situ* STM images (15 × 15 nm) of EG adsorbed on Au on rutile (110) before and after irradiation. This figure is used with permission from Elsevier[96]. (E-G) TEM images of shaped TiO_2 showing tunable selectivity in glycerol conversion. (H) SEM image of the Bi_2WO_6 catalyst and proposed mechanism for selective oxidation of glycerol under visible-light irradiation. This figure is used with permission from the Royal Society of Chemistry[97,100]. EG: Ethylene glycol.

controlling the electronic and surface structure of the TiO_2-based photocatalyst materials. As presented in Figure 2E-G, the selectivity in photocatalytic glycerol conversion can be tuned by varying the shape of anatase and rutile TiO_2. While Pt-loaded anatase with dominant {001} or {101} facets leads to the formation of formaldehyde and CO_2 with low conversion to glycolaldehyde, shaped rutile with a high percentage of {110} facets results in high selectivity towards glycolaldehyde (> 90%) without the formation of CO_2.

Photocatalytic conversion of polyols with the presence of oxygen has also been investigated. Augugliaro *et al.*[98] showed that most commercially available TiO_2-based photocatalysts will oxidize glycerol into 1,3-dihydroxyacetone, glyceraldehyde, formic acid, and carbon dioxide in aqueous phase. Such a process requires no metal cocatalyst, as the photogenerated H_{ads} will be consumed by the molecular oxygen to yield water. However, the selectivity in polyol conversion under oxygen conditions is more complex and difficult to control. We employed EG as the model polyol to investigate the reaction pathways and the role of metal NPs under aerated conditions using *in situ* IR-MS spectrometry[99]. Ethylene glycol undergoes the C-C bond

cleavage process to formaldehyde, which is subsequently oxidized into CO_2 or polymerized to paraformaldehyde with the photogenerated water. Similar to the reaction initiated under deaerated conditions, the removal of photogenerated H_{ads}^+ by O_2 and photogenerated e^- is the RDS. Interestingly, loading Ag and Au NPs on TiO_2 increases the selectivity to paraformaldehyde, whereas Pt cocatalyst promotes the complete oxidation of EG to CO_2. *In situ* IR-MS spectrometry reveals that Ag- and Au-modified TiO_2 can provide water directly through H_{ads}^+ interaction with O_2 and e_{CB}^-, whereas Pt/TiO_2 supply water indirectly via H_2 and formaldehyde oxidation.

The main drawbacks of TiO_2-based photocatalysts are poor efficiency under visible light and deep oxidation of polyol into CO_2. Zhang *et al.*[100] further developed a flower-like Bi_2WO_6 photocatalyst to overcome these challenges [Figure 2H]. The Bi_2WO_6 photocatalyst is characterized by a mild oxidation power (Eg ≈ 2.8 eV), which can selectively oxidize glycerol to 1,3-dihydroxyacetone under visible light radiation in water solution via the direct hole transfer process. Additionally, the 1,3-dihydroxyacetone molecule weakly adsorbes on Bi_2WO_6, which prevents deep oxidation and thus achieves high selectivity.

Although the photocatalytic oxidation of alcohols shows huge potential for the utilization of biomass as a chemical feedstock for the synthesis of value-added products, in-depth investigations are necessary to further gear up the productivity and selectivity under mild conditions. This also requires accelerating the reduction of molecular oxygen in a controlled manner for the rapid generation of ideal oxidative radical species, which is crucial in avoiding the use of extra oxidants [*e.g.*, Hydrogen peroxide (H_2O_2) and O_3].

Epoxidation reactions

Synthesis of epoxides via heterogeneous catalytic epoxidation of alkenes is a challenging and important reaction in both industry and fundamental research. Ag-, Au-, and Cu-based catalysts are typically employed for the selective oxidation of a series of alkenes (i.e., ethylene, propylene, and styrene), which are normally performed under elevated pressure (1-3 MPa) and moderate temperature (220 °C -280 °C) for optimized activity and selectivity[101,102]. Transition state analysis reveals that tuning the identity of metal catalyst (Ag and Cu) can promote the conversion of the common oxametallocycle intermediate to either epoxide or acetaldehyde in ethylene oxidation, thus avoiding the full oxidation of alkenes to CO_2[103].

Since these metal catalysts also show plasmonic absorption in visible light region, it is reasonable to employ them as photocatalysts for epoxidation reactions under visible light irradiation. Indeed, Christopher *et al.*[104,105] showed that Ag nanocubes (20 wt%, ~ 75 nm) loaded on α-Al_2O_3 support can realize selective oxidation of ethylene to ethylene oxide with a selectivity of ~50%. Although the photocatalytic epoxidation reaction still needs to be operated at elevated temperature to achieve reasonable quantum efficiency (~40% at 200 °C and ~4% at 150 °C), the epoxidation rate is significantly higher than that of the pure thermal catalytic process. This suggests that the process is more likely a photo-induced thermal process rather than a photocatalytic approach. Later, the same group further developed Cu NPs (2 wt%, ~ 45 nm) supported on SiO_2 for the selective oxidation of propylene[106]. Interestingly, such a system shows a higher selectivity in propylene epoxidation under visible light irradiation than that of the thermal process; thus, it is a photothermic-catalytic process. It is proposed that the high selectivity under irradiation is accompanied by light-induced redox of the surface Cu_2O layer to metallic Cu via localized surface plasmon resonance of the Cu core.

Zhang *et al.*[107] employed SERS coupled with theoretical calculations to understand the active sites of individual Ag NP catalyst for plasmon excitation-assisted ethylene epoxidation. It shows that graphene layers are first generated on the Ag surface under irradiation, which in turn promote the epoxidation of

ethylene at the edge defects sites. As shown in Figure 3A, TEM image reveals the activation of Ag/Al_2O_3 photocatalyst with *in situ* generated graphene layers on Ag NPs under irradiation with the presence C_2H_4 ($A\text{-}Ag/Al_2O_3$). Based on this evidence, they further developed a graphene/Ag/α-Al_2O_3 photocatalyst ($G\text{-}Ag/Al_2O_3$), which shows a similar feature in SERS spectra with distinct D and G bands of graphene compared with that of $A\text{-}Ag/Al_2O_3$ [Figure 3B]. Both the composite and the activated photocatalyst exhibit excellent performance in ethylene photo-epoxidation under ambient conditions compared with that of the conventional $Ag/\alpha\text{-}Al_2O_3$ catalyst [Figure 3C].

Recently, Huang *et al.*[47] showed that the selective photo-epoxidation of a series of aliphatic and aromatic alkenes can be realized in liquid phase using Cu NPs supported on titanium nitride (TiN) by O_2 or even air at moderate temperatures. The photocatalyst prepared by impregnation-reduction method exhibits well-dispersed metallic Cu NPs with a mean size of 4 nm supported on the TiN surface [Figure 3D], which shows excellent stability in photocatalytic styrene conversion. According to theoretical calculations, the Cu NPs remain in the metallic state under reaction conditions due to strong charge transfer between Cu NPs and the TiN support. Mechanistic study shows that the whole reaction takes place on the Cu surface. Firstly, the molecular oxygen reacts with cyclic ether solvent on the Cu surface under irradiation to produce oxygen adatoms (O_A). Then, the photogenerated O_A reacts with chemisorbed alkenes on Cu, forming a Cu-epoxide complex, and eventually desorbs as final products [Figure 3E]. Interestingly, they also observed product stereo-selectivity in *trans*-isomers for the epoxidation of stilbene.

The major advantage of photocatalytic epoxidation is the mild reaction conditions, which is ideal for some niche applications in medications and sterilizations that only require in situ generation of epoxides with relatively low concentration. This requires further investigations in robust, non-toxic photocatalyst materials, which can initiate the epoxidation of some light alkenes (i.e., ethylene and propene) under ambient conditions.

Oxidation of aromatics

Selective oxidation of aromatics to value-added products (i.e., alcohols or aldehydes) is important in the chemical industry as they are precursors for resins, electronics, and drugs[108,109]. The challenge in photocatalytic selective oxidation of aromatics is the development of photocatalysts with moderate oxidation power, which can partially oxidize specific functional groups while avoiding ring-opening and eventually CO_2 formation. For example, photocatalytic direct oxidation of benzene to phenol has attracted great interest, as such a process may overcome the Hock rearrangement that produces an excessive amount of acetone as a byproduct. Chen *et al.*[110] showed that Fe-doped g-C_3N_4 is active in the oxidation of benzene to phenol under visible light. Although H_2O_2 is needed as the oxidant and the conversion is relatively low, the low cost of the photocatalyst material shows promising potential for applications. Yoshida *et al.*[111] showed that Pt-TiO_2 can generate electrophilic oxygen species photocatalytically from water to initiate the oxidation of benzene to phenol under UV irradiation and deaerated conditions [Equation (5)]:

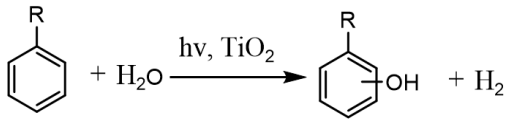

Eq. (5)

More importantly, a series of aromatics with different functional groups can be converted to corresponding phenolic compounds with relatively high selectivity. Mechanistic studies show that the reaction path is pH-dependent. Under neutral or acidic conditions, the photogenerated holes react with TiO_2 to produce surface

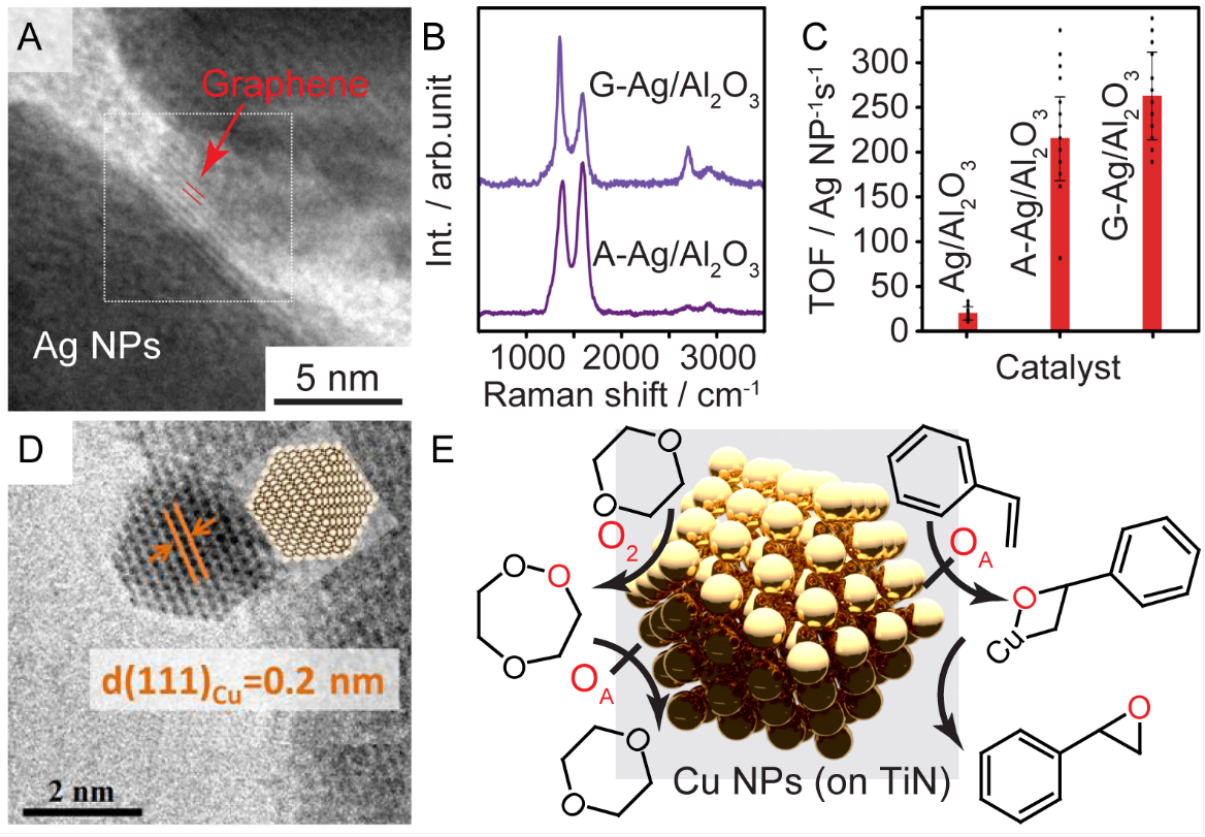

Figure 3. (A,B) TEM image and SERS showing graphene formation on Ag NPs during photo-epoxidation of C_2H_4. (C) TOF of C_2H_4 epoxidation using Ag-based photocatalyst. This figure is used with permission from A Creative Commons Attribution License[107]. (D,E) TEM image of single crystal Cu NP supported on TiN and the proposed reaction mechanisms in photo-epoxidation reaction. This figure is used with permission from the American Chemistry Society[47]. NPs: Nanoparticles; TOF: turnover frequency; SERS: surface-enhanced Raman scattering.

oxygen radicals, which attack the aromatic ring to form surface adsorbed phenoxy intermediates and eventually yield phenols. Under basic conditions, hydroxyl radical is the initial radical species that attacks the aromatic ring to produce phenols[112].

Researchers have further engineered the surface of photocatalysts with different strategies to improve the selectivity and conversion efficiency in benzene oxidation under ambient conditions using air or O_2 as the oxidant. Zhang *et al.*[113] incorporated TiO_2 NPs in hydrophobically modified mesocellular siliceous foam (TiO_2@MCF) for the synthesis of phenol. While the inner environment of the porous cage is hydrophobic due to surface silylation, the TiO_2 surface is hydrophilic after a post-UV treatment. Such structure has optimized the adsorption of benzene and desorption of phenol, thus avoiding further oxidation of phenol. Su *et al.*[114] showed that the selectivity for photo-oxidation of benzene to phenol can be enhanced by fine adjustment of the metal NPs that serve as a promoter. It is found that tuning the morphology and composition of Au-Pd metal NPs leads to the control of both polymerization of generated phenolic products and the complete oxidation of benzene. Specifically, $Au_{shell}Pd_{core}$-TiO_2 promotes the formation of phenol and switch-off undesired side reactions to quinones and CO_2, thus resulting in optimal performance and selectivity in photocatalytic benzene oxidation. Hosseini *et al.*[115] further supported Au-Pd NPs on visible light response materials (g-C_3N_4) to perform benzene oxidation and achieve high selectivity. A similar strategy has been employed to develop Cu_2O NPs supported on defective graphene with a long-

chain alkanethiols photocatalyst.[116] However, such systems require the addition of H_2O_2 and face the challenge of improving conversion of benzene. Ide *et al.*[117] encapsulated Au nano-discs between titanate interlayers ($K_{0.66}Ti_{1.73}Li_{0.27}O_{3.93}$) via surface modification with octadecyltrimethoxysilane to oxidize benzene under visible light using water as oxidant. Since the pristine titanate only absorbs UV light, the activity under visible light originates from the plasmonic absorption of the anisotropic-shaped Au NPs. Interestingly, it has been found that a high yield (62%) and selectivity (96%) to phenol can be achieved with the initial addition of phenol, although the promotion mechanism remains unclear.

Beyond the commonly used oxidants (i.e., O_2 and H_2O_2), photo-oxidative conversion of aromatic compounds can also be performed with the presence of other oxidants. Jaynes and Hill[118] showed that selective carbonylation of toluene and cyclic alkanes to corresponding aldehydes can be achieved under 1 bar of CO by employing polyoxotungstate ($[W_{10}O_{32}]^{3-}$ or $[PW_{12}O_{40}]^{3-}$), which is a type of polyoxometalates (POMs). During the reaction, the UV-excited photocatalyst first abstracts a hydrogen atom from the alkane to produce an alkyl radical, which is subsequently trapped by CO to yield an acyl radical. Then, the acyl radical is converted to aldehyde by reductive $H^{\bullet}$ donation from the protonated photocatalyst. To further employ POMs under visible light region, Suzuki *et al.*[119] synthesized a sandwich-type Ce^{3+}-containing silicotungstate (CePOM). An intramolecular charge transfer from Ce^{3+} to POM(W^{6+}) is observed upon visible light excitation, which can initiate photocatalytic oxidative dehydrogenation of a series of primary and secondary aromatic amines in the presence of O_2 (1 atm). Yamamoto *et al.*[120] showed that selectivity in oxidative coupling of benzene with cyclohexane is light sensitive using the Pd-modified TiO_2 photocatalyst. Under UV irradiation, the photogenerated hole species react with benzene and cyclohexane to form corresponding radicals, thus resulting in non-selective formation of all possible coupling products (phenylcyclohexane, bicyclohexyl, and biphenyl). In contrast, high selectivity towards cross-coupling product (phenylcyclohexane) can be achieved under visible light irradiation due to a ligand-to-metal charge transfer of benzene complex adsorbed on TiO_2, which produces benzene radical cation and selectively activates cyclohexane to form a cyclohexyl radical that attacks benzene molecule to form phenylcyclohexane. In addition, the Pd cocatalyst suppresses the formation of bicyclohexyl, thus resulting in a high selectivity towards the cross-coupling product. However, such a system shows a slow conversion rate due to poor light absorption under visible light.

Very recently, Cao *et al.*[121] reported a purely Bi-based semiconductor system (*p*-BWO nanosheets) for the efficient oxidation of toluene under visible light and ambient conditions (1 bar O_2). As demonstrated in Figure 4A, the photocatalyst is constructed by crystalline Bi_2WO_6 (lattice spacings of 2.72 and 2.73 Å for the (002) and (200) planes, respectively) that is surrounded by amorphous BiOCl substance. Such structure provides numerous active sites at the crystalline/amorphous boundaries (orange and blue arrows). These amorphous BiOCl layers crystallize *in situ* under a continuous bombardment of high-energy electron beams [Figure 4B], indicating they are very sensitive to excited electrons. Owing to the unique microstructure for efficient charge separation, the lattice oxygen of the *p*-BWO nanosheets is very active upon visible light irradiation, which can be involved in the oxidation of toluene (leached out) and eventually healed by molecular oxygen. The *p*-BWO nanosheets show a 166-fold enhancement in photo-oxidation of toluene compared with that of pristine Bi_2WO_6 [Figure 4C].

Selective cracking of aromatic biomass by photocatalysis has also drawn significant attention very recently. Wu *et al.*[122] showed that CdS quantum dots (QDs) are efficient photocatalysts for the selective cracking of branched-chain of various lignin model compounds via β-O-4 bond cleavage under visible light irradiation and deaerated conditions, as demonstrated in Figure 4D. Meanwhile, due to the relatively weak oxidation power of CdS QDs, the functional groups and the aromatic ring structures remain stable during the

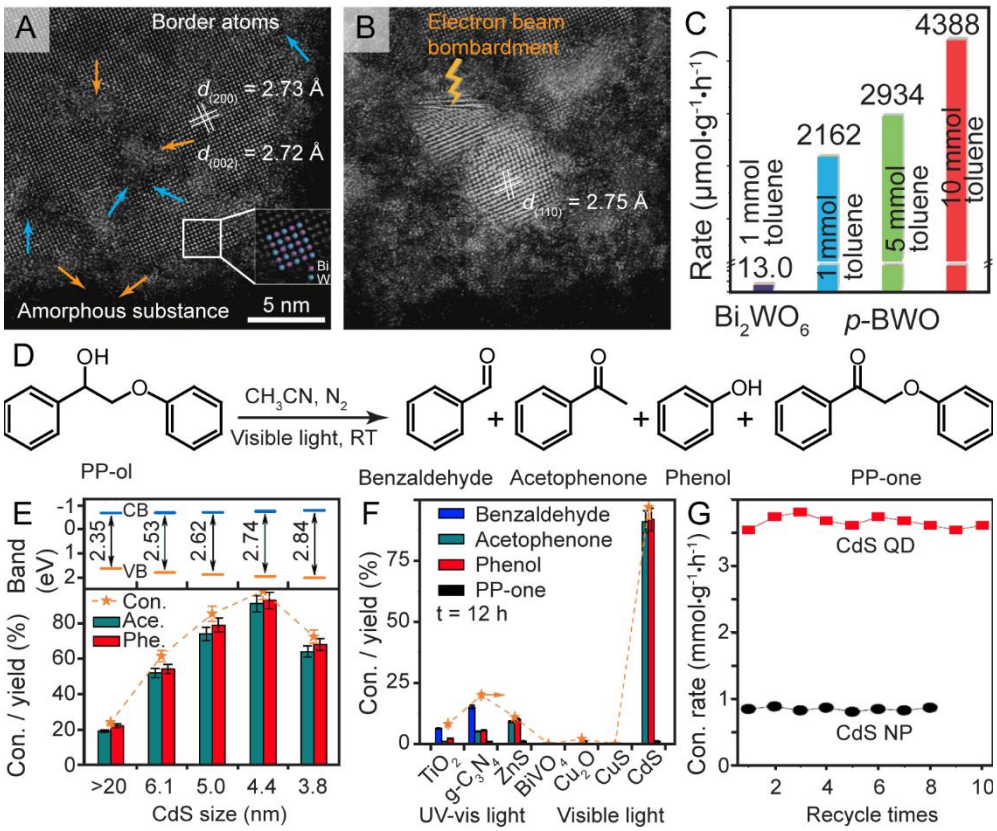

Figure 4. (A,B) STEM images of *p*-BWO before and after electron beam bombardment. (C) Photo-oxidation rate of toluene for Bi_2WO_6 and *p*-BWO at different substrate loadings. (D) Photocatalytic cleavage of β-O-4 bond in lignin model compound (PP-ol). (E) Energy-band positions and photocatalytic performances of CdS with different sizes. (F) Photocatalytic conversion of PP-ol by several typical semiconductors. (G) Reusability of CdS NPs and CdS QDs under visible light irradiation. This figure is used with permission from Nature Publishing Group[121,122]. NPs: Nanoparticles; QDs: quantum dots.

photocatalytic process. The optimized CdS QDs photocatalyst with an average particle size of 4.4 nm presents a satisfactory conversion of lignin compound, which also exhibits significant enhancement compared with other commonly used photocatalysts [Figure 4E and F]. The CdS QDs photocatalyst also shows an enhanced performance compared with that of the CdS NPs counterpart in terms of both conversion rate and stability [Figure 4G]. More importantly, the CdS QDs photocatalyst is capable of converting native lignins and can be recycled via a facile aggregation-colloidization strategy, which shows huge potential for industrial applications.

Photocatalysis for selective oxidation of aromatics to value-added products has experienced a booming development. Further development in catalytic efficiency and selectivity may be achieved by further optimization of the adsorption of reactants and intermediates. The design of functionalized photocatalysts and cocatalysts may be inspired by a series of classic heterogeneous catalysis works, especially those surface science-related fundamental works. In addition, extensive efforts should be paid to tune the redox potential of the photocatalyst to avoid over-oxidation of specific functional groups and unwanted ring-opening side reactions.

Oxidative coupling reactions

Selective formation of bonds between carbon and other heteroatoms (i.e., N, S, and O) via cross-coupling is one of the important reactions in synthetic chemistry. The oxidative coupling reactions generally employ

transition-metal catalysts to withdraw electrons from the reactants, which is accompanied by the addition of oxygen or deprotonation to the reactants. Employing metal-based molecules (i.e., $Ru[(bpz)_3](PF_6)_2$ and $Ru[bpy]_3Cl_2$) as homogeneous photocatalysts has shown that a series of oxidative coupling reactions can be realized under visible light irradiation (i.e., phenol-arene coupling[123] and amines-enol silanes coupling[124]). To further enhance the efficiency and the reusability of the homogeneous dye complex, Tan *et al.*[125] immobilized the $Ru[bpy]_3Cl_2$ molecule into a radical MOF, FJI-Y2 for the photocatalytic cross-dehydrogenative coupling of N-phenyltetrahydroisoquinoline derivatives with phosphite esters to form α-aminoquinoline phosphonates. As demonstrated in Figure 5A and B, the $[Ru^{II}(bpy)_3]$ cations are encapsulated into the porous FJI-Y2 MOF via intermolecular interaction between pyridine rings of dye cations and phenyl rings of the MOF ligands. The FJI-Y2 MOF is characterized by multiple 1D channels with a window size of ~8 × 12 $Å^2$, which offers an ideal platform with a large surface area and accessible active sites. It is also found that the dye-modified FJI-Y2 photocatalyst shows a higher performance than that of the homogeneous $[Ru^{II}(bpy)_3]Cl_2$ alone. The promotional effect originated from an efficient charge transfer due to intermolecular interactions between the 1,4,5,8-naphthalenediimide (NDI) group of the MOF and the $Ru^{II}(bpy)_3$ catalyst, as demonstrated in Figure 5C. Under visible light irradiation, the NDI groups are excited to NDI*, which is immediately quenched by the excited Ru^{II*} via a single electron transfer (SET) process. Such process generates a Ru^{I} complex and a radical cation $NDI^{+\cdot}$, which separately react with an electron donor (here, D, N-phenyltetrahydroisoquinoline) and an oxygen [O] via SET process to form the corresponding radical cation ($D^{+\cdot}$) and superoxide radical $[O]^{-\cdot}$, respectively. Meanwhile, the $NDI^{+\cdot}$ and Ru^{I} complex are relaxed to their ground states. The $[O]^{-\cdot}$ further abstracts an H atom from the $D^{+\cdot}$ to form the desired iminium ion, which undergoes nucleophilic addition to the desired product.

The oxidative coupling reaction can also be realized by traditional metal oxide photocatalyst systems. Zhang *et al.*[126] synthesized defect-rich WO_3 ($R\text{-}WO_3$) nanosheets via calcination of hydrothermally prepared defect-deficient WO_3 ($D\text{-}WO_3$) in N_2 atmosphere for aerobic coupling of primary amines to corresponding imines at room temperature [RT, Equation (6)]:

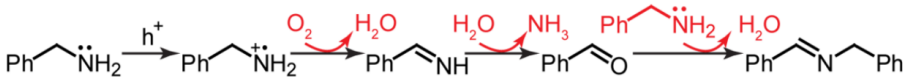

Eq. (6)

Such $R\text{-}WO_3$ material contains numerous small pits on surface, creating a large surface area with more under-coordinated sites (CUS) for catalytic reactions. In high-resolution TEM imagery, lattice disorder and dislocation are observed in the $R\text{-}WO_3$ nanosheets, revealing the presence of high-density defects [Figure 5D]. The massive defects result in a large number of electrons trapped at oxygen vacancies, as indicated by the significant signal of electron spin resonance (ESR) spectroscopy for $R\text{-}WO_3$ (g = 2.002) compared with that of $D\text{-}WO_3$ [Figure 5E]. Density functional theory (DFT) calculations indicate that molecular O_2 is chemisorbed at the oxygen vacancy of $D\text{-}WO_3$ surface via an end-on configuration, which is accompanied by a slight electron transfer from WO_3 CUS site to O_2 [Figure 5F]. The strong coupling between $R\text{-}WO_3$ and O_2 promotes oxygen reduction half reaction, thus accelerating the overall oxidative coupling.

Raza *et al.*[127] showed that the oxidative coupling of various amines to imines [Equation (6)] can also be realized by monolayer WS_2 nanosheets under visible-light irradiation. The WS_2 nanosheets synthesized via a modified liquid exfoliation method exhibit an average size of 120 nm with a height of 1 nm according to atomic force microscopy analysis, indicating most of the nanosheets are monolayer. The WS_2 photocatalyst shows a similar reaction mechanism to that of the WO_3 system; however, the monolayer WS_2 nanosheets

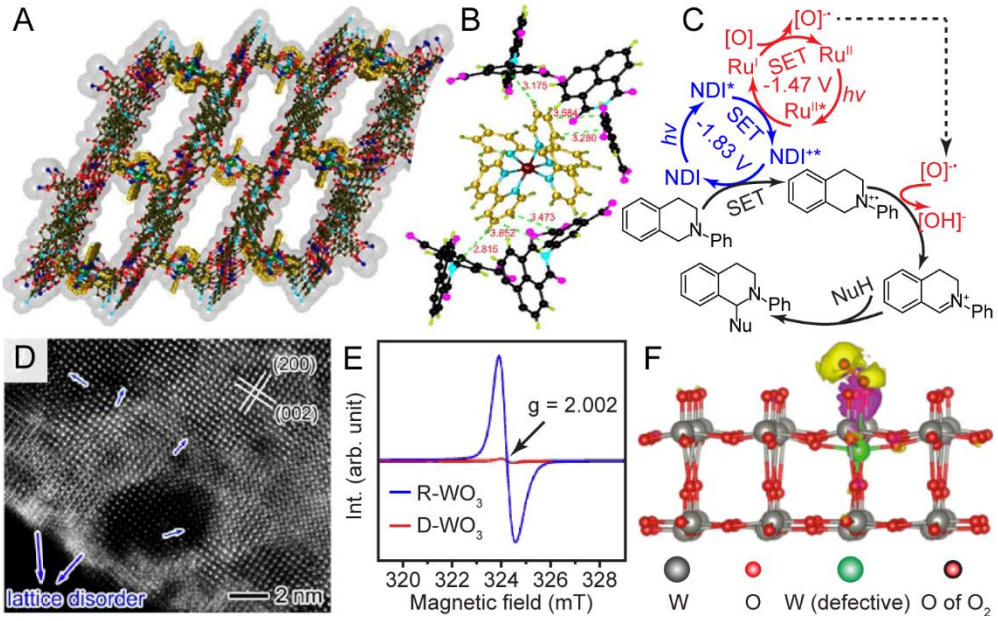

Figure 5. (A,B) $[Ru^{II}(bpy)_3]$ encapsulated in pores of FJI-Y2 MOF (highlighted as yellow atoms) and the interactions between the FJI-Y2 MOF ligands and $[Ru^{II}(bpy)_3]$ cations. (C) Cooperative catalysis mechanism of NDI radical and $[Ru^{II}(bpy)_3]$ photocatalyst via a SET pathway. This figure is used with permission from Elsevier[125]. (D) Atomic-resolution TEM image of R-WO_3 nanosheets. (E) ESR spectra of D-WO_3 and R-WO_3. (F) Simulated differential charge density for O_2 chemisorbed at a CUS W site of defective WO_3. This figure is used with permission from the American Chemistry Society[126]. MOF: Metal-organic frameworks; NDI: naphthalenediimide; SET: single electron transfer; ESR: electron spin resonance.

need to be operated under 50 °C. Xu and Fu[128] also developed core-shell structured sulfide-g-C_3N_4 to realize oxidative coupling of amines. A 4 nm thick shell of g-C_3N_{4shell} is coated on the CdS_{core} nanowire via a self-assembly process, which constructs a heterojunction interface for enhanced charge separation of photogenerated electrons and holes. Nevertheless, it has also been noticed that a much faster conversion rate can be achieved by using H_2O_2 as the oxidant, therefore suggesting that the formation of $•O_2^-$ radical is the rate-determining step for the photocatalytic oxidative coupling of various amines.

Our group recently reported that the identity of metal NP-decorated g-C_3N_4 is essential in controlling the selectively photocatalytic dehydrogenative homocoupling of primary amines into imines and secondary amines[129]. While Pt NPs drive the dehydrogenative homocoupling of primary amines into corresponding imines, Pd NPs promote self-hydrogenation of the photogenerated imines into secondary amines using the H atoms abstracted from the amines [Figure 6A]. Mechanism studies reveal that the adsorption of photogenerated imine molecule is relatively strong on Pd compared to on Pt NPs according to temperature programmed desorption (TPD, Figure 6B), thus facilitating the hydrogenation of imine into secondary amine. Moreover, a significant evolution of molecular hydrogen is observed for Pt/C_3N_4 under irradiation when primary amine and secondary amine are present, whereas no detectable H_2 is spotted for Pd/C_3N_4 [Figure 6C and D]. Moreover, a distinct delay of H_2 evolution is observed on Pd/C_3N_4 (~3 h after immense irradiation, red curve) in the photocatalytic hydrogenation of imine (2a) using isopropanol as the hydrogen donor [Figure 6E]. This further confirms that the abstracted hydrogen atoms from the amine molecules can be temporarily stored on Pd NPs, thus hydrogenating imine molecules into secondary amine without additional hydrogen donors (i.e., alcohols).

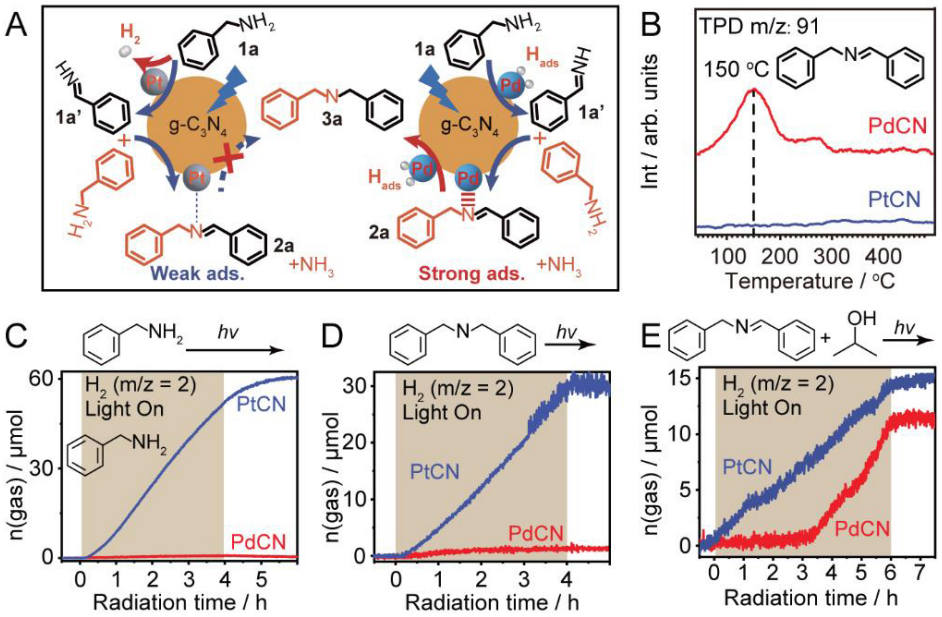

Figure 6. (A) Selective photocatalytic conversion of primary amines tuned by metal cocatalyst and the reaction pathways. (B) TPD analysis of imine adsorption on Pt/C_3N_4 and Pd/C_3N_4. (C,D) *In situ* MS analysis of H_2 evolution during photocatalytic conversion of amine and secondary amine on Pt/C_3N_4 and Pd/C_3N_4 under deaerated conditions. (E) H_2 evolution during photohydrogenation of 2a in isopropanol. The figures are used with permission from the American Chemistry Society[129]. TPD: Temperature-programmed desorption; MS: mass spectrometry.

Very recently, the dehydrogenative coupling of simple aliphatic alcohol (methanol) to the value-added product [ethylene glycol (EG)] was realized by Xie *et al.*[130] using the metal sulfide composite. While conventional photocatalysts (i.e., TiO_2, g-C_3N_4, and Cu_2O) only oxidize methanol into formaldehyde, CO, and CO_2, CdS NPs and nanorods produce a reasonable amount of EG. Interestingly, both the conversion rate of methanol and the selectivity to EG can be significantly enhanced by loading MoS_2 nanofoam cocatalyst onto the CdS nanorod [Figure 7A and B]. ESR analysis reveals that mainly hydroxymethyl radicals ($^{\bullet}CH_2OH$) instead of methoxy radicals ($CH_3O\bullet$) are generated under irradiation using CdS photocatalyst [Figure 7C], suggesting a preferential activation of C-H bond rather than O-H bond of methanol by photoexcited holes. Eventually, the photogenerated $^{\bullet}CH_2OH$ radicals readily desorb from catalyst surfaces for subsequent coupling. This work presents unique photocatalytic C-H activation that may offer an alternative process for cheap aliphatic alcohol conversion in the petroleum industry.

Nevertheless, plasmonic Au-Pd alloy NPs supported on ZrO_2 have also been employed as photocatalyst for a series of C-C coupling reactions (i.e., Sonogashira coupling, Stille coupling, and Hiyama coupling) with high yields[131]. It is proposed that the alloy NPs absorb visible light and transfer excited electrons to the Pd sites to initiate the reactions. Beyond conventional metal-based semiconductor and plasmonic metal NPs photocatalyst systems, Ghasimi *et al.*[132] demonstrated that the conjugated organic polymer can be used as a Pd-free photocatalyst for efficient Stille coupling reaction to construct aromatic C-C bond under visible light irradiation. The photocatalyst polymer, namely P-Az-B, can be obtained via Suzuki cross-coupling reaction of 1,3-dibromoazulene with 1,3,5-phenyltriboronic acid tris(pinacol) ester, where the 1,3-dibromoazulene is a co-monomer to obtain high porosity of the material. The P-Az-B photocatalyst exhibits excellent light absorption with an optical band gap of 2.03 eV. In addition, the highest occupied molecular orbital and the lowest unoccupied molecular orbital (LUMO) of P-Az-B (+1.14 and -1.10 V *vs.* saturated calomel electrode) are comparable to that of the Ru-based complex, suggesting its compatibility for driving

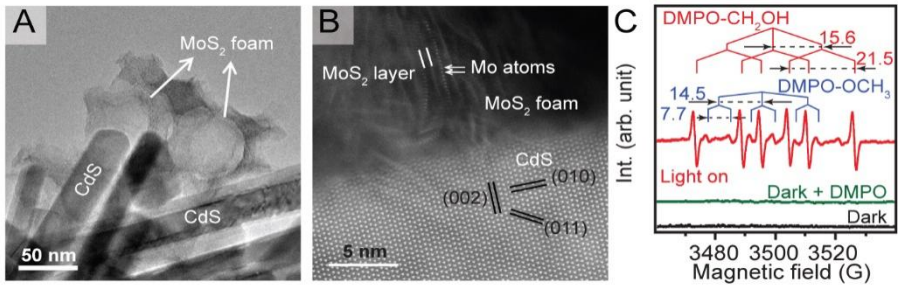

Figure 7. (A,B) TEM images of MoS_2 foam/CdS. (C) *In situ* ESR spectra of MoS_2 foam/CdS catalyst in methanol-DMPO solution with or without irradiation. This figure is used with permission from a Creative Commons Attribution License[130]. ESR: Electron spin resonance.

C-C coupling reactions. Upon visible light irradiation, the photogenerated hole and electron react with aryl stannane and the aryl iodide, resulting in the formation of destannylation radical and aryl halide radical, respectively. Then, the radicals desorb from the photocatalyst and react to create a substitutional intermediate, which finally leads to the formation of C-C bond by releasing the iodide anion.

The cross-coupling of aniline and alcohol for the synthesis of asymmetric secondary amines can also be realized by heterogeneous photocatalytic systems. Shiraishi *et al.*[133] demonstrated that the Pd/TiO_2 photocatalyst promotes the N-monoalkylation of amine with alcohol via tandem photocatalytic and catalytic reactions: (i) photo-oxidation of alcohol on Pd/TiO_2; (ii) condensation of photogenerated aldehyde with amine on TiO_2; and (iii) hydrogenation of the produced imine by the photogenerated surface H atoms on the Pd particles from alcohol oxidation. The rate-determining step is the imine hydrogenation, which strongly depends on the number of surface Pd atoms on the triangle site of Pd particles [Figure 8A]. Meanwhile, the strong adsorption of alcohols on larger triangle sites of Pd NPs should be avoided as it will suppress the imine hydrogenation. Therefore, Pd NPs with an optimum size of 2-2.5 nm contain a relatively larger number of triangle site Pd atoms but do not show strong alcohol adsorption, present the highest activity for imine hydrogenation and promote N-monoalkylation of amine with alcohol [Figure 8B]. Similarly, the rapid photocatalytic N-alkylation of pharmaceutically relevant amines with alcohols can also be realized by employing a mixed heterogeneous $Cu-Au/TiO_2$ photocatalyst[134]. By carefully controlling the reaction conditions, selective mono- and di-alkylation of primary amines and the non-symmetrical dialkylation of primary amines to hetero-substituted tertiary amines can be achieved. In this scenario, alcohol is typically used as the solvent, which serves as both the reactant to couple with amine and a hydrogen donor to supply H atoms for the hydrogenation of the photogenerated imines. Therefore, selectivity control over imine and secondary amine and the formation of aldehyde byproducts remain challenges.

A very recent work provides an alternative strategy for selective cross-coupling of amines and alcohols without the use of additional hydrogen donors[135]. This is realized by controlling the identity of the metal cocatalysts supported on TiO_2 to mediate the photocatalytic activation of alcohols, thus separating the stepwise dehydrogenative-condensation process to imine (Rh) and the direct condensation process to secondary amine (Fe, Figure 8C). TPD and ESR analysis reveals that Rh exhibits strong adsorption of alcohol with fast generation kinetics of the $^{\bullet}OH$ radicals [Figures 8D and E], thus leading to a rapid photo-oxidation of alcohol into aldehyde and the consecutive condensation of aldehyde with aniline. In contrast, the Fe/TiO_2 displays a weak interaction with alcohol and slow kinetics in $^{\bullet}OH$ formation, resulting in a mild activation of the alcohol for direct condensation with aniline to yield asymmetric secondary amine.

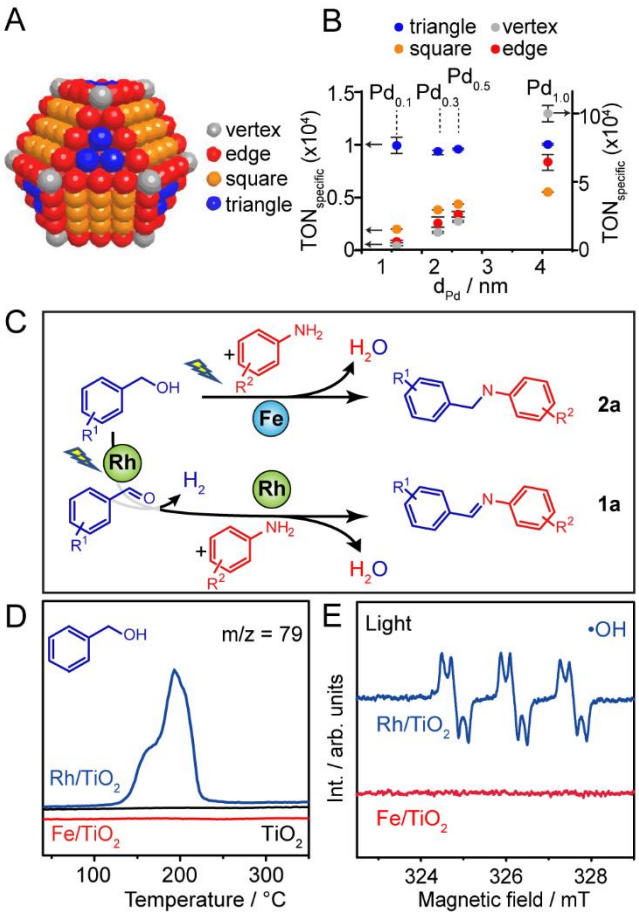

Figure 8. (A) The fcc cuboctahedron model of Pd particles. (B) Relationship between the Pd particle size and the turnover number for hydrogenation of imine. This figure is used with permission from the American Chemistry Society[133]. (C) Metal cocatalyst tuned photocatalytic cross-coupling of aniline and alcohol. (D) TPD analysis of benzyl alcohol adsorption on Rh/TiO_2 and Fe/TiO_2, respectively. (E) ESR spectra of Rh/TiO_2 and Fe/TiO_2 in DMSO under irradiation. This figure is used with permission from Elsevier[135]. TPD: Temperature programmed desorption; ESR: electron spin resonance; DMSO: dimethyl sulfoxide.

Up to date, the homo-coupling of some model compounds by photocatalysis has been well established and highly efficient photocatalysts have been developed. Further investigations in cross-coupling reactions are crucial for applications that require careful control over the active sites of the catalyst and reaction conditions. This calls for an in-depth understanding of reaction pathways, intermediates, and radical species. One could learn from traditional homogeneous catalysis of the reaction mechanisms to help the design of heterogeneous photocatalyst. Additionally, the quantification of unwanted byproducts and unknown products should not be neglected, as this may give some useful hints for the design of highly selective photocatalysts.

NANOSIZED PHOTOCATALYSTS FOR REDUCTION REACTIONS

Hydrogenation of CO_2 and CO

Photocatalytic CO_2 reduction is a very hot topic in photocatalysis and photo-electrocatalysis. Various photocatalysts ranging from simple oxides, sulfides, perovskites, MOFs[136], and plasmonic metal NPs[137] to composites[138] have been developed for CO_2 reduction with or without sacrificial electron donors. The design of cocatalyst has also been extensively investigated to further boost the photocatalytic CO_2 reduction performance[139-141]. Since there are a number of in-depth reviews on this topic[136,142], we focus on the

hydrogenation of CO_2 and CO by molecular H_2 and the incorporation of CO_2 into other reactants for the formation of more complicated chemicals.

Sastre *et al.*[143] showed that the p-type NiO photocatalyst can reduce CO to CH_4 with the presence of water under visible light irradiation at RT. It is also noticed that CO reduction to CH_4 can be significantly enhanced with the presence of H_2 as a reducing agent. In addition, the deposition of elemental carbon (coking) on the photocatalyst surface is also observed. It is therefore supposed that the NiO photocatalyst not only accelerates the CO reduction by water [Equation (7)] but also promotes a Fischer-Tropsch-like process following Equation (8):

$$CO + 2H_2O \xrightarrow{hv} CH_4 + 1.5O_2\ (\Delta G^0 = 541\ \text{kJmol}^{-1}) \quad \text{Eq. (7)}$$

$$CO + 2H_2 \xrightarrow{hv} CH_4 + 0.5O_2\ (\Delta G^0 = 35.6\ \text{kJmol}^{-1}) \quad \text{Eq. (8)}$$

Based on these findings, the same group further explored the photocatalytic Fischer-Tropsch process directly from CO_2 and H_2[144]. It has been found that, although NiO exhibits high conversion of CO_2 to CH_4, the photocatalyst gradually deactivates upon reuse. Meanwhile, nickel supported on porous silica-alumina ($Ni/Si_xAl_yO_z$) is an efficient and reusable photocatalyst for the reduction of CO_2 with comparable performance. As demonstrated in Figure 9A, it is proposed that the reaction is initiated via H_2 activation by the photogenerated charge carriers, where Ni-H species are generated to further activate CO_2 to form surface adsorbed, hydrogenated intermediates and eventually release as CH_4. Since the silica-alumina is inert support, the reaction is more likely a photo-thermal catalytic process that is driven by the localized hot electrons generated from plasmonic absorption of Ni metal NPs. Researchers should be aware that the $Ni/Si_xAl_yO_z$ photocatalyst only produces CH_4 and CO without the formation of hydrocarbons with longer chains. To further promote the photocatalytic Fischer-Tropsch process, Guo *et al.*[145] deposited worm-like Ru nanostructures on graphene as photocatalyst for the conversion of CO to more complicated hydrocarbons under H_2 atmospheres. Although the Ru/graphene photocatalyst shows a decent selectivity to liquid fuel products under visible light irradiation (C^{5+}, > 70%), such a system requires a relatively high operation temperature (150 °C), and the activity is more dependent on heat rather than light.

Very recently, Zhang's group showed that the synthesis of hydrocarbons from syngas (CO and H_2) can be realized by photo-thermal catalytic approach at RT[58,146-149]. This type of nanostructured photocatalysts is generally derived from hydrogen reduction of layered double hydroxides (LDH, i.e., ZnCoAl, ZnFeAl, and CoFeAl) at elevated temperatures (300 °C -700 °C), yielding metal/metal oxide composites (i.e., Co/Co_3O_4, Fe/FeO_x, and CoFe alloy) leached out from the LDH and naturally loaded on the corresponding inert support (ZnO, Al_2O_3). The activity and selectivity of these LDH-derived photocatalysts can be tuned by optimizing the annealing temperature and identity of the metal species in the LDH. While the photocatalyst derived from ZnCoAl LDH shows a reasonable CO conversion (15.4%) and selectivity towards light olefin (C_2-$C_4^=$, ~19%), the performance can be further enhanced by employing ZnFeAl LDH as the photocatalyst precursor (Con. > 20%, Sel. > 40%) due to a suppression of CO_2 formation. Furthermore, direct hydrogenation of CO_2 can also be realized by fabricating the CoFe alloy NPs from annealing of CoFeAl LDH nanosheets under H_2 atmosphere, as shown in Figure 9B and C. The CoFe alloy NPs synthesized at 650 °C show remarkable selectivity toward hydrocarbons (60% CH_4, 35% C_{2+}). It should be clear that the catalytic activity of these photocatalysts originates from the photothermal effect, as the temperature of the catalyst bed increases rapidly upon irradiation with the presence of photocatalyst [Figure 9D].

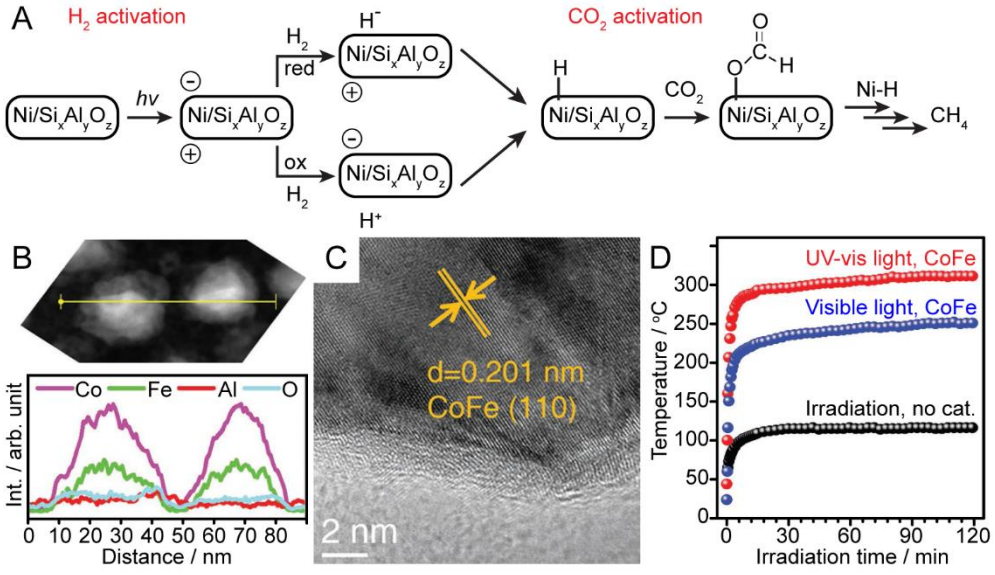

Figure 9. (A) Complete photocatalytic CO_2 hydrogenation with H_2 using Ni supported on silica-alumina. This figure is used with permission from the American Chemistry Society[144]. (B,C) EDS line-scan and HRTEM image of the CoFe alloy NPs used for photothermal CO_2 hydrogenation to hydrocarbons with H_2. (D) Temperature profiles during photothermal CO_2 hydrogenation. This figure is used with permission from Wiley-VCH[146].

For carboxylation with CO_2, Ye *et al.*[150] showed that radical chemistry possesses great potential to bring CO_2 to a new stage using either a transition-metal catalyst or a photocatalyst. Nevertheless, incorporation of CO_2 reduction with oxidation of other reactants to synthesize valuable chemicals has also emerged recently. Yang *et al.*[151] showed that the photocatalytic reduction of CO_2 can be coupled with the oxidation of amine by using Cu/TiO_2 photocatalyst. While CO_2 is reduced to CH_3OH by photo-induced electrons, benzylamine reacts with photogenerated holes and undergoes dehydrogenation coupling to produce imine. Such a system provides an economic strategy to fully utilize the photogenerated charge carriers. Chen *et al.*[152] reported the utilization of Cu_2O/Cu nanocomposite for photocatalytic coupling of CO_2 with benzyl alcohol. Under visible light irradiation, benzyl acetate rather than C1 products is selectively produced over Cu_2O/Cu, as described in Equation (9). Upon irradiation, the photogenerated holes react with benzyl alcohol to form benzaldehyde with the release of two protons. The protons along with photogenerated electrons interact with surface-adsorbed CO_2 to generate CH_2O via hydrogenation of the surface-adsorbed CO* intermediate, during which CO_2 undergoes a facile cleavage of the C-O bond on Cu sites. CH_2O further couples with a neighboring CO* to form surface adsorbed H_2C-CO. The H_2C-CO intermediate converts to surface-adsorbed H_3C-CO via H abstraction from benzyl alcohol and subsequently undergoes a coupling reaction with the benzyl oxygen ion to produce benzyl acetate. However, researchers should be aware that the Cu_2O/Cu material transforms to Cu_2O/CuO after photocatalytic reaction, which needs to be regenerated by $NaBH_4$.

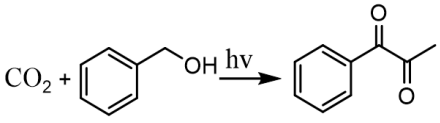

Eq. (9)

Photocatalytic CO_2 reduction is a challenging and intriguing reaction; however, the value of the products and the inherent slow reaction kinetics render its future questionable from an economical viewpoint.

Nevertheless, fundamental investigations are still important in this field, but they should be focused on reaction mechanisms rather than reporting performance. It is also important to use standard procedures for performance testing and reporting.

Hydrogenation of O_2

H_2O_2 is widely used in many applications including medication, bleaching, and production of organic chemicals. Previously, industrial synthesis of H_2O_2 was realized by hydrolysis of ammonium peroxydisulfate ($[NH_4]_2S_2O_8$) that is obtained by electrolysis of ammonium bisulfate (NH_4HSO_4) in sulfuric acid. Nowadays, H_2O_2 is mainly manufactured by the anthraquinone process, as demonstrated in Equation (10)[153]:

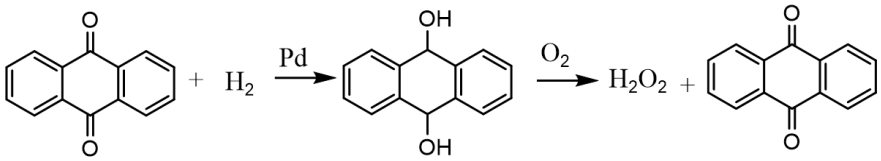

Eq. (10)

where the anthraquinone (i.e., 2-ethylanthraquinone) is hydrogenated to the corresponding anthrahydroquinone and consequently oxidizes back to anthraquinone and produces H_2O_2. The economics of this process depends on the Pd-based hydrogenation catalyst, the effective recycling of the extraction solvents, and the cost of quinones.

Since it has been proven that reactive oxygen species including $O_2^{\bullet-}$, $OH^{\bullet}$, and H_2O_2 are produced during the photocatalytic decomposition of organic pollutants, it is reasonable to consider the photosynthesis of H_2O_2 by employing a designed semiconductor photocatalyst under mild conditions with appropriate hydrogen sources. Teranishi *et al.*[154] showed that H_2O_2 (10 mM level) can be synthesized by simply using Au NP-modified TiO_2 with ethanol as the hydrogen source under aerobic conditions. Kinetic analysis reveals that, while Au NPs on TiO_2 promote the formation of H_2O_2 compared with that of pristine TiO_2 or Pt/TiO_2, the decomposition rate of H_2O_2 on Au/TiO_2 is also significantly suppressed. It is therefore proposed that the hydrogenation of O_2 and the degradation of H_2O_2 take place on the metal surface and the TiO_2 surface, respectively, and surface engineering of the photocatalyst material is the key to further optimize the synthesis of H_2O_2. The photocatalytic H_2O_2 production over Au/TiO_2 can be further enhanced by adding borate or phosphate in alkaline water solution[155], which is ascribed to an anion-mediated hole transfer from Au/TiO_2 to electron donor (methanol). In addition to the anion effect, Moon *et al.*[156] showed that the metal promoter on TiO_2 can be replaced by reduced graphene oxide (rGO) for the photocatalytic production of H_2O_2. Interestingly, by adding cobalt salt to the phosphate-containing catalyst suspension, cobalt phosphate complex (CoPi) that is often served as an electrocatalyst can be formed *in situ* on the rGO/TiO_2 surface. The loading of CoPi as cocatalyst further reduces the overpotential of water oxidation, therefore enabling photocatalytic production of H_2O_2 even without organic hydrogen resources (i.e., alcohols).

More efforts have been devoted to realizing the selective synthesis of H_2O_2 under visible light conditions. Shiraishi *et al.*[157] employed g-C_3N_4 as the visible light response photocatalyst to generate H_2O_2 selectively (> 90%) with the presence of alcohol and O_2. Mechanistic studies reveal that the high selectivity to H_2O_2 originates from the efficient formation of surface-adsorbed 1,4-endoperoxide species (C-O-O-N), which suppresses the one-electron reduction path of O_2 to superoxide radicals. He *et al.*[158] showed that the dimension of carbon support materials is crucial in tuning the recombination rate of charge carriers and light absorption properties, which is essential for boosting the evolution rate of H_2O_2. Li *et al.*[159] demonstrated that the performance of g-C_3N_4 can be further improved by creating carbon vacancies, which

reduce the bandgap and promote the delocalization of excited electrons of the material. The carbon vacancies not only provide more sites for interfacial charge transfer from the photocatalyst to adsorbed O_2, but they also alternate the H_2O_2 generation pathway from a two-step single-electron process to a one-step two-electron direct reduction.

Kim *et al.*[160] further explored the possibility of coupling industrial H_2O_2 synthetic process with photocatalysis. As demonstrated in Figure 10A, the anthraquinone molecule [anthraquinone-2-carboxylic acid (AQ)] is anchored onto g-C_3N_4 via a catalyst-free, direct dehydration coupling of the -COOH of AQ and the -NH_2 of g-C_3N_4. Upon visible light excitation, isopropanol is oxidized on the g-C_3N_4 surface to acetone and releases protons. Meanwhile, the photogenerated electrons and abstracted protons transfer to the anchored AQ molecule, reducing it to surface-anchored anthrahydroquinone (AQH_2). Eventually, the anchored AQH_2 is oxidized back to AQ in the presence of O_2, resulting in the production of H_2O_2. The efficient anchoring of AQ has been confirmed by X-ray photoelectron spectroscopy (XPS, Figure 10B). While the C1s peaks of g-C_3N_4 are assigned to the adventitious carbon and defect-derived sp2-carbon (284.8 eV) and the N-C = N bond in the triazine units (288.2 eV), a strong aromatic C-C bond (284.8 eV) is observed when AQ is coupled with g-C_3N_4. In addition, Fourier transform infrared spectroscopy (FT-IR) has also spotted increases in absorption at 1278 and 1676 cm^{-1}, which correspond to C-N and C = O stretching vibrations due to the formation of amide bond. Owing to the efficient interfacial charge transfer and the superior activity of AQ in O_2 reduction, such an anchored system exhibits a high apparent quantum yield in H_2O_2 production of 19.5% at 380 nm, which is significantly higher than that of pristine g-C_3N_4 or g-C_3N_4 modified with metallic co-catalysts.

Very recently, Teng *et al.*[161] showed that a single Sb atom dispersed on g-C_3N_4 (Sb-SAPC) can achieve a remarkable apparent quantum yield of 17.6% for H_2O_2 synthesis under 420 nm irradiation. The solar-to-chemical conversion efficiency of Sb-SAPC15 reaches 0.61%, which is higher than most water-splitting photocatalysts [Figure 10C]. TEM imaging shows that high-density Sb atoms are uniformly dispersed over the entire carbon nitride matrix [Figure 10D]. Raman spectroscopy has been performed to identify the intermediate in the photocatalytic process with the presence of isopropanol as the electron donor [Figure 10E]. A new absorption at 855 cm^{-1} is observed for the Sb-SAPCs, which can be assigned to the O-O stretching of an Sb-OOH species that corresponds to the end-on adsorption configuration of molecular oxygen. Such end-on adsorption notably suppresses the $4e^-$ oxygen reduction reaction, thus leading to a high selectivity of the $2e^-$ process for H_2O_2 synthesis.

Photocatalysis provides an alternative approach for the on-site synthesis of H_2O_2, which is ideal for coupling with some specialized fine chemical syntheses that require a relatively low concentration of H_2O_2. This requires leveling up the concentration of photogenerated H_2O_2 from ppm level to sub wt% level. One possible solution is coupling the oxygen reduction with water oxidation to produce H_2O_2 via both cathodic and anodic reactions using designed photocatalysts. In addition, the degradation kinetics of photogenerated H_2O_2 is worthy of investigation. It is also necessary to evaluate the poisoning effect of H_2O_2 at elevated concentrations for the optimization of photocatalysts.

Hydrogenation of organic molecules

Early investigations showed that fine TiO_2 NPs and ZnS quantum dots photocatalyst can be used to hydrogenate a series of organic molecules (i.e., propene, aromatic ketones, and amines) upon UV excitation[162-164], although the light utilization, quantum efficiency, conversion, and selectivity are far from satisfactory in general. To overcome these challenges, many efforts have been focused on surface engineering of photocatalyst materials. Hao *et al.*[164] reported surface engineered heterogeneous

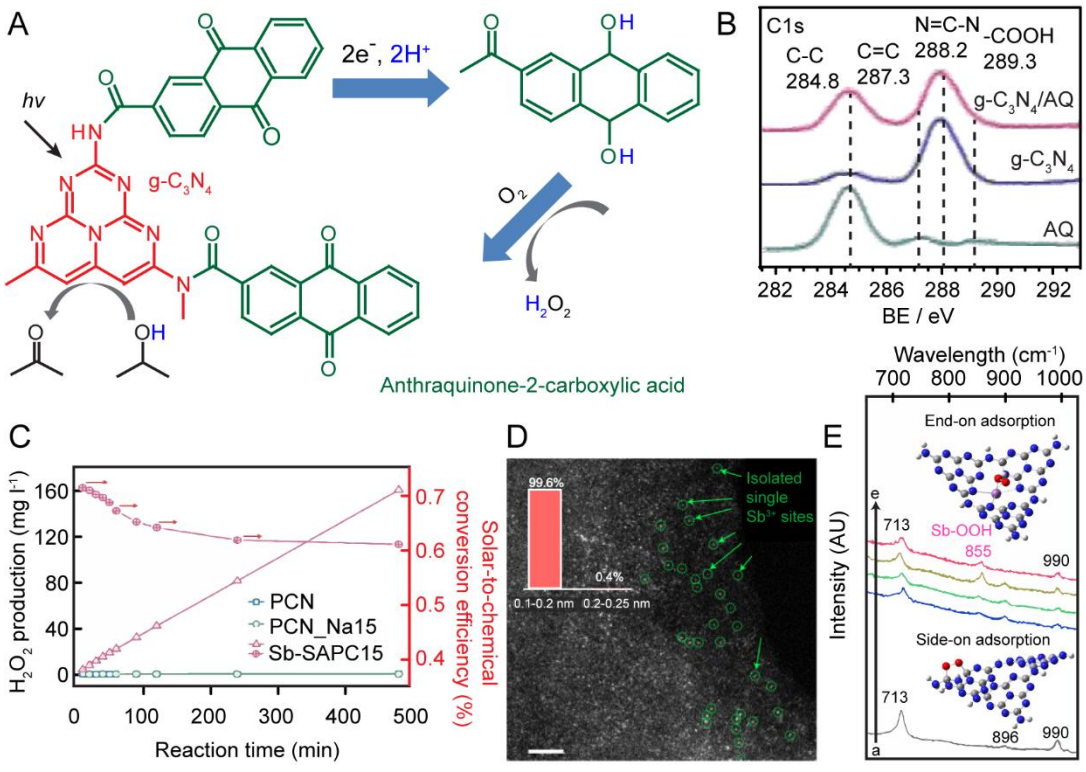

Figure 10. (A) g-C_3N_4 coupled with AQ(-COOH) for photocatalytic hydrogen peroxide generation under solar light irradiation. (B) XPS spectra of C1s on AQ(-COOH), g-C_3N_4, and g-C_3N_4/AQ(-COOH). This figure is used with permission from Elsevier[160]. (C) Solar-to-chemical conversion efficiency of PCN, PCN_Na15, and Sb-SAPC15 under AM 1.5 illumination for H_2O_2 production. (D) TEM image of the Sb-SAPC15 (Scale bar, 2 nm). (E) Raman spectra recorded during photoreaction in isopropanol solution with saturated oxygen. This figure is used with permission from Nature Research[161]. XPS: X-ray photoelectron spectroscopy.

photocatalysts for the hydrogenative fixation of N_2 to NH_3. Zhang *et al.*[165] showed that functionalization of TiO_2 with metal NPs can significantly promote the hydrogenative cyclization of levulinic acid (LA) into γ-valerolactone (GVL, a potential green fuel) selectively using isopropanol as the hydrogen source, as demonstrated in Equation (11):

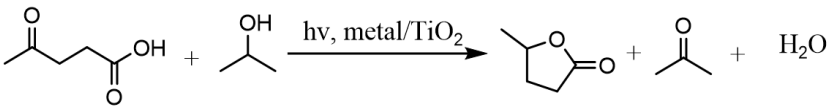

Eq. (11)

Here, isopropanol is dehydrogenated to acetone as the main product, donating a proton to LA that is cyclized to form GVL via the formation of acetyl propionyl radical. It is observed that while the polymorph composition of TiO_2 influences the conversion rate of LA, the identity of metal NPs controls the selectivity. Au NPs exhibit the highest LA conversion (79%) and GVL selectivity (85%) compared with that of Pd and Pt promoters, which is compatible with thermo-catalytic hydrogenation approach using Cu/ZrO_2 and Ru/C catalysts.

Lots of efforts have also been made to initiate hydrogenation reactions upon visible light radiation. Kohtani *et al.*[166] showed that, by anchoring organic dye molecules on pristine TiO_2 NPs, hydrogenation of selected aromatic ketones to corresponding alcohols with the presence of a hydrogen donor (trimethylamine) can be achieved under visible light excitation (> 400 nm). Although the utilization of metal-free dyes (fluorescein

and rhodamine B) is an economical and feasible solution, the poor stability limits its applications. Jiao *et al.*[167] developed a Pd supported on β-SiC photocatalyst for the hydrogenation of furan molecules under visible light excitation at RT [Equation (12)]. Although β-SiC is a narrow bandgap semiconductor (~2.4 eV), it is found that loading of Pd NPs (3 wt%) is essential to initiate the efficient hydrogenation of furan and its derivatives. The authors proposed that a Mott-Schottky contact of SiC and Pd enhances the charge transfer of photogenerated electrons from SiC to Pd NPs, thus promoting the catalytic activity; however, the photo-thermal catalytic approach induced by the plasmonic absorption of Pd NPs cannot be ruled out.

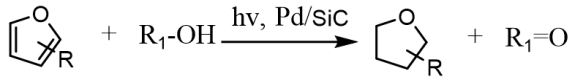

Eq. (12)

The same group further employed SiC with Au NPs for the selective hydrogenation of cinnamaldehyde using isopropanol as a hydrogen source under deaerated conditions [Equation (13)][168]:

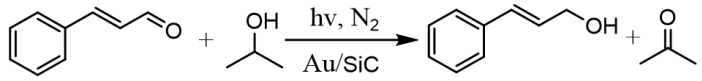

Eq. (13)

Figure 11A presents that Au NPs with a particle size ranging from 3-8 nm are evenly deposited on the SiC support. Remarkably, the Au/SiC system exhibits excellent selectivity and reasonable conversion in the whole visible light range, as demonstrated in Figure 11B. A very high turnover frequency (TOF, 487 h^{-1}) can be achieved at optimum conditions (30 mg catalyst and 20 mg KOH in 10 mL isopropanol and Xe-lamp with light intensity of 1.0 W•cm^{-2}). Nevertheless, the Au/SiC photocatalyst is capable of hydrogenating a series of α,β-unsaturated aldehydes to their corresponding unsaturated alcohols with high conversion and selectivity. It should also be noted that, in contrast to the hydrogenation of furans by Pd/SiC, the hydrogenation of cinnamaldehyde by Au/SiC is definitely a photo-thermal catalytic process that is induced by the plasmonic absorption of Au NPs. While the oxidation of 2-propanol takes place on the positively charged Au NPs surface, α,β-unsaturated aldehydes are adsorbed on the Au/SiC interface and reduced by the photogenerated electrons to unsaturated alcohols.

Shiraishi *et al.*[169] showed that the photocatalytic selective hydrogenation of a series of nitroaromatics to anilines with isopropanol as the hydrogen donor is sensitive to the polymorph composition of TiO_2 [Equation (14)]:

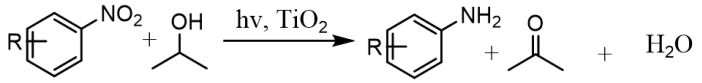

Eq. (14)

Interestingly, while anatase and P25 TiO_2 show poor activity and selectivity towards aniline, photoactivated rutile TiO_2 samples all show high performance in selective hydrogenation of nitroaromatics. It is proposed that the adsorption of nitroaromatics on rutile is responsible for the enhanced performance. As demonstrated in Figure 11C, the adsorption and hydrogenation of nitroaromatics on the photoexcited TiO_2 surface take place via either asymmetric adsorption on hydroxyl (TiOH) sites or symmetric adsorption on bridging oxygen vacancy (O_b vac.) sites. While the symmetric adsorption site can donate two photogenerated electrons to a nitroaromatic molecule, the asymmetric adsorption site only provides one electron at once, thus resulting in a poor performance in reduction. Diffuse reflectance infrared Fourier

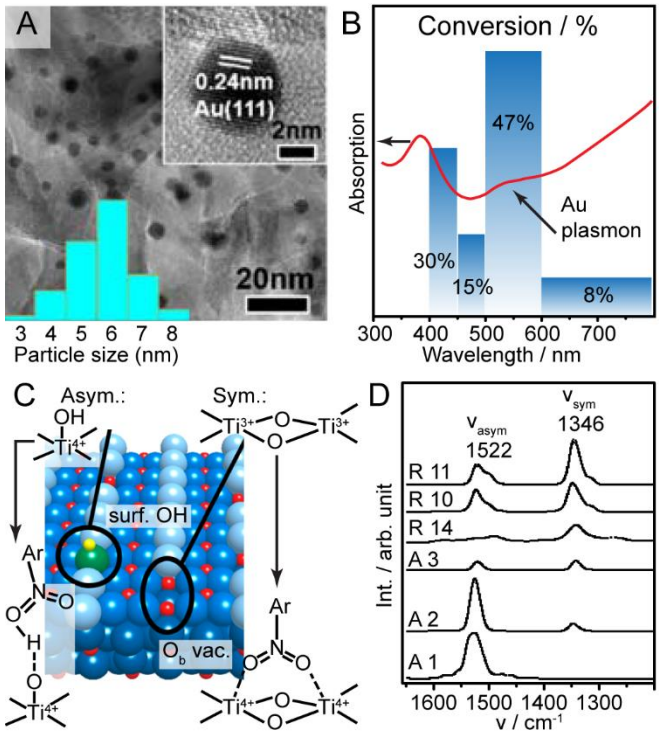

Figure 11. (A) TEM image of the 1 wt% Au/SiC photocatalyst and size distribution of Au NPs. (B) Selective photocatalytic hydrogenation of cinnamaldehyde by Au/SiC at different radiation wavelengths. (C) Asymmetric and symmetric adsorption of nitrobenzene on rutile TiO_2 (110) surface. Light blue and green balls are O_b atoms, while red and yellow balls are Ti and H atoms. (D) DRIFT spectra of nitrobenzene adsorbed on selected anatase (A) and rutile (R) TiO_2 at 303 K. This figure is used with permission from the American Chemistry Society[168,169]. NPs: Nanoparticles; DRIFT: diffuse reflectance infrared Fourier transform.

transform (DRIFT) spectroscopy has confirmed a significant density of symmetric adsorption sites on different rutile TiO_2 compared with that of anatase samples [Figure 11D], therefore leading to a fast aniline formation rate with high quantum yields (> 25%).

New materials have also been developed to drive the hydrogenation of nitroarenes under visible light conditions. Toyao *et al.*[170] synthesized an amino-functionalized Ti(IV)-MOF modified with Pt NPs (Pt/Ti-MOF-NH_2) for this purpose with reasonable stability. *In situ* ESR analysis reveals that the excited electrons on the organic linker transfer to the deposited Pt NPs via the titanium-oxo clusters, which promote the spatial charge transfer, thus resulting in enhanced performance. At the optimized Pt loading (1.5 wt%), Pt/Ti-MOF-NH_2 shows enhanced performance in both H_2 production and nitrobenzene reduction. However, low quantum efficiencies are observed for this system (~1%-2% under visible light irradiation), probably due to the rapid evolution of molecular H_2 that competes with the hydrogenation of nitrobenzene. Gao *et al.*[171] employed nanosized Ni_2P as the cocatalyst to modify CdS as a photocatalyst to realize the hydrogenation of a series of nitroarenes with Na_2S/Na_2SO_3 as sacrificial electron donors. In this system, water donates a proton to hydrogenate nitroarenes, as the Na_2S/Na_2SO_3 contains no proton. It is also observed that the photocatalytic H_2 evolution competes with the photosynthesis of aniline on the Ni_2P surface. Therefore, further surface engineering of the photocatalyst to suppress the H_2 evolution is essential to enhance the reduction of nitroarenes.

Very recently, Xiao *et al.*[172] demonstrated that chemoselective hydrogenation of various nitroarenes to corresponding anilines can be achieved by simply using the pristine g-C_3N_4 photocatalyst under visible light

radiation. The process shows excellent yields (82%-100%) and is even applicable to gram-scale reactions. However, it should be noted that such a process is operated at elevated temperature (70 °C-90 °C) and requires the addition of hydrazine hydrate ($N_2H_4·H_2O$) as the hydrogen source and hole scavenger (strong reducing agent with very high toxicity), which hinders its application in large scale due to safety issues. Nevertheless, Huang *et al.*[173] showed that Au supported on ZrO_2 photocatalyst can initiate the hydrogenation of nitroaromatics under visible light with formic acid and water as the hydrogen source. Since ZrO_2 is a large bandgap semiconductor (> 5 eV), the activity in visible light spectrum originates from the plasmonic excitation of Au NPs. In addition, Au/ZrO_2 is a versatile photocatalyst for the selective hydrogenation of various unsaturated bonds (i.e., C=C, C≡C, C=O, and C=N) under mild reaction conditions. Theoretical calculations reveal that direct photoexcitation of hybridized orbitals that are generated from chemisorbed reactants and metals is the driving force of the hydrogenation reaction.

Heterogeneous photocatalysis provides an ambient platform for hydrogenation reactions that employs hydrogen-containing molecules instead of high-pressure H_2. Such a mild reaction condition may also benefit semi-hydrogenation of alkynes and selective hydrogenation of complicated pharmaceutical molecules with vulnerable functional groups. In any case, the utilization of abundant and safe hydrogen donors (i.e., alcohols, ammonia) is recommended rather than the use of toxic, expensive, and risky hydrogen sources (*e.g.*, hydrazine). The design of cocatalysts with tunable hydrogen adsorption energy is also vital for efficient and selective hydrogenation, which may be promoted by the experience of heterogeneous hydrogenation investigations.

Reductive coupling reactions

Reductive coupling reactions (i.e., C-C, C-N, N=N) via homogeneous catalysis have been well investigated[174-184], especially in transition metal-catalyzed cross-coupling reactions promoted under visible light[183]. However, the need for expensive catalysts, catalyst separation, harsh reaction conditions, and toxic reducing agents (i.e., PH_3, Tl, and NaTeH) limit their applications. Therefore, there is a big demand to develop heterogeneous photocatalyst systems that can realize coupling reactions selectively under ambient conditions. Zhang *et al.*[184] demonstrated the effectiveness of semi-heterogeneous metallaphotocatalysis using polymeric carbon nitride photocatalyst for C-N cross-coupling reactions. Moreover, Wang *et al.*[185] showed that, by constructing unique plasmonic Au-Pd nanostructures, Suzuki coupling reaction of a series of aromatic compounds can be realized via harvesting visible-to-near-infrared light [Equation (15)]:

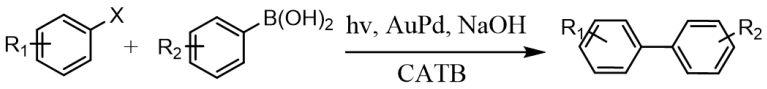

Eq. (15)

Here, the Au-Pd nanostructures consist of Au nanorods for light harvesting via plasmonic excitation, whereas the supported Pd NPs, through seeded growth, serve as catalytic active sites that are frequently used in conventional Suzuki coupling reactions. In addition, cetyltrimethylammonium bromide is required to bring bromobenzene into the aqueous reaction solution under basic conditions. Such a system shows a rapid temperature rise under infrared illumination, revealing a photo-thermal catalytic behavior that originated from the oscillation of localized hot electrons. The higher efficiency observed for the photo-induced coupling compared with that of the thermally induced process indicates that the local temperature may be significantly higher on the plasmonic catalyst surface than in the solution. More importantly, the Au-Pd nanostructures have been further tailored to directly harvest sunlight to drive coupling reactions, which show industrial potential for fine chemical synthesis. This design concept of Au-Pd was also employed by Xiao and coauthors for various C-C coupling reactions[131]. However, the conversion rate in

terms of turnover frequency, selectivity, and quantum efficiency still needs to be enhanced for applications. Lanterna *et al.*[186] later showed that the plasmonic Au NPs can be supported on TiO_2 to realize visible light-induced reductive C-C coupling of a variety of substituted benzyl bromides [Equation (16)]:

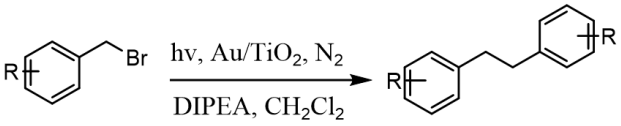

Eq. (16)

Here, the reductive coupling of benzyl bromides requires careful selection of both electron donors and solvents, where the combination of diisopropylethylamine and CH_2Cl_2 yields the optimum photocatalytic performance. Although the neat Au/TiO_2 photocatalyst system shows decent conversion and selectivity to desired products in general, further engineering of the material is needed to improve the stability.

Li and coworkers recently depicted the rational design of metal cocatalyst for photocatalytic dehalogenative coupling of benzyl bromide based on the Sabatier principle[187]. The optimal activity and selectivity require appropriate adsorption energies of the intermediates (benzyl radical, bromine atom, and surface adsorbed hydrogen atoms (H_{ads})) on the metal cocatalyst. DFT calculations predict that Cu is the promising candidate for this reaction among a series of transition metals owing to the optimized adsorption of benzyl radical and Br atom [Figure 12A]. This prediction is confirmed experimentally, where Cu indeed presents high conversion and selectivity in homocoupling of benzyl bromide without the formation of toluene [Figure 12B]. Remarkably, this design strategy can be generalized for the modification of other photocatalysts. The Cu deposited on g-C_3N_4 (Cu/C_3N_4) presents a decent performance towards the conversion of benzyl bromide into bibenzyl under visible light irradiation.

Filippini *et al.*[188] reported the amorphous g-C_3N_4 (am-CN) material for visible light-driven C-C bond formation towards the synthesis of valuable perfluoroalkylated intermediates from the corresponding iodides. The binding of perfluorobutyl iodide (C_4F_9I) occurs via halogen bonding with the N atom of the am-CN. This step affects the rate of the halogen dissociation of C_4F_9I to form the $\cdot C_4F_9$ radical [Figure 12C]. The affinity of reagents toward the solid catalyst is further characterized by the T_1/T_2 ratio in ^{19}F NMR relaxation measurements. The am-CN presents a higher surface affinity for the fluorinated substrate compared with other CN-based photocatalysts and thus shows the highest activity for this reaction [Figure 12D].

Beyond C-C coupling, the applications of supported metal NPs as photocatalysts have also been extended into N=N coupling reactions to produce azoxybenzenes and azobenzenes, which are important precursors for the dye, medical, and electronic industries. Zhu and coauthors reported the successful synthesis of azoxybenzenes and azobenzenes using supported Au and Cu NPs photocatalysts from nitrobenzene using isopropanol as the hydrogen source under visible light irradiation and basic conditions, as demonstrated in Equation (17)[189-191]:

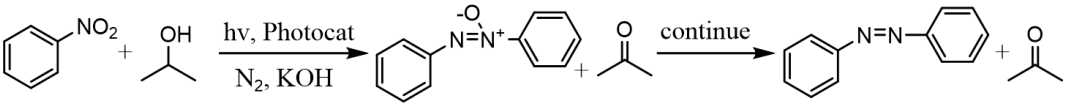

Eq. (17)

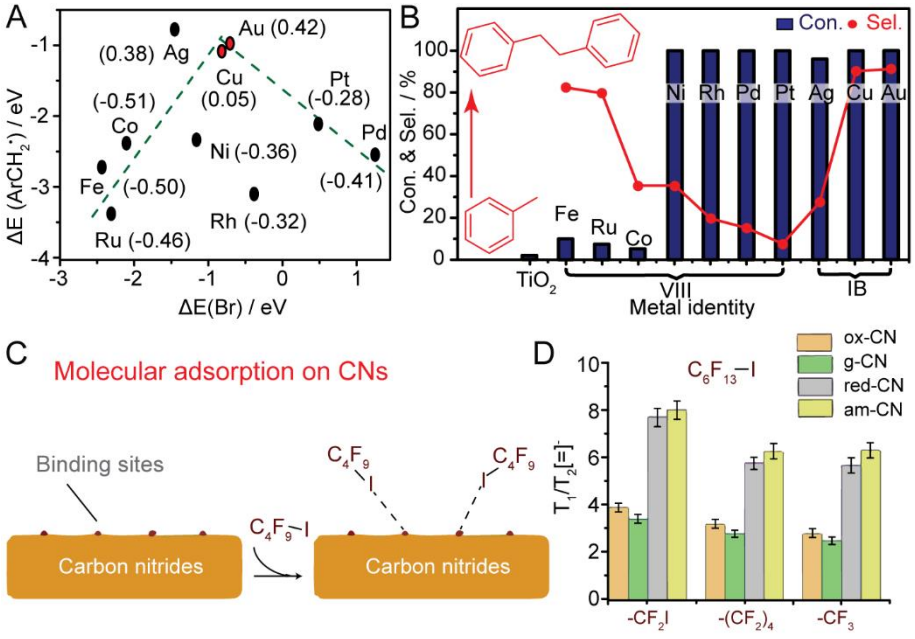

Figure 12. (A) $\Delta E(ArCH_2^{\bullet})$ as a function of ΔE(Br) for the screening of metal cocatalysts for photocatalytic dehalogenative coupling of benzyl bromide (the numbers in parentheses are $\Delta E(H_{ads})$ of the corresponding metals). (B) Photocatalytic benzyl bromide coupling using a series of selected metals supported on TiO_2. This figure is used with permission from the American Chemistry Society[187]. (C) Picture of molecular adsorption on CNs. (D) T_1/T_2 ratio of different moieties of perfluorohexyl iodide in various CN-based materials. This figure is used with permission from American Association for the Advancement of Science[188].

Here, the nitroaromatics undergo a gradual removal of oxygen by photogenerated protons and electrons via the formation of nitrosobenzene (NBS) and N-phenylhydroxylamine (NPH) radicals, which then generate azoxybenzene via dehydration coupling and eventually to azobenzene via removal of oxygen[192]. The selectivity of azoxybenzene or azobenzene can be tuned by controlling the chemical composition of the plasmonic metal NPs. While Au NPs supported on ZrO_2 exhibit high selectivity towards azobenzene, the Ag-Cu alloy NPs supported on ZrO_2 favor the selective formation of azoxybenzene. In addition, the selectivity can also be controlled by tuning the reaction temperature and employing Cu supported on graphene photocatalyst, though the activity decreases at low temperatures. These findings extend the potential application of the plasmonic metal NPs in photothermal catalysis for fine chemical synthesis; however, the high cost, low efficiency, and poor selectivity of such catalytic systems at RT limit their applications.

N=N coupling reaction can also be realized by using conventional semiconductor photocatalysts. Pal *et al.*[193] showed that the classical CdS quantum dots can be employed to reduce nitrobenzene to azoxybenzene with relatively high selectivity (68%) under visible light irradiation. It has been found that CdS with a small particle size (~2.8 nm) and the loading of Rh as cocatalyst are necessary to achieve a higher activity and selectivity towards azoxybenzene. Recently, our group showed that a series of azo- and azoxy-aromatic compounds can be selectively synthesized from their corresponding nitroaromatics via controlling the irradiation wavelength by simply using the pristine g-C_3N_4 under basic conditions with isopropanol as the hydrogen source[194]. Firstly, nitrobenzene can be converted into NBS and NPH. NBS and NPH are then further reduced to azoxy- and azo-aromatics. The azo-aromatics may be photoreduced into amines [Figure 13A]. While azobenzene is gradually formed in a two-step reduction of nitrobenzene under 410 nm irradiation with azoxybenzene as the intermediate [Figure 13B], azoxybenzene is the sole product throughout the 450 nm irradiation [Figure 13C]. Notably, high conversion of nitrobenzene (> 95%) and

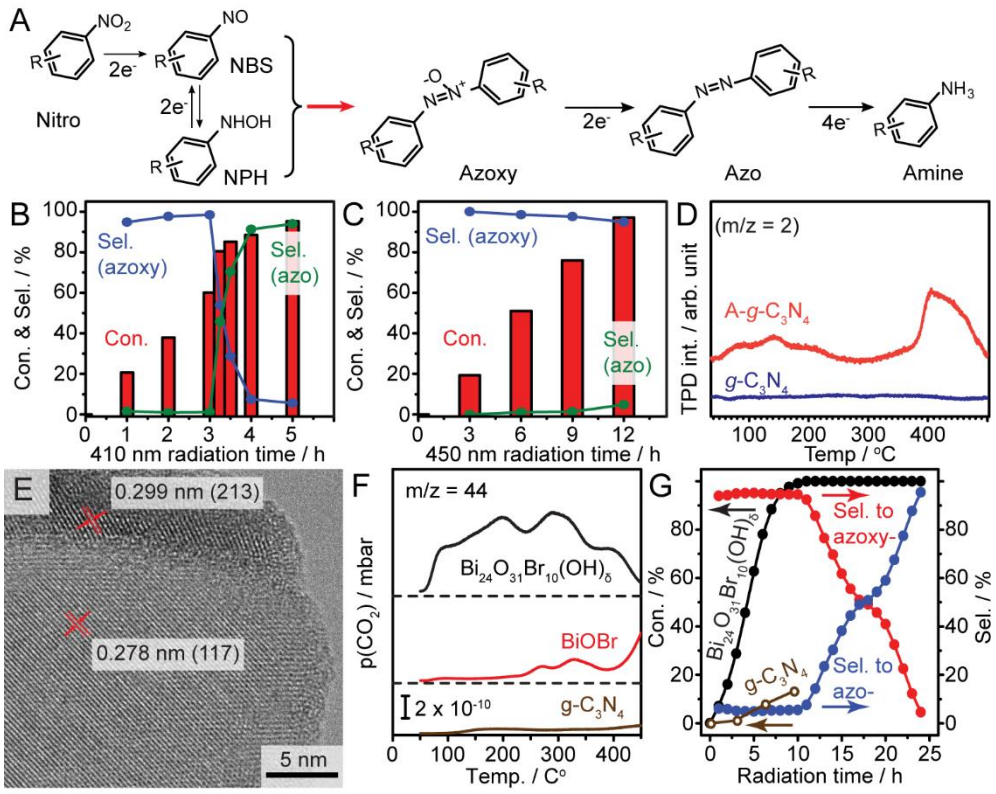

Figure 13. (A) Reaction path for the photoconversion of nitroaromatic compounds. (B,C) Light-tuned selective photosynthesis of azo- and azoxy-aromatics from nitrobenzene reduction using g-C_3N_4. (D) TPD spectra revealing the desorption of H_{ads} from g-C_3N_4 and A-g-C_3N_4 surfaces. This figure is used with permission from a Creative Commons Attribution License[191]. (E) HRTEM image of the solid base $Bi_{24}O_{31}Br_{10}(OH)_\delta$ photocatalyst. (F) Basicity comparison of $Bi_{24}O_{31}Br_{10}(OH)_\delta$, BiOBr, and g-$C_3N_4$ by CO_2-TPD. (G) Photocatalytic selective nitrobenzene conversion under solar irradiation. This figure is used with permission from the American Chemistry Society[48]. TPD: Temperature-programmed desorption.

selectivity towards both desired products (> 94%) are reached for a series of nitroaromatics with different functional groups, which broaden its applications for the synthesis of complicated azo- and azoxy-compounds.

Moreover, the photocatalytic reductive coupling of nitroaromatics can be realized under solar irradiation at a large scale (80 L in volume) with high selectivity to azoxybenzene and a reasonable conversion. The origin of the activity is associated with the adsorption energy of surface adsorbed hydrogen atoms (H_{ads}) that are generated by photo-oxidation of isopropanol, as confirmed by TPD of the pre-irradiated photocatalysts [Figure 13D]. While no desorption peak of H_2 over active g-C_3N_4 indicates weakly bonded H_{ads} on the catalyst surface, two obvious H_2 desorption peaks observed over the inactive amorphous g-C_3N_4 (A-g-C_3N_4) suggest strong adsorption of the photogenerated H_{ads} on A-g-C_3N_4. Therefore, weakly bonded H_{ads} on g-C_3N_4 promotes the reduction of surface adsorbed nitrobenzene to form azo- or azoxy-benzene.

Although the g-C_3N_4 system shows great potential in photocatalytic reductive N=N coupling reactions, the low quantum efficiency (1.4% at 410 nm and 0.4% at 450 nm irradiation) and the need for a basic environment limit its application at a large scale. Since the photocatalytic hydrogen abstraction from alcohol is the initial step in reductive coupling, we expect that a photocatalyst coupled with engineered basic sites can improve the photocatalytic performance. Therefore, we developed basic-site-engineered bismuth oxybromide [$Bi_{24}O_{31}Br_{10}(OH)_\delta$] nanosheets to boost nitrobenzene conversion under visible light irradiation

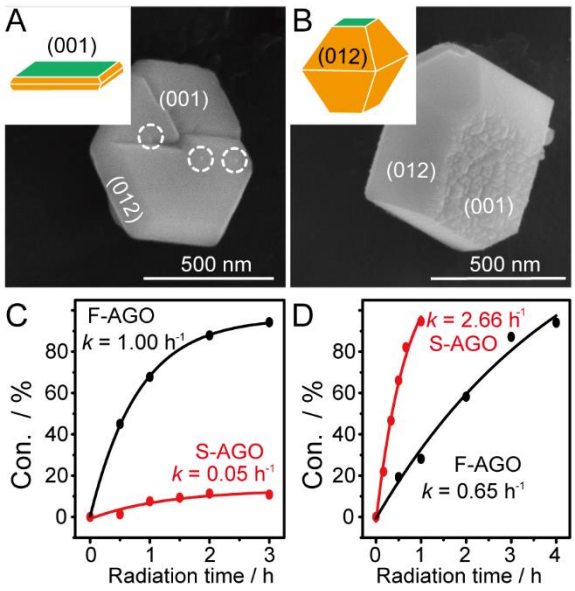

Figure 14. (A,B) SEM of S-AGO and F-AGO. (C) Photocatalytic reductive coupling of benzyl bromide in isopropanol with 10 mM KOH under N_2 conditions. (D) Photocatalytic oxidative coupling of 2,4,6-trimethylaniline in acetonitrile under aerated conditions. This figure is used with permission from the American Chemistry Society[195]. S-AGO: Stretched $AgGaO_2$; F-AGO: flat $AgGaO_2$.

and base-free conditions[48]. As presented in the HRTEM image of Figure 13E, the $Bi_{24}O_{31}Br_{10}(OH)_\delta$ nanosheets exhibit two types of lattice fringes (interplanar spacing of 0.278 and 0.299 nm) that match the (117) and (213) lattice planes of classical crystalline $Bi_{24}O_{31}Br_{10}$, respectively. CO_2-TPD reveals that the freshly prepared $Bi_{24}O_{31}Br_{10}(OH)_\delta$ nanosheets present a broad distribution of active sites with different basicities, whereas the typical BiOBr and g-C_3N_4 show almost no basicity [Figure 13F]. Indeed, the basic-site-engineered $Bi_{24}O_{31}Br_{10}(OH)_\delta$ nanosheets exhibit a robust hydrogen abstraction from isopropanol and fast hydrogen transfer from the catalyst to the adsorbed nitrobenzene according to *in situ* spectroscopy analysis, thus resulting in remarkable quantum efficiencies under visible light irradiation (42% at 410 nm and 32% at 450 nm). Nevertheless, the $Bi_{24}O_{31}Br_{10}(OH)_\delta$ nanosheets exhibit excellent performance in up-scaling and stability under solar irradiation. As depicted in Figure 13G, a complete conversion of nitrobenzene selectively to azoxybenzene and azobenzene (> 95%) in a sequential fashion is achieved under solar irradiation by employing the $Bi_{24}O_{31}Br_{10}(OH)_\delta$ photocatalyst, implying that the selective synthesis of two important products can simply be tuned via controlling irradiation time without the need of further separation process. In comparison, the g-C_3N_4 only converts ~20% of nitrobenzene under similar reaction conditions, which is less efficient than that of the $Bi_{24}O_{31}Br_{10}(OH)_\delta$ nanosheets.

Besides that, a very recent work shows that shape-engineered $AgGaO_2$ delafossites with dominant (001) and (012) facets are efficient photocatalysts for efficient and selective photocatalytic redox coupling reactions under visible light [Figures 14A and B][195]. Efficient separation of the photogenerated charge carriers is observed over the two facets. The flat $AgGaO_2$ (F-AGO) with electron-rich (001) facets shows an obvious enhancement over the stretched $AgGaO_2$ (S-AGO) with hole-rich (012) facets in the reductive homocoupling of benzyl bromide and N-N coupling of nitrobenzene [Figure 14C]. In contrast, S-AGO performs better than F-AGO in the oxidative homocoupling of aniline and C-N coupling of amines [Figure 14D]. DFT calculation reveals that the difference in work functions of the (001) and (012) facets is the driving force for the tuned surface redox chemistry, which offers a noble metal-free strategy for the engineering of delafossite-based photocatalysts for synthetic chemistry.

Similar to the photocatalytic oxidative coupling reactions, the development of cross-coupling is far behind the homo-coupling investigations due to the lack of in-depth mechanistic understanding of reaction pathways. Thus, significant efforts should be paid to realize some representative cross-coupling reactions for applications.

CONCLUSION AND OUTLOOK

In this review, we summarize recent advances in photocatalytic synthesis from an application-orientated prospective to illustrate the development in the design of photocatalyst materials. Various reactions catalyzed by nanostructured photocatalysts are categorized into oxidative and reductive reactions, which are further subdivided into alcohol oxidation, epoxidation, oxidation of aromatics, oxidative coupling, hydrogenation reactions, and reductive coupling. The advantages and limitations of these nanostructured photocatalyst materials, including metal oxides, supported plasmonic metal nanostructures, organic polymers, anchored homogeneous catalysts, and dye-sensitized heterostructures, are presented. In addition, fundamental understandings of specific reaction mechanisms are demonstrated to guide the rational design of nanostructured photocatalysts.

Although many challenging reactions can be realized by employing various engineered heterogeneous photocatalyst materials, there are still critical challenges that need to be solved for scaling-up applications. First, a high selectivity, rather than a fast conversion rate, is crucial for all types of reactions from the industrial perspective, as the energy-consuming separation process may be eliminated. For photocatalytic oxidation processes, strong oxidants should be avoided to prevent over-oxidation. For the synthesis of complicated organic molecules, it is also desirable to have a control over the stereo-selectivity, which may be solved by anchoring the designed homogeneous redox catalyst with heterogeneous photocatalyst materials. The selectivity control calls for an in-depth understanding of specific reaction mechanisms to aid the design of engineered nanostructured photocatalyst materials. Besides, it is paramount to avoid using harsh reaction conditions and toxic compounds for reduction reactions (i.e., strong basic or acidic conditions, high temperature, strong reductants, and toxic solvents), as these diminish the advantages of the photocatalytic process. The mild reaction condition is also essential for recycling used photocatalysts and solvents. Nevertheless, the design and development of a continuous reactor (i.e., flow cell) customized for photocatalytic applications are urgently needed to evaluate photocatalyst materials and the scaling-up of photocatalytic processes.

DECLARATIONS

Authors' contributions

Prepared the manuscript: Li Y, Su R
Corrected the manuscript: Zhang D, Qiao W, Xiang H, Besenbacher F, Li Y

Availability of data and materials

Not applicable.

Financial support and sponsorship

R.S. would like to thank the NSFC (projects number: 21972100) and the Priority Academic Program Development of Jiangsu Higher Education Institutions (PAPD, project number: NH10800120) for financial support. R. S. acknowledged Significant funding from Synfuels China Technology Co. Ltd.

Conflicts of interest

All authors declared that there are no conflicts of interest.

Ethical approval and consent to participate

Not applicable.

Consent for publication

Not applicable.

REFERENCES

1. Ertl G. Surface science and catalysis-studies on the mechanism of ammonia synthesis: The P. H. emmett award address. *Catalysis Reviews* 2006;21:201-23. DOI
2. Yin H, Chen Z, Peng Y, et al. Dual active centers bridged by oxygen vacancies of ruthenium single-atom hybrids supported on molybdenum oxide for photocatalytic ammonia synthesis. *Angew Chem Int Ed Engl* 2022;61:e202114242. DOI PubMed
3. . Wiley Online Library. Ullmann's encyclopedia of industrial chemistry. 2000. DOI
4. Tuxen A, Kibsgaard J, Gøbel H, et al. Size threshold in the dibenzothiophene adsorption on MoS_2 nanoclusters. *ACS Nano* 2010;4:4677-82. DOI PubMed
5. Su R, Lü Z, Chen K, et al. Novel in situ method (vacuum assisted electroless plating) modified porous cathode for solid oxide fuel cells. *Electrochemistry Communications* 2008;10:844-7.
6. Fujishima A, Honda K. Electrochemical photolysis of water at a semiconductor electrode. *Nature* 1972;238:37-8. DOI PubMed
7. Sunada K, Watanabe T, Hashimoto K. Studies on photokilling of bacteria on TiO_2 thin film. *Journal of Photochemistry and Photobiology A: Chemistry* 2003;156:227-33.
8. Su R, Dimitratos N, Liu J, et al. Mechanistic insight into the interaction between a titanium dioxide photocatalyst and Pd cocatalyst for improved photocatalytic performance. *ACS Catal* 2016;6:4239-47. DOI
9. Su R, Tiruvalam R, He Q, et al. Promotion of phenol photodecomposition over TiO_2 using Au, Pd, and Au-Pd nanoparticles. *ACS Nano* 2012;6:6284-92. DOI PubMed
10. Wang X, Sø L, Su R, et al. The influence of crystallite size and crystallinity of anatase nanoparticles on the photo-degradation of phenol. *Journal of Catalysis* 2014;310:100-8. DOI
11. Goto Y, Hisatomi T, Wang Q, et al. A particulate photocatalyst water-splitting panel for large-scale solar hydrogen generation. *Joule* 2018;2:509-20. DOI
12. Su R, Besenbacher F, Hutchings G. Alternative materials to TiO_2. DOI
13. Liu N, Schneider C, Freitag D, et al. Black TiO_2 nanotubes: cocatalyst-free open-circuit hydrogen generation. *Nano Lett* 2014;14:3309-13. DOI PubMed
14. Cao J, Ren L, Li N, Hu C, Cao M. Mesoporous $Ta(_3)N(_5)$ microspheres prepared from a high-surface-area, microporous, amorphous precursor and their visible-light-driven photocatalytic activity. *Chemistry* 2013;19:12619-23. DOI PubMed
15. Burton LA, Colombara D, Abellon RD, et al. Synthesis, characterization, and electronic structure of single-crystal SnS, Sn_2S_3, and SnS_2. *Chem Mater* 2013;25:4908-16.
16. Wang Y, Zhang Z, Zhu Y, et al. Nanostructured VO_2 photocatalysts for hydrogen production. *ACS Nano* 2008;2:1492-6. DOI PubMed
17. Bao N, Shen L, Takata T, Domen K. Self-templated synthesis of nanoporous CdS nanostructures for highly efficient photocatalytic hydrogen production under visible light. *Chem Mater* 2008;20:110-7.
18. Das R, Sarkar S, Kumar R, et al. Noble-metal-free heterojunction photocatalyst for selective CO_2 reduction to methane upon induced strain relaxation. *ACS Catal* 2022;12:687-97.
19. Liu Q, Wang S, Mo W, et al. Emerging stacked photocatalyst design enables spatially separated $Ni(OH)_2$ redox cocatalysts for overall CO_2 reduction and H_2O oxidation. *Small* 2022;18:e2104681. DOI
20. Chen Y, Zhang Y, Fan G, et al. Cooperative catalysis coupling photo-/photothermal effect to drive Sabatier reaction with unprecedented conversion and selectivity. *Joule* 2021;5:3235-51. DOI
21. Ghasimi S, Prescher S, Wang ZJ, Landfester K, Yuan J, Zhang KA. Heterophase photocatalysts from water-soluble conjugated polyelectrolytes: an example of self-initiation under visible light. *Angew Chem Int Ed Engl* 2015;54:14549-53. DOI PubMed
22. Zhang H, Liu G, Shi L, Liu H, Wang T, Ye J. Engineering coordination polymers for photocatalysis. *Nano Energy* 2016;22:149-68. DOI
23. Zhang G, Liu G, Wang L, Irvine JT. Inorganic perovskite photocatalysts for solar energy utilization. *Chem Soc Rev* 2016;45:5951-84. DOI PubMed
24. Dong B, Cui J, Liu T, et al. Development of novel perovskite-like oxide photocatalyst $LiCuTa_3O_9$ with dual functions of water reduction and oxidation under visible light irradiation. *Adv Energy Mater* 2018;8:1801660. DOI
25. Wang J, Wang C, Lin W. Metal-organic frameworks for light harvesting and photocatalysis. *ACS Catal* 2012;2:2630-40. DOI PubMed

26. Wang S, Wang X. Multifunctional metal-organic frameworks for photocatalysis. *Small* 2015;11:3097-112. DOI PubMed
27. Fu S, Yao S, Guo S, et al. Feeding carbonylation with CO_2 via the synergy of single-site/nanocluster catalysts in a photosensitizing MOF. *J Am Chem Soc* 2021;143:20792-801. DOI PubMed
28. Cheng X, Dao X, Wang S, Zhao J, Sun W. Enhanced photocatalytic CO_2 reduction activity over NH_2-MIL-125(Ti) by facet regulation. *ACS Catal* 2021;11:650-8. DOI
29. Lu H, Hao Q, Chen T, et al. A high-performance Bi_2O_3/Bi_2SiO_5 p-n heterojunction photocatalyst induced by phase transition of Bi2O3. *Applied Catalysis B: Environmental* 2018;237:59-67. DOI
30. Low J, Yu J, Jaroniec M, Wageh S, Al-Ghamdi AA. Heterojunction photocatalysts. *Adv Mater* 2017;29:1601694. DOI PubMed
31. Yang Y, Sun C, Wang L, et al. Constructing a metallic/semiconducting TaB_2/Ta_2O_5 core/shell heterostructure for photocatalytic hydrogen evolution. *Adv Energy Mater* 2014;4:1400057. DOI
32. Hu J, Chen D, Mo Z, et al. Z-scheme 2D/2D heterojunction of black phosphorus/monolayer Bi_2WO_6 nanosheets with enhanced photocatalytic activities. *Angew Chem Int Ed Engl* 2019;58:2073-7. DOI
33. Yang J, Wang D, Han H, Li C. Roles of cocatalysts in photocatalysis and photoelectrocatalysis. *Acc Chem Res* 2013;46:1900-9. DOI PubMed
34. Maeda K, Abe R, Domen K. Role and function of ruthenium species as promoters with TaON-based photocatalysts for oxygen evolution in two-step water splitting under Visible Light. *J Phys Chem C* 2011;115:3057-64. DOI
35. Vercammen J, Bocus M, Neale S, et al. Shape-selective C-H activation of aromatics to biarylic compounds using molecular palladium in zeolites. *Nat Catal* 2020;3:1002-9. DOI
36. Wang Y, Lv H, Grape ES, et al. A tunable multivariate metal-organic framework as a platform for designing photocatalysts. *J Am Chem Soc* 2021;143:6333-8. DOI PubMed PMC
37. Rosso C, Filippini G, Prato M. Use of nitrogen-doped carbon nanodots for the photocatalytic fluoroalkylation of organic compounds. *Chemistry* ;2019:16032-6. DOI PubMed
38. Zhao X, Deng C, Meng D, et al. Nickel-coordinated carbon nitride as a metallaphotoredox platform for the cross-coupling of aryl halides with alcohols. *ACS Catal* 2020;10:15178-85. DOI
39. Huang Y, Liu C, Li M, et al. Photoimmobilized Ni clusters boost photodehydrogenative coupling of amines to imines via enhanced hydrogen evolution kinetics. *ACS Catal* 2020;10:3904-10. DOI
40. Li S, Kim S, Davis AH, et al. Photocatalytic chemoselective C-C bond cleavage at room temperature in dye-sensitized photoelectrochemical cells. *ACS Catal* 2021;11:3771-81. DOI
41. Mazzanti S, Kurpil B, Pieber B, Antonietti M, Savateev A. Dichloromethylation of enones by carbon nitride photocatalysis. *Nat Commun* 2020;11:1387. DOI PubMed PMC
42. Khamrai J, Ghosh I, Savateev A, Antonietti M, König B. Photo-Ni-dual-catalytic $C(sp^2)$-$C(sp^3)$ cross-coupling reactions with mesoporous graphitic carbon nitride as a heterogeneous organic semiconductor photocatalyst. *ACS Catal* 2020;10:3526-32. DOI
43. Ithisuphalap K, Zhang H, Guo L, Yang Q, Yang H, Wu G. Photocatalysis and photoelectrocatalysis methods of nitrogen reduction for sustainable ammonia synthesis. *Small Methods* 2019;3:1800352. DOI
44. Zhao Y, Zhao Y, Waterhouse GIN, et al. Layered-double-hydroxide nanosheets as efficient visible-light-driven photocatalysts for dinitrogen fixation. *Adv Mater* 2017;29:1703828. DOI PubMed
45. Chen L, Tang J, Song L, et al. Heterogeneous photocatalysis for selective oxidation of alcohols and hydrocarbons. *Applied Catalysis B: Environmental* 2019;242:379-88. DOI
46. Parrino F, Bellardita M, García-lópez EI, Marcì G, Loddo V, Palmisano L. Heterogeneous photocatalysis for selective formation of high-value-added molecules: some chemical and engineering aspects. *ACS Catal* 2018;8:11191-225. DOI
47. Huang Y, Liu Z, Gao G, et al. Stable copper nanoparticle photocatalysts for selective epoxidation of alkenes with visible light. *ACS Catal* 2017;7:4975-85. DOI
48. Dai Y, Li C, Shen Y, et al. Efficient solar-driven hydrogen transfer by bismuth-based photocatalyst with engineered basic sites. *J Am Chem Soc* 2018;140:16711-9. DOI PubMed
49. Ma D, Liu A, Li S, Lu C, Chen C. TiO_2 photocatalysis for C-C bond formation. *Catal Sci Technol* 2018;8:2030-45. DOI
50. Fagnoni M, Dondi D, Ravelli D, Albini A. Photocatalysis for the formation of the C-C bond. *Chem Rev* 2007;107:2725-56. DOI PubMed
51. Corrigan N, Shanmugam S, Xu J, Boyer C. Photocatalysis in organic and polymer synthesis. *Chem Soc Rev* 2016;45:6165-212. DOI PubMed
52. Chen TQ, MacMillan DWC. A metallaphotoredox strategy for the cross-Electrophile coupling of α-Chloro carbonyls with aryl halides. *Angew Chem Int Ed Engl* 2019;58:14584-8. DOI PubMed PMC
53. Vasilopoulos A, Krska SW, Stahl SS. $C(sp^3)$-H methylation enabled by peroxide photosensitization and Ni-mediated radical coupling. *Science* 2021;372:398-403. DOI PubMed PMC
54. Liu Z, Nan X, Lei T, et al. Photo-induced reductive cross-coupling of aldehydes, ketones and imines with electron-deficient arenes to construct aryl substituted alcohols and amines. *Chinese Journal of Catalysis* 2018;39:487-94. DOI
55. Terrett JA, Cuthbertson JD, Shurtleff VW, MacMillan DW. Switching on elusive organometallic mechanisms with photoredox catalysis. *Nature* 2015;524:330-4. DOI PubMed PMC
56. Nakajima M, Fava E, Loescher S, Jiang Z, Rueping M. Photoredox-Catalyzed Reductive Coupling of Aldehydes, Ketones, and Imines with Visible Light. *Angew Chem Int Ed Engl* 2015;54:8828-32. DOI PubMed

57. Zhao G, Yang C, Guo L, Sun H, Lin R, Xia W. Reactivity insight into reductive coupling and aldol cyclization of chalcones by visible light photocatalysis. *J Org Chem* 2012;77:6302-6. DOI PubMed
58. Marzo L, Pagire SK, Reiser O, König B. Visible-light photocatalysis: does it make a difference in organic synthesis? *Angew Chem Int Ed Engl* 2018;57:10034-72. DOI PubMed
59. Dong Z, MacMillan DWC. Metallaphotoredox-enabled deoxygenative arylation of alcohols. *Nature* 2021;598:451-6. DOI PubMed PMC
60. Torres GM, Liu Y, Arndtsen BA. A dual light-driven palladium catalyst: Breaking the barriers in carbonylation reactions. *Science* 2020;368:318-23. DOI PubMed
61. Xu B, Troian-Gautier L, Dykstra R, Martin RT, Gutierrez O, Tambar UK. Photocatalyzed diastereoselective isomerization of cinnamyl chlorides to cyclopropanes. *J Am Chem Soc* 2020;142:6206-15. DOI PubMed PMC
62. Yang Q, Wang YH, Qiao Y, et al. Photocatalytic C-H activation and the subtle role of chlorine radical complexation in reactivity. *Science* 2021;372:847-52. DOI PubMed
63. Constantin T, Zanini M, Regni A, Sheikh NS, Juliá F, Leonori D. Aminoalkyl radicals as halogen-atom transfer agents for activation of alkyl and aryl halides. *Science* 2020;367:1021-6. DOI PubMed
64. Lee GS, Kim D, Hong SH. Pd-catalyzed formal Mizoroki-Heck coupling of unactivated alkyl chlorides. *Nat Commun* 2021;12:991. DOI PubMed PMC
65. Chen C, Peters JC, Fu GC. Photoinduced copper-catalysed asymmetric amidation via ligand cooperativity. *Nature* 2021;596:250-6. DOI PubMed PMC
66. Suzuki K, Mizuno N, Yamaguchi K. Polyoxometalate photocatalysis for liquid-phase selective organic functional group transformations. *ACS Catal* 2018;8:10809-25. DOI
67. Kobielusz M, Mikrut P, Macyk W. Materials for sustainable energy. Available from: https://www.elsevier.com/books/materials-for-sustainable-energy/van-eldik/978-0-12-815077-1 [Last accessed on 21 Apr 2022].
68. Miyabe H, Kohtani S. Photocatalytic single electron transfer reactions on TiO_2 semiconductor. *Sci China Chem* 2019;62:1439-49.
69. Bloh JZ, Marschall R. Heterogeneous photoredox catalysis: reactions, materials, and reaction engineering. *Eur J Org Chem* 2017;2017:2085-94. DOI
70. Chen Y, Lu L, Yu D, Zhu C, Xiao W. Visible light-driven organic photochemical synthesis in China. *Sci China Chem* 2019;62:24-57.
71. Colmenares JC, Luque R. Heterogeneous photocatalytic nanomaterials: prospects and challenges in selective transformations of biomass-derived compounds. *Chem Soc Rev* 2014;43:765-78. DOI PubMed
72. Fang Y, Zheng Y, Fang T, et al. Photocatalysis: an overview of recent developments and technological advancements. *Sci China Chem* 2020;63:149-81.
73. Cheng H, Xu W. Recent advances in modified TiO_2 for photo-induced organic synthesis. *Org Biomol Chem* 2019;17:9977-89. DOI PubMed
74. Gisbertz S, Pieber B. Heterogeneous photocatalysis in organic synthesis. *ChemPhotoChem* 2020;4:456-75. DOI
75. Bamwenda GR, Tsubota S, Nakamura T, Haruta M. Photoassisted hydrogen production from a water-ethanol solution: a comparison of activities of Au□TiO2 and Pt□TiO2. *Journal of Photochemistry and Photobiology A: Chemistry* 1995;89:177-89.
76. Bahruji H, Bowker M, Davies PR, Pedrono F. New insights into the mechanism of photocatalytic reforming on Pd/TiO_2. *Applied Catalysis B: Environmental* 2011;107:205-9. DOI
77. Wang X, Maeda K, Thomas A, et al. A metal-free polymeric photocatalyst for hydrogen production from water under visible light. *Nat Mater* 2009;8:76-80. DOI PubMed
78. Wu B, Liu D, Mubeen S, Chuong TT, Moskovits M, Stucky GD. Anisotropic growth of TiO_2 onto gold nanorods for plasmon-enhanced hydrogen production from water reduction. *J Am Chem Soc* 2016;138:1114-7. DOI PubMed
79. Samanta S, Martha S, Parida K. Facile synthesis of Au/g-C_3N_4 nanocomposites: an inorganic/organic hybrid plasmonic photocatalyst with enhanced hydrogen gas evolution under visible-light irradiation. *ChemCatChem* 2014. DOI
80. Ruberu TPA, Nelson NC, Slowing II, Vela J. Selective alcohol dehydrogenation and hydrogenolysis with semiconductor-metal photocatalysts: toward solar-to-chemical energy conversion of biomass-relevant substrates. *J Phys Chem Lett* 2012;3:2798-802. DOI
81. Lu H, Zhao J, Li L, et al. Selective oxidation of sacrificial ethanol over TiO_2-based photocatalysts during water splitting. *Energy Environ Sci* 2011;4:3384. DOI
82. Zhang H, Wu Y, Li L, Zhu Z. Photocatalytic direct conversion of ethanol to 1,1- diethoxyethane over noble-metal-loaded TiO_2 nanotubes and nanorods. *ChemSusChem* 2015;8:1226-31. DOI PubMed
83. Pillai UR, Sahle–demessie E. Selective oxidation of alcohols in gas phase using light-activated titanium dioxide. *Journal of Catalysis* 2002;211:434-44. DOI
84. Park JY, Baker LR, Somorjai GA. Role of hot electrons and metal-oxide interfaces in surface chemistry and catalytic reactions. *Chem Rev* 2015;115:2781-817. DOI PubMed
85. Li H, Qin F, Yang Z, Cui X, Wang J, Zhang L. New reaction pathway induced by plasmon for selective benzyl alcohol oxidation on BiOCl possessing oxygen vacancies. *J Am Chem Soc* 2017;139:3513-21. DOI PubMed
86. Nakato Y, Ueda K, Yano H, Tsubomura H. Effect of microscopic discontinuity of metal overlayers on the photovoltages in metal-coated semiconductor-liquid junction photoelectrochemical cells for efficient solar energy conversion. *J Phys Chem* 1988;92:2316-24. DOI
87. Sakamoto H, Ohara T, Yasumoto N, et al. Hot-Electron-Induced Highly Efficient O2 Activation by Pt Nanoparticles Supported on

Ta2O5 Driven by Visible Light. *J Am Chem Soc* 2015;137:9324-32. DOI PubMed

88. Sugano Y, Shiraishi Y, Tsukamoto D, Ichikawa S, Tanaka S, Hirai T. Supported Au-Cu bimetallic alloy nanoparticles: an aerobic oxidation catalyst with regenerable activity by visible-light irradiation. *Angew Chem Int Ed Engl* 2013;52:5295-9. DOI PubMed
89. Landry MJ, Gellé A, Meng BY, Barrett CJ, Moores A. Surface-plasmon-mediated hydrogenation of carbonyls catalyzed by silver nanocubes under visible light. *ACS Catal* 2017;7:6128-33. DOI
90. Han C, Yang X, Gao G, et al. Selective oxidation of methanol to methyl formate on catalysts of Au-Ag alloy nanoparticles supported on titania under UV irradiation. *Green Chem* 2014;16:3603-15. DOI
91. Xiao Q, Liu Z, Bo A, et al. Catalytic transformation of aliphatic alcohols to corresponding esters in O_2 under neutral conditions using visible-light irradiation. *J Am Chem Soc* 2015;137:1956-66. DOI PubMed
92. Su R, Tiruvalam R, Logsdail AJ, et al. Designer titania-supported Au-Pd nanoparticles for efficient photocatalytic hydrogen production. *ACS Nano* 2014;8:3490-7. DOI PubMed
93. Jiang X, Fu X, Zhang L, Meng S, Chen S. Photocatalytic reforming of glycerol for H_2 evolution on Pt/TiO_2: fundamental understanding the effect of co-catalyst Pt and the Pt deposition route. *J Mater Chem A* 2015;3:2271-82. DOI
94. Sanwald KE, Berto TF, Eisenreich W, Gutiérrez OY, Lercher JA. Catalytic routes and oxidation mechanisms in photoreforming of polyols. *Journal of Catalysis* 2016;344:806-16. DOI
95. Berto TF, Sanwald KE, Eisenreich W, Gutiérrez OY, Lercher JA. Photoreforming of ethylene glycol over Rh/TiO_2 and Rh/GaN:ZnO. *Journal of Catalysis* 2016;338:68-81. DOI
96. Jin X, Li C, Xu C, et al. Photocatalytic C C bond cleavage in ethylene glycol on TiO_2: a molecular level picture and the effect of metal nanoparticles. *Journal of Catalysis* 2017;354:37-45. DOI
97. Chong R, Li J, Zhou X, et al. Selective photocatalytic conversion of glycerol to hydroxyacetaldehyde in aqueous solution on facet tuned TiO_2-based catalysts. *Chem Commun (Camb)* 2014;50:165-7. DOI PubMed
98. Augugliaro V, El Nazer HH, Loddo V, et al. Partial photocatalytic oxidation of glycerol in TiO_2 water suspensions. *Catalysis Today* 2010;151:21-8.
99. Li C, Wang X, Cheruvathur A, et al. In-situ probing photocatalytic C-C bond cleavage in ethylene glycol under ambient conditions and the effect of metal cocatalyst. *Journal of Catalysis* 2018;365:313-9. DOI
100. Zhang Y, Zhang N, Tang Z, Xu Y. Identification of Bi_2WO_6 as a highly selective visible-light photocatalyst toward oxidation of glycerol to dihydroxyacetone in water. *Chem Sci* 2013;4:1820. DOI
101. Sajkowski DJ, Boudart M. Structure sensitivity of the catalytic oxidation of ethene by silver. *Catalysis Reviews* 1987;29:325-60. DOI
102. Nijhuis TA, Makkee M, Moulijn JA, Weckhuysen BM. The Production of propene oxide: catalytic processes and recent developments. *Ind Eng Chem Res* 2006;45:3447-59. DOI
103. Torres D, Lopez N, Illas F, Lambert RM. Why copper is intrinsically more selective than silver in alkene epoxidation: ethylene oxidation on Cu(111) versus Ag(111). *J Am Chem Soc* 2005;127:10774-5. DOI PubMed
104. Christopher P, Xin H, Linic S. Visible-light-enhanced catalytic oxidation reactions on plasmonic silver nanostructures. *Nat Chem* 2011;3:467-72. DOI PubMed
105. Christopher P, Xin H, Marimuthu A, Linic S. Singular characteristics and unique chemical bond activation mechanisms of photocatalytic reactions on plasmonic nanostructures. *Nat Mater* 2012;11:1044-50. DOI PubMed
106. Marimuthu A, Zhang J, Linic S. Tuning selectivity in propylene epoxidation by plasmon mediated photo-switching of Cu oxidation state. *Science* 2013;339:1590-3. DOI PubMed
107. Zhang X, Kumari G, Heo J, Jain PK. In situ formation of catalytically active graphene in ethylene photo-epoxidation. *Nat Commun* 2018;9:3056. DOI PubMed PMC
108. Jin JK, Wu K, Liu XY, et al. Building a Pyrazole-benzothiadiazole-pyrazole photosensitizer into metal-organic frameworks for photocatalytic aerobic oxidation. *J Am Chem Soc* 2021;143:21340-9. DOI PubMed
109. Dai Y, Ren P, Li Y, et al. Solid base $Bi_{24}O_{31}Br_{10}(OH)_\delta$ with Active lattice oxygen for the efficient photo-oxidation of primary alcohols to aldehydes. *Angew Chem Int Ed Engl* 2019;58:6265-70. DOI
110. Chen X, Zhang J, Fu X, Antonietti M, Wang X. Fe-g-C_3N_4-catalyzed oxidation of benzene to phenol using hydrogen peroxide and visible light. *J Am Chem Soc* 2009;131:11658-9. DOI PubMed
111. Yoshida H, Yuzawa H, Aoki M, Otake K, Itoh H, Hattori T. Photocatalytic hydroxylation of aromatic ring by using water as an oxidant. *Chem Commun (Camb)* 2008:4634-6. DOI PubMed
112. Yuzawa H, Aoki M, Otake K, Hattori T, Itoh H, Yoshida H. Reaction mechanism of aromatic ring hydroxylation by water over platinum-loaded titanium oxide photocatalyst. *J Phys Chem C* 2012;116:25376-87.
113. Zhang G, Yi J, Shim J, Lee J, Choi W. Photocatalytic hydroxylation of benzene to phenol over titanium oxide entrapped into hydrophobically modified siliceous foam. *Applied Catalysis B: Environmental* 2011;102:132-9. DOI
114. Su R, Kesavan L, Jensen MM, et al. Selective photocatalytic oxidation of benzene for the synthesis of phenol using engineered Au-Pd alloy nanoparticles supported on titanium dioxide. *Chem Commun (Camb)* 2014;50:12612-4. DOI PubMed
115. Hosseini SM, Ghiaci M, Kulinich SA, et al. Au-Pd@g-C_3N_4 as an efficient photocatalyst for visible-light oxidation of benzene to phenol: experimental and mechanistic study. *J Phys Chem C* 2018;122:27477-85. DOI
116. He J, Zhang M, Primo A, García H, Li Z. Selective photocatalytic benzene hydroxylation to phenol using surface-modified Cu_2O supported on graphene. *J Mater Chem A* 2018;6:19782-7. DOI
117. Ide Y, Matsuoka M, Ogawa M. Efficient visible-light-induced photocatalytic activity on gold-nanoparticle-supported layered titanate.

J Am Chem Soc 2010;132:16762-4. DOI PubMed

118. Jaynes BS, Hill CL. Radical carbonylation of alkanes via polyoxotungstate photocatalysis. *J Am Chem Soc* 1995;117:4704-5. DOI
119. Suzuki K, Tang F, Kikukawa Y, Yamaguchi K, Mizuno N. Visible-light-induced photoredox catalysis with a tetracerium-containing silicotungstate. *Angew Chem Int Ed Engl* 2014;53:5356-60. DOI PubMed
120. Yamamoto A, Ohara T, Yoshida H. Visible-light-induced photocatalytic benzene/cyclohexane cross-coupling utilizing a ligand-to-metal charge transfer benzene complex adsorbed on titanium oxides. *Catal Sci Technol* 2018;8:2046-50. DOI
121. Cao X, Chen Z, Lin R, et al. A photochromic composite with enhanced carrier separation for the photocatalytic activation of benzylic C-H bonds in toluene. *Nat Catal* 2018;1:704-10. DOI
122. Wu X, Fan X, Xie S, et al. Solar energy-driven lignin-first approach to full utilization of lignocellulosic biomass under mild conditions. *Nat Catal* 2018;1:772-80. DOI
123. Eisenhofer A, Hioe J, Gschwind RM, König B. Photocatalytic phenol-arene C-C and C-O cross-dehydrogenative coupling: photocatalytic phenol-arene C-C and C-O cross-dehydrogenative coupling. *Eur J Org Chem* 2017;2017:2194-204. DOI
124. Zhao G, Yang C, Guo L, Sun H, Chen C, Xia W. Visible light-induced oxidative coupling reaction: easy access to Mannich-type products. *Chem Commun (Camb)* 2012;48:2337-9. DOI PubMed
125. Tan Y, Lin S, Liu C, et al. Boosting photocatalytic cross-dehydrogenative coupling reaction by incorporating [RuII(bpy)$_3$] into a radical metal-organic framework. *Applied Catalysis B: Environmental* 2018;227:425-32. DOI
126. Zhang N, Li X, Ye H, et al. Oxide defect engineering enables to couple solar energy into oxygen activation. *J Am Chem Soc* 2016;138:8928-35. DOI PubMed
127. Raza F, Park JH, Lee H, Kim H, Jeon S, Kim J. Visible-light-driven oxidative coupling reactions of amines by photoactive WS_2 nanosheets. *ACS Catal* 2016;6:2754-9. DOI
128. Xu Y, Chen Y, Fu W. Visible-light driven oxidative coupling of amines to imines with high selectivity in air over core-shell structured CdS@C_3N_4. *Applied Catalysis B: Environmental* 2018;236:176-83. DOI
129. Yu J, Liu Q, Qiao W, et al. Catalytic role of metal nanoparticles in selectivity control over photodehydrogenative coupling of primary amines to imines and secondary amines. *ACS Catal* 2021;11:6656-61. DOI
130. Xie S, Shen Z, Deng J, et al. Visible light-driven C-H activation and C-C coupling of methanol into ethylene glycol. *Nat Commun* 2018;9:1181. DOI PubMed PMC
131. Xiao Q, Sarina S, Bo A, et al. Visible light-driven cross-coupling reactions at lower temperatures using a photocatalyst of palladium and gold alloy nanoparticles. *ACS Catal* 2014;4:1725-34. DOI
132. Ghasimi S, Bretschneider SA, Huang W, Landfester K, Zhang KAI. A Conjugated microporous polymer for palladium-free, visible light-promoted photocatalytic stille-type coupling reactions. *Adv Sci (Weinh)* 2017;4:1700101. DOI PubMed PMC
133. Shiraishi Y, Fujiwara K, Sugano Y, Ichikawa S, Hirai T. N-Monoalkylation of amines with alcohols by tandem photocatalytic and catalytic reactions on TiO_2 loaded with Pd nanoparticles. *ACS Catal* 2013;3:312-20. DOI
134. Wang LM, Morioka Y, Jenkinson K, Wheatley AEH, Saito S, Naka H. N-Alkylation of functionalized amines with alcohols using a copper-gold mixed photocatalytic system. *Sci Rep* 2018;8:6931. DOI PubMed PMC
135. Lv D, Li Y, Qiao W, et al. Metal cocatalyst mediated photocatalytic dehydrogenative-condensation and direct condensation cross-coupling of aniline and alcohol. *Applied Catalysis B: Environmental* 2022;309:121264. DOI
136. Alkhatib II, Garlisi C, Pagliaro M, Al-ali K, Palmisano G. Metal-organic frameworks for photocatalytic CO_2 reduction under visible radiation: a review of strategies and applications. *Catalysis Today* 2020;340:209-24. DOI
137. Yu S, Wilson AJ, Heo J, Jain PK. Plasmonic control of multi-electron transfer and C-C coupling in visible-light-driven CO_2 reduction on Au nanoparticles. *Nano Lett* 2018;18:2189-94. DOI PubMed
138. Iwase A, Yoshino S, Takayama T, Ng YH, Amal R, Kudo A. Water splitting and CO_2 reduction under visible light irradiation using Z-scheme systems consisting of metal sulfides, CoOx-loaded $BiVO_4$, and a reduced graphene oxide electron mediator. *J Am Chem Soc* 2016;138:10260-4. DOI PubMed
139. Wang S, Hou Y, Wang X. Development of a stable $MnCo_2O_4$ cocatalyst for photocatalytic CO_2 reduction with visible light. *ACS Appl Mater Interfaces* 2015;7:4327-35. DOI PubMed
140. Ye M, Wang X, Liu E, Ye J, Wang D. Boosting the photocatalytic activity of P25 for carbon dioxide reduction by using a surface-alkalinized titanium carbide mxene as cocatalyst. *ChemSusChem* 2018;11:1606-11. DOI PubMed
141. Iizuka K, Wato T, Miseki Y, Saito K, Kudo A. Photocatalytic reduction of carbon dioxide over Ag cocatalyst-loaded $ALa_4Ti_4O_{15}$ (A = Ca, Sr, and Ba) using water as a reducing reagent. *J Am Chem Soc* 2011;133:20863-8. DOI PubMed
142. Chang X, Wang T, Gong J. CO_2 photo-reduction: insights into CO_2 activation and reaction on surfaces of photocatalysts. *Energy Environ Sci* 2016;9:2177-96. DOI
143. Sastre F, Corma A, García H. Visible-light photocatalytic conversion of carbon monoxide to methane by nickel(II) oxide. *Angew Chem Int Ed Engl* 2013;52:12983-7. DOI PubMed
144. Sastre F, Puga AV, Liu L, Corma A, García H. Complete photocatalytic reduction of CO_2 to methane by H_2 under solar light irradiation. *J Am Chem Soc* 2014;136:6798-801. DOI PubMed
145. Guo X, Jiao Z, Jin G, Guo X. Photocatalytic Fischer-Tropsch synthesis on graphene-supported worm-like ruthenium nanostructures. *ACS Catal* 2015;5:3836-40.
146. Chen G, Gao R, Zhao Y, et al. Alumina-supported CoFe Alloy catalysts derived from layered-double-hydroxide nanosheets for efficient photothermal CO_2 hydrogenation to hydrocarbons. *Adv Mater* 2018;30:1704663. DOI PubMed

147. Zhao Y, Li Z, Li M, et al. Reductive transformation of layered-double-hydroxide nanosheets to fe-based heterostructures for efficient visible-light photocatalytic hydrogenation of CO. *Adv Mater* 2018:e1803127. DOI PubMed
148. Li Z, Zhang X, Liu J, et al. Titania-supported Ni_2P/Ni catalysts for selective solar-driven CO hydrogenation. *Adv Mater* 2021;33:e2103248.
149. Li Z, Liu J, Shi R, Waterhouse GIN, Wen X, Zhang T. Fe-based catalysts for the direct photohydrogenation of CO_2 to value-added hydrocarbons. *Adv Energy Mater* 2021;11:2002783. DOI
150. Ye JH, Ju T, Huang H, Liao LL, Yu DG. Radical Carboxylative Cyclizations and Carboxylations with CO_2. *Acc Chem Res* 2021;54:2518-31. DOI PubMed
151. Yang T, Yu Q, Wang H. Photocatalytic reduction of CO_2 to CH_3OH coupling with the oxidation of amine to imine. *Catal Lett* 2018;148:2382-90. DOI
152. Chen Y, Wang M, Ma Y, Li Y, Cai J, Li Z. Coupling photocatalytic CO_2 reduction with benzyl alcohol oxidation to produce benzyl acetate over Cu_2O/Cu. *Catal Sci Technol* 2018;8:2218-23. DOI
153. Campos-Martin JM, Blanco-Brieva G, Fierro JL. Hydrogen peroxide synthesis: an outlook beyond the anthraquinone process. *Angew Chem Int Ed Engl* 2006;45:6962-84. DOI PubMed
154. Teranishi M, Naya S, Tada H. In situ liquid phase synthesis of hydrogen peroxide from molecular oxygen using gold nanoparticle-loaded titanium(IV) dioxide photocatalyst. *J Am Chem Soc* 2010;132:7850-1. DOI PubMed
155. Xiong X, Zhang X, Liu S, Zhao J, Xu Y. Sustained production of H_2O_2 in alkaline water solution using borate and phosphate-modified Au/TiO_2 photocatalysts. *Photochem Photobiol Sci* 2018;17:1018-22. DOI PubMed
156. Moon G, Kim W, Bokare AD, Sung N, Choi W. Solar production of H_2O_2 on reduced graphene oxide-TiO_2 hybrid photocatalysts consisting of earth-abundant elements only. *Energy Environ Sci* 2014;7:4023-8. DOI
157. Shiraishi Y, Kanazawa S, Sugano Y, et al. Highly selective production of hydrogen peroxide on graphitic carbon nitride (g-C_3N_4) photocatalyst activated by visible light. *ACS Catal* 2014;4:774-80. DOI
158. He B, Feng M, Chen X, Sun J. Multidimensional (0D-3D) Functional nanocarbon: promising material to strengthen the photocatalytic activity of graphitic carbon nitride. *Green Energy Environ* 2021;6:823-45. DOI
159. Li S, Dong G, Hailili R, et al. Effective photocatalytic H_2O_2 production under visible light irradiation at g-C_3N_4 modulated by carbon vacancies. *Applied Catalysis B: Environmental* 2016;190:26-35. DOI
160. Kim H, Choi Y, Hu S, Choi W, Kim J. Photocatalytic hydrogen peroxide production by anthraquinone-augmented polymeric carbon nitride. *Applied Catalysis B: Environmental* 2018;229:121-9. DOI PubMed
161. Teng Z, Zhang Q, Yang H, et al. Atomically dispersed antimony on carbon nitride for the artificial photosynthesis of hydrogen peroxide. *Nat Catal* 2021;4:374-84. DOI
162. Joyce-pruden C, Pross JK, Li Y. Photoinduced reduction of aldehydes on titanium dioxide. *J Org Chem* 1992;57:5087-91. DOI
163. Yanagida S, Yoshiya M, Shiragami T, Pac C, Mori H, Fujita H. Semiconductor photocatalysis. I. Quantitative photoreduction of aliphatic ketones to alcohols using defect-free zinc sulfide quantum crystallites. *J Phys Chem* 1990;94:3104-11. DOI
164. Hao D, Liu Y, Gao S, et al. Emerging artificial nitrogen cycle processes through novel electrochemical and photochemical synthesis. *Materials Today* 2021;46:212-33. DOI
165. Zhang H, Zhao M, Zhao T, Li L, Zhu Z. Hydrogenative cyclization of levulinic acid into γ-valerolactone by photocatalytic intermolecular hydrogen transfer. *Green Chem* 2016;18:2296-301. DOI
166. Kohtani S, Nishioka S, Yoshioka E, Miyabe H. Dye-sensitized photo-hydrogenation of aromatic ketones on titanium dioxide under visible light irradiation. *Catalysis Communications* 2014;43:61-5. DOI
167. Jiao Z, Guo X, Zhai Z, Jin G, Wang X, Guo X. The enhanced catalytic performance of Pd/SiC for the hydrogenation of furan derivatives at ambient temperature under visible light irradiation. *Catal Sci Technol* 2014;4:2494-8. DOI
168. Hao CH, Guo XN, Pan YT, et al. Visible-light-driven selective photocatalytic hydrogenation of cinnamaldehyde over Au/SiC catalysts. *J Am Chem Soc* 2016;138:9361-4. DOI PubMed
169. Shiraishi Y, Togawa Y, Tsukamoto D, Tanaka S, Hirai T. Highly efficient and selective hydrogenation of nitroaromatics on photoactivated rutile titanium dioxide. *ACS Catal* 2012;2:2475-81. DOI
170. Toyao T, Saito M, Horiuchi Y, et al. Efficient hydrogen production and photocatalytic reduction of nitrobenzene over a visible-light-responsive metal–organic framework photocatalyst. *Catal Sci Technol* 2013;3:2092. DOI
171. Gao WZ, Xu Y, Chen Y, Fu WF. Highly efficient and selective photocatalytic reduction of nitroarenes using the Ni_2P/CdS catalyst under visible-light irradiation. *Chem Commun (Camb)* 2015;51:13217-20. DOI PubMed
172. Xiao G, Li P, Zhao Y, Xu S, Su H. Visible-light-driven chemoselective hydrogenation of nitroarenes to anilines in water through graphitic carbon nitride metal-free photocatalysis. *Chem Asian J* ;2018:1950-5. DOI PubMed
173. Huang Y, Liu Z, Gao G, et al. Visible light-driven selective hydrogenation of unsaturated aromatics in an aqueous solution by direct photocatalysis of Au nanoparticles. *Catal Sci Technol* 2018;8:726-34. DOI
174. Buckler SA, Doll L, Lind FK, Epstein M. Phosphine as a reducing agent. *J Org Chem* 1962;27:794-8. DOI
175. Galbraith HW, Degering EF, Hitch EF. The Alkaline reduction of aromatic nitro compounds with glucose. *J Am Chem Soc* 1951;73:1323-4. DOI
176. Mckillop A, Raphael RA, Taylor EC. Thallium in organic synthesis. XI. Preparation of azoxy compounds. *J Org Chem* 1970;35:1670-2. DOI
177. Osuka A, Shimizu H, Suzuki H. Reduction of aromatic and aliphatic Nitro compounds by sodium hydrogen telluride. *Chem Lett*

1983;12:1373-4. DOI
178. Fortman GC, Nolan SP. N-Heterocyclic carbene (NHC) ligands and palladium in homogeneous cross-coupling catalysis: a perfect union. *Chem Soc Rev* 2011;40:5151-69. DOI PubMed
179. Zhang G, Scott BL, Hanson SK. Mild and homogeneous cobalt-catalyzed hydrogenation of C=C, C=O, and C=N bonds. *Angew Chem Int Ed Engl* 2012;51:12102-6. DOI PubMed
180. Zhang X, Smith RT, Le C, et al. Copper-mediated synthesis of drug-like bicyclopentanes. *Nature* 2020;580:220-6. DOI PubMed PMC
181. Laudadio G, Deng Y, van der Wal K, et al. C(sp^3)-H functionalizations of light hydrocarbons using decatungstate photocatalysis in flow. *Science* 2020;369:92-6. DOI PubMed
182. Dong XY, Cheng JT, Zhang YF, et al. Copper-catalyzed asymmetric radical 1,2-carboalkynylation of alkenes with alkyl halides and terminal alkynes. *J Am Chem Soc* 2020;142:9501-9. DOI PubMed
183. Li Z, Jin J, Huang S. Recent advances in transition metal-catalyzed cross-coupling reactions directly promoted by visible light. *Chin J Org Chem* 2020;40:563. DOI
184. Zhang Z, Xu Y, Zhang Q, et al. Semi-heterogeneous photo-Cu-dual-catalytic cross-coupling reactions using polymeric carbon nitrides. *Science Bulletin* 2022;67:71-8. DOI
185. Wang F, Li C, Chen H, et al. Plasmonic harvesting of light energy for Suzuki coupling reactions. *J Am Chem Soc* 2013;135:5588-601. DOI PubMed
186. Lanterna AE, Elhage A, Scaiano JC. Heterogeneous photocatalytic C-C coupling: mechanism of plasmon-mediated reductive dimerization of benzyl bromides by supported gold nanoparticles. *Catal Sci Technol* 2015;5:4336-40. DOI
187. Li Y, Ren P, Zhang D, et al. Rationally designed metal cocatalyst for selective photosynthesis of bibenzyls via dehalogenative C-C homocoupling. *ACS Catal* 2021;11:4338-48. DOI
188. Filippini G, Longobardo F, Forster L, et al. Light-driven, heterogeneous organocatalysts for C-C bond formation toward valuable perfluoroalkylated intermediates. *Sci Adv* 2020;6:eabc9923. DOI PubMed PMC
189. Zhu H, Ke X, Yang X, Sarina S, Liu H. Reduction of nitroaromatic compounds on supported gold nanoparticles by visible and ultraviolet light. *Angew Chem Int Ed Engl* 2010;49:9657-61. DOI PubMed
190. Liu Z, Huang Y, Xiao Q, Zhu H. Selective reduction of nitroaromatics to azoxy compounds on supported Ag-Cu alloy nanoparticles through visible light irradiation. *Green Chem* 2016;18:817-25. DOI
191. Guo X, Hao C, Jin G, Zhu HY, Guo XY. Copper nanoparticles on graphene support: an efficient photocatalyst for coupling of nitroaromatics in visible light. *Angew Chem Int Ed Engl* 2014;53:1973-7. DOI PubMed
192. Brezová V, Tarábek P, Dvoranová D, Staško A, Biskupič S. EPR study of photoinduced reduction of nitroso compounds in titanium dioxide suspensions. *Journal of Photochemistry and Photobiology A: Chemistry* 2003;155:179-98. DOI
193. Pal B, Torimoto T, Okazaki K, Ohtani B. Photocatalytic syntheses of azoxybenzene by visible light irradiation of silica-coated cadmium sulfide nanocomposites. *Chem Commun (Camb)* 2007:483-5. DOI PubMed
194. Dai Y, Li C, Shen Y, et al. Light-tuned selective photosynthesis of azo- and azoxy-aromatics using graphitic C_3N_4. *Nat Commun* 2018;9:60. DOI PubMed PMC
195. Sun Y, Li Y, Li Z, et al. Flat and stretched delafossite α-$AgGaO_2$: manipulating redox chemistry under visible light. *ACS Catal* 2021;11:15083-8. DOI

Yaru Li

Yaru Li obtained her B.Sc. from Taiyuan University of Technology, China in 2017. She started her PhD study at Institute of Coal Chemistry, Chinese Academy of Sciences (ICCCAS) and SynCat@Beijing, Synfuels China Technology Co. Ltd under the supervison of Prof. Xiang and Prof. Su in 2017. She focuses on selective photosynthesis of value-added chemicals by metal cocatalyst mediated coupling reactions.

Dongsheng Zhang

Dongsheng Zhang obtained his B.Sc. in pharmacology and his M.Sc in organic chemistry at Nanchang University and Huaqiao University, respectively. In 2020, he joined Soochow institute for energy and materials innovations (SIEMIS) at the Soochow University as a PhD student, focusing on green synthesis of azoxy-aromatics, primary amines, hydrogen peroxide by heterogeneous photocatalysis under the supervision of Prof. Su.

Wei Qiao

Wei Qiao earned his B.Sc. in chemistry from Shanxi University of China in 2013. After that, he obtained his PhD degree in physical chemistry at ICCCAS in 2019. He is currently a postdoctoral researcher at SIEMIS, Soochow University, focusing on the design and development of photo-/electro-catalysts for fine chemical synthesis.

Hongwei Xiang

Hongwei Xiang graduated from Jilin University (China) in 1984. He completed PhD at ICCCAS in 1995. He visited the Chemical Engineering Department of West Virginia University as a research scholar in 1996. He is currently a researcher and doctoral supervisor of the State Key Laboratory of Coal Conversion at ICCCAS, focusing on the Fischer-Tropsch synthesis, the development and fundamental understanding of iron-based catalyst.

Yongwang Li

Yongwang Li completed his M.Sc. and PhD at ICCCAS from 1986-1994. After that, he joined Institute of Petroleum Research, GENT University (Belgium) as a postdoctoral fellow in 1995, and Institute of Catalysis, University of Leuven (Belgium) in 1996, before becoming a professor at ICCCAS. He is the founder of Synfuels China Technology Co. Ltd. and Syncat@Bejing. He is engaged in industrial chemistry and engineering, computational simulation, reaction kinetics, reactor and process development, thermochemistry and structural chemistry. He is also interested in the development of fundamental science tools.

Flemming Besenbacher

Flemming Besenbacher received his PhD from Aarhus University in Denmark in 1978. He is a professor and doctor of natural sciences at the Interdisciplinary Nanoscience Centre (iNANO) and the Department of Physics and Astronomy at Aarhus University. He is a member of the Danish Academy of Natural Sciences, the Danish Academy of Science and Technology, and the Royal Danish Academy of Sciences. He is engaged in the development and application of scanning probe microscopy and other surface science technologies, which have been applied in many fields such as physics, chemistry, biology, and medicine.

Ren Su

Ren Su received his PhD from Aarhus University in Denmark in 2012 and continued as a postdoctoral researcher at Aarhus University and Cardiff University. He is a professor at SIEMIS at Soochow University in collaboration with Synfuels China Technology Co. Ltd. as a research scientist. His research interests focus on fundamental understanding of photo(electro)catalysis by in-situ techniques and their applications in organic synthesis.

Yao. *Chem Synth* 2022;2:10
DOI: 10.20517/cs.2022.13

Chemical Synthesis

Editor's Choice

Open Access

Boosting lithium-selenium batteries

Xiangdong Yao*

State Key Laboratory of Inorganic Synthesis and Preparative Chemistry, College of Chemistry, Jilin University, Changchun 130012, Jilin, China.

*__Correspondence to:__ Prof. Xiangdong Yao, State Key Laboratory of Inorganic Synthesis and Preparative Chemistry, College of Chemistry, Jilin University, Changchun 130012, Jilin, China. E-mail: xdyao@jlu.edu.cn

How to cite this article: Yao X. Boosting lithium-selenium batteries. *Chem Synth* 2022;2:10. https://dx.doi.org/10.20517/cs.2022.13

Received: 2 Jun 2022 **Accepted:** 10 Jun 2022 **Published:** 14 Jun 2022

Academic Editor: Huiqiao Li **Copy Editor:** Peng-Juan Wen **Production Editor:** Peng-Juan Wen

Lithium-selenium (Li-Se) batteries have been recognized as one of the most promising candidates for next-generation energy storage devices due to their high energy density and high conductivity of Se[1,2]. However, the shuttle effect has become a major shackle restricting their commercial development[3,4]. Confining active material selenium inside the cathode is an effective method to suppress this phenomenon[5]. Moreover, rapid transportation of electrons and ions is indispensable for achieving high electrochemical performance Li-Se batteries[6].

Combining the microporous carbon particles that provide Se loading space and adsorption to polyselenides with a highly conductive meso/macropores network is a design direction to suppress the shuttle effect and achieve high reaction kinetics[7]. Microporous-rich metal-organic framework (MOF) and high conductivity CNTs become the ideal compositions. The current work presents tunable size zeolitic imidazolate framework-8 (ZIF-8) derived microporous carbon particles strung by MWCNTs (ZIF-8-C@MWCNTs-X, X = 1-5) with a simple *in-situ* solvothermal reaction [Figure 1][8]. The active Se is dispersed in the designed ZIF-8-C@MWCNTs host materials by a simple melt-diffusion method.

Compared with Se@ZIF-8-C cathode battery, the electrochemical performance of Se@ZIF-8-C@MWCNTs achieves high improvement due to the accelerated electron/ions transfer brought by the interconnected MWCNTs. Moreover, the size of ZIF-8-C particles is a critical factor for electrochemical kinetics in the charge/discharge process. For too small particles of ZIF-8-C, the problem of shuttle effect is serious due to

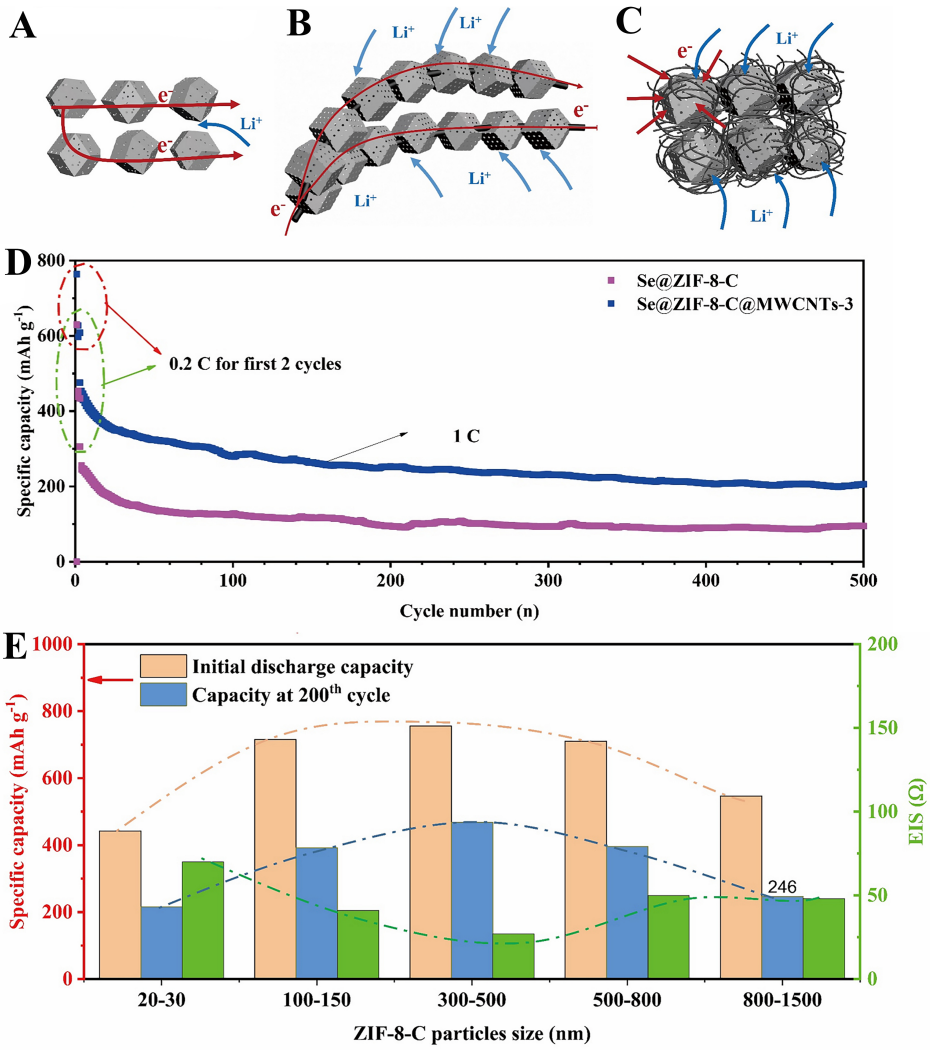

Figure 1. Schematic mechanism of the (A) Se@ZIF-8-C, (B) ZIF-8-C@MWCNTs-1 and (C) Se@ZIF-8-C@MWCNTs-5 electrodes for lithium ion and electron movement. (D) Cycling performance of Se@ZIF-8-C and Se@ZIF-8-C@MWCNTs-3 at high current density of 1 C, (E) summary of the specific capacity and impedance of the Se@ZIF-8-C@MWCNTs-X (X = 1-5) positive electrodes according to the particle size of the internal ZIF-8 derived porous carbon.

the easily diffused out polyselenide. Otherwise, too large particle size leaves the ions transfer difficult. At an optimized particle size of 300-500 nm, both the suppressed shuttle effect and the rapid ions transfer are achieved. Se@ZIF-8-C@MWCNTs-3 with the optimized ZIF-8-C size exhibited the best cycle stability with a high capacity of 468 mAh g^{-1} at 0.2 C after 200 cycles. Even at the high rate of 1 C, the capacity of Se@ZIF-8-C@MWCNT-3 can remain at 206 mAh g^{-1} after 500 cycles.

In the designed Se@ZIF-8-C@MWCNTs system, ZIF-8-C particle functions as a reaction block, where the Se confined inside of the micropores undergoes a rapid electrochemical reaction. While the interconnected MWCNTs works as transfer block to ensure the supply of required electrons and ions. This kind of block mode design realizes both the confinement of the reaction and the rapid mass transportation. Compared with the conflated design system, the modular system enables the electrochemical reaction inside the battery to proceed in an orderly manner as living organisms. The efficient synergy of different modules is the premise for the system to maximize its value, which is reflected in the particle size of ZIF-8-C nanocarbons

in the Se@ZIF-8-C@MWCNTs system. The Se@ZIF-8-MWCNTs system obtains the best match at the size of 300-500 nm.

The design concept of coordinated development of work blocks has a significant effect on the working mechanism of the system. It could give a guiding for other reaction environments. The strategy in this work realized the *in-situ* interconnection of the ZIF-8 derived reactor and MWCNTs highways. The effect of particle size on the reaction kinetics provides suggestions for further structural design and high performance Li-Se batteries.

DECLARATIONS

Author's contribution

The author contributed solely to the article.

Availability of data and materials

Not applicable.

Financial support and sponsorship

None.

Conflicts of interest

The author declared that there are no conflicts of interest.

Ethical approval and consent to participate

Not applicable.

Consent for publication

Not applicable.

REFERENCES

1. Jin Y, Liu K, Lang J, et al. High-energy-density solid-electrolyte-based liquid Li-S and Li-Se batteries. *Joule* 2020;4:262-74. DOI
2. Sun J, Du Z, Liu Y, et al. State-of-the-art and future challenges in high energy lithium-selenium batteries. *Adv Mater* 2021;33:e2003845. DOI PubMed
3. Eftekhari A. The rise of lithium-selenium batteries. *Sustain Energy Fuels* 2017;1:14-29. DOI
4. Song JP, Wu L, Dong WD, et al. MOF-derived nitrogen-doped core-shell hierarchical porous carbon confining selenium for advanced lithium-selenium batteries. *Nanoscale* 2019;11:6970-81. DOI PubMed
5. Lei Y, Liang X, Yang L, et al. Li-Se batteries: insights to the confined structure of selenium in hierarchical porous carbon and discharge mechanism in the carbonate electrolyte. *Carbon* 2022;191:122-31. DOI
6. Li C, Wang Y, Li H, et al. Weaving 3D highly conductive hierarchically interconnected nanoporous web by threading MOF crystals onto multi walled carbon nanotubes for high performance Li-Se battery. *J Energy Chem* 2021;59:396-404. DOI
7. Wang X, Tan Y, Liu Z, et al. New insight into the confinement effect of microporous carbon in Li/Se battery chemistry: a cathode with enhanced conductivity. *Small* 2020;16:e2000266. DOI PubMed
8. Li H, Li C, Wang Y, et al. Selenium confined in ZIF-8 derived porous carbon@MWCNTs 3D networks: tailoring reaction kinetics for high performance lithium-selenium batteries. *Chem Synth* 2022;2:8. DOI

Tan *et al. Chem Synth* 2022;2:11
DOI: 10.20517/cs.2022.14

Chemical Synthesis

Research Highlight

Open Access

Check for updates

A breakthrough in 2-indolylmethanol-involved organocatalytic asymmetric reactions

Wei Tan, Feng Shi*

School of Chemistry and Materials Science, Jiangsu Normal University, Xuzhou 221116, Jiangsu, China.

***Correspondence to:** Prof. Feng Shi, School of Chemistry and Materials Science, Jiangsu Normal University, Shanghai Road No. 101, Tongshan District, Xuzhou 221116, Jiangsu, China. E-mail: fshi@jsnu.edu.cn

How to cite this article: Tan W, Shi F. A breakthrough in 2-indolylmethanol-involved organocatalytic asymmetric reactions. *Chem Synth* 2022;2:11. https://dx.doi.org/10.20517/cs.2022.14

Received: 7 Jun 2022 **Accepted:** 17 Jun 2022 **Published:** 22 Jun 2022

Academic Editors: Bao-Lian Su, Alain Krief **Copy Editor:** Peng-Juan Wen **Production Editor:** Peng-Juan Wen

Keywords: Asymmetric catalysis, 2-indolylmethanol, (4 + 3) cycloaddition, organocatalysis

The organocatalytic asymmetric construction of chiral indole-based scaffolds has become an important research field because the wide distribution of such scaffolds in natural products, pharmaceuticals, chiral organocatalysts, and ligands[1]. Among different approaches, 2-indolylmethanols have been recognized as a class of versatile platform molecules in organocatalytic asymmetric transformations for constructing chiral indole-based scaffolds[1-3]. As summarized in Figure 1A, under the catalysis of chiral Brønsted acid (B*-H)[4-5], 2-indolylmethanols readily undergo dehydration to generate carbocation intermediates **A**-**B** and vinyliminiums **C**, which can be illustrated as delocalized cations **D**. Due to the steric effect of the two R groups (particularly when R is an aryl group), nucleophiles (Nu) more readily attack carbocation **B** than carbocation **A**, thus resulting in the C3-umpolung reactivity of 2-indolylmethanols[1-2]. Namely, the C3-position of the indole ring is changed from nucleophilic to electrophilic. Nevertheless, in some cases, 2-indolylmethanols can also display C3-nucleophilicity to undergo catalytic asymmetric (4 + 3)[6] and (3 + 3)[7] cycloadditions. Based on these unique reactivities, a series of organocatalytic asymmetric C3-substitutions and (3 + n) cycloadditions of 2-indolylmethanols have been achieved in a high regio- and enantioselective manner, leading to the construction of a variety of chiral indole-based scaffolds.

Despite the rapid progress in this research field, there are still some challenges in 2-indolylmethanol-involved organocatalytic asymmetric reactions. As shown in Figure 1B, most of the above-mentioned

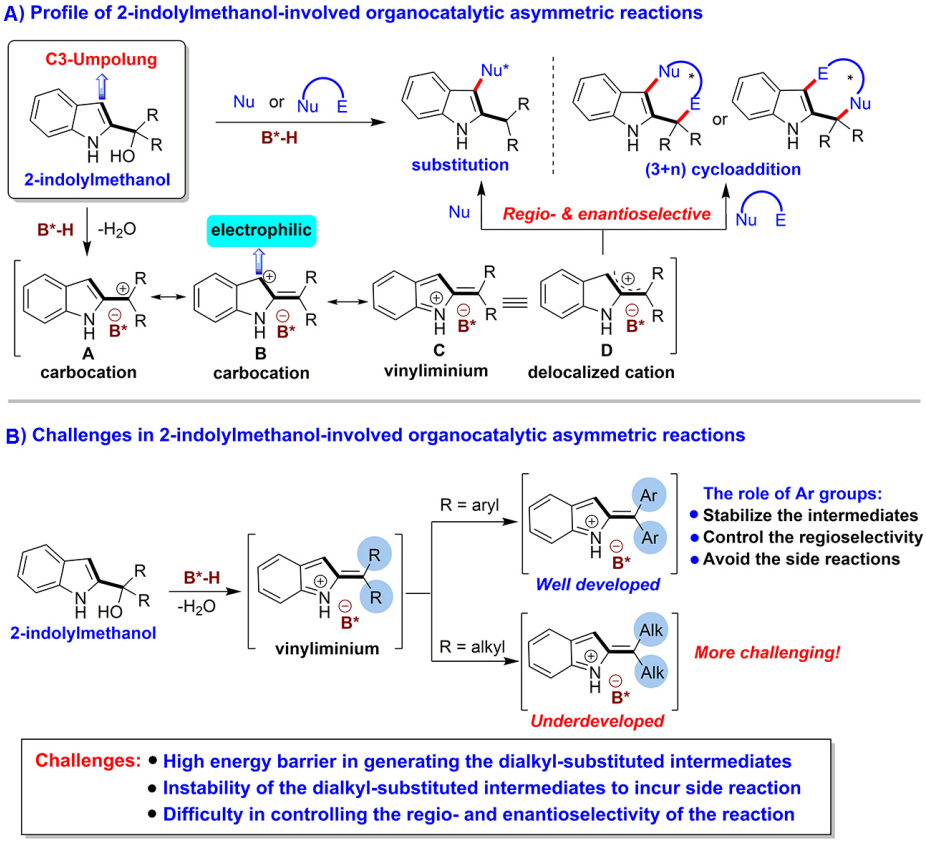

Figure 1. Profile of 2-indolylmethanol-involved organocatalytic asymmetric reactions and the existing challenges.

transformations utilize diaryl-substituted 2-indolylmethanols as reactants. However, in sharp contrast, dialkyl-substituted 2-indolylmethanols have scarcely been utilized as successful reactants in organocatalytic asymmetric reactions. This is because the two aryl groups play important roles in stabilizing the intermediates (vinyliminium and carbocation), controlling the regioselectivity, and avoiding the side reactions. On the contrary, there are great challenges in realizing highly regio- and enantioselective transformations of dialkyl-substituted 2-indolylmethanols, which mainly include: (1) high energy barrier in generating the dialkyl-substituted intermediates; (2) instability of the dialkyl-substituted intermediates to incur side reaction; and (3) difficulty in controlling the regio- and enantioselectivity of the reaction. Therefore, developing innovative strategies to solve these challenges is highly valuable.

To solve these challenging issues, on the basis of their previous studies on silylium-based asymmetric counteranion-directed catalysis (Si-ACDC)[8-9], List and coworkers recently designed an asymmetric (4 + 3) cycloaddition of dialkyl-substituted 2-indolylmethanols **1** with dienolsilane **2a** by using IDPi (imidodiphosphorimidates) as strongly acidic and confined organocatalysts [Figure 2][10]. Specifically, they utilized dialkyl-substituted 2-indolylmethanols **1** as three-atom building blocks to participate in the enantioselective (4 + 3) cycloaddition with dienolsilane **2a** under the catalysis of strongly acidic and confined IDPi **4a** or **4b**. After a subsequent TFA-promoted removal of silyl group, a series of novel bicyclo[3.2.2]cyclohepta[*b*]indoles **3** bearing three stereogenic centers were synthesized in overall excellent yields with high enantioselectivities. In addition, considering the accessibility of these intriguing bicyclo[3.2.2]cyclohepta[*b*]indole frameworks, they performed some useful synthetic transformations of products **3** and accomplished the synthesis of enantioenriched indole derivatives **5-8**.

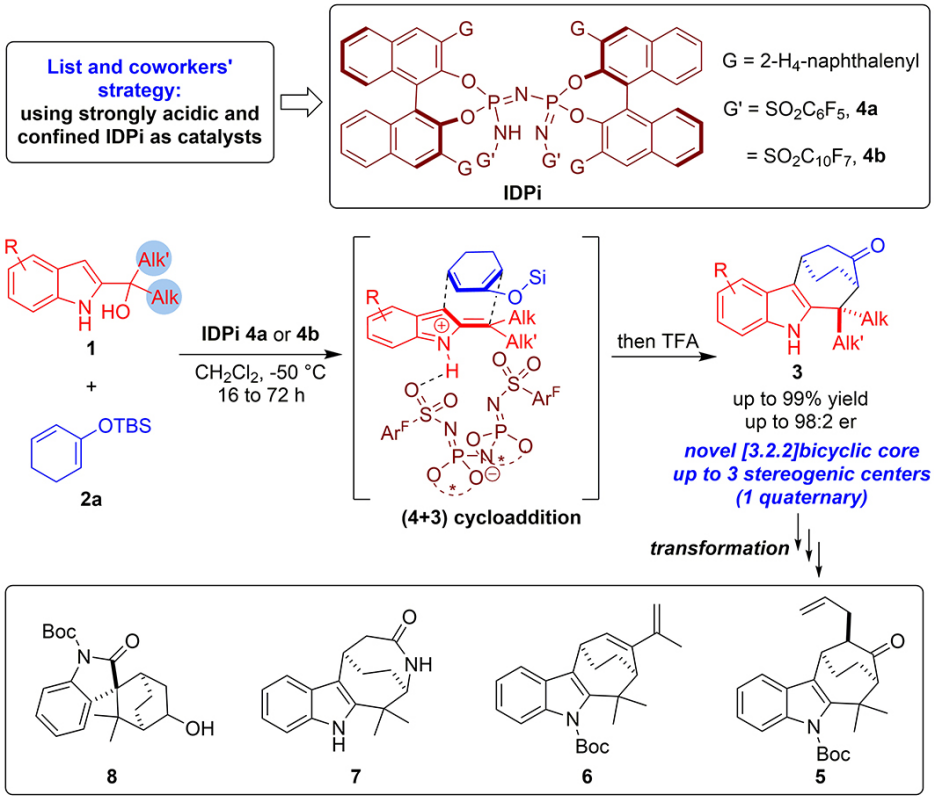

Figure 2. Organocatalytic asymmetric (4 + 3) cycloaddition of dialkyl-substituted 2-indolylmethanols with dienolsilane.

To gain some insights into the reaction mechanism, they performed a series of control experiments and theoretical calculations on this organocatalytic asymmetric (4 + 3) cycloaddition. Based on these investigations, they suggested a possible reaction pathway, which involved an overall concerted yet asynchronous cycloaddition process. As illustrated in Figure 3, initially, strongly acidic and confined IDPi reacted with dienolsilane **2a** via a silyl transfer process to generate the active silylium Lewis acid **I**, which could deliver silyl group to 2-indolylmethanol **1a** and form complex **II** via hydrogen-bonding interaction. Then, complex **II** underwent the C-O bond cleavage to produce intermediate **III** along with the release of TBSOH, which was the rate-limiting step with an energy barrier of 14.0 kcal/mol. Subsequently, intermediate **III** reacted with dienolsilane **2a** to undergo a concerted yet highly asynchronous (4 + 3) cycloaddition, which was the enantio-determining step with an energy barrier of 9.6 kcal/mol. The resulted adduct **IV** underwent a rearomatization process to give intermediate product **3aa'** with the regeneration of IDPi. Finally, the target product **3aa** was obtained by TFA-promoted removal of the silyl group in **3aa'**.

In short, List and coworkers established an organocatalytic asymmetric (4 + 3) cycloaddition of dialkyl-substituted 2-indolylmethanols with dienolsilane by using strongly acidic and confined imidodiphosphorimidates as competent organocatalysts, which afforded novel bicyclo[3.2.2]cyclohepta[*b*]-indoles in overall high yields with excellent enantioselectivities. This approach provides a powerful strategy to overcome the great challenges in realizing highly regio- and enantioselective transformations of dialkyl-substituted 2-indolylmethanols, which is a breakthrough in the field of 2-indolylmethanol-involved organocatalytic asymmetric reactions. This work has made indelible contributions to the chemistry of 2-indolylmethanols and demonstrated the power of asymmetric organocatalysis, which will further promote the development of the related fields.

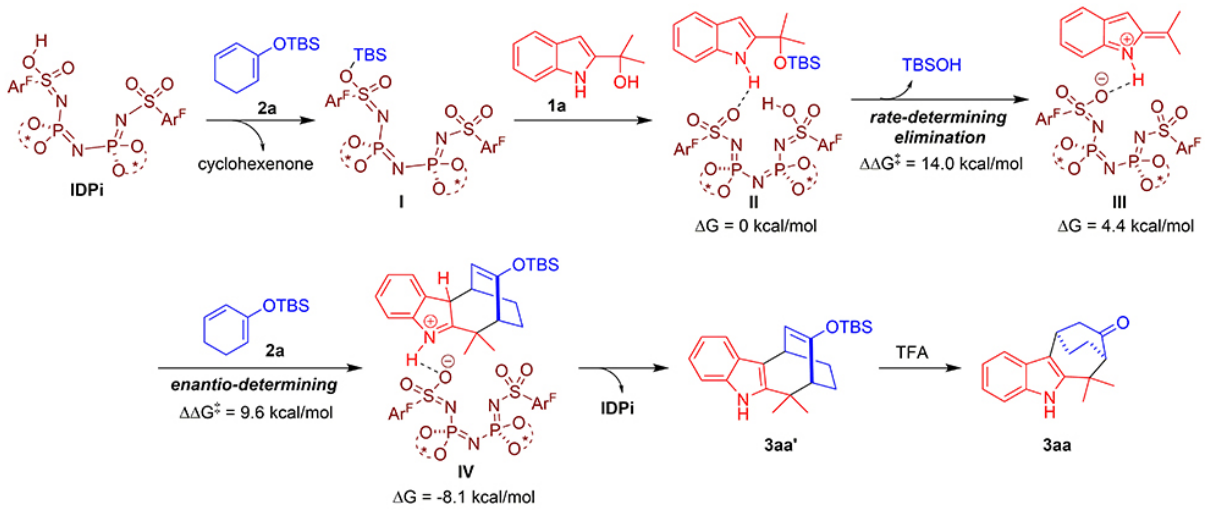

Figure 3. Suggested reaction pathway and activation mode.

DECLARATIONS

Acknowledgments

We sincerely thank all leading chemists and co-workers involved in the development of 2-indolylmethanol-related chemistry.

Authors' contributions

Wrote the draft manuscript: Tan W

Revised and rewrote some parts of the manuscript: Shi F

Availability of data and materials

Not applicable.

Financial support and sponsorship

We thank for NSFC (22125104 and 21831007), Natural Science Foundation of Jiangsu Province (BK20210916) and High Education Natural Science Foundation of Jiangsu Province (No. 21KJB150009) for financial supports.

Conflicts of interest

Both authors declared that there are no conflicts of interest.

Ethical approval and consent to participate

Not applicable.

Consent for publication

Not applicable.

REFERENCES

1. Zhang YC, Jiang F, Shi F. Organocatalytic asymmetric synthesis of indole-based chiral heterocycles: strategies, reactions, and outreach. *Acc Chem Res* 2020;53:425-46. DOI PubMed
2. Mei GJ, Shi F. Indolylmethanols as reactants in catalytic asymmetric reactions. *J Org Chem* 2017;82:7695-707. DOI PubMed
3. Bera K, Schneider C. Brønsted acid catalyzed [3 + 2]-cycloaddition of cyclic enamides with in situ generated 2-methide-2H-indoles: enantioselective synthesis of indolo[1, 2-a]indoles. *Org Lett* 2016;18:5660-3. DOI PubMed
4. Akiyama T. Stronger brønsted acids. *Chem Rev* 2007;107:5744-58. DOI PubMed
5. Lin X, Wang L, Han Z, Chen Z. Chiral spirocyclic phosphoric acids and their growing applications. *Chin J Chem* 2021;39:802-24. DOI
6. Sun M, Ma C, Zhou SJ, et al. Catalytic asymmetric (4 + 3) cyclizations of in situ generated *ortho*-quinone methides with 2-indolylmethanols. *Angew Chem Int Ed Engl* 2019;58:8703-8. DOI PubMed
7. Li TZ, Liu SJ, Sun YW, et al. Regio- and enantioselective (3 + 3) cycloaddition of nitrones with 2-indolylmethanols enabled by cooperative organocatalysis. *Angew Chem Int Ed Engl* 2021;60:2355-63. DOI PubMed
8. James T, van Gemmeren M, List B. Development and applications of disulfonimides in enantioselective organocatalysis. *Chem Rev* 2015;115:9388-409. DOI PubMed
9. Gatzenmeier T, van Gemmeren M, Xie Y, Höfler D, Leutzsch M, List B. Asymmetric Lewis acid organocatalysis of the Diels-Alder reaction by a silylated C-H acid. *Science* 2016;351:949-52. DOI PubMed
10. Ouyang J, Maji R, Leutzsch M, Mitschke B, List B. Design of an organocatalytic asymmetric (4 + 3) cycloaddition of 2-indolylalcohols with dienolsilanes. *J Am Chem Soc* 2022;144:8460-6. DOI PubMed PMC

Zeng *et al. Chem Synth* 2022;2:12
DOI: 10.20517/cs.2022.11

Chemical Synthesis

Short Communication

Open Access

Coordination-driven [2+2] metallo-macrocycles isomers: conformational control and photophysical properties

Yunting Zeng[1], Junjuan Shi[1], Kehuan Li[1], Jiaqi Li[1], Hao Yu[1], Fang Fang[2], Xin-Qi Hao[3], Houyu Zhang[1], Ming Wang[1,*]

[1]State Key Laboratory of Supramolecular Structure and Materials, College of Chemistry, Jilin University, Changchun 130012, Jilin, China.
[2]Instrumental Analysis Center, Shenzhen University, Shenzhen 518055, Guangdong, China.
[3]College of Chemistry and Green Catalysis Center, Zhengzhou University, Zhengzhou 450001, Henan, China.

Correspondence to: Prof. Ming Wang, State Key Laboratory of Supramolecular Structure and Materials, College of Chemistry, Jilin University, No. 2699 Qianjin Street, Changchun 130012, Jilin, China. E-mail: mingwang358@jlu.edu.cn

How to cite this article: Zeng Y, Shi J, Li K, Li J, Yu H, Fang F, Hao XQ, Zhang H, Wang M. Coordination-driven [2+2] metallo-macrocycles isomers: conformational control and photophysical properties. *Chem Synth* 2022;2:12. https://dx.doi.org/10.20517/cs.2022.11

Received: 12 May 2022 **First decision:** 8 Jun 2022 **Revised:** 14 Jun 2022 **Accepted:** 27 Jun 2022 **Published:** 30 Jun 2022

Academic Editors: Bao-Lian Su, Teng Ben **Copy Editor:** Jia-Xin Zhang **Production Editor:** Jia-Xin Zhang

Abstract

In recent years, fluorescent supramolecular materials have received significant attention due to their wide application prospects. However, the relationship between the conformation of supramolecules and their photophysical properties remains an open question. In this study, two rhomboidal metallacycle isomers, **SA** and **SB,** self-assembled with trans- and cis-isomers of tetraphenylethylene-based ditopic pyridyl ligands (**LA** and **LB**), and a 120° di-platinum (II) acceptor were prepared. Compared with metallacycle **SB** constructed by cis-tetraphenylethylene (TPE)-based ligand **LB**, the curved rhomboidal metallacycle **SA** constructed with trans-TPE-based ligand **LA** can restrict molecular motions of the aromatic groups on TPE and exhibits better light-emitting properties. Moreover, curved **SA** also exhibited better fluorescence stability than isomer **SB** towards molecules with strongly electron-withdrawing groups. This work provides a new platform to explore the relationship between conformation and the corresponding photophysical properties.

Keywords: Supramolecular self-assembly, metallacycles, isomer, conformational control, coordination-induced emission

INTRODUCTION

In the past decades, fluorescence materials have attracted considerable attention for their widespread applications in biological imaging[1], environmental sensing[2], fluorescent probes[3], and other fields[4] due to their high luminous efficiency and stimulus responsiveness. However, conventional organic fluorophores often suffer from aggregation-caused quenching (ACQ) in a concentrated solution or the solid state, which limits their practical application[5]. To overcome the undesirable ACQ, in 2001, Tang and co-workers developed fluorescent species exhibiting the opposite effect, known as aggregation-induced emission (AIE)[6]: tetraphenylethylene (TPE), 1,1,2,3,4,5-hexaphenylsilole, triphenylamine, distyrylanthracene, etc[7]. The characteristic of molecules with AIE activity is that their initial free rotation is restricted in an aggregation state, resulting in reduced non-radiative decay and strong fluorescence emission. However, AIE active molecules have relatively low luminous efficiency in dilute solution because the free rotation of benzene rings leads to high non-radiative decay.

Among the diverse field of supramolecular chemistry, coordination-driven self-assembly offers a straightforward synthetic approach for constructing diverse metal-organic complexes (MOCs)[8], ranging from two-dimensional (2D) metallacycles to three-dimensional (3D) metallacages. The metal coordination bonds not only provide definite directionality and high predictability but also have moderate bond energies (15-25 kcal/mol) to ensure self-modulation and thermodynamic stability during self-assembly. These unique advantages allow MOCs to be well constructed with specific stoichiometry and precise geometry and, thus, provide the impetus for applications in catalysis, sensing, and optics[9]. Recently, MOCs combined with AIEgens have also drawn particular attention as multifunctional platforms for exploring AIE properties. However, how to provide the bright emission of AIEgens in dilute solution is still a big challenge. Rational synthesis strategies should be developed to restrict the rotation of phenyl rings by slightly adjusting the conformation of the AIE group via metal coordination. In this way, the non-radiative decay in the excited state can be further reduced, thus giving a bright emission in dilute solution, which is also known as coordination-induced emission (CIE).

Herein, we provide such a CIE strategy via constructing two rhomboidal metallacycle isomers **SA** and **SB** by the self-assembly of trans- and cis-isomers of TPE-based ditopic pyridyl ligands (**LA** and **LB**) with a di-platinum (II) acceptor. It is worth mentioning that these two ligands can be easily obtained through one-pot synthesis and separation by column chromatography. In contrast to **SB** constructed by cis-TPE-based ligand **LB**, the curved rhomboidal metallacycle **SA** based on trans-TPE-based ligand **LA** could restrict molecular motions of the TPE aromatic groups, inducing the integration of AIE and CIE and thus showing double the quantum yield as **SB**. Moreover, curved **SA** also exhibited better fluorescence stability than isomer **SB** towards strongly electron-withdrawing molecules.

RESULTS AND DISCUSSION

The synthesis and characterization of the 120° di-Pt(II) acceptor **1** and the two ditopic ligands **LA** and **LB** are shown in the supplementary materials [Supplementary Figures 1-11]. The two isomeric ligands **LA** and **LB** can be obtained in a 1:1 product ratio by one-pot Suzuki coupling reactions and column chromatography (SiO_2). As shown in Scheme 1, the obtained 180° trans-TPE-based ligand **LA** and 60° cis-TPE-based ligand **LB** were assembled with the same 120° di-Pt(II) acceptor **1** in a 1:1 stoichiometric ratio in DMSO at 80 °C, affording the metallacycles **SA** and **SB**, respectively. After 10 h, the final discrete metallacycles were obtained in quantitative yields (94% for **SA** and 92% for **SB**) by sedimentation and centrifugation.

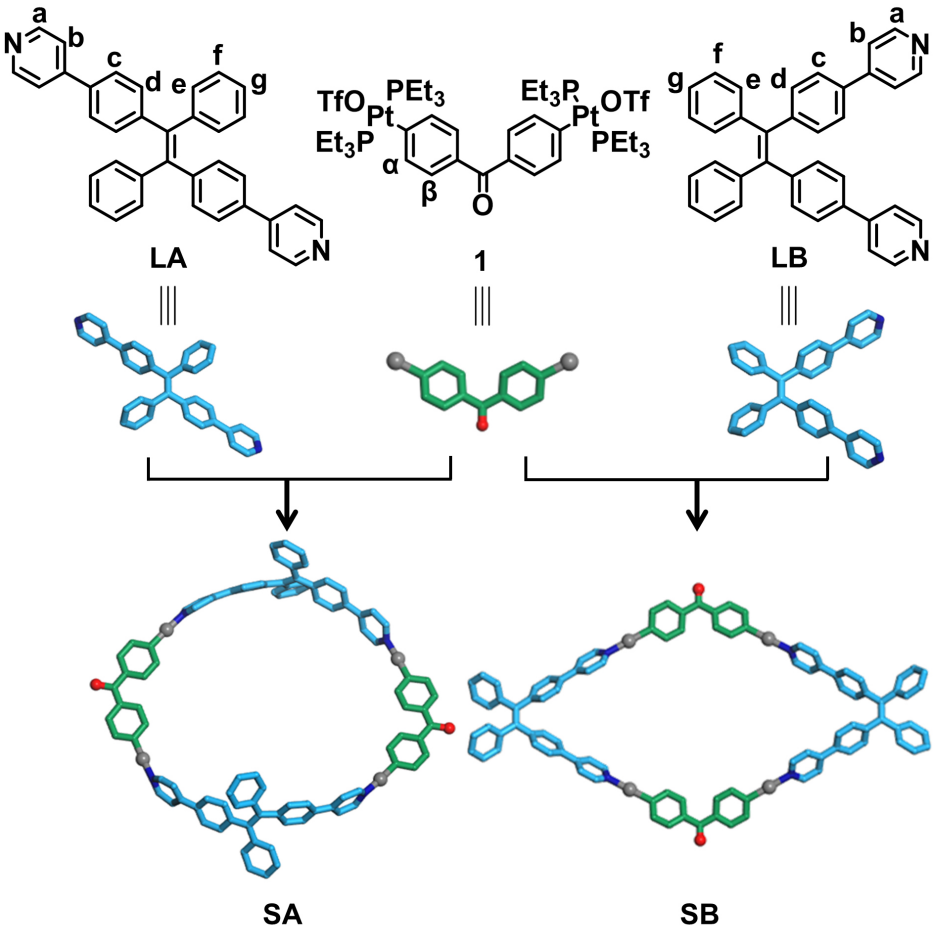

Scheme 1. Self-assembly of metallacycles **SA** and **SB** (energy-minimized structures). Carbon atoms of ligands **LA** and **LB** are blue, carbon atoms of acceptor **1** are green, nitrogen atoms are dark blue, oxygen atoms are red, phosphorus atoms are pink, and platinum atoms are grey.

The formation of discrete metallacycles **SA** and **SB** with highly symmetric architecture was first investigated by multinuclear NMR analysis [^{1}H, ^{31}P{^{1}H}, ^{13}C, 2D correlation spectroscopy, and 2D diffusion-ordered NMR spectroscopy (DOSY)] [Figure 1A-H and Supplementary Figures 12-23]. It is evident from the ^{1}H NMR spectra [Figure 1A-E] that no linear structures were formed. If a linear structure were formed, the proton signal of the ligands in these complexes would show more peaks due to the asymmetric chemical environment. In the ^{1}H NMR spectra [Figure 1A-E], the signals of protons corresponding to the pyridyl units and phenyl rings in metallacycles **SA** and **SB** exhibited downfield shifts relative to those of the free TPE ligands due to the loss of electron density after the formation of Pt-N coordination bonds. For metallacycle **SB**, the signals of the pyridyl and phenyl protons split into two sets upon metal coordination, being consistent with the previously reported MOC structures[10]. 2D diffusion-ordered spectroscopy (DOSY) in DMSO-d_6 showed a single band at log D = -10.19 for **SA** and -10.26 for **SB** [Supplementary Figures 17 and 23] further proving the formation of a single discrete structure. The diameters of **SA** and **SB** derived from the log D values by the Stokes-Einstein equation were 3.04 and 3.58 nm in DMSO, respectively, which matched well with the size of the expected structure. The ^{31}P{^{1}H} NMR spectrum of di-Pt(II) acceptor **1** and metallacycle **SA** both exhibited a single peak with concomitant ^{195}Pt satellites (δ = 18.99 ppm for **1** and δ = 13.16 ppm for **SA**) [Figure 1F and G]. However, the ^{31}P{^{1}H} NMR spectrum of metallacycle **SB** exhibited doublets (ca. 13.14 and 13.19 ppm) with concomitant ^{195}Pt satellites,

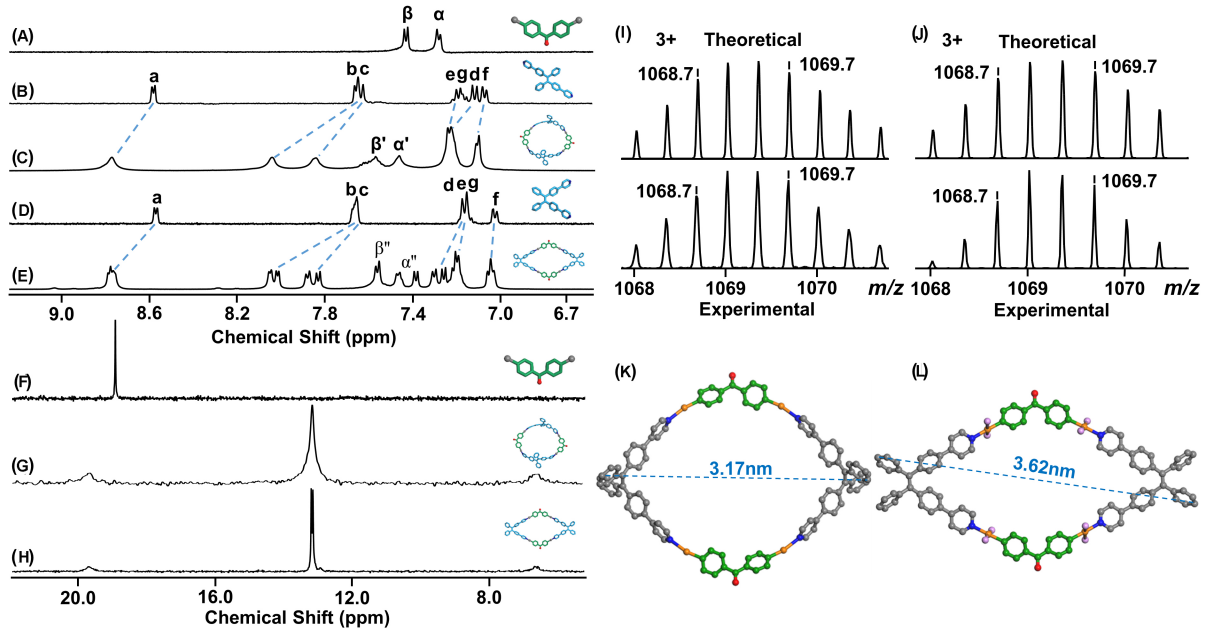

Figure 1. ^{1}H NMR spectra (500 MHz, 300 K) in DMSO-*d6* of: **1** (A); **LA** (B); **SA** (C), **LB** (D); and **SB** (E). ^{31}P{^{1}H} NMR spectra (500 MHz, 300 K) in DMSO-*d6* of: **1** (F); **SA** (G); and **SB** (H). ESI-MS spectra of **SA** (I) and **SB** (J). DFT-optimized ground-state structure of **SA** (K) and single-crystal X-ray structure of **SB** (L). Carbon atoms of ligands **LA** and **LB** are gray, carbon atoms of acceptor **1** are green, nitrogen atoms are dark blue, oxygen atoms are red, phosphorus atoms are pink, and platinum atoms are orange. Hydrogens and counterions OTf^- (trifluoromethanesulfonate) anions are omitted for clarity.

which could be attributed to the different chemical environments of phosphorus inside and outside the metallacycle [Figure 1H][11]. Compared with di-Pt(II) acceptor **1**, these peaks were shifted upfield by approximately 5.83 and 5.82 ppm for **SA** and **SB**, respectively. Furthermore, electrospray ionization mass spectrometry (ESI-MS) proved effective in determining the molecular formation of the obtained assemblies. One set of peaks with different charge states in the **SA** and **SB** systems was observed from the full ESI-MS spectra, due to the loss of different numbers of OTf^- counterions [Supplementary Figures 24 and 25]. In the ESI-MS spectrum of **SA** [Figure 1I and Supplementary Figure 26], a peak at m/z = 1068.7 Da corresponding to $[M\text{-}3OTf]^{3+}$ was observed. After the deconvolution of m/z, the molecular weight of **SA** was calculated to be 3652.94 Da, demonstrating the formation of a [2+2] assembly. Metallacycle **SB** showed the same fragments as obtained for **SA** (m/z = 1068.7 for $[M\text{-}3OTf]^{3+}$, m/z = 1677.5 for $[M\text{-}2OTf]^{2+}$ [Figure 1J and Supplementary Figure 27] and had the same molecular weight (for the relevant calculation method, see Section 4 of the Supplementary Materials). These peaks were isotopically resolved and in good agreement with their calculated theoretical distributions, indicating the formation of distinct metallacycle structures **SA** and **SB**. We failed to obtain single crystals of **SA** suitable for X-ray scattering due to its curved configuration that restricted the easy stacking of the metallacycle molecules. Instead, density functional theory (DFT) calculations were performed to simulate the supramolecular structures of **SA** [Figure 1K]. Fortunately, single crystals of **SB** were successfully obtained by slowly diffusing isopropyl ether into the acetone solution of **SB** over four weeks; the corresponding single-crystal structure is shown in Figure 1L. The detailed crystal information is shown in Supplementary Figures 28 and 29 and Supplementary Table 1. From the optimized structure of **SA** and the crystal structure of **SB**, it is evident that both were rhomboidal metallacycles, and **SA** exhibited a certain degree of bending. This unique structural feature laid a solid foundation for subsequent studies on the different luminous behaviors of the metallacycles.

After the successful construction of metallacycles **SA** and **SB**, their photophysical properties were studied. The absorption spectra of ligands and metallacycles are shown in Figure 2A. Ligands **LA** and **LB** displayed two similar broad absorption bands at 270 and 330 nm, originating mainly from pyridine and TPE. Due to the metal to ligand charge transfer (MLCT) after coordination and forming **SA** and **SB**, the two absorption bands were, respectively, red-shifted to 315 and 355 nm in SA and 315 and 365 nm in SB. Moreover, these assemblies exhibited significantly enhanced molar absorption coefficients because of the inclusion of two ligands in one metallacycle structure. Next, fluorescence spectra of ligands and metallacycles were also recorded [Figure 2B]. Ligands **LA** and **LB** showed weak emission at 485 nm in DMSO, which can be ascribed to the non-radiative relaxation pathway via intramolecular rotations of the phenyl and pyridyl rings. After assembling ligands into rhomboidal metallacycles, the emission intensity was enhanced and red-shifted by ~20 nm (505 nm). Compared to the normal rhombus metallacycle **SB**, the molecular motions of the aromatic groups on TPE are more restricted by coordination bonds in the curved metallacycle **SA**, decreasing the non-radiative decay and thus giving a brighter emission. Consequently, the obtained Φ_F value of **SA** in DMSO was 6.47%, significantly higher than the Φ_F of **SB** in DMSO (3.21%). The absorption and emission spectra of metallacycles **SA** and **SB** in the solid state were further explored [Supplementary Figure 30A]. Two similar broad absorption bands at 320 and 430 nm were observed from solid **SA** and **SB**. Solid **SA** also exhibited a long-wavelength absorption band centered at 525 nm, mainly corresponding to intramolecular charge transfer. Interestingly, a different fluorescence emission behavior was observed for metallacycles **SA** and **SB** in the solid state. Again, the intensity of the maximum emission peak of **SB** was significantly lower than that of **SA** and was 30 nm red-shifted compared with **SA.** Notably, the Φ_F values of metallacycles **SA** and **SB** in solid state were 26.17% and 23.14%, respectively, which were substantially higher than those obtained in the solution and displayed a typical AIE effect [Supplementary Figure 30B].

To investigate the AIE properties of metallacycles **SA** and **SB**, their fluorescence emission spectra in DMSO and DMSO/H_2O mixture solutions were recorded [Figure 2]. Adding water to the DMSO solution reduced the solubility of **SA** and **SB**, thereby promoting aggregate formation. Upon successive increments in the water content, the fluorescence intensities of **SA** chronologically increased and reached a maximum at 90% H_2O content [Figure 2C]. Its fluorescence quantum yield continued to increase with the rising water content and matched well with the change in fluorescence emission intensity [Figure 2D]. As anticipated, the fluorescence results demonstrate the AIE behavior of **SA**. Metallacycle **SB** displayed a similar AIE phenomenon [Figure 2E and F]. Interestingly, in the aggregated states (H_2O content = 90%), the fluorescence intensity of **SA** increased up to 27 times (Φ_F = 60.28%), whereas **SB** displayed only a 14-fold fluorescence enhancement (Φ_F = 26.08%). The more curved structure of metallacycle **SA** may promote the tight packing of TPE units in the aggregated state, enhancing its fluorescence remarkably. Moreover, the restricted movement of phenyl rings of TPE in **SA** further enriched its fluorescent performance compared to **SB**.

AIE-active molecules often show the phenomenon of fluorescence quenching due to the charge transfer between AIE moieties and molecules with strongly electron-withdrawing groups. Thus, we expected that the twisted and high luminous efficient structure of **SA** could effectively reduce the charge transfer process and quenching phenomenon. Inspired by the excellent AIE luminescence properties observed for rhombus metallacycles **SA** and **SB** in this study, we investigated the fluorescence stability of these two isomers in the DMSO/H_2O mixture with 90% H_2O content towards 2,4,6-trinitrotoluene (TNT). The quenching processes could be monitored by the change in emission intensity in response to TNT addition [Figure 3A and B]. Upon adding TNT, the emission of the aggregates was gradually quenched. The fluorescence quenching could be clearly observed even at a TNT concentration as low as 0.1 μg/mL, consistent with the previous

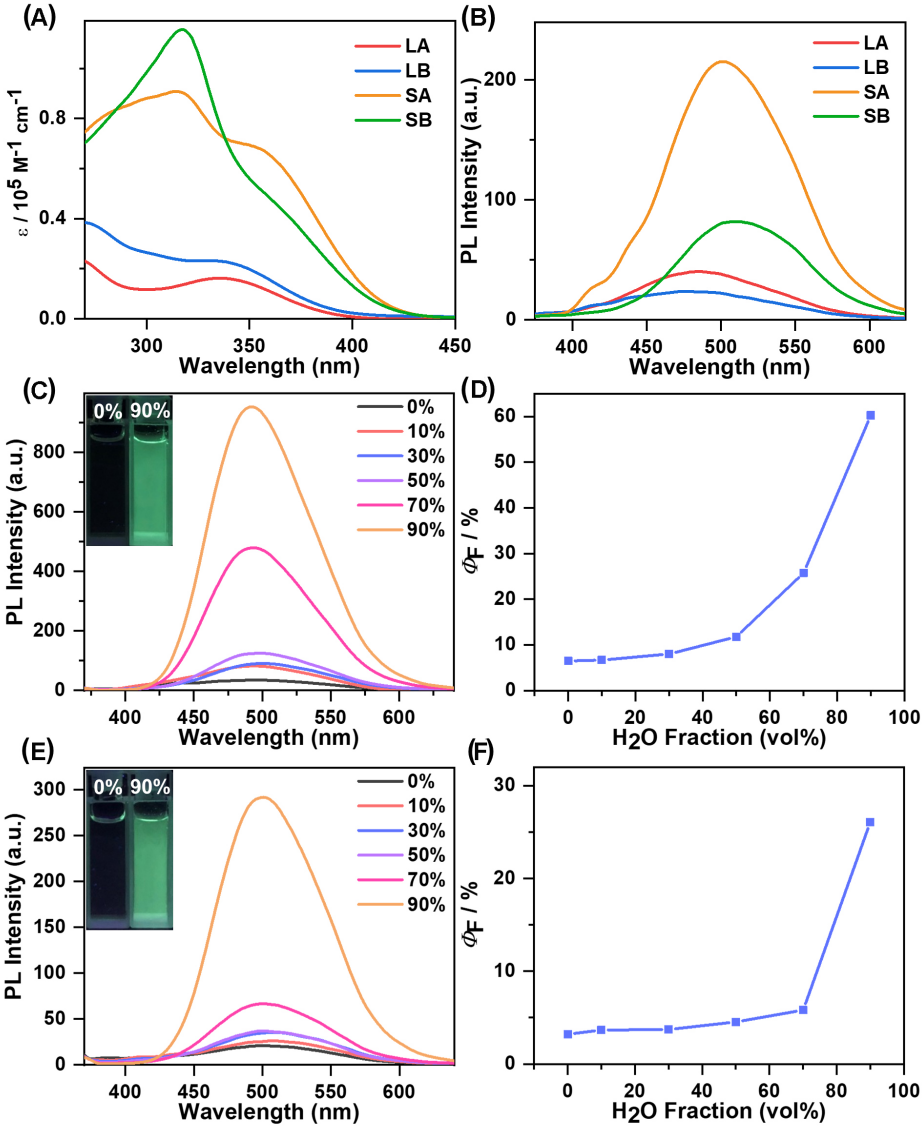

Figure 2. (A) UV-Vis spectra of **LA**, **LB**, **SA**, and **SB** in DMSO (λ_{ex} = 320 nm, c = 10.0 μM). (B) PL spectra of **LA**, **LB**, **SA**, and **SB** in DMSO (λ_{ex} = 320 nm, c = 10.0 μM). PL spectra of **SA** (C) and **SB** (D) recorded in DMSO/H_2O mixtures containing different H_2O fractions. The respective inserts show **SA** and **SB** dissolved in DMSO/H_2O with 0% (left) and 90% H_2O (right). Quantum yields of **SA** (E) and **SB** (F) versus increasing H_2O fractions in DMSO/H_2O mixtures, determined using rhodamine B (Φ_F = 69.0%) at 365 nm (λ_{ex} = 320 nm, c = 1.00 μM).

report[12]. Impressively, although metallacycles **SA** and **SB** had the same components, their quenching efficiency and quenching rate by TNT were completely different. For metallacycle **SB**, quenching efficiency was 21.41% when 0.1 μg/mL of TNT was added to its solution, while it was only 8.86% for **SA** under the same condition. For 10.0 μg/mL TNT concentration, the initial fluorescence intensity of **SB** reduced by 96.76%, but only 76.79% for **SA**. The fluorescence quenching of **SA** could reach 97.68% only when the TNT concentration was increased to 100 μg/mL [Figure 3C]. To determine the quenching constants of metallacycles **SA** and **SB** with TNT, the respective relative fluorescence intensity (I_0/I) was plotted against the TNT concentration. Upon applying a linear Stern-Volmer equation $I_0/I = K[TNT] + 1$[2], from the mean of linear fitting, the quenching constants of **SB** were calculated to be 7.289×10^5 M^{-1}. However, the best fit

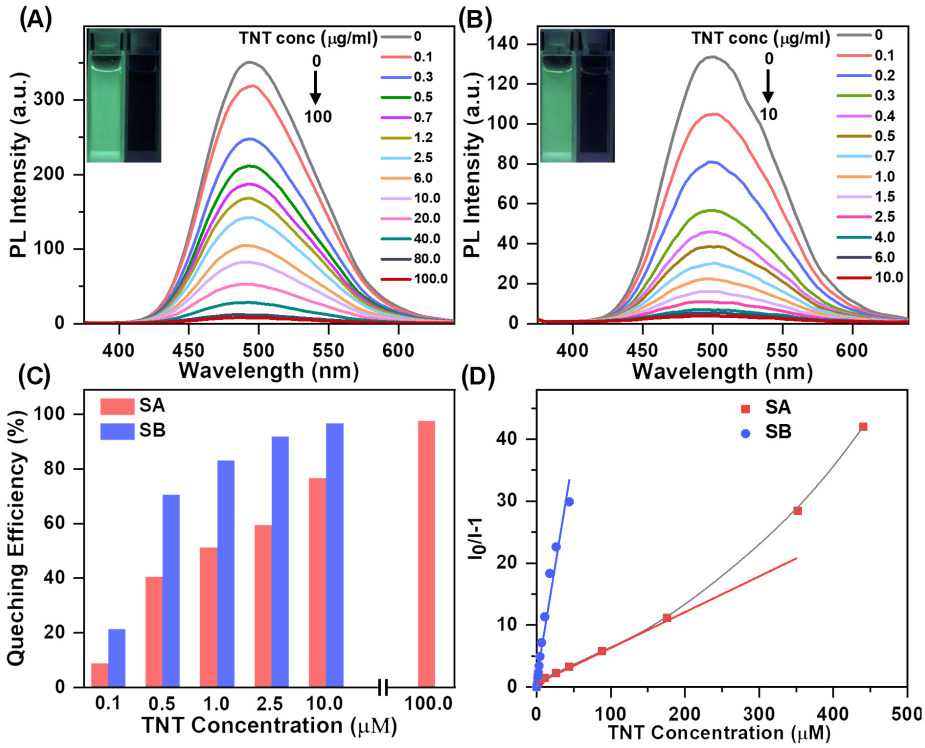

Figure 3. Fluorescence emission spectra of metallacycles **SA** (A) and **SB** (B) in a DMSO/H_2O (1/9) mixture containing different amounts of TNT (λ_{ex} = 320 nm, c = 1.00 μM). (C) The fluorescence quenching efficiencies of metallacycles **SA** and **SB** at different TNT concentrations in a DMSO/H_2O (1:9) mixture. (D) Plot of relative fluorescence intensities (I_0/I, I = peak intensity and I_0 = peak intensity at [TNT] = 0 μM) versus TNT concentrations in a DMSO/H_2O (1:9) mixture (λ_{ex} = 320 nm, c = 1.00 μM).

was obtained with the linear fitting for metallacycle **SA** when the TNT concentration was lower than 176 μg/mL, and the quenching constant was calculated to be 5.774×10^4 M^{-1}. With the further increase of TNT concentration, the quenching process of **SA** showed a curvy enhancement [Figure 3D]. The structural differences of metallacycles **SA** and **SB** led to the large difference in their quenching constants. The key mechanism in binding TNT with chromophoric receptors was generally considered to be through the π-π stacking interactions. Since **SA** is a rhombic metallacycle with a curved structure, its π-π stacking interactions with TNT was hindered, which further affected the fluorescence quenching effect.

CONCLUSION

Two TPE-based metallacycles (named **SA** and **SB**) were constructed using cis-trans isomers of a TPE-based dipyridyl ligand and 120° di-Pt(II) acceptor. The rhombus metallacycle **SA** constructed with the trans-TPE-based dipyridyl ligand had a more curved structure than the rhombus metallacycle **SB** constructed with the cis-TPE-based dipyridyl ligand. The curved **SA** structure restricted the molecular motions of the aryl groups on TPE, resulting in the CIE phenomenon and remarkable light-emitting properties. In addition, **SA** with twisted configuration and high quantum yield showed better fluorescence stability than **SB** in the presence of TNT. This work provides a new platform to explore the relationship between the conformation of the AIE group and the corresponding photophysical properties.

DECLARATIONS

Acknowledgments

This study was supported by the National Natural Science Foundation of China (22071079 for Wang M). The authors thank the staff from the BL17B beamline of the National Facility for Protein Science in Shanghai (NFPS) at Shanghai Synchrotron Radiation Facility for assistance during data collection.

Authors' contributions

Completed the synthesis, conducted NMR characterization, optical tests, and prepared the draft manuscript: Zeng Y
Performed MS characterization: Li K, Fang F
Performed DFT calculations: Li J, Zhang H
Performed part of the X-ray crystal structure data collection: Yu H
Designed the experiments and wrote the manuscript: Shi J, Hao XQ, Wang M

Availability of data and materials

Not applicable.

Financial support and sponsorship

This study was supported by the National Natural Science Foundation of China (22071079 for Wang M).

Conflicts of interest

All authors declared that there are no conflicts of interest.

Ethical approval and consent to participate

Not applicable.

Consent for publication

Not applicable.

REFERENCES

1. Leung CW, Hong Y, Chen S, Zhao E, Lam JW, Tang BZ. A photostable AIE luminogen for specific mitochondrial imaging and tracking. *J Am Chem Soc* 2013;135:62-5. DOI PubMed
2. Liu J, Zhong Y, Lu P, et al. A superamplification effect in the detection of explosives by a fluorescent hyperbranched poly(silylenephenylene) with aggregation-enhanced emission characteristics. *Polym Chem* 2010;1:426-9. DOI
3. Yang SK, Shi X, Park S, Ha T, Zimmerman SC. A dendritic single-molecule fluorescent probe that is monovalent, photostable and minimally blinking. *Nat Chem* 2013;5:692-7. DOI PubMed PMC
4. Zhang Z, Guo K, Li Y, et al. A colour-tunable, weavable fibre-shaped polymer light-emitting electrochemical cell. *Nature Photon* 2015;9:233-8. DOI
5. Hoeben FJ, Jonkheijm P, Meijer EW, Schenning AP. About supramolecular assemblies of pi-conjugated systems. *Chem Rev* 2005;105:1491-546. DOI PubMed
6. Luo J, Xie Z, Lam JW, et al. Aggregation-induced emission of 1-methyl-1,2,3,4,5-pentaphenylsilole. *Chem Commun (Camb)* 2001:1740-1. DOI PubMed
7. Mei J, Leung NL, Kwok RT, Lam JW, Tang BZ. Aggregation-induced emission: together we shine, united we soar! *Chem Rev* 2015;115:11718-940. DOI PubMed
8. Qin Y, Wang Y, Yang H, Zhu W. Recent advances on the construction of diarylethene-based supramolecular metallacycles and metallacages via coordination-driven self-assembly. *CS* 2021. DOI
9. Newkome GR, Moorefield CN. From 1 → 3 dendritic designs to fractal supramacromolecular constructs: understanding the pathway to the Sierpiński gasket. *Chem Soc Rev* 2015;44:3954-67. DOI PubMed
10. Yan X, Wang H, Hauke CE, et al. A suite of tetraphenylethylene-based discrete organoplatinum(ii) metallacycles: controllable

structure and stoichiometry, aggregation-induced emission, and nitroaromatics sensing. *J Am Chem Soc* 2015;137:15276-86. DOI PubMed

11. Guo Z, Li G, Wang H, et al. Drum-like metallacages with size-dependent fluorescence: exploring the photophysics of tetraphenylethylene under locked conformations. *J Am Chem Soc* 2021;143:9215-21. DOI PubMed
12. Qin A, Lam JWY, Tang L, et al. Polytriazoles with aggregation-induced emission characteristics: synthesis by click polymerization and application as explosive chemosensors. *Macromolecules* 2009;42:1421-4. DOI

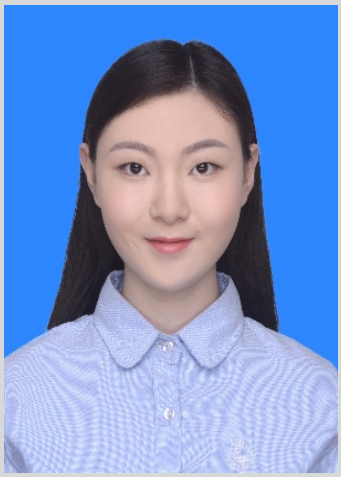

Yunting Zeng

Yunting Zeng obtained her BS from Jilin University, China in 2018. In the same year, she started her PhD study under the guidance of Professor Ming Wang from Jilin University (China). She focuses on the construction of 2D and 3D luminescent supramolecular architectures.

Junjuan Shi

Junjuan Shi received her BS in 2016 from Changchun University of Technology. After that, she obtained her PhD degree under the guidance of Professor Ming Wang at Jilin University (China) in 2021. She joined the group of Prof. Xiaopeng Li at the University of South Florida (US) as a joint training of doctoral student during 2018–2020. Currently, she is a Postdoctoral Researcher at Jilin University under the "Dingxin Scholar Program." Her research interests include the construction and function of 2D supramolecular architectures.

Kehuan Li

Kehuan Li received his BS from Jilin University, China in 2018. After that, he started PhD study under the guidance of Professor Ming Wang from Jilin University (China). He joined the group of Prof. Xiaopeng Li at the Shenzhen University (China) as a joint training of doctoral student during 2021–2022. His research interests include the self-assembly and self-sorting behavior based on dissymmetrical ligands.

Jiaqi Li

Jiaqi Li received her BS from Shanxi Datong University in 2017. Now she is a PhD student under the supervision of Professor Houyu Zhang in the College of Chemistry, Jilin University. Her research is focused on the molecular design of highly efficient organic light emitting materials using first-principles computational methods.

Hao Yu

Hao Yu received his BS in 2017 from Changchun University of Technology. In the same year, he started his PhD study under the guidance of Professor Ming Wang from Jilin University (China). He focuses on the construction and function of 3D supramolecular architectures, self-assembly based on dissymmetrical ligands.

Fang Fang

Fang Fang received her PhD in chemistry from the Cleveland State University and Cleveland Clinic Foundation (USA) in 2012 under the supervision of Prof. Qing Wang. She obtained a PharmD in Pharmacy from University of South Florida (USA) in 2018. She now works as a senior technician at Instrumental Analysis Center of Shenzhen University. Her research interests focus on characterization of synthetic macromolecules and nanomaterials.

Xin-Qi Hao

Xin-Qi Hao received his BSc and PhD degrees in 2002 and 2007, respectively, supervised by Prof. Mao-Ping Song from the College of Chemistry, Zhengzhou University. In 2012, he joined Professor Michael J. Krische's group in University of Texas at Austin (USA) as a Postdoctoral Researcher. In 2007, he joined the college of Chemistry, Zhengzhou University and became a full professor in 2016. His research interests focus on organometallic chemistry, organic synthetic chemistry, and supramolecular chemistry.

Houyu Zhang

Houyu Zhang earned his PhD degree in the department of chemistry at Hong Kong University of Science and Technology in 2002. During 2002-2005, he was a postdoctoral researcher in the department of physics, University of Modena and Reggio Emilia, Italy. After that, he became an associate professor at the Jilin University in 2005. Now he is a professor in the college of chemistry, Jilin University. His research is directed at understanding of supramolecular aggregates and organic photoelectronic materials with the emphasis on structure-property relationships, charge transport properties, and excited state dynamics.

Ming Wang

Ming Wang received his PhD from the Changchun Institute of Applied Chemistry, Chinese Academy of Sciences in 2010. Then he joined Professor Pooi See Lee's group in Nanyang Technological University (Singapore) as a Postdoctoral Researcher. In 2013, he continued as a postdoctoral researcher in Xiaopeng Li's group in Texas State University (USA). He is now a professor in the College of Chemistry of Jilin University. His research interests focus on the construction of metallo-supramolecular architectures, self-assembly based on dissymmetrical ligands, and function development of discrete supramolecular structures.

El Khawaja *et al. Chem Synth* 2022;2:13
DOI: 10.20517/cs.2022.10

Chemical Synthesis

Review

Open Access

Boosting VOCs elimination by coupling different techniques

Rebecca El Khawaja[1], Savita Kaliya Perumal Veerapandian[6], Rim Bitar[6], Nathalie De Geyter[6], Rino Morent[6], Nicolas Heymans[4], Guy De Weireld[4], Tarek Barakat[3], Yang Ding[3], Grêce Abdallah[2,6], Shilpa Sonar[2,6], Axel Löfberg[2], Jean-Marc Giraudon[2], Christophe Poupin[1], Renaud Cousin[1], Fabrice Cazier[5], Dorothée Dewaele[5], Paul Genevray[5], Yann Landkocz[1], Clémence Méausoone[1], Nour Jaber[1], Dominique Courcot[1], Sylvain Billet[1], Jean-François Lamonier[2,*], Bao-Lian Su[3,*], Stéphane Siffert[1,*]

[1]Univ. Littoral Côte d'Opale, U.R. 4492, Unit of Environmental Chemistry and Interactions with Living Organisms (UCEIV), SFR Condorcet FR CNRS 3417, Dunkerque F-59140, France.
[2]Univ. Lille, CNRS, Centrale Lille, Univ. Artois, UMR 8181, Unité de Catalyse et Chimie du Solide (UCCS), Lille F-59000, France.
[3]Univ. Namur, Namur Institute of Structured Matter (NISM), Laboratory of Inorganic Materials Chemistry, B-5000, Belgium.
[4]Univ. Mons, Thermodynamics and Mathematical Physics Unit, Mons B-7000, Belgium.
[5]Univ. Littoral Côte d'Opale, CCM, Centre Commun de Mesures, Dunkerque F-59140, France.
[6]Univ. Ghent, Research Unit Plasma Technology (RUPT), Department of Applied Physics, Ghent 9000, Belgium.

***Correspondence to:** Prof. Stéphane Siffert, Univ. Littoral Côte d'Opale, U.R. 4492, Unit of Environmental Chemistry and Interactions with Living Organisms (UCEIV), SFR Condorcet FR CNRS 3417, Dunkerque F-59140, France. E-mail: siffert@univ-littoral.fr; Prof. Jean-François Lamonier, Univ. Lille, CNRS, Centrale Lille, Univ. Artois, UMR 8181, Unité de Catalyse et Chimie du Solide (UCCS), Lille F-59000, France. E-mail: jean-francois.lamonier@univ-lille.fr; Prof. Bao-Lian Su, Univ. Namur, Namur Institute of Structured Matter (NISM), Laboratory of Inorganic Materials Chemistry, B-5000, Belgium. E-mail: bao-lian.su@unamur.be

How to cite this article: El Khawaja R, Veerapandian SKP, Bitar R, Geyter ND, Morent R, Heymans N, Weireld GD, Barakat T, Ding Y, Abdallah G, Sonar S, Löfberg A, Giraudon JM, Poupin C, Cousin R, Cazier F, Dewaele D, Genevray P, Landkocz Y, Mé ausoone C, Jaber N, Courcot D, Billet S, Lamonier JF, Su BL, Siffert S. Boosting VOCs elimination by coupling different techniques. *Chem Synth* 2022;2:13. https://dx.doi.org/10.20517/cs.2022.10

Received: 28 Apr 2022 **First Decision:** 25 May 2022 **Revised:** 13 Jun 2022 **Accepted:** 24 Jun 2022 **Published:** 30 Jun 2022

Academic Editor: Ying Wan **Copy Editor:** Peng-Juan Wen **Production Editor:** Peng-Juan Wen

Abstract

Volatile Organic Compounds (VOCs) are known to be hazardous and harmful to human health and the environment. In mixtures or during repeated exposures, significant toxicity of these compounds in trace amounts has been revealed. *In vitro* air-liquid interface approaches underlined the interest in evaluating the impact of repeated VOC exposure and the importance of carrying out a toxicological validation of the techniques in addition to the standard chemical analyses. The difficulties in sampling and measuring VOCs in stationary source emissions are due to both the complexity of the mixture present and the wide range of concentrations. The coupling of VOC

treatment techniques results in efficient systems with lower operating energy consumption. Three main couplings are outlined in this review, highlighting their advantages and relevance. First, adsorption-catalysis coupling is particularly valuable by using adsorption and catalytic oxidation regeneration initiated, for example, by selective dielectric heating. Then, several key aspects of the plasma catalysis process, such as the choice of catalysts suitable for the non-thermal plasma (NTP) environment, the simultaneous removal of different VOCs, and the in situ regeneration of the catalyst by NTP exposure, are discussed. The adsorption-photocatalysis coupling technology is also one of the effective and promising methods for VOC removal. The VOC molecules strongly adsorbed on the surface of the photocatalyst can be directly oxidized by the photogenerated hole on the photocatalyst (e.g., TiO_2).

Keywords: VOC removal, adsorption materials, coupling techniques, catalysis, plasma, photocatalysis

INTRODUCTION

According to World Health Organization (WHO), air pollution is responsible for one out of every nine premature deaths, or more than seven million deaths each year[1]. Residential, industrial, agricultural, and road transportation activities are the most important anthropogenic sources of air pollution. Many pollutants are now found in higher concentrations in indoor air than in outdoor air. This is especially concerning because humans spend over 80% of their time in enclosed spaces such as their homes, means of transportation, and workplaces. Volatile organic compounds (VOCs) are a type of gaseous air pollution. VOCs are harmful to human health and the environment, and they play a role in climate change. On an industrial level, the current policy for reducing VOC emissions prioritizes the total or partial substitution of VOCs used at the source. However, when this substitution is not possible due to technical constraints, it is required to develop alternative methods that are suitable for low VOC concentrations, have high energy efficiency, and allow for the entire treatment without the generation of by-products. To address this industrial issue, new innovative treatment methods adapted to the industry and based on the coupling of methods are required.

First, adsorption and catalytic technologies are often not very effective in removing low-level VOCs from off-gases when they are used separately. Indeed, after a period of use, an adsorbent becomes saturated and must be regenerated. The corresponding catalytic treatment results in high energy consumption at low VOC concentrations. An innovative approach combining both techniques can be proposed. The original process is based on the selective adsorption of the pollutant coupled with a catalytic oxidation process. The adsorption will remove the VOCs present in low concentrations in the air, and the final removal of the pollutant is done during the adsorbent regeneration step. Indeed, during this stage, the high concentration of VOCs in the effluent allows the catalytic oxidation process to be used under optimal conditions. Two tracks are considered: in the first one, the adsorption is done on an adsorbent and the oxidation during the desorption step is done on a catalyst (existing process). In the second, more innovative one, the same material is used successively as an adsorbent and then as a catalyst at higher temperatures.

Second, the use of non-thermal plasma (NTP) is attracting increased attention in the field of air purification, particularly for the removal of low concentration VOCs from industrial and/or indoor air. This treatment at room temperature and atmospheric pressure is very attractive because conventional technologies typically require a lot of energy to reach operating temperature. However, studies have shown that industrial implementation of this technology is hampered by three main drawbacks: (1) formation of unwanted by-products; (2) relatively poor energy efficiency; and (3) low degradation. To overcome these problems, the combination of heterogeneous catalysis with a non-thermal plasma can be proposed. By combining the advantages of the two processes, an efficient VOC removal process is expected.

Finally, photocatalysis is based on the principle of activation of a semiconductor using the energy provided by light. The adsorption of a photon forms an electron-hole pair that allows the formation of free radicals, which react with the VOCs to transform them into CO_2 and water. One of the main advantages of photocatalysis is being able to work at room temperature and thus be free of any thermal inertia. The photocatalytic reactor consists of a UV lamp surrounded by transparent substrates coated with a thin layer of the selected photocatalyst and allowing the passage and treatment of the gas flow. To optimize the operation of the reactor, it is preceded by adsorption, which traps and concentrates the VOCs. The VOCs are then periodically desorbed by heating and directed to the photocatalytic reactor, thus regenerating the adsorption column.

Some conditions need to be taken into consideration when working on a large industrial scale. The process needs to be studied from physical, legal, and economical points of view. The implemented process should be optimized while considering the feasibility of scaling it from the laboratory scale. In addition, the physicochemical properties of the materials should be deeply studied in harsh conditions. The regeneration of the materials is also thought through to keep a highly efficient and eco-friendly process. Despite being emitted at low concentrations, a mixture of VOCs is expected to be found in industrial emissions. Hence, the catalytic activity of the materials is important; more precisely, it needs to selectively convert the VOC into H_2O and CO_2, without leading to new problems such as the formation of by-products, adding to the maintenance cost.

In this review, we devote part of this paper to the toxicology of these VOCs, followed by a section on their measurement, which is often difficult, especially when they are in complex mixtures (industrial emissions). We also discuss how these VOCs are really measured on industrial sites. The treatment techniques are presented next, using the combinations of adsorption-catalysis, plasma catalysis, and adsorption-photocatalysis.

TOXICITY AND MEASUREMENTS OF VOCs

Volatile organic compounds

Before starting, it is important to know that the physico-chemical characteristics that define VOCs depend on the organisms, and there are several definitions of this family of chemicals. However, most definitions agree on the presence of the molecule in vapor form under standard conditions of temperature and pressure.

According to the United States Environmental Protection Agency (US-EPA), volatile organic compounds are any compound of carbon, excluding carbon monoxide, carbon dioxide, carbonic acid, metallic carbides, or carbonates and ammonium carbonate, which participates in atmospheric photochemical reactions, except those designated by US-EPA as having negligible photochemical reactivity. VOCs are organic chemical compounds whose composition makes it possible for them to evaporate under normal indoor atmospheric conditions of temperature and pressure. This is the general definition of VOCs that is used in the scientific literature and is consistent with the definition used for indoor air quality. Since the volatility of a compound is generally higher the lower its boiling point temperature, the volatility of organic compounds is sometimes defined and classified by their boiling points. For its part, the European Union uses the boiling point, rather than its volatility, in its definition of VOCs. A VOC is any organic compound, excluding methane, having an initial boiling point less than or equal to 250 °C measured at a standard atmospheric pressure of 101.3 kPa. VOCs are sometimes categorized by the ease of their emission. Finally, the World Health Organization (WHO) categorizes indoor organic pollutants as very volatile organic compounds (VVOCs), VOCs, or semi-volatile organic compounds (SVOs).

The higher the volatility (the lower the boiling point), the more likely the compound will be emitted from a product or surface into the air. VVOCs are so volatile that they are difficult to measure and are found almost entirely as gases in the air rather than in materials or on surfaces. The least volatile compounds found in air constitute a far smaller fraction of the total present indoors, while the majority will be in solids or liquids that contain them or on surfaces including furnishings and building materials.

VOCs are widely used and produced at home or by industry. VOCs form families of pollutants, including the series of aromatic hydrocarbons that are higher homologs of benzene, known as BTEX (benzene, toluene, ethylbenzene, and m/p/o-xylene), aldehydes (such as formaldehyde, acrolein, and crotonaldehyde), and chloride compounds (such as trichloroethylene). VOCs represent a class of pollutants of interest due to their abundance in the ambient and indoor atmospheres, deleterious effects on public health, and function in atmospheric chemistry[2]. Sources are numerous and include vehicle exhaust, petrol stations, industrial activity, landfills and waste treatment plants, and combustion for domestic heating[2]. In addition, VOCs are widely used in many consumer products such as paints, varnishes, permanent felts, correction products (Tipp-Ex), glues, shoe polish, leather cleaners, solvents, and detergents. They can also be emitted by the use of other products, such as printers, photocopiers, *etc.*[3,4]. Smoking is also an important source of VOCs such as BTEX, trimethylbenzene, and naphthalene, as shown by several metrological studies conducted in Spain and Texas, before and after the ban on smoking in public places[5,6].

Health effects of VOCs

Air pollution constitutes a mixture that exposes the respiratory system where gas exchanges with the body take place. Since they evaporate easily at room temperature, human exposure to airborne VOCs is inevitable. Early studies reported associations between respiratory symptoms and sources of indoor air pollution. Then, with the development of specific instruments to better quantify indoor air quality, researchers were able to analyze the association between respiratory symptoms and direct measurements of pollutants. The first indoor pollutants associated with respiratory effects were dust allergens, NO_2, and fine particles. More recently, VOCs, emitted from various sources and suspected of being irritants, have been independently associated with short- and long-term respiratory symptoms. They have a short half-life in the body, but their exposure is recurrent and ubiquitous. Numerous VOCs are individually known to be toxic. Some are classified as carcinogenic or reprotoxic at the European level or by the WHO. Since 1993, benzene has been classified as a Group 1 carcinogen by the International Agency for Research on Cancer (IARC) and has been linked to non-malignant hematological disorders (thrombocytopenia, leucopenia, or anemia), and it has a role in the occurrence of leukemia and/or non-Hodgkin's lymphoma[7]. Formaldehyde causes cancer of the nasopharynx and leukemia (Group 1)[8]. Trichloroethylene causes cancer in the kidney (Group 1)[9]. Acrolein is probably carcinogenic to humans (Group 2A)[10]. Ethylbenzene and crotonaldehyde are possibly carcinogenic to humans (Group 2B). Xylenes are not classifiable (Group 3)[10]. Toluene is likely to harm the fetus (H304) and is classified as a Category 2 reproductive toxicant by the EU following studies showing effects on fetal development in animals, in particular delayed growth and skeletal development. In humans, the intentional inhalation of large quantities of toluene is thought to harm the fertility of female drug users, embryonic development[11], and the regulatory mechanisms of the endocrine system[12].

The health effects attributed to VOCs mainly concern the respiratory tract and the lungs, which are preferential target organs for gases and aerosols, but also the central nervous system (CNS)[3,13,14]. Indeed, some VOCs, such as BTEX, easily cross the blood-brain barrier[15]. Furthermore, a review of the literature on BTEX suggests the presence of endocrine mechanisms underlying many effects related to BTEX exposure, while they have generally only been assessed as potential carcinogens[16].

Concerning respiratory effects, epidemiological investigations have shown in children aged 6 months to 3 years and 5 to 11 years a significant relationship between pulmonary exposure to benzene and an increase in certain inflammatory diseases such as asthma, bronchitis, and morning cough after adjustment for other pollutants[17,18]. Exposure to a benzene concentration of 10 μg/m³ would triple the risk of developing asthma in children. The significant impact of a 10 μg/m³ increase in exposure to toluene, ethylbenzene, and *m*-xylene on the development of asthma has also been shown, with odds ratios of 1.84, 2.54, and 1.61, respectively, after adjustment for co-exposures[18]. A French case-control study found that toluene exposure was significantly associated with the induction of asthma in urban and rural children[19]. In Portugal, increased levels of individual and mixed endocrine disruptors were found in classrooms with more children with respiratory symptoms[20]. In this study, the authors concluded that even low levels of exposure can increase the risk of asthma and respiratory symptoms. Regarding VOCs in mixtures, in a cross-sectional survey of 490 French dwellings, the Indoor Air Quality Observatory (OQAI) showed that co-exposure to the BTEX + styrene mixture and exposure to undecane and trimethylbenzene were associated with asthma risk[21]. In America, the association between exposure to BTEX and asthma prevalence was previously observed in adults (OR = 1.63)[22] and in children (OR = 1.27)[23]. The latter study also showed a significant association between exposure to pollutants including BTEX and the frequency of the following symptoms: cough and chronic phlegm, bronchitis, persistent wheezing, and shortness of breath[23]. Respiratory symptoms include the occurrence of rhinitis associated with ethylbenzene, o-xylene, and trichloroethylene[21].

Toxicity of VOCs

Experimental methods for studying toxicity

When identifying the mechanisms of action of a toxic agent, one of the first questions to ask is the choice of study model. Obviously, even if most studies are conducted in experimental models, the purpose of all toxicological research is to protect humans from the effects of the toxic substances that surround them. Consequently, this research must not be limited to the consideration and sometimes the inactivation of pathophysiological mechanisms in cell cultures or laboratory animals. The toxicologist must, therefore, constantly be confronted with the validation of their study model and the demonstration of its relevance, particularly when the general public asks him, sometimes naively, if their observations can be extrapolated to humans.

According to the classic hypothesis of the complementarity of study models, the predictability of measured effects decreases proportionally with the scale of observation. Exposed human populations, such as those presented in the previous paragraph, would thus be the models of choice, as their predictability for the whole species is almost absolute. This assertion can be verified when individuals potentially sensitive to the harmfulness of xenobiotics are included in the exposed population groups for reasons of age, pregnancy, or pre-existing pathology. Several ethical, moral, and scientific considerations obviously prevent their use in identifying mechanisms of toxicity, although humans are not necessarily excluded from toxicological studies. By way of illustration, the development of a drug escapes these limitations and notably includes tests on a limited number of healthy volunteers during the first phase of clinical trials. In this way, not only is the distribution of the product in the body assessed, but also its toxicity, via the search for possible negative reactions. In environmental and occupational toxicology, recourse to human exposure remains rare. One of the main challenges scientists face in understanding the toxicity of pollution is the complexity of actual exposure. People are not exposed to one or two pollutants but a mixture of very different molecules present in varying doses.

To individualize the mechanisms of action of each of the pollutants, several experimental methods can be used. The strong point of experimentation is to have complete control of the exposure parameters in terms of toxicant, dose, and duration of exposure on the one hand and homogeneity of the exposed living model on the other hand. Among these methods, the oldest are animal experiments. These methods are called *in vivo*. Healthy animals of the same age and sex are divided into groups and subjected to various exposure conditions. Homogeneity is important, and exposure to the pollutant should be the only difference between the groups. These methods allow the acute and chronic toxicity of pollutants to be assessed for extrapolation to humans. The advantage of *in vivo* models is that they integrate all the potential effects of a toxicant and its metabolites in a physiological context. Thus, for example, the interactions between organs are preserved. However, many precautions must be taken in the transposition of cross-species data. Several parameters, such as the choice of species, the mode of administration, and the exposure window, must be taken into consideration when using data from *in vivo* studies. The selection of an animal model can thus lead to under- or overestimations of the dangers for humans. These studies provide a wealth of information (see, e.g., the reviews on the toxicity of trichloroethylene, dichloroethane, benzene, toluene, xylenes, and formaldehyde[24-30]). However, these studies have their limitations, including the cost, the number of animals sacrificed, and the difficulty of transferring the effects of the animal model to humans.

Non-animal methods

Once the cells have been selected, they must be exposed, i.e., brought into contact with the toxicant. The emergence of alternative models such as *in vitro* toxicology, which are becoming more and more efficient, makes it possible to fill certain gaps and particularly to test more exposure conditions. More than a century after the beginnings of cell culture, there is now a large number of cell lines or primary cultures that can be acquired from cell banks. Faced with this variety, it is necessary to choose the right cell strain to carry out one's research. Researching the mechanisms of action of atmospheric pollutants needs to focus on cells from the human respiratory system.

In the literature, two main methods of exposing cell culture to a gas mixture exist: the cells can either be immersed in the culture medium in which the mixture bubbles or grown on an insert[31]. In a submerged exposure system, cells are placed in the growth medium. This method simplifies the experimental procedure and is less expensive than the system using inserts[32]. However, this system may generate inaccuracies in the assessment of the toxicity of gas mixtures as it allows interactions between the tested chemicals and the components of the medium. Moreover, the actual exposure concentration is difficult to assess. The relevance of this system is limited to compounds soluble in the medium, which restricts its use. The physiology of respiratory cells is not respected. It is important to maintain the lung cells at the interface between air, representing the alveolar lumen, and a liquid, corresponding to the lung tissue. *In vitro* exposure methods to gas mixtures should allow the closest possible contact between the cells and the compounds being tested. In addition, a humidified atmosphere must be maintained to avoid drying out the cells[33]. These requirements are met by air-liquid interface (ALI) exposure systems. Grown on inserts, cells are fed and hydrated by the culture medium on the basolateral side and exposed on the apical side[34]. ALI insert culture models promote the differentiation of epithelial cells. The cell layer produced by this method is very similar to the epithelial morphology of the airway *in vivo*[35]. Although these systems are expensive in terms of equipment, they have the advantage of eliminating any direct interaction between the tested toxicants and the components of the culture medium.

Direct and dynamic exposure of human cells to chemicals in the atmosphere can be achieved using the ALI exposure device Vitrocell®[36]. We have set up this system in the laboratory to test the toxicity of single and

mixed VOCs, such as benzene, toluene, ethylbenzene, xylene, trimethylbenzene, and formaldehyde, as well as the products formed during the catalytic degradation of these VOCs.

Catalytic oxidation is indeed an effective technique to remediate industrial VOC emissions. Catalysis aims at degrading pollutants, but under certain conditions, it can lead to the formation of by-products. These by-products can be toxic and sometimes even more toxic than the VOCs to be removed. For example, the catalytic degradation of toluene can lead to the formation of benzene, a known carcinogen [Figure 1][37].

However, the performance of the catalyst is assessed by measuring VOC conversion or CO_2 emissions, but rarely according to by-product formation. The combination of an ALI exposure device and the catalyst test gives us the opportunity to realize an untargeted toxicological validation of the catalyst. Moreover, the use of a biological system allows the consideration of synergies and competition between the toxic effects of VOCs and emitted by-products.

Toxicity of acute exposure to VOCs

In the various projects, the objective of the toxicology part was, first of all, to know the toxicity of the VOCs measured in an industrial environment, and then to characterize the potential impact on human health of the emissions of various catalytic systems designed for the oxidation of these VOCs. As toluene is one of the model solvents, most studies have then focused on the assessment of its toxicity and that of its products formed by catalytic oxidation. In this way, we firstly assessed the toxicity of toluene and particularly the activation of the mechanisms involved in its biotransformation by cytochromes P450[37]. We were then able to couple the cell exposure system to the Pd/γ-Al_2O_3 catalyst formulated for the catalytic degradation of toluene [Figure 2][38]. This allowed us to test the degradation efficiency of this catalytic system. Indeed, the development of catalysts relies on the measurement of some known products, such as water and carbon dioxide, plus benzene in the case of toluene degradation. However, the formation of by-products is rarely studied. Besides, it is important that these by-products should not have higher toxicity than the initial VOCs.

After exposing the cell cultures for 1 h to the more or less diluted catalyst effluent, different toxicity markers were measured. Firstly, we did not identify any impact in terms of cell death. Secondly, the measurement of gene expression in the exposed cells showed an induction of xenobiotic metabolizing enzymes (XME) such as cytochromes P450. These enzymes have a certain substrate specificity, and the results show that the effluents of the tested catalysts contained small amounts of polycyclic organic compounds of the PAH type. By measuring the activation of XMEs classically induced by polycyclic organic compounds, as well as the activation of AhR, in lung cells exposed to emissions from the catalytic degradation of toluene, we could thus suggest the formation of high molecular weight compounds that may confer residual toxicity to the catalyst emissions [Figure 3][39]. These compounds were not detected in the routine micro-GC analysis used in the chemical optimization of catalyst systems. This hypothesis supports the scientific relevance of using toxicological evaluation in the development of chemically and toxicologically efficient catalysts. Using dedicated by-product identification analyses, four- and five-ring PAHs were identified.

Toxicity of repeated exposure to VOCs

The VOC toxicity study was conducted after acute and repeated exposure, i.e., human lung cell cultures were exposed to diluted VOCs for 1 h per day for 1-5 consecutive days[40]. Our study was the first to carry out repeated exposure to VOCs. Only this repeated exposure allowed the detection of CYP1A1 gene

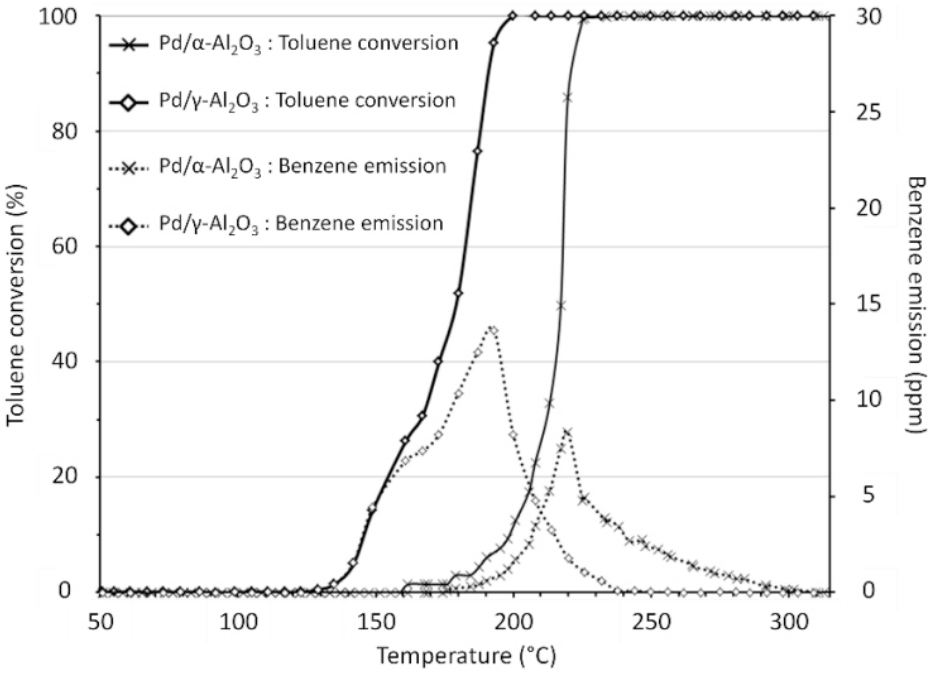

Figure 1. Light-off curves of Al_2O_3 catalysts impregnated by Pd and production of benzene versus temperature. The dotted lines correspond to the benzene production (in ppm) as a function of the toluene light-off curve[37].

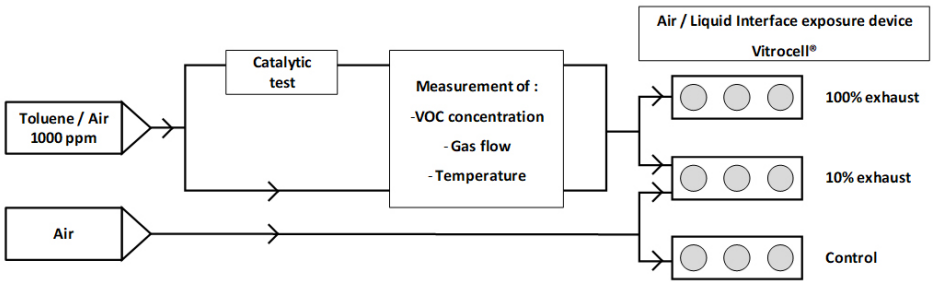

Figure 2. Experimental setup of the coupling of the cell exposure system to the catalyst formulated for the catalytic degradation of toluene[38].

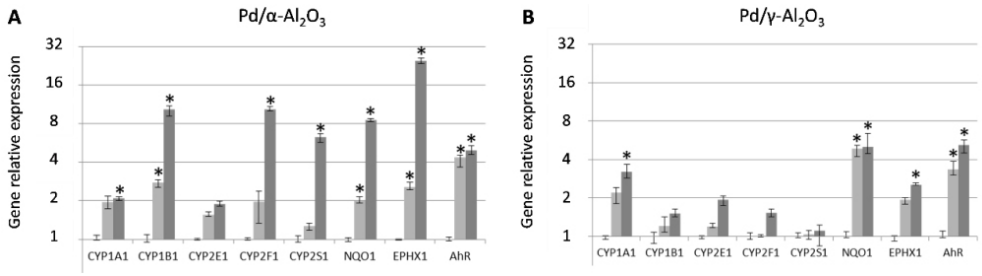

Figure 3. XMEs (CYP1A1, CYP1B1, CYP2E1, CYP2F1, CYP2S1, NQO1, and EPHX1) and AhR receptor in A549 cells exposed for 1 h to the emission of the catalytic degradation of toluene by $Pd/\alpha Al_2O_3$ (A) and $Pd/\gamma Al_2O_3$ (B) at 10% (100 ppm, light grey) or 100% (1000 ppm, dark grey). Gene induction was measured by RT-qPCR (n = 3) and analyzed by ΔΔCt method[39] using air-exposed cells as reference and 18S as a normalization gene. Data are shown as median RQ values *vs.* controls and interquartile range. Significant up- or down-expression was considered if RQ was > 2.0 or < 0.5, respectively.

induction, which was not previously shown in the acute studies. The studied VOCs are among the most detected chemicals in the industrial partners of the project. The toxicity of toluene homologs was studied to evaluate their substitution in industrial processes. The cellular exposure concentrations retained correspond to the regulatory doses (8 h and 15 min French Occupational Exposure Limit Values, i.e., 20 and 100 ppm). Toxic effects were assessed through parameters of cytotoxicity, inflammatory response, and gene expression of XMEs. Exposure of BEAS-2B cells to toluene and its higher homologs revealed the involvement of compound-specific metabolic pathways. Therefore, we were able to identify the different expression profiles of these four molecules despite their structural homology [Table 1]. As expected, CYP2E1 gene expression was significantly induced after cell exposure to benzene, with significant expression from Day 3 onwards. This induction corresponds to the known mechanism by which benzene is oxidized to its first metabolite, 1,2-epoxybenzene[41-43]. This ring oxidation is characteristic of benzene. This transformation was expected for its higher homologs. However, a decrease in CYP2E1 expression over time upon exposure to toluene and *m*-xylene may be related to the activation of secondary biotransformation pathways in BEAS-2B cells. A significant induction of IL-6 was also observed, with a higher concentration for xylene than for the other molecules. Using a proteomic analysis of bronchial cells exposed to toluene at 20 ppm, 3325 proteins were analyzed, of which 2423 were quantified. The statistical analysis allowed the identification of overexpressed proteins involved in metabolism pathways, amino acid and antibiotic biosynthesis, cell-cell adhesion, and defense against oxidative stress.

Non-cancerous human bronchial cells were also exposed to the by-products of the catalytic degradation of toluene under subacute conditions to assess the repeated exposure of people. The cellular response to toluene exposure was evaluated at the cytotoxic, gene expression, and protein levels, highlighting the advantages of applying repeated exposure protocols compared to classic toxicology approaches[44]. These results provide a reference for the assessment of cellular exposures to products of catalyst operation.

In addition, the toxicology study again suggested the identification of chemically undetected by-products. The measured XME gene induction was not only due to the presence of unconverted toluene and benzene by-product. It also revealed the presence of other by-products of catalytic oxidation, such as PAHs, not detected by the standard analytical method used for catalyst development. The repeated exposure mode allowed us to reveal the presence of very low levels of by-products due to the delayed expression of genes, such as those of the CYP1A1 and ALDH families. Consequently, this ALI *in vitro* approach underlined, on the one hand, the value of assessing the impact of repeated exposure to VOCs and, on the other hand, the relevance of performing toxicological validation of catalysts in addition to standard chemical analysis. This approach was therefore also followed to assess the toxicity of formaldehyde and the products of its treatment by photocatalysis. This showed an alteration of the aldehyde metabolism pathways even at very low concentrations of exposure.

VOCs emission measurements

The difficulties in the measurement of VOCs in industrial emissions are due to the complexity of the mixtures and the extent of the ranges of concentrations encountered. Emitted VOC mixtures can contain saturated or unsaturated hydrocarbons, benzene rings, chlorinated hydrocarbons, esters, ketones, alcohols, and amines, as shown in Table 2[45]. The quantity emitted can range from ppb to whole percentages, which means that major and trace compounds may have to be measured simultaneously. To these difficulties are added the conditions of temperature, pressure, humidity, and dustiness to which VOCs will be subjected during their emission. All these conditions and difficulties lead to sampling trains and/or analyses, which are described below. We also focus on the so-called channeled emissions.

Table 1. Relative expression of XME-encoding genes after exposure of BEAS-2B cells to benzene, toluene, m-xylene, or mesitylene for 1 h/day for five days

Days	Benzene 20 ppm			Benzene 100 ppm			Toluene 20 ppm			Toluene 100 ppm			m-Xylene 20 ppm			m-Xylene 100 ppm			Mesitylene 20 ppm			Mesitylene 100 ppm		
	1	3	5	1	3	5	1	3	5	1	3	5	1	3	5	1	3	5	1	3	5	1	3	5
CYP1A1	=	=	=	=	+	=	=	=	=	=	=	+	=	=	=	=	=	=	=	=	=	=	+	=
CYP1B1	=	=	=	=	=	=	=	=	=	=	=	=	=	=	=	=	=	=	=	=	=	=	=	=
CYP2E1	=	+	+	=	+	+	+	+	=	+	+	+	=	=	=	+	+	=	=	+	+	=	+	+
CYP2S1	=	=	=	=	=	=	=	=	=	=	=	=	=	+	=	=	+	=	=	=	=	=	=	=
CYP2F1	=	=	=	=	=	=	=	=	=	=	=	=	=	=	=	=	=	=	=	=	=	=	=	=
EPHX1	=	+	=	=	+	=	=	=	=	=	=	=	=	=	+	=	=	+	=	=	=	=	=	+
NQO1	=	=	=	=	=	=	=	=	=	=	=	=	=	=	=	=	=	=	=	=	=	=	=	=
GSTM1	=	=	=	=	=	=	=	=	=	=	=	=	=	=	=	=	=	=	=	=	=	=	=	=
DHDH	=	=	=	=	=	=	=	=	=	=	=	=	=	=	=	=	=	=	=	+	=	=	+	=
ADH1A	=	=	=	=	=	+	=	=	=	=	=	=	=	=	=	=	=	=	=	=	=	=	=	=
ALDH2	=	=	=	=	=	=	=	=	=	=	=	=	=	+	+	=	+	+	=	=	=	=	=	+
ALDH3B1	=	=	=	=	=	=	=	=	=	=	=	=	=	=	++	=	=	++	=	=	+	=	=	++

Expression of the 12 genes was measured by RT-qPCR (n = 3) and analyzed by the ΔΔCt method[39] using cells exposed to filtered air as a reference and the geometric mean Ct of 18S, GAPDH, and B2M as normalization genes (=, no significant gene expression change; -, RQ < 0.5 ; +, RQ > 2 ; ++, RQ > 4).

In general, successive steps of filtration, gaseous effluent transfer via an inert line (heated or not according to the studied processes), and abatement of moisture are necessary before the actual sampling phase of the VOC, which can imply a supplementary concentration step depending on the emission levels.

Moreover, two different analytical approaches can be chosen to characterize as well as possible the compounds emitted by the process studied, depending on the target of the study and the feasibility of on-site implementation. In the first approach used, for example, to evaluate emission levels, sampling on site can be carried out, and deferred analyses will be conducted in the laboratory. The difficulty is to be representative of the process during the sampling. This will also create additional problems with packaging, transport, and conservation (conditions and duration) of the samples. In the second approach used, for example, to understand the correlation between VOC emissions and production phases, samples and analyses on-site and/or on-line can be carried out.

Before on-site measurement, documentary preparation work is necessary with at least a study of the process and the safety data sheets (SDS) of the chemicals handled, examination of the analytical reports and previous results if available, and, if relevant, the legal requirements concerning the emissions. A preliminary laboratory phase may also be conducted on raw materials (i.e., chemicals handled) in conditions close to the process to anticipate their possible discharges and

Table 2. VOCs detected in stacks emissions of several industrial activities

Industrial activity	Compounds	Detected compounds	
Production of components with formophenolic resin	Aldehydes Phenols Aromatics Furans	Aldehydes: formaldehyde, hydroxybenzaldehyde, benzaldehyde Phenols: phenol and derivated compounds Furans: benzofuran, methyl and dimethylfuran	Aromatics: methylethylbenzene Toluene, xylene Propylbenzene Trimethylbenzene Tetramethylbenzene
Fabrication of surfactants and detergents	Amines Oxides	Methylamine, dimethylamine, trimethylamine Ethylene and propylene oxides	
Synthesis of organic compounds	Alcohols Halogenated compounds Aromatics	Alcohols: methanol, ethanol Chlorides: chloromethane, dichloromethane, chloroform chlorobenzene	Aromatics: ethylbenzene, toluene Dimethylbenzene Methylethylbenzene Propylbenzene
Collection of biogas from buried waste *(exhaust of the thermic treatment technique)*	Aromatics Cyclical compounds Alkanes Halogenated and sulfur compounds	Limonene, -pinene, cyclohexane Chlorobenzene, dichlorobenzene Thiophene	
Varnishing of metal supports (food industry, automobile)	Alcohols Aromatics Ketones	Alcohols: methanol, ethanol, butanol, butoxyethanol, butoxyethoxyethanol, butylglycol acetate, methoxypropanol Ketones: methylethylketone, methylisobutylketone	Aromatics: xylene Methylethylbenzene Propylbenzene Trimethylbenzene Diethylbenzene Methylpropylbenzene Ethyldimethylbenzene Tetramethylbenzene
Agri-industry *(odour problems)*	Sulfur compounds Esters Aldehydes Ketones	Sulfur compounds: dimethylsulfide, dimethyldisulfide, dimethyltrisulfide, thiophene derivated compounds	

identify relevant VOCs not announced in the SDS. This is consistent with the definition of VOCs given by the European Directive 1999/13/EC concerning the reduction of the emissions of volatile organic compounds (VOCs), which states that a "volatile organic compound" is any organic compound, excluding methane, having a vapor pressure of 0.01 kPa or more at a temperature of 293.15 K or having corresponding volatility under specific conditions of use. For our diagnosis, it concerns, in particular, the operating temperatures encountered in the process. These preliminary steps are strongly recommended based on our experience in this field. Our approach is described in Figure 4.

Raw material analysis

To simulate the process "specific conditions of use" of VOCs, a relevant technique can be static headspace coupled to gas chromatography (GC). The detector coupled to GC can be mass spectrometry (HS-GC/MS) in the case of a complex matrix or flame ionization detector (HS-GC/FID) when the matrix contains few compounds. The basic principle of the static headspace technique (HS) is to encapsulate the matrix to analyze in a vial. As an example, a small droplet (~10-20 µL) of raw materials is sealed in a 20 mL headspace vial. The vial is then heated at a selected temperature (close to the process one or around 80 °C if the matrix is water-based), and the gas phase formed over the matrix is injected in GC. The volume injected is, for example, 1 mL. The different VOCs present in the sample are then separated by GC, and the retention time of each compound is used for their identification. In HS-GC/FID, compounds are only identified by their retention time. In HS-GC/MS, the VOCs are also analyzed by mass spectrometry, and the identification of each molecule is made by comparison between the experimental mass spectrum and the reference spectra of the NIST Library (US National Institute of Standards and Technology). The HS method has the advantage of being quite easy to implement, requiring little handling and no solvent. Its main limitation is related to the small volume of gas injected, which implies a low sensitivity. Care must be taken with the temperatures

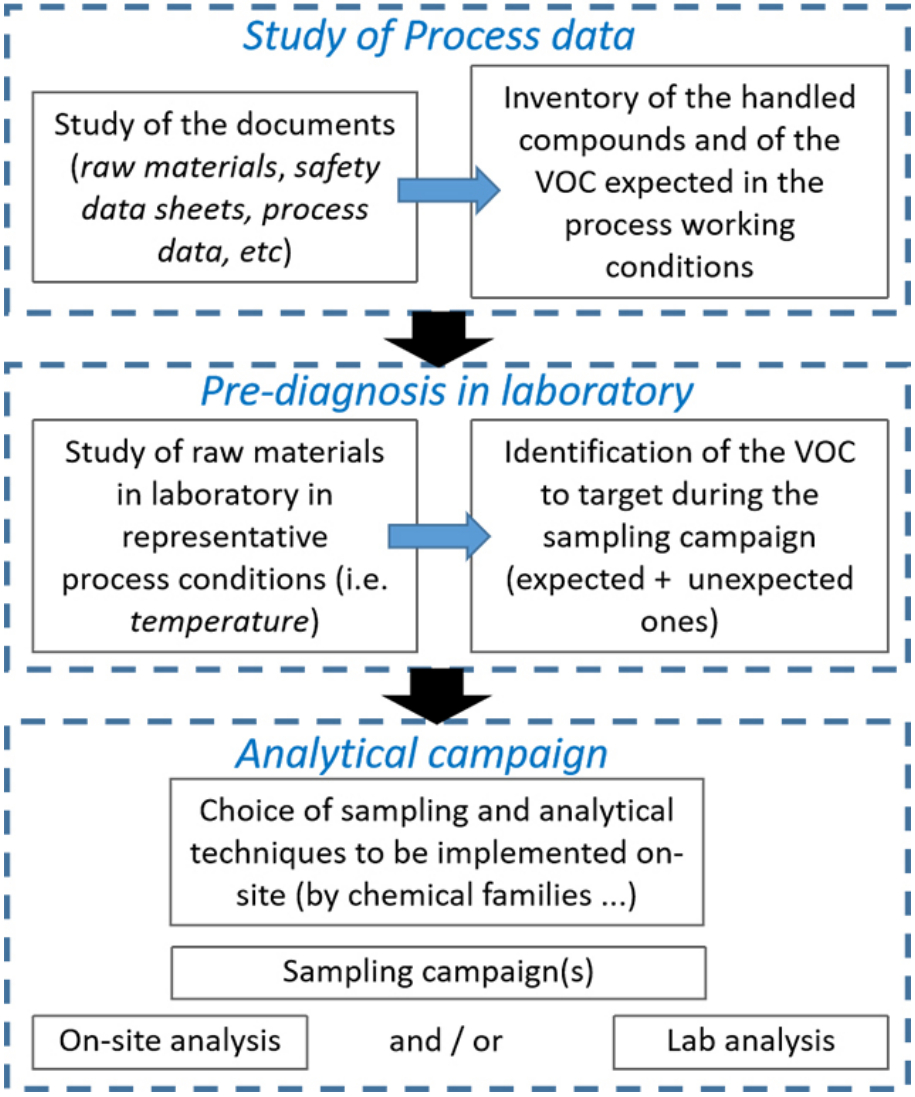

Figure 4. Analytical approach to perform for on-site VOCs analysis. VOCs: Volatile organic compounds.

of the HS-GC technique (vial heating, injector temperature, *etc.*) if the targeted VOCs present a risk of thermal degradation. Caution also has to be taken for VOC quantification as the gas phase can be saturated by the most volatile VOC, thus masking the less volatile ones. This phenomenon is linked to the fact that the vial is hermetically sealed which limits the volume available for the formation of the gas phase; this is not the case in the "open" operating conditions encountered in most industrial processes.

It should be noticed that HS-GC analysis does not represent the composition of the raw sample, which may contain water or non-volatile compounds, but simulates the volatile part likely to be found in the gaseous effluent. Table 3 gives an example HS-GC analysis of some raw materials analyzed at a temperature close to the process one in a metallic can production industry. Data in brackets indicate the concentration announced in the SDS.

The dynamic headspace technique may partly solve these limitations since an additional step of condensation of the extracted volatile compounds on a trap is added, which concentrates the VOC. The trap

Table 3. Comparison of HS-GC analysis results and SDS data

Compounds (%)	Varnish A	Varnish B	Lacquer C
Ethanol	5 [2,5 - 10]		
Methyl ethyl ketone	91 [50 - 100]		
Butanol	2 [0 - 2,5]	47 [2,5 - 10]	6
Methyl isobutyl ketone	Trace		
Ethyl benzene	Trace		Trace
m,p-xylene	1		Trace
O-xylene	Trace		Trace
2-butoxy ethanol		52 [2,5 - 10]	11 [< 5]
Trimethyl benzene			11
Ethyl methyl benzene			1
Di-isobutyl ketone	Trace		
Tetramethylbenzene			47
Indane			1
Diethyl benzene			7
Dimethyl ethenyl benzene			1
Naphtalene			2
Methyl naphtalene			Trace
2-diméthyl-aminoéthanol		[0,1 - 2,5]	

can either be adsorbent or temperature-based using cryogenic fluids or "Pelletier" effect. Trace amounts of VOCs can thus be determined. The choice of the sorbent used for the trap has to be carefully considered as its selectivity among some VOCs families may become a disadvantage (untrapped types of VOCs that are thus not detected). Caution also has to be taken to avoid pollution of the trap.

Choice of sampling and analytical techniques

After the study of process data and pre-diagnosis in the laboratory by raw material analysis, the selection of the relevant sampling and analytical techniques can be made. This selection has to take into account the constraint of the site to be investigated (for example, accessibility of sampling points) and the technical capacities of the laboratory, such as the ability to perform on-site diagnosis. The range of concentrations to measure and the type of process to be investigated also have to be considered: continuous, discontinuous or cyclic phenomenon, batch production, *etc.* Moreover, the gaseous effluents to be investigated (working area, diffuse, or stack emissions) and the associated conditions (temperature, humidity, dust level, and pressure) will condition the technical choices that will be relevant for sampling and analysis.

For stack emissions, a precious help to guide the specific VOCs sampling conditions (relevant period, volume to collect, *etc.*) is to use continuous monitoring of parameters such as total hydrocarbon or combustion gases (O_2, CO/CO_2 NO_x, and SO_2). Some industrial stacks are equipped with these analyzers, but they can also be implemented specially for a sampling campaign. Total organic content is measured by a flame ionization detector (FID), which often allows measuring methane hydrocarbons (MHC), non-methane hydrocarbons (NMHC), and total hydrocarbons [THC, or total organic carbon (TOC)]. This analyzer can be calibrated with methane (CH_4) or propane (C_3H_8) standard. Concentrations can thus be determined in methane (or propane) equivalent and then converted to carbon equivalent. Combustion gases are measured by specific analyzers based on the technique, such as paramagnetism (O_2), IR, or UV for the other gases. The use of the data provided by these continuous monitors allows better monitoring and/or understanding of the process as one can follow in real time the emission levels. It is then possible to decide what are the relevant periods for sampling. A significant change in THC and/or combustion gas levels is

generally associated with a change in the VOC mixture composition. High levels of THC (and NMHC) will allow short samplings of VOCs to avoid, for example, saturation of absorbent or adsorbent media. Oppositely, low NMHC levels will require sampling of larger volumes of gaseous effluents to increase the concentration factors on the selected sampling media and thus improve the detection limits of the specific VOC targeted.

Sampling

The sampling techniques can be divided into two categories: non-selective sampling with or without preconcentration (containers) and selective sampling with preconcentration using adsorbent, absorbent, impingers, *etc.* The first one has the advantage of bringing back the whole air sample to the laboratory, whereas the second one is selective and adapted to targeted compounds.

Non-selective sampling without preconcentration in containers (gasbags, canisters, ampoules, *etc.*) allows non-selective sampling, requires less equipment, and is fast and easy to perform. Gas bags allow taking 1-200 L gas samples, and a pump is used to fill the bag with the gas. Some cautions must be taken as the bag composition must be adapted to the gaseous compounds targeted: inert materials such as Tedlar® or Teflon® are often used as they do not generate a retention phenomenon or reaction on the walls of the bag. They are valid for all ambient gases or common solvents (H.C. and chlorinated solvents). Another wall composition exists for specific VOCs. Gas bags can be cleaned (nitrogen flushing) and used several times. Their normal operating temperature is between -73 and 105 °C. Canisters are metallic containers that are placed under vacuum. When opening the closing valve, the gaseous effluent is sucked into the container. Canisters can be equipped with a flow control kit, and sampling times from instantaneous to 24 h can be obtained. The stability of the container content depends on the gaseous effluent composition, and thus they have to be analyzed as soon as possible. Direct analysis of the various container types' content is possible if the VOC levels of the effluent collected are compatible with the detection limits of the analytical system used. Injection into GC is carried out by gas syringe, gas loop, or pumping. If the VOC level is too low for direct analysis, preconcentration on adsorbent tubes or other media can be performed.

Non-selective sampling using condensation of VOCs at low temperature using dry ice or liquid nitrogen is possible but is very constraining on-site in terms of implementation, conservation, and transport of samples and can be impacted by simultaneous trapping of water. Other techniques are thus often preferred.

Sampling with preconcentration using sorbent tubes or impingers allows more or less selective collection of VOCs at quite low concentrations. Caution must be taken to avoid the saturation of the sampling media which would lead to an underestimation of the VOC concentrations. To overcome this risk, two sampling units are often placed in series, the second one serving as a guard: the absence or presence of low VOC content on the second unit (< 10% of the first one) ensures that the first one was not saturated.

The impinger technique consists in bubbling gaseous effluents in an appropriate solution for trapping the VOC family targeted by absorption in a liquid. The liquid used for trapping can be aqueous solutions adjusted to a suitable pH (amines, phenols, carboxylic acids, *etc.*), solvents for dissolution of VOCs, or reagents that transform by chemical reaction the VOC targeted in less volatile compounds [e.g., dinitrophenylhydrazine (DNPH) to trap aldehydes and ketones]. Impingers allow managing the sampling of higher concentrations than sorbent tubes as their volume (and thus of the trapping solution used) can be adjusted, keeping in mind that high volume may impair the detection limit. The evolution of the volume of the solution in the impingers has to be checked (e.g., by weighting) between the beginning and the end of

sampling in order to check if no evaporation or loss has occurred. As a quite large volume of solution is available for analysis, it allows multiple injections in GC or HPLC.

The adsorbent tubes allow the trapping of most gases and vapors. Their use has been widely studied since the 1990s[46-49], with higher attention on VOCs and their impact on health and the environment. Numerous reference documents describe sampling and analytical conditions for VOC characterization in stationary sources[50] or working areas[51] using sorbent tubes. Adsorption of VOCs on a solid support is based on the physisorption or chemisorption phenomenon. Depending on the type of tube, a conditioning step may be done before use (e.g., nitrogen flushing and solvent elution); preconditioned tubes can be purchased. For each batch of tubes employed, an unsampled one must be used as a blank to check the absence of contamination during the storage, transport, and implementation on-site. At the end of the sampling process, the tubes are closed with sealed caps to prevent any external contamination before the extraction step and analysis. Ideally, the tubes should be analyzed as soon as possible. To extend the storage time before analysis to several weeks, the tubes can be stored in a dark and cold place (minimum 4 °C, ideally -18 °C). The maximum storage delay depends on the sorbent tube type and the kind of VOC trapped.

The determining factors for the choice of a solid support can be thermal stability, porosity, selectivity of adsorption [Figure 5], sensitivity to water, ease of use, *etc.*

Solid adsorbents are divided into three categories: porous polymers (Porapak®, Chromosorb®, XAD®, PUF, Tenax®, *etc.*), carbonaceous adsorbents (graphitized carbons (carbotrap® and carbopack®) and molecular sieves (carboxen® and carbosieve®), and inorganic adsorbents (alumina, silica, thermotrap®, florisil®, and other inorganic sieves). Other tubes containing silica grafted or impregnated with a chemical reagent are also available (e.g., DNPH tubes).

The properties of some common adsorbents are given in Table 4. Commercial tubes containing multibed adsorbents to get them more polyvalent are available.

Hydrophilic sorbents (e.g., activated carbons) require the removal of water at the beginning of the sampling line. However, if polar compounds are targeted, the use of desiccants (calcium chloride, magnesium perchlorate, calcium carbon, silica gel, and Nafion® membrane) upstream of the adsorbent cartridges should be avoided, as they tend to retain polar compounds such as alcohols, ketones, acids, *etc.* Nafion® tube may be used in some cases.

Schematically, in the case of sampling on sorbent tubes, the gaseous effluent to be analyzed is drawn by means of a pump through the tube containing the adsorbent used to trap the organic compounds targeted. The various elements that can be integrated into a VOC sampling train are as follows, if sampling is performed in a stack: (1) pitot tube for flow measurement, temperature, and pressure sensors; (2) glass fiber filter for particulate matter trapping (to be maintained above 130 °C to avoid water condensation and light VOC adsorption); (3) transfer line (heated at 130 °C if the emitted gases are not at ambient temperature), which should be as short as possible; (4) water trapping system if the sampling tubes used are hydrophilic; (5) module containing the adsorbent tubes and/or the impingers (this module may be refrigerated); (6) condensate collection system; (7) flow meter to control the volume of gas sampled; and (8) pumping unit. Dynamic or static dilution systems can be integrated into the sampling train if the gas concentrations are too high or in order to limit water condensation. This solution should be considered if polar compounds are targeted, as in this case, a water trapping system (4) should be avoided. The sampling system should be made of materials that are physically and chemically inert to the gas constituents (stainless steel, glass,

Table 4. Properties of some common adsorbents

Commercial name	Type	Volatility range (carbon & BP)	Water affinity	Desorption	Note
TENAX® TA	PP	C6-C26; 100-400 °C	Hydrophobic	Thermal (max desorption temperature: 250 °C)	Degradation giving benzene derivatives Regeneration only a few times Quite polyvalent
TENAX® GR	PP	C7-C30; 100-450 °C	Hydrophobic	Thermal	Alkyls benzene, PAH, PCB, heavy alcohols
Chromosorb® 102 & 106	PP	C5-C12; 50-200 °C	Hydrophobic	Thermal (stab. max: 250 °C)	Chlorinated, oxygenated, organometallic compounds
Porapak® Q/HayeSep® Q	PP	C5-C12; 50-200°C	Hydrophobic	Thermal	Polar compounds
Carbosieve® II Carbosieve® III	CA (CMS)	C1-C2 C2-C4; -60-80 °C	Hydrophilic	Thermal (High thermal stability)	High specific surface
Carboxen® 563 Carboxen® 564, 569	CA (CMS)	C3-C5; 50-200 °C C2-C5	Hydrophobic	Solvent	Sampling of low volumes & VVOC
Carbopack® B/Carbotrap® B/Anasorb® GCB1/Carbograph® 1TD Carbopack® C/Carbotrap® C/Anasorb® GCB2/Carbograph® 2TD	CA (GCB)	C5-C12 > 75 °C C8-C20	Hydrophobic	Thermal (High thermal stability) or solvent	High adsorption capacity Polar compounds
Amberlite XAD-2	PP	specific	Slight	Solvent	Apolar compounds, PAH, PCB, dioxins
Coconut charcoal Petroleum charcoal	CA	C2-C5 -80-50 °C	Hydrophilic	Solvent (CS2)	VVOC
Silica gel	IA	C2-C5	Hydrophilic	Solvent	Polar compounds

PP: Porous polymer; CA: carbonaceous adsorbent; IA: inorganic adsorbent; CMS: carbon molecular sieves; GCB: graphitized carbon black; VVOC: very volatile organic compounds.

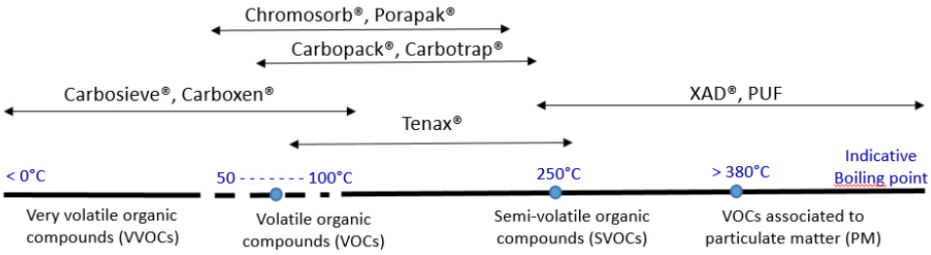

Figure 5. Adsorbent use and properties.

PTFE, and polypropylene fluoride are reliable materials).

Depending on the situation encountered, the different elements of the chain should be specifically selected. For example, if the gaseous effluents contain no or few solid particles, the use of filters may be unnecessary. If a water vapor trapping system is used upstream of the tubes (hydrophilic adsorbents), the condensate collection system downstream of the tube is not necessary. Oppositely, hydrophobic adsorbents (e.g., Tenax) do not require a water vapor trapping system upstream. In this case, a condensate collection system may still be necessary downstream of the tubes to protect the flow meter and pump. If the sampling train includes impingers and their efficiency may be affected by dilution of the trapping solutions that they contain, a water vapor trapping system should be used.

As a caution, it may be interesting if feasible to duplicate samplings or to vary the sampling flow or sampling volume.

Delayed analysis in laboratory

Identification and quantification can then be performed by GC/MS (VOC, PAH, PCB, and other persistent compounds) or HPLC/UV (aldehydes, phenols, *etc.*).

Samples collected in impingers may need specific preparation (pH adjustment) before analysis and can be analyzed several times with different chromatographic conditions or diluted if needed to improve the analytical conditions. Sampling tubes must be either eluted with a solvent or desorbed thermally to release the trapped VOCs. When eluted by solvent (CS_2, methanol, acetone, or acetonitrile), they can be analyzed by HPLC or GC depending on the VOC to be detected, and injection can be repeated if necessary as the injection volume is low (1 μL) compared to the elution volume (milliliters). The drawback is that the presence of the solvent can mask the most volatile products during the GC analysis as a solvent delay must be applied. Solvent elution also decreases the detection sensitivity because of the dilution of the sample in the solvent. Thermal desorption concerns only GC analysis, as the VOCs are released in the gas phase[52]. The tube is heated at high temperatures in order to desorb the molecules by thermal agitation. The carrier gas carries the molecules to the GC. No solvent has to be used, and the GC method does not require a solvent delay, allowing the detection of VVOCs. Thermal desorption gives maximum sensitivity, but in most equipment configurations, the analysis cannot be repeated. Duplicate sampling can thus be interesting.

Figure 6 shows the coupling of a thermodesorber and a GC. If needed, a split can be applied to dilute the desorbed VOCs. The use of an on-line preconcentrator using a trap at -15 °C (Peltier cooled trap) followed by a flash thermal desorption focuses the VOCs before injection in the GC, which improves peak resolution and chromatographic separation.

Table 5 presents the possible analytical techniques for specific VOCs targeted by the French legislation concerning industrial emissions (Arrêté intégré of the 2nd of February 1998).

Some of these techniques are described in the documentary booklet FD X43-319 (2010) concerning the "Stationary source emissions - Guide for sampling and analyzing VOC" established by the French standardization organization Afnor.

On-line analysis: example of a detailed process characterization used for treatment test evaluation at laboratory pilot scale

Sampling on-site followed by analyses in the laboratory is the classical configuration. However, on-site analysis can also be performed with specific analyzers.

An on-site campaign for detailed characterization of the VOC composition of industrial gaseous effluents is described hereafter. This campaign aimed to collect data on a real industrial process to gain information for the development of treatment technology at the laboratory pilot scale. The species-by-species knowledge of VOCs, or even by family, is essential for developing an efficient catalytic oxidation process. This requires the use of semi-continuous analytical techniques and adsorbent tube sampling to identify the VOCs present in the effluents. The process studied is a car production industry and, more specifically, the car painting process. The measurements were performed in the painting booth air extractors stacks on three consecutive days.

Table 5. Sampling and analytical techniques proposed for specific VOCs

VOC concerned	Sampling	Extraction/Analysis
Acetaldehyde, formaldehyde, 2-furaldehyde, acroleine, chloroacetaldehyde	DNPH (impingers or silica impregnated tubes)	Elution/HPLC-UV
Chloroform, chloromethane, dichloromethane, 1,2-dichloroethane, 1,1,2,2-tetrachloroethane, tetrachloroethylene, Tetrachloromethane, 1,2-dichloroethylene, 1,1,2-trichloroethane, 1,2-dibromoethane, 2-dibromo 3-chloropropane	Activated carbon tube	Thermal desorption/GC-FID or GC-MS
Vinyl chloride, acrylonitrile, methyl acrylate, pyridine, 1,4-dioxane, 1,2-é poxypropane, epichlorhydrine, 1,3-butadiene	Activated carbon tube	Thermal desorption/GC-FID or GC-MS
Biphenyls, chlorotoluene, 1,2-dichlorobenzene, benzene	Tenax tube	Thermal desorption/GC-MS
Benzo(a)pyrene, dibenzo(a,h)anthracene	Filter (VOC adsorbed on particles) and XAD (gaseous)	Solvent extraction/GC-MS
2-naphtylamine, diethylamine, dimethylamine, ethylamine, trimethylamine, aniline	Silicagel tubes or impingers filled with acid solution	Elution (tube)/GC-FID, HPLC-UV
Nitrobenzene, nitrotoluene, o-toluidine, benzidine	Silicagel tubes	GC-FID or GC-MS
Phenol, 2,4,5-trichlorophenol, 2,4,6-trichlorophenol, 2,4-dichlorophenol	Impingers filled with basic solution	HPLC-UV

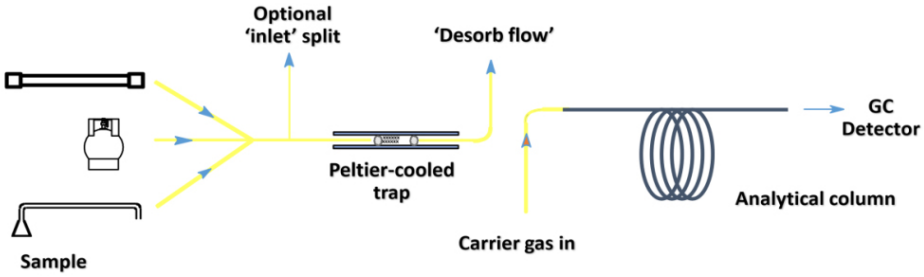

Figure 6. Principal of thermal desorber coupled to GC. GC: Gas chromatography.

Figure 7 describes the different measurement devices that were used during the campaign to characterize the effluents in the stacks. A mobile laboratory was placed near the studied point and a PTFE sampling line at ambient temperature was drawn between the stacks located on the roof of the production building and the mobile laboratory. A volumetric pump ensures the transfer of the effluents towards the various continuous and semi-continuous measurement devices (THC/NMHC/MHC analyzer, mobile µ-GC, and GC-FID), which are placed in parallel. These analyzers sample the amount of flue gas they require, thanks to their internal pump. A cooler is located between the sampling point and the pump to avoid the condensation of moisture in the sampling train. At the same time, a short sampling line is used to perform, on the roof directly in the stacks, sampling on adsorbent tubes with a portable system that includes a volumetric pump, a flow meter, and a needle valve to regulate the pumping rate.

Thus, the characterization of the effluents was divided into three types of complementary analyses or measurements [Table 6].

First, the measurement of physical parameters such as temperature, flow rate, and hygrometry was performed at each stack. These parameters are important for the dimensioning of a treatment unit since they will influence the working conditions and the size of the unit. They are also used to convert the concentrations into mg/Nm^3 and calculate the emission rate.

Table 6. Mobile equipment used

Measurement type	Mode	VOC targeted	Equipment used	Model	Use
Physical parameters	Manuel	-	T, RH% and flow measurement probes	AMI 300 (Kimo Sauermann)	on-site
Total VOC	Continuous	C_x	THC/NMHC/MHC analyzer	Graphite 655 (COSMA)	
Specific VOC	Semi-continuous	C_2-C_{12}	µGC/MS	Hapsite® (Inficon)	
		C_6-C_{12}	GC/FID	AirmoVOC® (Chromatotec)	
	Manual	C_2-C_5	"AirToxic®" sampling tubes analyzed by GC/MS	TurboMass TD/GC Clarus 680/MS Clarus 600S (PerkinElmer)	laboratory
		C_6-C_{12}	"Tenax®" sampling tubes analyzed by GC/MS		

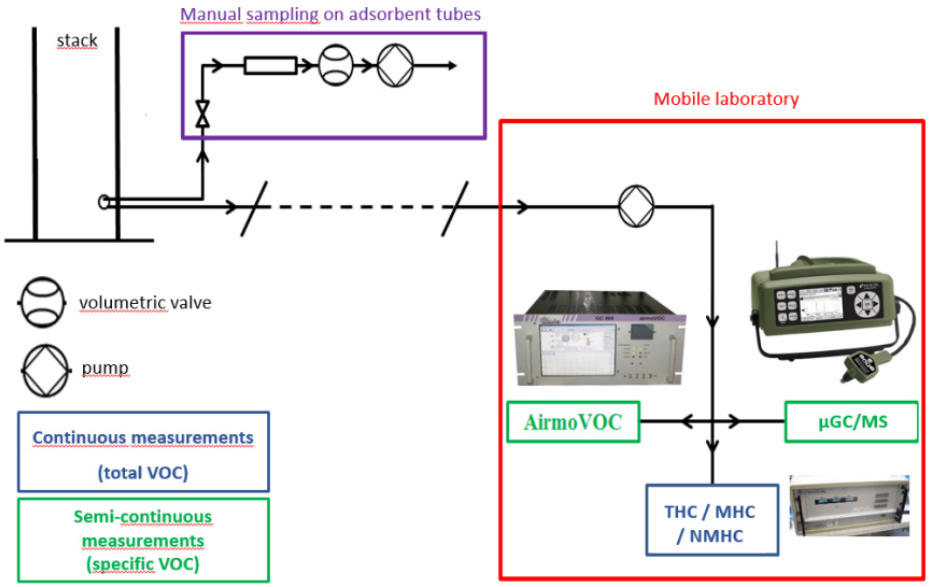

Figure 7. On-site equipment.

Then, continuous monitoring of total organic content of the effluents was performed with a total hydrocarbon analyzer (COSMA Graphite 655) equipped with a FID. The analyzer is calibrated every day thanks to a methane (CH_4) standard at 3000 ppm. Concentrations are thus determined in methane equivalent and then converted to carbon equivalent. This step consists of monitoring the emissions from the stacks and thus highlighting the production steps or cycles. This analysis allows following the evolution and concentration level of non-methane hydrocarbons (NMHC) over time. It is, therefore, a global measurement that does not allow the identification of the species present in the effluents but is complementary to the specific analyses.

Finally, specific VOC analyzers were used to identify and quantify the VOC contributing to the NMHC signal. Two different micro-chromatograph analyzers were used to identify and quantify the specific VOCs present in the flue gas:

• µGC coupled with a FID (µGC/FID; AirmoVOC® C6-C12, Chromatotec): an air sample is automatically trapped on Tenax resin over 2 min and analyzed every 15 min.

• μGC coupled with a mass spectrometer (μGC/MS; Hapsite, Inficon): analyses are performed in parallel with the μGC/FID to help identify the VOCs.

The two systems allow monitoring, identifying, and quantifying the specific VOCs emitted by the process lines. Calibration of the μGC/FID for the VOCs detected in the raw materials was performed in the lab before the on-site measurement campaign. Identifications of the molecules were confirmed by the μGC/MS. These semi-continuous measurements were completed by samplings on adsorbent tubes.

SORPTION-CATALYSIS COUPLING FOR VOC ABATEMENT

Adsorption and catalytic oxidation are both efficient ways of environmental remediation of VOCs. However, these techniques are sometimes not sufficient or adequate for some industrial applications, which produce low concentrated VOC emissions. In this context, it is interesting to develop integrated methods where the individual techniques are combined to overcome their respective drawbacks, leading to more efficient, cost-effective, and selective technologies. These methods permit concentrating and then oxidizing VOCs from contaminated industrial emissions, based on the fine relation between adsorption and catalysis since the activity of catalysts results from their adsorption capacity and the effective activity of their active phase. The following section provides a brief overview of the adsorption and catalysis systems for VOC removal, while presenting the most common materials used for each process. We also review the trend of hybrid treatments in laboratory research with new adsorbents and catalytic active phases.

Thermal oxidation *vs.* catalytic oxidation

Thermal oxidation, also known as incineration, is commonly used in industry as a removal technique of VOCs with 95%-99% efficiency. Thermal oxidation possesses a high operating cost since high temperatures (> 800 °C) are required to achieve complete elimination of VOCs. Three conditions referred to as the "3T rule" for an optimal thermal reaction should be taken into consideration: sufficient temperature, retention time, and turbulence level are necessary for a good conversion yield. Using oxygen from the air, this conventional process converts polluting molecules into CO_2 and H_2O, which are less dangerous to the environment. Emissions with high VOC concentrations (> 5000 ppm) can be efficiently treated, since the reaction is self-maintaining through the energy released by the oxidation reaction. However, this system is not suitable in the presence of heteroatoms such as sulfur, nitrogen, or halogens in the gas flow. In this case, oxidation would lead to the formation of by-products SO_2 and NO_x, as well as acid vapor from halogenated compounds. These undesirable compounds are more toxic than the starting reagent. Catalytic combustion is an alternative way of eliminating VOCs, which considerably reduces energy costs and the formation of harmful by-products. The presence of a catalyst, which increases the speed of the oxidation reaction, allows the reaction to take place at lower temperatures (200-500 °C), thus resulting in energy cost savings. Catalytic systems are well adapted to treat dilute gaseous streams of VOCs (> 1%). Various catalysts can be used for this reaction, which should present high activity, high selectivity, good mechanical and thermal properties, and low cost[53].

Many studies are carried out on the synthesis and design of efficient catalysts for catalytic oxidation. The choice of the catalytic material depends on many factors related to the catalytic conditions, especially the nature and concentration of VOCs. The lifetime of the catalysts is also an important parameter to consider. Catalysts can be divided into two categories: supported noble metal catalysts (Pt, Pd, Au, *etc.*) and simple/mixed transition metal oxides (Cu, Mn, Ce, Fe, Co, *etc.*). Noble metals are widely used for VOC oxidation because of their high catalytic performance despite their high cost and low resistance to sintering and poisoning. Noble metals are found as active phases carried on porous materials (zeolites, SiO_2, Al_2O_3, *etc.*), ensuring their dispersion on the surface and inside the pores. The catalytic performance of noble

metals depends on several parameters, such as the physicochemical properties of the active metal and/or the support, the interaction between the active phase and the support, the preparation method, and the state of the active phase particles (dispersion and size). In the literature, there is a strong use of palladium and platinum as active noble metals for oxidation reactions[54-56]. These are part of some industrial commercial catalyst formulations. However, transition metal catalysts are a cheaper alternative to noble metal catalysts and are recognized for their low cost, excellent reducibility, good thermal stability, and resistance to poisoning[57-59].

VOCs adsorption

VOC adsorption is a process that refers to the migration of a compound in the gas phase to a solid phase by the surface reaction. The compound will bind to the outer and inner surfaces of the porous material, the so-called adsorbent. Adsorbents are usually divided into organic (polymer) and inorganic (carbons, zeolites, silica gels, and clays) adsorbents. Natural materials or some industrial and agricultural wastes can also be used directly or as a resource needed for the elaboration of adsorbents. Adsorption properties may change from one adsorbent to another. Different behaviors may be noticed depending on the type of the adsorbent, its nature, its porosity, or even the type of VOC and its concentration. According to the functional group of VOCs, different interactions can be generated, such as unspecific interactions (van der Waals force) or specific ones (pi-complexation, H-bonding, electrostatic interaction, *etc.*). To choose the adequate adsorbent for VOC removal, the adsorbent should present:

• Good textural properties (surface area, pore size distribution, pore volume, *etc.*).

• Good surface chemical properties (acidity/basic properties and affinity with polar or non-polar compounds).

• Mechanical strength (to avoid the decrease in the performance and the loss of material during adsorption-desorption cycles).

• High thermal and hydrothermal stability (to ensure the cyclic adsorption-regeneration usage).

• High selectivity for VOCs compared to other adsorbable species (such as water vapor).

• High adsorption capacity.

• High hydrophobicity (to overcome the competitive adsorption from water vapor commonly present in the flue gas).

• Insensitivity to the permanent gases constituting the effluent (such as N_2, O_2, CO_2, *etc.*).

Therefore, the adsorption capacity is strongly dependent on the physicochemical properties of the materials, especially their textural ones[60]. The adsorbent can act as a solid catalyst, can be used as a support for a catalytic phase ensuring a high dispersion of the active species, and can be used prior to the catalytic set to eliminate organic or inorganic compounds (H_2S, VOCs, *etc.*). In the following section, we outline the most common types of adsorbents for the removal of VOCs: activated carbons, biochar, and zeolites.

Most used adsorbents for VOC removal

Activated carbons

Activated carbons (ACs) have shown high adsorption potential for VOC removal. Known to be earth-abundant and inexpensive, ACs have been extensively used on an industrial scale. The high capacity of adsorption of activated carbons is linked to their highly developed porous structures, their large accessible surfaces, and the very particular interactions that they have with many organic and inorganic compounds[61-63]. The high degree of microporosity of AC is responsible for the high surface area, which can reach 2700-3600 m^2/g[64]. Then, varying the porous structure of AC, the pore size distribution and connectivity can highly influence the capacity of adsorption of VOCs.

ACs can be found in the form of pellets, granular, spheres, powder, or fibers. The most common raw materials used to produce activated carbon are wood, coal, petroleum pitch, willow peat, lignite, polymers, nutshell flour, or coconut shells. Depending on the precursor and the activation method, the prepared AC will have very different physical and chemical properties. Physical, chemical, or combined activation can be used for the preparation of AC samples in bi- or trimodal porosity. Alkali treatments by KOH activation revealed the capacity to add pores network and increase the pore volume[63,65-67]. Five types of ACs synthesized from different raw materials (wood, coal, and coconut shell) were studied by Yang *et al.*[62]. They showed that the surface area, pore volume, and pore structure controlled the capacity of ACs for toluene adsorption. With wood precursors, the ACs showed the highest surface area and the largest mesopores volume, favoring the better adsorption of toluene[62]. Besides, studies showed that, even when the surface area is higher than 2000 m^2/g, the adsorption capacity of ACs can be reduced by the lack of mesopores in the structure[68].

However, some critical problems can restrict the widespread application of ACs for VOC removal:

- High pressure drop problems when used as traditional packed beds.

- Limited applicability for low molecular weight VOCs (e.g., formaldehyde).

- High hygroscopicity (strong competitive adsorption of water vapor through the capillary condensation of water vapor in the micropores).

- High transmission resistance.

- Pore blocking.

- Promoting polymerization and/or oxidation of some toxic compounds.

- Flammability (fire risk, particularly during the exothermic adsorption process)[61,69].

In addition to the above, the main limitation of AC usage is their regeneration process. Due to their carbonaceous structure, thermal regeneration in a gas stream containing oxygen is not suitable. The fixation of oxygen groups on its surface will reduce the pore volume, thus affecting the adsorption capacity afterward[70,71]. Normally, regeneration should cause the least damage possible to the material while maintaining most of the initial textural properties of the adsorbent, including the surface area and porosity.

Considering the strong adsorption force inside the micropores, chemical and/or thermal treatments can be used to eliminate the adsorbed compounds and regenerate the ACs.

Biochar

Biochar is a key member of the carbonaceous materials that can be used as sorbents. It is produced by slow pyrolysis of biomass in an anaerobic atmosphere at relatively low temperatures (< 700 °C). Biochar is considered a low-cost material and a very promising substitute for AC for the capture of atmospheric pollutants[72] due to the feedstock availability and the moderate pyrolytic conditions. The latter control the structural (surface area, pore size, and bulk properties) and molecular (carbonized or non-carbonized fractions) characteristics of the biochar[73]. Biochars can undergo physical or chemical activation in order to increase the surface area and, thus, the adsorption capacity of the sorbents. At high temperatures, physical activation takes place in the presence of oxidizing gases (steam, CO_2, air, *etc.*). Many authors have established that thermal activation under CO_2 atmosphere produces more microporous char, whereas steam favors the formation of mesopores[74,75]. Some authors clarified the efficacy of the structure-activity relationship on the adsorption capacity of VOCs. Their results show that the hierarchization and functionalization promoted the adsorption of phenol over biochars. The incorporation of a mesoporous network facilitated the intraparticle diffusion of the VOC and overcame the steric hindrance[76]. Han *et al.*, on the other hand, proved that biochar's adsorption capacity is related to the micropore volume[77]. Carbonization and chemical activation can be accomplished in one single process by treating biochar at 300-800 °C in the presence of activating agents such as acid, KOH, alkali, metal salt, *etc.*[78,79]. The choice of the pyrolysis temperature is also essential since it controls both the non-carbonized organic matter content and the surface morphology[80]. In general, the surface area increases with the increase of the pyrolysis temperature, favoring the adsorption capacity of the biochar[72].

Vikrant *et al.* evaluated the adsorption performances of 12 standard biochars made of six different raw materials (Miscanthus straw pellets, oil seed rape straw pellets, rice husk, sewage sludge, softwood pellets, and wheat straw pellets)[81]. Two temperatures were selected for the pyrolysis (500 and 700 °C). These non-activated adsorbents were tested against gaseous benzene, xylene, methylethylketone (MEK), and other VOCs. They reported that the preparation method can highly influence the structure morphology, especially the textural properties of the material[81]. Besides, it can also control the oxygenated groups, which are responsible for surface acidity and increasing the adsorption of hydrophilic VOCs[80]. According to Rawal *et al.*, the acidity and polarity (hydrophilic/hydrophobic) of the surface are determined by the surface oxygen- and nitrogen-containing functional groups of activated biochar[82], which present some distribution properties. Basic functional groups, including nitrogen, are usually found in micropores. However, oxygen-containing acidic (polar) groups are primarily present in meso/macropores, while oxygen-containing non-polar ones are broadly dispersed on the multilayer's surface[76]. Yang *et al.* revealed the increase of phenol adsorption over aminated materials, which shows the strong connection to the nitrogen-functional groups on the biochar's surface[83].

Zeolites

For many years, natural and synthetic zeolites have been the material of choice for various applications and industrial uses. Zeolites are crystalline alumino-silicates with a structural formula $M_{x/n}(AlO_2)_X(SiO_2)_y(H_2O)_Z$ (M: charge compensating cation). Their three-dimensional (3D) microporous structure is formed by a regular succession of TO_4 tetrahedra (SiO_4 or AlO_4^-) interconnected by oxygen atoms. These are considered primary building units (PBU) that lead first to the formation of secondary building units (SBU) and then to

composite building units (CBU). The crystalline structure of zeolite is therefore the result of the periodic assembly of CBU and SBU[84,85]. Zeolites are divided into four categories defined by the number of T atoms in the pore apertures:

• Small pore size zeolites: apertures with eight T-atoms, with pore diameters from 0.3 to 0.45 nm (LTA, CHA, GIS, *etc.*).

• Intermediate pore size zeolites: 10 T-atom apertures, with pore diameters between 0.45 and 0.6 nm (MFI, FER, MWW, *etc.*).

• Wide pore zeolites: 12 T-atom diameter pore size ranging from 0.6 to 0.8 nm (FAU, MOR, BEA*, *etc.*).

• Very large pore zeolites: apertures of ≥ 14 T atoms, with pore diameters ≥ 0.9 nm (CLO, VFI, AET, *etc.*).

Conventional zeolites are recognized for distinct properties, including their high surface area (up to 900 m^2/g), large pore volume (up to 0.5 cm^3/g), uniform pore size, high thermal stability (that can exceed 1000 °C), and low cost. Zeolites thus present remarkable adsorption capacity for a wide variety of VOCs. The influence of the channel size and pore structure was investigated in toluene adsorption for three hydrophobic zeolites (mordenite, ZSM-5, and faujasite). This study showed that toluene could be efficiently adsorbed by FAU zeolite. However, the adsorption capacity was reduced when ZSM-5 or MOR was used, indicating a fine relation between the molecular size of the VOC and the pore and channel structure[86]. In addition, Kim *et al.* carried out some experiments to study the adsorption behavior of mordenite and faujasite for VOCs[87]. They showed that mesopore volumes of zeolites played a key role in VOC adsorption by the faujasite zeolites (X and Y), whereas the adsorption performance of the mordenite was more related to its crystal structure. Aromatics (benzene, toluene, *etc.*) were more easily adsorbed into the faujasite structure than mordenite due to their large sizes. This was not the case for non-aromatic compounds (methanol, ethanol, *etc.*), where mordenite showed good adsorption capacity. In addition, the authors pointed out that the adsorption capacity did not seem to be linked to Si/Al ratio or acidic properties since the more performant catalyst in the mentioned work (HY901 and MS13X) consists of higher and lower Si/Al ratios and similar acid sites[87]. Those results do not concur with the study of Li *et al.* who found that increasing the Si/Al ratio helped increase the adsorption capacity of p-xylene over commercial zeolites by more than 25%[88].

The surface polarity of the zeolite is highly considered during the adsorption process since it controls the competition between water molecules and VOCs. Water will interact more with the hydrophilic framework of the zeolite compared to relatively hydrophobic VOCs. Research pointed out the efficacy of high-temperature hydrothermal treatment for hydrophobic zeolite synthesis. The nature of the cation was reported to influence the ease of this modification. For example, it has been observed that sodium ions stabilize the framework structure of NaY zeolite, thus influencing the rate of the dealumination process[89]. Researchers are showing more interest in the development of a hydrophobic adsorbent with rapid regeneration, with more advantages at an industrial scale. Lv *et al.* investigated the adsorption of VOC over hydrophobic AC combined with zeolite[90]. First, NaY zeolite underwent pretreatment (hydrothermal dealumination, acid treatment, and salinization) and was added physically to 30% of AC. The composite materials gained in adsorption capacity (from 46 to 97 mg/g) and regeneration rate. Therefore, complete regeneration was assured in 30 min under microwave irradiation. The fire-resistant characteristic of the zeolite permitted overcoming the flammability of AC along with the discharge[90]. As reported in many studies, the most effective way to improve the hydrophobicity of the zeolite is to increase Si/Al ratio by

removing Al or adding Si to the framework of the zeolite[91,92]. The more dealuminated the zeolite is, the more hydrophobic the sample will be. As reported in the literature, pressure swing, temperature swing, purge gas stripping, reactive regeneration, and microwave heating[91-93] have all been considered effective ways for zeolite regeneration.

Coupling adsorption and catalysis for VOC removal

Over the last decade, developments in the adsorption process have focused on the improvement of adsorbents (functionalization, hierarchization, *etc.*) as well as coupling the adsorptive removal with the catalytic oxidation. Adsorption and catalysis technologies are not very effective in removing VOCs present in low concentrations (< 100 ppm) in flue gas when used separately. Many hybrid systems based on the adsorption-catalysis pathway have been introduced to the industrial market in this context. Those original processes are based on selective adsorption of the pollutant coupled with a catalytic oxidation process. The first step of the process is the adsorption of the VOC on the surface of the adsorbent or the catalyst. In fact, the VOCs condense on the surface, and when most of the surface is saturated with VOCs, they start to desorb as part of the regeneration process of the material. Therefore, the molecular dissociation and surface diffusion ensure the contact between the active phase and the VOCs, which are oxidized and destroyed. The final elimination of the pollutant takes place during the regeneration stage of the adsorbent. During this stage, the high concentration of VOCs (> 1000 ppm) in the effluent allows the catalytic oxidation process to be used under optimal conditions. In bifunctional systems, the advantages of adsorption (high adsorption selectivity and large adsorption capability) and oxidation (complete and cost-effective decomposition) are combined in the hybrid adsorption-catalytic technology, which exhibits high adsorption capacity, catalytic activity, and selectivity to totally convert VOCs into H_2O and CO_2. These systems are provided as a new practical, efficient, and economical alternative to conventional VOC removal treatments. Small concentrations of VOCs in industrial emissions will thus be easier to control and treat.

In the following section, recent hybrid treatments at a laboratory scale are reviewed. Two approaches are considered: (1) adsorption is first carried out on an adsorbent followed by catalytic oxidation carried out on a catalyst; and (2) the same material is used successively as an adsorbent and as a catalyst at a higher temperature.

Sequential treatments

Sequential treatments are conventional techniques where the VOC is first captured by an adsorbent and then delivered to a reactor system for its catalytic oxidation. In this case, both parts are usually tested alone to determine their adsorption and catalytic activity. The bifunctional systems should aim for total oxidation of the adsorbed VOCs into CO_2 and H_2O while avoiding the formation of toxic by-products during the process. The preconcentration of VOCs on the adsorbent seems to be a potentially cost-effective way to reduce VOC emissions [Figure 8].

Guillemot *et al.* focused on the elimination of MEK via a bifunctional system based on adsorption and catalysis[94]. The experiment was done over HFAU-Pt/FAU systems, where the adsorbent (HFAU) and the catalyst (Pt/HFAU) were carried out in the same reactor, but in two different beds. The study revealed three essential points concerning this type of VOC removal system:

- The adsorbent should present a high catalytic adsorption capacity. However, the capacity before a breakthrough is a factor that needs to be taken into consideration, especially when the experiment will eventually be scaled up to an industrial level.

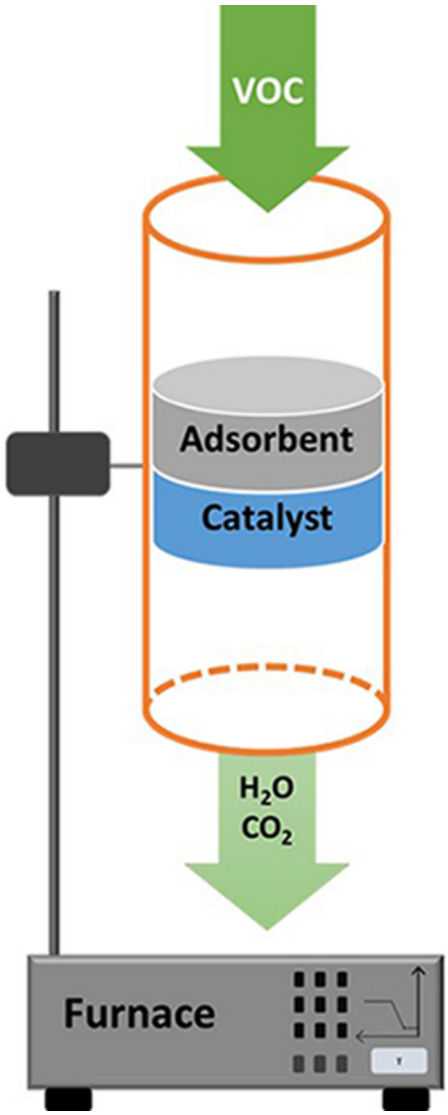

Figure 8. Experimental setup of sequential treatments of VOCs. VOCs: Volatile organic compounds.

• In industrial conditions, the inhibiting effect of water is highlighted; the competition between H_2O and the VOC causes a faster breakthrough, and the C/Co can be higher than 1.

• Coke formation is an important factor to consider since, depending on its nature, it can cause the deactivation of either the adsorbent (thus influencing its adsorption capacity by blocking the pores and adsorption sites) or the catalysts by deactivating the active phase and limiting the accessibility to them. As evidenced in the presented work, protonic zeolites are more likely to be deactivated via the formation of large molecules after isomerization reactions by hydrogen spillover. As for the catalyst, the rate of deactivation is related to its synthesis method and the dispersion of the metallic particles.

This hybrid system was stable for three adsorption-desorption cycles. The formation of carbon does not increase from one cycle to the next. Overall, 5.58 and 0.49 wt% of carbon were detected on the adsorbent and the catalysts, respectively. Therefore, it was presented as a promising system for the adsorption-catalysis approach.

Another heterogeneous catalytic system was studied by Urbutis *et al.* CuO-CeO_2/NaX was tested for the removal of toluene based on the recognized activity of copper and ceria oxides, also on the adsorption capacity of NaX zeolite materials[95]. The adsorption of the VOCs from the effluent gas flow was the initial step of the adsorption-catalysis process. Secondly, the desorption was induced with thermal treatment by increasing the temperature of the reactor. Carbon monoxide and benzene were detected during the oxidation but were totally converted into CO_2 and H_2O at higher temperatures (~250 °C). Urbutis *et al.* also investigated the influence of the operating parameters of this bifunctional system[95]. The efficiency of the system was related to the saturation level of $CuOCeO_2$/NaX (toluene conversion is reduced with a high saturation degree) and the flow rate of the regenerative air (longer contact time between the oxygen of the airflow and the catalytic system). The same tendency was demonstrated for another VOC: o-xylene. However, this study showed that higher temperatures are required to totally desorb this VOC. It is worth mentioning that benzene was not a by-product of this reaction. Finally, this dual system presents some complications that involve competing effects between the endothermic reaction of desorption and the exothermic reaction of the catalytic oxidation. Overall, the VOC is first adsorbed at room temperature into the internal surface of the material. A source of energy is then required to heat the catalytic bed to the catalytic temperature and ensure the desorption process of the adsorbed VOC[95]. Wang *et al.* reported that Ru loaded on hierarchical HZSM-5 zeolite may be a promising material for the removal of bulky VOCs such as toluene, o-xylene, and TMB[96]. A fine relationship between the textural properties and the catalytic ones was established. Depending on the type of VOC treated, the adsorption capacity of the hierarchical Ru/HZSM-5 samples was almost 2, 7.5, and 35 times higher after the incorporation of the mesoporous network into HZSM-5. The latter also improved the low-temperature reducibility of Ru, which enhanced its catalytic performance. The adsorption-catalysis process was held in two reactors. The Ru/HZSM-5 catalyst was first used as an adsorbent at room temperature. After the breakthrough, VOC flow was replaced by air while increasing the temperature to desorb the VOC. The desorbed species passed through a second reactor where the bifunctional catalyst was kept at 300 °C for the catalytic oxidation step. No by-products were noticed, and the carbon balance remained stable (> 95%) during three cycles. The test conditions allowed a self-regeneration of the hybrid system[96].

Nigar *et al.* compared the catalytic activity of a catalyst PtY placed in a single bed reactor to another combined system where a double fixed bed reactor was used[97]. In the double bed configuration, DAY zeolite was used for the adsorptive bed, while Pt/NaY zeolite was used for the single and double catalytic bed configurations. MW-assisted desorption was experienced. The microwave heating procedure helps produce a concentrated VOC flow that is then eliminated by catalytic oxidation. This approach is essential when the VOC emission sources contain only a few ppm of volatile compounds (< 1000 ppm). Once the MW is on, the catalytic bed is heated, promoting the adsorption of n-hexane on DAY. The authors established that the double bed configuration was very promising since only half of the catalytic load was used for approximately the same activity towards the total oxidation of n-hexane. To study the stability of this system, 11 cycles were achieved given almost total oxidation of n-hexane (99% conversion)[97].

Other alternative heating technologies were developed, showing even more interest in elaborating efficient systems with lower operating energy consumption. Desorption and regeneration processes can be established by thermal treatment. Depending on the thermal conductivity of the reactor, external heating might induce significant temperature gradients between the catalytic bed and the reactors walls. New regeneration-desorption methods are then introduced to the literature to overcome this drawback. They reflect the possibility of using techniques assisted by MW or other irradiations. Some authors proposed a new concept for hybrid bifunctional systems: adsorption and regeneration by catalytic oxidation-initiated selective dielectric heating. Radio-frequency energy was used during this experiment, studying NaY and

Pt/NaY zeolite-based materials for the total oxidation of toluene. The regeneration was ensured regularly with scheduled pulses (every 20 min). This continuous process ensures homogeneity of heating, leading to a sequence of purification phases of VOCs[98].

Successive adsorbent-catalytic systems

The combination of adsorption and catalysis processes in a single reactor has the advantage of increasing efficiency, improving catalyst productivity, and reducing capital investment and the need for external energy supply. The adsorbent is regenerated in an energy-supplied system by taking benefits of the exothermic nature of the oxidation reaction.

Hybrid systems based on successive adsorbent-catalytic systems occur in two steps [Figure 9]. First, the VOC flow is introduced into the reactor, where the bifunctional material is deposited. This is progressively saturated with VOCs. In the second step, the VOCs are desorbed during the regeneration process. An oxygen flow is sent to the reactor as a supply for the oxidation reactor or as a purge gas. The endothermic aspect of the desorption of VOCs is overcome by the heat and energy provided by its combustion. In some cases, the regeneration stream is heated upstream of the reactor, allowing the necessary heat transfer to initiate the destruction of the VOCs.

As reported in the literature, the adsorption capacity and the catalytic performance are directly related to the material in the first place. The adsorbent-catalyst configuration is recently being improved to obtain a higher surface area and a more porous network. Some authors focused their research on the configuration of monoliths, foams, honeycomb structures, laminate structures, *etc.* to favor the good dispersion of the active phases. Joung *et al.* worked on a novel Pt/carbon nanotube (CNT) for the catalytic oxidation of BTEX[99]. Based on the characterization techniques, they showed that the multi-walled carbon nanotube configuration resulted in not only a hydrophobic material but also a larger VOC adsorption surface. The material is therefore more convenient for industrial use, resistant to water vapor, and ensures strong adsorption of BTEX. The latter is oxidized by the active phase, which is very well dispersed on the support, thus also enhancing the catalytic performance of the material[99]. Hybrid systems consisting of nanogold/FeO_2 and nano-Au/CeO_2 supported on granular activated carbon were studied for the removal of toluene. These systems showed a good efficiency for this reaction (76%). The Mars Van Krevelen mechanism was used to explain the process and the different steps leading to the total oxidation of VOCs. First, the presence of metal oxides (FeO_2 and CeO_2) was proven responsible for the good dispersion of Au nanoparticles, which caused the weakening of the metal-O bonds. The active oxygen species (lattice oxygen) thus gained better mobility. In this study, the conversion of the support with and without the metal oxide was investigated to compare and determine the essential role of gold nanoparticles. Even though the granular activated carbon showed high adsorption capacity, no conversion at low temperatures of toluene was noticed for FeO_2/GAC or CeO_2/GAC. The oxidation starts only at higher temperatures of 175-480 °C. This was mainly related to the low mobility of oxygen species, thus influencing the reducibility of the active species. In addition, this study tested the efficiency of toluene removal as a function of the temperature. After 30 min at 75, 100, 125, 150, and 200 °C, a decrease in the adsorption capacity was noticeable. Kim *et al.* showed that the toluene desorption temperature is 150 °C, which explained why the hybrid systems tested were no more efficient at higher temperatures, with a decrease in the removal efficiency by 13%[100]. In fact, since the first step of the catalytic system is adsorption, the more the VOC is desorbed at reactive sites, the less is the conversion of toluene. In the fixed bed reactor used in this study, the toluene is adsorbed on two types of sites: (i) adsorption sites (which are first saturated); and (ii) catalytic sites[101].

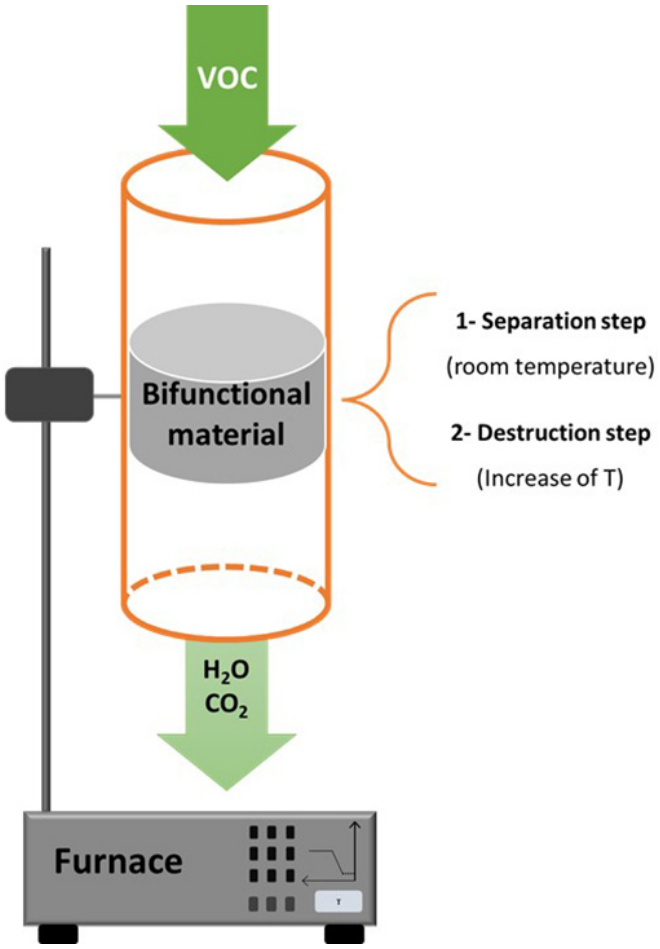

Figure 9. Experimental setup of successive adsorbent-catalytic systems.

The efficient performance of a zeolite-based catalyst is ensured by two essential factors: (i) the accessibility of active sites within the zeolite crystals; and (ii) the diffusion of reactants and products through the pores. The small pore sizes (< 2 nm) of microporous zeolites can inhibit the diffusion of molecules within the structure, implying a loss in adsorption and catalytic activity while increasing the possibility of deactivation by coking. This porosity limits the use of zeolites for large VOCs and explains why the use of carbonaceous adsorbents or polymers is sometimes favored for industrial applications. The latter present a broad range of pore sizes and are therefore more suitable for the adsorption of large VOCs.

The literature reveals the existence of several strategies for reducing the constraints on the transport of molecules within the zeolite structure. Modifying the porosity of the zeolite is one of the most interesting ways to overcome this major drawback by incorporating a new pore network with a different porosity range. Conventional microporous zeolites are now bi- or trimodal inorganic materials after what is called the "hierarchization process". Two approaches can be considered: (i) bottom-up modification via the addition of hard or soft templates during the hydrothermal synthesis of zeolite; and (ii) top-down modification that consists of post-synthetic treatments such as desilication, dealumination, acid washing, *etc.* Through this process, many authors revealed the importance of the dealumination. As zeolite is initially hydrophilic (having a high affinity to water and polar molecules), dealumination allows an increase in the hydrophobic character of zeolite by chemically replacing the Al with Si without modifying the zeolite

structure. Hierarchical zeolites showed interesting advantages as heterogeneous catalysts for the removal of VOCs due to the shorter diffusion path and the greater accessibility of the active sites compared to conventional zeolites. Research is underway to further exploit these advantages by developing bifunctional catalysts with high adsorption capacity as well as catalytic efficiency.

After acid and alkaline treatment, hierarchical mordenite was used as sorbent support for platina metallic particles. With a mesoporous volume of 0.16 cm^3/g and a pore size of 8.5 nm, these Pt/MOR catalysts showed interesting performance for toluene oxidation. The hierarchization favored the dispersion of the Pt particles on the support. The diffusion of toluene was eased, and its interaction with the Pt particles was favored. On the other hand, the improvement of the catalytic oxidation was also related to the medium adsorption strength and high adsorption capacity of the hierarchical mordenite. These two parameters play a key role in the diffusion of VOCs in the porous structure of the zeolite, particularly the internal one. The adsorption capacity was also compared to Pt/Al_2O_3, which revealed a peak at 700 °C in toluene adsorption-desorption profiles. This peak was assigned to strong adsorption strength and, thus, a delay in desorption and a more complicated regeneration. Using XPS analysis, it was demonstrated that the improvement of Pt dispersion on hierarchical mordenite led to an increase of the active oxygen species (an increase of O_{ads}/O_{lat})[102]. Yao *et al.* evaluated the catalytic performance of the Rh_1Cu_y/ZSM-5 materials with different copper content (y = 1, 3, 5, 10) for the total oxidation of toluene using a Langmuir-Hinshelwood model[103]. They found that the strong adsorption of the toluene on the support is crucial for a good catalytic performance. This study showed that 3 wt% of Cu was adequate content to obtain a performant bimetallic catalyst from a catalytic (50% of toluene was converted into CO_2 at 253 °C) or adsorption (higher adsorption capacity) point of view. First, this result was mainly related to the surface area of Rh_1Cu_3/ZSM-5, which promoted the toluene adsorption. It also relied on the better interactions between Rh and Cu oxides, leading to an increase in the chemisorbed oxygen species in the lattice layer of the catalyst. Based on the L-H model, the catalytic activity was then enhanced. The stability of Rh_1Cu_3/ZSM-5 was also studied and showed that it can be stable for 100 h, compared to monometallic catalysts or ZSM-5 alone[103]. Aziz *et al.* studied the impact of the synthesis method on the catalytic and absorptive capacity of Co supported on ZSM-5 materials[104]. Their adsorption-catalysis performance was tested for cyclic VOCs (BTEX) in air. The results show that, depending on the synthesis methods, the adsorption capacity was related to the micropore volume. However, the adsorption capacity is strongly related to the characteristics of the VOC such as molecular size and interaction with the surface depending on the groups attached to it[104]. Beauchet *et al.* showed that the catalytic performance followed the order: CsX > NaX > HY[105]. It appears that the conversion ratio of the VOC is strongly dependent on the acidic/basic sites of zeolite since better adsorption is detected for basic zeolites, which showed better catalytic conversion. It is also related to the functional group of the VOCs, which can control the strength of the adsorption. For example, unlike isopropanol, o-xylene does not possess a functional group, and thus, the adsorption capacity will be weaker[105]. Baek *et al.* studied a variety of transition metal catalysts (Ag, Mn, Co, Zn, Fe, Ni, and Cu) loaded on HY zeolite[106]. Ag/HY catalyst revealed the lowest temperatures for the total oxidation of toluene and MEK (310 and 310 °C, respectively). These results show another dual functional adsorbent/catalyst system for the reduction of VOCs at low concentrations[106].

Nevertheless, the hybrid system may risk deactivation due to the sintering of the metals at the high temperatures of the reaction. Therefore, some researchers are trying to fix the metals inside the framework of the zeolite in order to overcome this disadvantage that can influence the catalytic performance and the regeneration of the zeolite. The confinement of the metallic particles inside the zeolite' structure helps the size control and the active phase site adjustment[107]. For example, this sinter-resistance strategy was effective for the oxidation of toluene by Pt@ZSM-5 nanosheets. The support demonstrates good pore diffusion

properties related to its ultrashort diffusion path and rich interlayer mesopores, leading to higher adsorption capacity[108]. In fact, there are three typical ways of producing metal-containing zeolites[109]. First, a simple impregnation method is usually required for metal/zeolite preparation. During thermal treatments (calcination and reduction), metallic particles might migrate and tend to form aggregates and clusters. Conversely, the crystalline frameworks and the microporous network can produce strong confinement effects, limiting the sintering of the particles at higher temperatures in the case of metal@zeolite materials. However, the diffusion of the VOCs might be limited and the accessibility to the active phase will be affected. In this case, and depending on the type of the VOC, the shape selectivity of the zeolite will be highlighted. Finally, in metal-zeolite samples, metallic particles are incorporated into the framework of the zeolite as cations. After extraction and reduction procedures, the catalyst will turn into one of the forms mentioned above depending on the experimental conditions[109].

Chen *et al.* studied the total oxidation of toluene based on the adsorption-catalysis pathway. They worked on a series of Pt nanoparticles in the range between 1.3 and 2.3 nm on MFI zeolite. The best catalytic performance was evaluated depending on the highest Pt dispersion and the Pt^0 particles. Thus, it was concluded that 1.9Pt/MFI was the optimal bifunctional catalyst[110]. A bifunctional catalyst was developed on hierarchical silicalite-1 enveloping Pd-CeO_2 nanowires for the oxidation of propane. After a "one-pot two-step strategy", the synthesized materials appeared to have high catalytic activity, thermal/hydrothermal stability, and recyclability. The support trapped the low alkane VOC concentration at low temperature, and then the hydrocarbons were converted into CO_2 and H_2O via catalytic oxidation[111]. Mono- and bimetallic based in NaY or NaY_{nano} catalysts were tested for the total oxidation of ethyl acetate. The samples with different amounts of metal (Cu, Pd, Ag, and Zn) were prepared by ion exchange on both microporous and nanoporous NaY. The better catalytic performance was related to the surface area of the samples and the quantity of metals deposited[112].

Composite-based materials: Shi *et al.* compared the efficiency of noble metal catalysts (Ag/HZSM-5) and nonmetal catalysts (Ag-MnOx-CeO_2) for the removal of formaldehyde[113]. Both catalysts performed both HCHO adsorption and catalytic total oxidation into H_2O and CO_2. No by-product was detected. In this study, Ag-MnOx-CeO_2 was found to be more active for both functions since the mixed oxides ensured a better dispersion of the Ag clusters, inducing better redox properties of Ag. Interestingly, the presence of H_2O promoted the adsorption capacity of formaldehyde on mixed oxide-based samples contrary to the zeolitic one. In this case, water molecules competed with VOC for accessible actives sites[113]. Mixed metals oxides were studied for the total abatement of toluene by TiO_2/SiO_2 and ZrO_2/SiO_2 microporous-mesoporous systems. Ti-based catalysts showed more efficiency for this application due to their larger surface area and pore volume. The results were also related to the structural defects and hydroxyl groups. These materials displayed a higher adsorptive capacity (3.8 mmol/g compared to 2.9 mmol/g for Zr samples for 550 ppm of toluene at 25 °C) in a system where the flow was first adsorbed and concentrated at low temperatures (25 °C) and then oxidized at higher T (250 °C) given a conversion around 86%. This removal of VOCs was done on a lab-scale reactor where the catalytic bed is divided into two parts: an adsorptive part and an oxidizing part. First, the polluted air passes through the rector, where the VOCs are adsorbed on the material at room temperature. After that, the reactor is heated at higher temperatures (250 °C) to activate the catalytic phase of the materials. Thus, the adsorbed VOCs are destroyed and converted into H_2O and CO_2. It is also important to notice that no coke formation was noticed after the process[114].

PLASMA CATALYSIS COUPLING FOR VOC ABATEMENT

Plasma catalysis

NTP is a partially ionized gas consisting of ions, electrons, neutral species, and photons, where the electron temperature (10,000-250,000 K)[115] is orders of magnitude higher than the temperature of heavy constituents such as ions and neutral species[116]. Due to this non-equilibrium state, the overall temperature of NTP is maintained close to the ambient temperature, and there is no need to heat the entire treated gas[117]. Thus, a highly reactive environment is created without heating the entire gas as in the thermal process[118]. The accelerated energetic electrons generated in NTP collide with a carrier gas, which is predominantly air for environmental applications and generate highly reactive species, such as ground and excited atomic oxygen and nitrogen, and vibrationally and electronically excited oxygen and nitrogen molecules. These reactive species, in turn, react with the diluted VOCs and convert them into less toxic substances such as H_2O, CO_2, and other by-products. NTP contains a diverse mix of various ions and radicals, and, thus, it is difficult to control the reaction to produce a particular product with high yield and high selectivity. Although NTP has been proposed and investigated as an end-of-pipe technology for the removal of VOCs, NO_x, *etc.*[119], the formation of toxic by-products, poor energy efficiency (particularly for low VOC concentration), and mineralization efficiency still hinder the commercialization of this technique[120,121].

To overcome the above-mentioned shortcomings and to take advantage of individual techniques such as NTP (e.g., highly reactive environment and rapid ignition/response) and heterogeneous catalysis (e.g., improved product selectivity and total VOC oxidation)[122], researchers investigated plasma catalysis for air cleaning applications such as VOC abatement [Figure 10][123]. The main strength of plasma catalysis lies in the synergetic effect of the two individual technologies, which enhances the mineralization efficiency and reduces the formation of unwanted by-products and intermediates[124]. Several experimental investigations showed that plasma catalysis enhances CO_2 selectivity and energy efficiency, in particular for low VOC concentration[125,126]. In plasma catalysis, the catalytic materials are placed either within the plasma discharge [known as in-plasma catalysis (IPC) or single-stage plasma catalysis] or in the downstream of the plasma discharge [known as post-plasma catalysis (PPC) or two-stage plasma catalysis][127,128]. In the latter, the role of the NTP is to alter the gas composition and, thus, the reactants that encounter the catalyst surface. Therefore, the complexity of the underlying mechanism of PPC is much reduced and better understood when compared to the IPC process[129].

Despite various advantages of plasma catalysis over the individual techniques, several problems must be resolved before practical implementation, which mainly include the high energy consumption for treating low VOC concentrations and deposition of polymeric substance on the catalyst during VOC decomposition, which deteriorates the catalyst performance. This review addresses several key aspects of the plasma catalysis process such as the choice of catalysts suitable for NTP environment, simultaneous removal of various VOCs, energy saving process through cycle operation of adsorption and NTP discharge, long-term stability of catalyst in plasma catalysis, and *in situ* regeneration of the catalyst by NTP exposure.

Post-plasma catalysis

Several plasma process parameters, such as humidity level, initial VOC concentration, temperature, oxygen content, and gas flow rate, influence the abatement of the most common VOCs using the plasma catalysis system. In the following, we discuss the most important results and the influence of different operating parameters on the abatement processes of different VOCs for post-plasma catalytic systems.

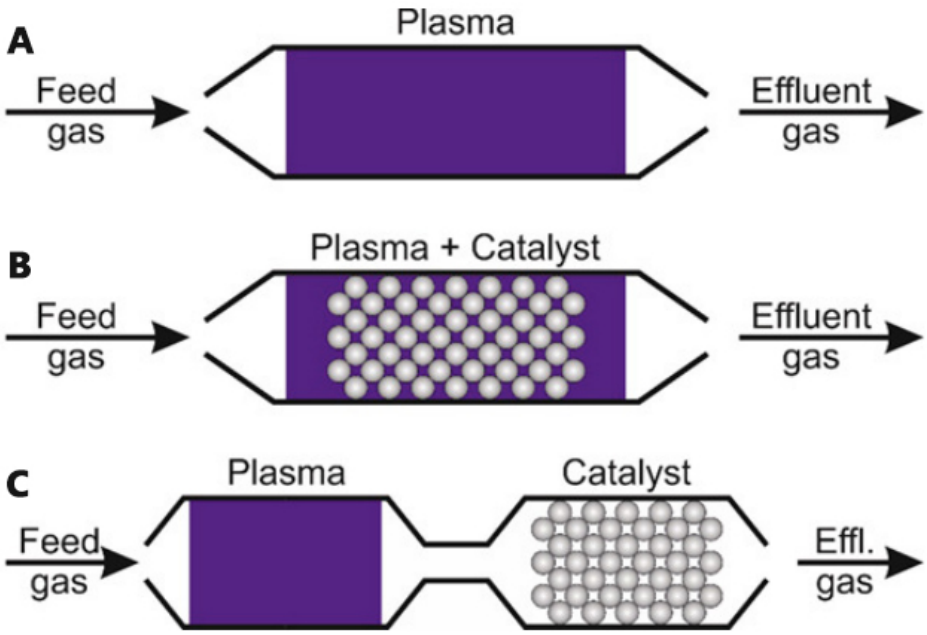

Figure 10. The schematic representation of plasma catalysis configurations: (A) NTP alone; (B) in-plasma catalysis; and (C) post-plasma catalysis. This figure is quoted with permission from Ollegott *et al.*[123]. NTP: Non-thermal plasma.

BTX compounds

Benzene, toluene, and xylene (BTX) are typical volatile organic compounds and are harmful to the environment and human health[130]. Therefore, the removal of BTX for the purification of indoor air and gaseous industrial streams is very important and necessary.

Toluene

Magureanu *et al.* investigated the toluene total oxidation in air in a plasma catalytic system formed by a dielectric barrier discharge (DBD) and Mn-based phosphate catalysts ($MnPO_4$, Mn-APO-5, and Mn-SAPO-1), tested at 400 °C and placed downstream the plasma reactor[131]. The initial concentration of toluene (560 ppm) was decomposed by reactions with oxygen on the catalyst surface under purely catalytic conditions at an energy density range of 900-2700. The toluene removal efficiencies reached using the PPC system and the catalysts $MnPO_4$, Mn-APO-5, and Mn-SAPO-1 were 70%, 65%, and 70%, respectively. The maximum CO_2 yield (33%) was obtained at 400 °C using Mn-SAPO in the PPC system.

A combination of photocatalyst with NTP was carried out by Huang *et al.*[132]. The experimental results show that the toluene removal efficiency was proportional to the ozone consumption rate in the PPC system, in which catalytic ozonation played a vital role in toluene decomposition. The dominant active species in the combined system are active oxygen species generated from ozone catalytic decomposition. Huang *et al.* showed that the toluene removal efficiency was increased by 35% and the ozone concentration present at the outlet was reduced by 70% in the PPC system, compared with the results obtained in the plasma-alone system[132].

In addition, a system combining a DBD reactor with $MnO_2Co_3O_4$ catalysts was developed and tested by Chang *et al.* to decompose toluene and minimize unnecessary reaction products [Figure 11][124]. Catalyst characterization indicated that the Mn/Co molar ratio remarkably affected the crystal structures, physico-

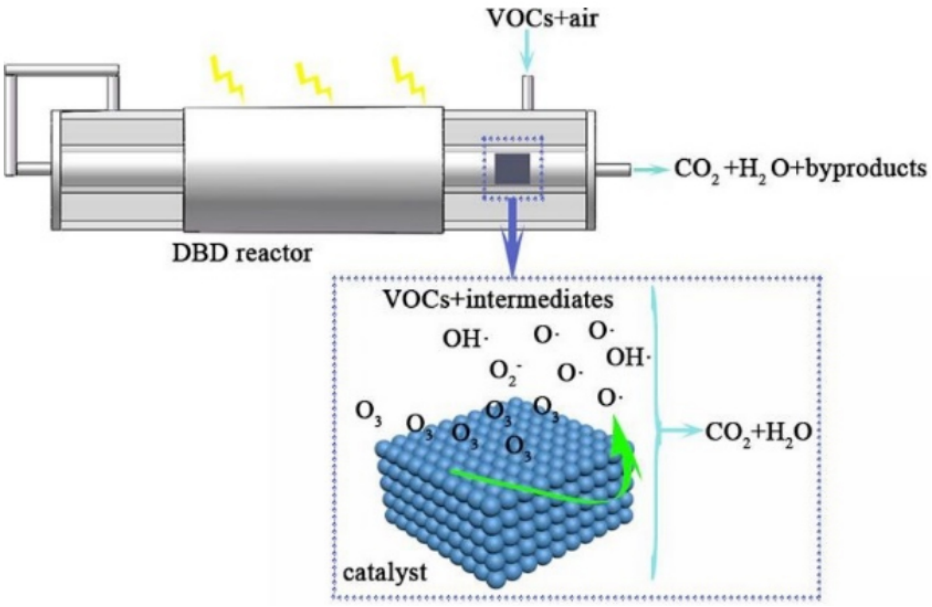

Figure 11. Schematic representation of the post-plasma catalytic system developed by Chang *et al.*[124].

chemical properties of the catalyst, and subsequently influenced their catalytic activity. In particular, in the PPC system over Mn_1Co_1 catalyst, the toluene removal efficiency, energy yield, CO_x yield, and CO_2 yield were increased by 26.77%, 1.76 g kWh^{-1}, 25.65%, and 21.07%, respectively, compared with that in the plasma-alone system at specific energy densities of 423.58, 92.59, 456.76, and 456.76 J/L, respectively. It was shown that the synergistic effect of the Mn and Co species was the main factor in accelerating the production and transmission of active oxygen species, which in turn were responsible for the oxidation of toluene.

A similar plasma reactor system was developed by Tang *et al.* to investigate the toluene decomposition in air at atmospheric pressure[126]. Three Ag-based composite oxide catalysts, located downstream the DBD reactor, were used to recycle O radicals for the ozone decomposition and certainly the VOC decomposition. Tang *et al.* found that the toluene removal efficiencies were about 62% and 100% in the plasma-alone and PPC systems, respectively, at a specific energy density of 60 J/L[126]. In terms of ozone and/or toluene decomposition, the efficiencies of the three catalysts were in the order of: Ag-Mn-O > Ag-Co-O > Ag-Ce-O. Moreover, the Ag-Mn-O catalyst showed very good stability at room temperature.

Subrahmanyam *et al.* used a DBD system for the abatement of toluene by modifying a sintered metal fiber (SMF) filter, which acts as an inner electrode, with Mn and Co oxides[133]. Several parameters such as the VOC concentration, input energy, and the SMF modification were investigated. Figure 12 presents the influence of SMF modification and energy density on the conversion of 100 ppm of toluene. At an energy density of 235 J/L, nearly 100% conversion was achieved with both MnO_x/SMF and CoO_x/SMF. It was also observed that SMF modification with Mn and Co oxides enabled an increase in the total oxidation selectivity. All the catalytic electrodes were able to keep the same activity during almost 3 h of toluene decomposition. This result confirms that the electrodes maintained their stability during toluene destruction.

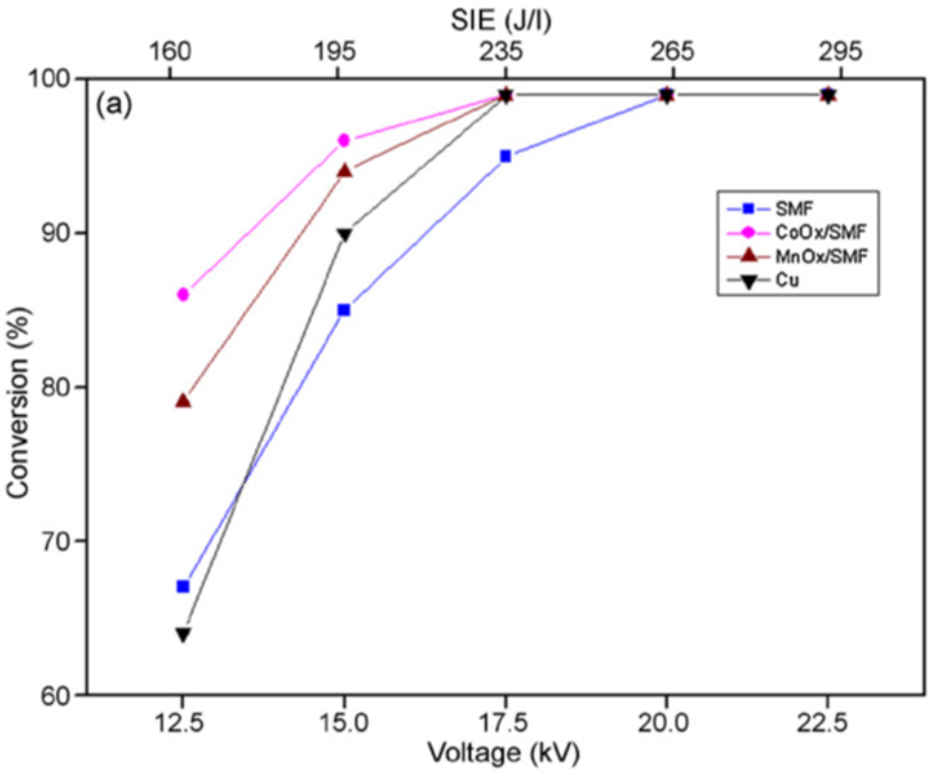

Figure 12. Influence of SMF modification and energy density on the conversion of 100 ppm toluene[133]. SMF: Sintered metal fiber.

In another study, Van Durme *et al.* used several catalysts that were tested downstream of a DC corona discharge[134]. In particular, the effect of relative humidity (RH) was investigated on both ozone and toluene removal. With Pd/Al_2O_3 catalyst, it was shown that toluene removal efficiency was about > 90% and 37% in dry air and air with 74% RH (25 °C), respectively. This proved that the PPC system is less efficient when the relative humidity increases. The negative humidity effect was mostly attributed to changing van der Waals interactions.

Because extensive papers have been published on the post-plasma catalytic abatement of toluene, only a summarized discussion is given on selected papers. Several other studies that represent the abatement of toluene using a DBD reactor and a corona discharge system are not discussed in detail but are summarized in Tables 7 and 8, respectively.

Benzene

Ge *et al.* compared a DC corona discharge system and a combined plasma-MnO_2 catalytic (CPMC) air cleaner for the removal of low-concentration benzene in air[145]. The catalyst MnO_2 was located downstream of the discharge reactor for both systems. The effects of discharge power and *RH* on benzene removal efficiency were investigated in a closed chamber. It was found that the benzene removal efficiency increased with discharge power in both systems by fixing the initial benzene concentration at 150 ppm. Moreover, with the increase of *RH* up to 20% in air, benzene removal efficiency firstly increased and then decreased in NTP, while it gradually decreased in CPMC.

Table 7. Overview of published papers on toluene removal using catalysts placed downstream a DBD plasma reactor

Authors	Catalyst	T_{cata} (°C)	Carrier gas	Flow rate (mL/min)	Concentration range (ppm)	Maximum removal efficiency (%)	Energy density (J/L)
Hayashi *et al.*[135]	Fe_2O_3/MnO honeycomb	20	Dry air	2500	85	65	72
Ban *et al.*[136]	Ti-MPS Mn (5 wt%)-Ti-MPS Mn (10 wt%)-Ti-MPS	-	Air	200	1000	45 58 75	300
Burton *et al.*[137]	TiO_2/Al_2O_3/Ni foam	-	Dry air	200	50	95	900
Harling *et al.*[138]	MnO_2 MnO_2-CuO	-	Air	10^4	70	> 99 > 99	 340
Delagrange *et al.*[139]	N150 (MnO_2-Fe_2O_3) Al_2O_3 MnO_2 (9 wt%)/Al_2O_3 Activated carbon (AC) MnO_2 (3 wt%)/AC	-	Air	588	240	76 74 88 98.5 99.7	172
Demidyuk *et al.*[140]	Al_2O_3 Ag_2O (7 wt%)/Al_2O_3 MnO_2 (7 wt%)/Al_2O_3	425 300 330	Dry air	1000	500	78 > 99 > 99	60
Harling *et al.*[141]	TiO_2 Al_2O_3 Ag (0.5 wt%)/TiO_2 Ag (0.5 wt%)/Al_2O_3	600	Dry air	1000	500	95 > 99 95-99 99	60

Table 8. Overview of published papers on toluene removal using catalysts placed downstream a corona discharge plasma reactor

Authors	Catalyst	T_{cata} (°C)	Carrier gas	Flow rate (mL/min)	Concentration range (ppm)	Maximum removal efficiency (%)	Energy density (J/L)
Demidiouk *et al.*[142]	Pt-honeycomb	240	Air	2×10^4	330	90-95	142
Li *et al.*[143]	TiO_2	-	Air	1000	80-100	70	330
Van Durme *et al.*[144]	$CuOMnO_2/TiO_2$	20	Dry Air	10^4	0.5	78	2.5
Van Durme *et al.*[134]	Cu-Mn/TiO_2 (a) N140 N150 Pd (0.5 wt%)/Al_2O_3 Cu-Mn/TiO_2 (b)	20	Air (50%RH)	10^4	0.5	40 47 34 47 62	14 16 16 10 20

In another study, Jiang *et al.* combined the use of alumina-supported catalysts with a surface/packed-bed hybrid discharge reactor to degrade an initial benzene concentration of 370 mg/m^3[146]. The catalysts used were γ-Al_2O_3 supported MO_x (M = Ag, Mn, Cu, or Fe) with varying the M loading amount. The results show that the benzene degradation was enhanced and the mineralization process was strongly improved towards total oxidation when combining the plasma reactor with all MO_x/γ-Al_2O_3 catalysts. In particular, AgO_x/γ-Al_2O_3 exhibited the best catalytic activity in benzene degradation of the catalysts in the PPC system. The highest benzene degradation efficiency of 96% and CO_x selectivity of 99% were obtained for the AgO_x/γ-Al_2O_3 catalyst with an optimum Ag loading amount of 15%.

Hu *et al.* developed a bipolar pulsed series surface/packed-bed discharge (SSPBD) reactor[147]. TiO_2/zeolite, MnO_2/zeolite, and MnO_2-TiO_2/zeolite catalysts, located downstream of the plasma reactor at room temperature, were tested separately for the degradation of benzene. The highest benzene degradation efficiency of 83.7% and CO_2 selectivity of 68.1% were obtained by the MnO_2-TiO_2/zeolite at 10.33 W, which were 4.9% and 5.6% higher than TiO_2/zeolite. It could be attributed to the incorporation of Mn into TiO_2 catalyst, which was ascribed to the charge transfer between Ti^{4+} and Mn^{4+} on the surface of MnO_2-TiO_2

/zeolite catalyst enabling the formation of hydroxyl radicals. In addition, MnO_2-TiO_2/zeolite presented a better performance in ozone suppression than TiO_2/zeolite, which was mainly due to the strong ozone decomposing ability of MnO_2.

Xylene

Extensive studies have shown that the manganese oxide (MnO_x) catalyst, one of the most noticeable transition metal oxides, is the most appropriate catalyst for the conversion of ozone to atomic oxide species and promotes oxidation of VOCs with atomic oxide. This fact was demonstrated by Zhang *et al.* in performing xylene oxidation degradation in a PPC system[148]. A double plate dielectric barrier discharge (DPDBD) reactor was used in dry air at room temperature. The MnO_x catalysts were prepared using three different precursors: manganese nitrate (MN), manganese acetate (MA), and manganese sulfate (MS). Zhang *et al.* showed that MnO_x (MN) had excellent performance with strong capacity in xylene oxidation (94.1%), CO_2 selectivity (80.1%), O_3 suppression (76.4%), and NO_2 prohibition (78.5%) compared to MnO_x (MA) and MnO_x(MS)[148]. The anions present in the precursors had an important role in the distribution of the MnO_x material on the support, which explained the excellent catalytic activity of the catalysts.

In a comparable study, Wang *et al.* introduced Mn/Al_2O_3 catalysts downstream of the discharge zone of a DBD reactor for the removal of o-xylene[149]. The catalysts were prepared with different precursors: manganese acetate, manganese chloride (MC), manganese sulfate, or manganese nitrate precursor solutions. They showed that o-xylene conversion was significantly increased with the addition of Mn/Al_2O_3 catalysts even at 0.2 J/L, which constitutes a very low specific energy density (SED). Among the different prepared catalysts, Mn/Al_2O_3-MA exhibited the highest catalytic activity for o-xylene removal. In particular, 6 wt% Mn loading was the optimum condition for the preparation of catalysts for high o-xylene conversion, as shown in Figure 13.

Furthermore, Piroi *et al.* investigated the decomposition of p-xylene by placing AlAg catalysts in a catalytic reactor heated up 500 °C, located downstream a DBD plasma reactor[150]. In a plasma-alone system, the conversion of p-xylene increased with increasing the specific input energy (SIE), ranging between 24% and 66% for SED between of 72 and 264 J/L, respectively. Moreover, the CO_2 selectivity was below 45% for all applied SED. Under a purely catalytic system, the catalyst started to be active and allowed a conversion of 11% when reaching 500 °C. In the case of the PPC system, the p-xylene conversion efficiency was not significantly altered, although the selectivity towards CO_2 was significantly improved compared to the results obtained with plasma alone. In addition, Piroi *et al.* demonstrated the importance of the catalyst temperature which has a remarkable influence on the CO_2 selectivity as well. Above 300 °C the CO_2 selectivity reached 65%-70%[150].

Another important study is related to the removal of low-concentration BTX (a mixture of benzene, toluene, and *p*-xylene; 1.0-1.5 ppm of each compound) in air. Fan *et al.* developed a plasma-catalytic system by introducing MnO_x/Al_2O_3 catalyst after the discharge zone of a link tooth wheel-cylinder plasma reactor[151]. They showed the conversion of benzene, toluene, and *p*-xylene reached 94%, 97%, and 95%, respectively, at a SIE of 10 J/L. In addition, this PPC system allowed a reduction in the emission of O_3 and NO_2 as compared to the plasma-alone system. For instance, the O_3 outlet concentration decreased from 46.7 ppm for plasma-alone to 1.9 ppm for PPC, while the NO_2 emission correspondingly decreased from 1380 to 40 ppb.

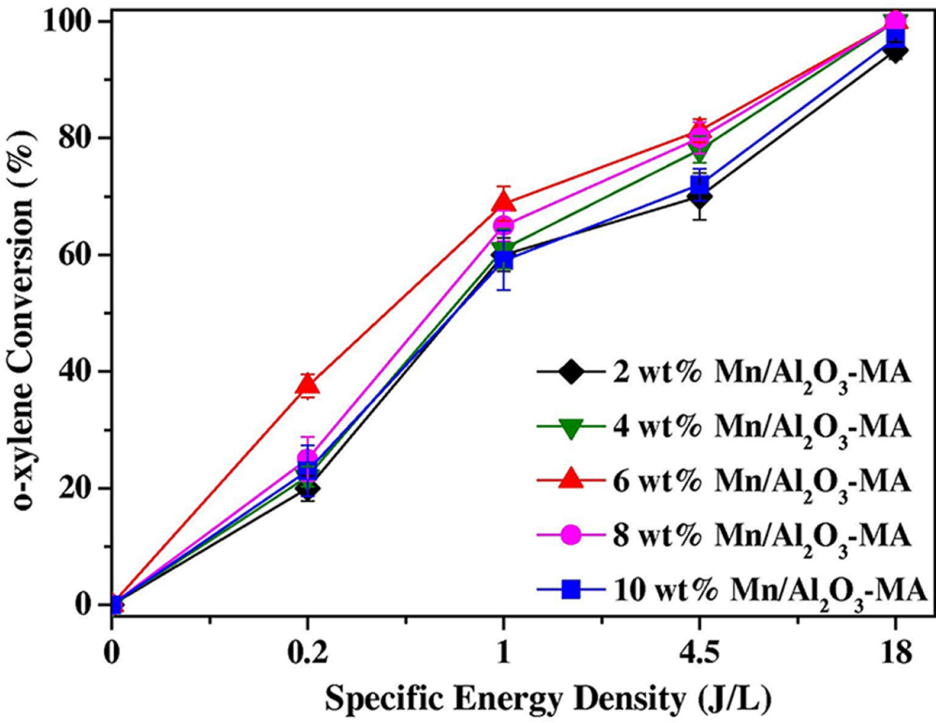

Figure 13. Effects of loading amounts of Mn/Al_2O_3-MA on o-xylene conversion[149].

Trichloroethylene

Oda *et al.* developed a PPC system using manganese oxide (MnO_2) as a catalyst in direct (contaminated air is directly processed by the plasma) and indirect processes (plasma processed clean air is mixed with the contaminated air)[152]. It was shown that MnO_2 catalyst was very efficient in enhancing the decomposition efficiency for both processes. For instance, when using 100 ppm as the initial TCE concentration, more than 99% of this VOC was decomposed at the discharge power of 0.5 W for both processes. The catalyst's effectiveness in dissociating ozone generated enough oxygen radicals, which are strong oxidizers for TCE removal.

In addition, Han *et al.* examined the effect of manganese dioxide on the TCE removal in similar direct and indirect processes[153] as the ones used by Oda *et al.*[152]. For the direct process, the decomposition efficiency was enhanced to about 99% at 40 J/L with passing through the catalyst. This was because the oxygen species, which were generated from collisions between excited species/electrons with O_2, mainly oxidized TCE into DCAC. In addition, further oxygen species were produced during the ozone degradation at the surface of the catalyst, which led to the oxidation of the remaining TCE into trichloroacetaldehyde (CCl_3-CHO, TCAA). It was also obtained that the CO_x yield increased from 15% to 35% at 120 J/L when MnO_2 was present. When the energy density was raised to 400 J/L, a CO_x yield of 98% was established. For the indirect process, similar conclusions were obtained, although the CO_x yield was lower than for the direct process.

Magureanu *et al.* tested the oxidation of TCE using a plasma-catalytic DBD in the absence and presence of gold nanoparticles embedded in mesoporous silica catalysts[154]. The catalyst with the least amount of Au (0.5 wt.%) showed the most efficiency in TCE oxidation (> 99%) and the increase in the CO_x selectivity at 670 J/L. As for MnO_2, the Au/SBA-15 was able to dissociate the ozone generated by plasma to oxygen radicals that decompose TCE. It was also shown that the isolated gold cations were the active sites that

explained the catalytic behavior.

In a study conducted by Vandenbroucke *et al.*, a DC multi-pin-to-plate corona/glow discharge reactor was used[155]. The catalyst Pd/γ-Al_2O_3, located downstream of the plasma reactor, was set at 100 °C. The maximal removal efficiency obtained was 80% at an ED of 300 J/L and an initial TCE concentration of 600-700 ppm. The combination of plasma with a post-plasma catalyst clearly showed synergetic effects for the removal of TCE.

A similar DC glow discharge was also tested by Sultana *et al.*[127]. Fe-doped manganese oxide octahedral molecular sieves (referred to as K-OMS-2) of the cryptomelane-type structure were located downstream of the plasma reactor. It was found that both TCE conversion and CO_2 yield globally increased as a function of ED. Fe-K-OMS-2 showed better performance for TCE removal in moist air in comparison to the iron-free manganese oxide octahedral sieve (K-OMS-2). This result was attributed to high surface oxygen mobility and an increase of structural defects resulting from improved textural properties of the Fe-K-OMS-2 catalyst. These characteristics were responsible for enhancing O_3 decomposition and TCE catalytic total oxidation efficiencies. Sultana *et al.* also investigated the influence of ceria catalyst on the abatement of TCE using the same PPC reactor configuration[127]. CeO_2 is known as a catalyst with unique properties such as a higher oxygen storage/transport capacity. Moreover, it has a good ability to shift between reduced and oxidized states (Ce^{3+} to Ce^{4+}), enabling an increase in oxygen vacancies and subsequently contributing to the enhancement of the catalytic activity. When using the catalyst-alone system at high temperatures, the maximum TCE removal efficiency reached 90% at 550 °C. Meanwhile, the CO_x selectivity reached a plateau (87%) at 450 °C. These results confirm the importance of high temperature in achieving both high TCE abatement and selectivity. However, in the PPC system, the TCE removal efficiency increased by around 10% (90%) at 100 °C catalyst temperature compared to the plasma-alone system (79.6%). Hence, the PPC system process had a great capability as abatement technology for low concentrated TCE air streams at a lower energy cost. An overview of several studies on TCE abatement using a PPC system is presented in Table 9.

Formaldehyde-acetaldehyde

Li *et al.* developed a PPC system by combining a DBD reactor and MnO_2 catalysts with different phase structures for acetaldehyde degradation[159]. With the introduction of α-MnO_2/Al_2O_3, the acetaldehyde removal efficiency was the highest (84.1%), which means that this catalyst exhibited the best catalytic activity among the different types of MnO_2/Al_2O_3 catalysts. This is due to the existence of OH groups, higher VOC adsorption capacity, and higher mobility of oxygen in the sample. In parallel to the PPC test for acetaldehyde removal, the degradation of benzene was also tested using similar catalysts. A lower removal efficiency, lower production of NO_x, and more residual ozone were obtained.

In another study performed by Li *et al.*, other types of catalysts were located downstream of the DBD reactor to study the acetaldehyde decomposition process[160]. Metal ion-modified cryptomelane-type manganese oxide octahedral molecular sieves M′-OMS-2 (M′ = Co, Ce, Cu) supported on alumina were selected for their study due to: (i) the excellent properties of the cryptomelane in catalysis reaction and easy release of lattice oxygen; and (ii) the positive effect of the metal ions on the cryptomelane catalytic activity. They showed removal efficiencies of 94.8%, 87.7%, 79.6%, and 50.2% for Cu-OMS-2/Al_2O_3, Ce-OMS-2/Al_2O_3, K-OMS-2/Al_2O_3, and plasma-alone, respectively, at 15.2 kV. However, a total degradation of acetaldehyde was obtained when using Co-OMS-2/Al_2O_3 catalyst in the PPC system and under the same conditions. This can be ascribed to more substitution of manganese by cobalt on the catalyst's surface.

Table 9. Overview of published papers on TCE removal using PPC reactors

Authors	Plasma reactor	Catalyst	T_{cata} (°C)	Carrier gas	Flow rate (mL/min)	Concentration range (ppm)	Maximum removal efficiency (%)	Energy density (J/L)
Han *et al.*[156]	DBD	MnO_2	20	Air	500	250	95-99	240
Vandenbroucke *et al.*[155]	DC negative glow discharge	Pd (0.05 wt%)/Al_2O_3	100	Humid air	2000	600-700	80	300
Vandenbroucke *et al.*[157]	DC negative glow discharge	MnO_2	300	Dry air	500	500	90	240
Nguyen Dinh *et al.*[158]	DC negative glow discharge	$LaMnO_3^{+}{}_{\delta}$	150	Humid air	500	510	93	460

Chang *et al.* investigated the formaldehyde degradation in a PPC system over a series of MnO_x-Fe_2O_3 catalysts located downstream of a DBD plasma reactor[161]. The influence of several working parameters such as gas flow rate, discharge power, and the molar ratio of Fe/Mn on formaldehyde removal were investigated using a response surface methodology (RSM). They showed that the optimal process operating conditions (discharge power of 5 W, gas flow rate of 0.5 L/min, and the molar ratio of Fe/Mn of 0.71) can be selected to reach the optimum formaldehyde removal efficiency (95.01%) and CO_2 selectivity (86.20%). Hence, this study confirmed that RSM is an effective tool to enhance the performance of the PPC working parameters.

Methanol

Zhu *et al.* developed a PPC reactor for the abatement of methanol over Mn-Ce oxide catalysts with different Mn/Ce molar ratios at low temperatures[162]. The main results show that the catalyst with Mn/Ce ratio of 1:1 had the best catalytic activity in the decomposition of the methanol and led to the highest energy efficiency of the plasma-catalytic process. The use of the $Mn_{50}Ce_{50}$ oxide catalyst located downstream of the DBD plasma reactor resulted in a methanol removal efficiency of 95.4% at 15 W and a gas flow rate of 1 L/min. In addition, the highest energy efficiency of the plasma-catalytic process was 47.5 g/kWh at 1.9 W.

Moreover, Norsic *et al.* investigated the decomposition of methanol at low concentration (25-150 ppm) using an NTP reactor coupled with different metal oxide based catalysts (MnO_2, CeO_2, CuO, MnO_2-CeO_2, and MnO_2-CuO supported on Al_2O_3)[163]. They showed the effectiveness of bi-metallic oxides of $MnO_2/CeO_2/Al_2O_3$ and $MnO_2/CuO/Al_2O_3$ in terms of methanol conversion, carbon oxides selectivity, and ozone utilization. In particular, for an initial concentration of methanol of 50 ppm, 4 g of $MnO_2/CeO_2/Al_2O_3$ coupled to the DBD plasma reactor were needed to result in 100% methanol conversion with 48% and 52% selectivity to CO and CO_2, respectively.

In-plasma catalysis

An overview of the published work on IPC abatement of VOCs is given in Table 10. From the Table 10, it can be concluded that dielectric barrier discharge (DBD) is one of the widely investigated NTP reactor configurations for IPC, where at least one insulating layer is present between the high voltage (discharge) electrode and ground electrode[184]. When the voltage applied across the discharge gap exceeds the breakdown voltage, numerous microdischarges occur. The presence of the dielectric barrier limits the amount of energy and charge imparted to every microdischarge, resulting in the distribution of microdischarge over the entire electrode, which makes the DBD reactor suitable for applications such as O_3 generation and air cleaning[185]. In the DBD reactor, the catalyst is usually introduced as a packed bed in the form of pellets[186], powder[187], granules, or fibers. The presence of packing material in the discharge gap enhances the electric field near their contact points, increases the VOC residence time, and reduces the plasma volume, resulting in better VOC removal efficiency. The physical properties of the packing material,

Table 10. Overview of published work on IPC for VOC abatement

VOC	Reactor	Catalyst	Carrier gas	Flow rate (L/min)	VOC_{in} (ppm)	η_r (%)	S_{CO_x} (%)	By-products	Ref.
Benzene	DBD	TiO_2/MnO_x/SMF	Air	0.5	1000	70	30	-	[164]
	DBD	MnO_x	Air	0.1	200	100	50	-	[165]
	Corona	CuO/AC	Humid air (50%)	16.7	200	90	-	C_6H_5OH, $C_6H_6O_2$, $C_6H_5NO_3$	[166]
	HSPBD	Ag-Ce/γ-Al_2O_3	Air	0.5	400	80	60	O_3, NO_2	[167]
Toluene	DBD	Nb_2O_5	Air	0.067	800	96	-	NO_x	[118]
		1w% Au/Al_2O_3							
	DBD	Au/CeO/Al_2O_3	Air	0.2	100	100	90	O_3, N_2O, N_2O_5	[168]
	DBD	NiO-TiO_2	Dry air	0.1	40	96	70	-	[169]
			Humid air (5 vol%)			47.6	-		
	DBD	Ca-Ni/ZSM-5	Air	0.1	100	90	70	N_2O, O_3 HCOOH	[170]
	DBD	CeO_2/γ-Al_2O_3 @ 200 °C	Humid air (1 vol%)	0.5	0.87 g/m^3	80	> 60	C_6H_5CHO, C_6H_5OH, C_7H_8O	[171]
	DBD	5% Ni/γ-Al_2O_3	Air	0.1	160	89	-	-	[172]
	DBD	CeO_2-MnO_2	Air	0.25	1500	96	91	Organic compound	[173]
	DBD	Ag/ZSM-5	Air	1	150	96	100	O_3, N_2O	[174]
	DBD	60Co/MCM-41	Air	0.2	100	100	80	O_3	[175]
Xylene	DBD	Mn/γ-Al_2O_3	Air	2	500	82	41	-	[176]
	DBD	Pd-OMS-2/γ-Al_2O_3	Air	6	9	100	60	HCOOH, CH_3CHO	[177]
	DBD	Mn/Al_2O_3	Air	-	200	95	13	C_8H_8O, $C_8H_{10}O$, O_3	[178]
Formaldehyde	DBD	Cu1-Ce1	Air	1	57.7	95	> 95	-	[179]
	DBD	8000 ppm $NaNO_2$ /RR	Air	8.5	50 mg/m^3	90	-	CH_3OH	[180]
		Ag/CeO_2	Humid air (1% H_2O)	0.6	276	99	86	-	[181]
Acetaldehyde	DBD	Au NP/TiO_2/SiO_2	Air	0.1	1000	70	-	-	[182]
	DBD	Ag/TiO_2/SiO_2	Air	0.1	1000	98	-	CH_4COO, CH_3NO_2, CH_3OH, C_2H_6CO	[183]

such as the dielectric constant, shape, and size, play an important role in determining the discharge characteristics of the packed bed dielectric barrier discharge (PBDBD) reactor.

There are many reviews focused on in-plasma catalytic removal of VOCs[188-193]. Recently, Li *et al.* wrote a comprehensive review on the use of DBD reactors for VOC abatement[194]. Therefore, this section only gives an account of work that has been carried out in the past five years.

Reactor structure

New configurations of discharge electrode materials such as iron oxide and metallic nanowire/multi-walled carbon nanotubes/sponge have been investigated for phenol degradation. The results show that this novel electrode configuration has high discharge efficiency and lower energy consumption[195]. The performance of the PBDBD reactors can be influenced by the thickness of the dielectric barrier. Mei *et al.* investigated the effect of dielectric barrier thickness (1.5, 2.0, and 2.5 mm) on CO_2 conversion and reported that the conversion and energy efficiency were reduced by ~15% for a fixed SIE (120 kJ/L)[196]. In this study, when the dielectric barrier thickness increased, the plasma volume and the residence time decreased, resulting in reduced conversion efficiency. Moreover, the charge transfer efficiency was decreased by 19% with the increase in thickness from 1.5 to 2.5 mm. Although AC power supply has been widely used for economic

reasons, in the past few years, some experimental works also focused on using bipolar pulse power supply to power DBD reactors. The discharge current and, thus, the power deposition is higher for the pulsed power supply when compared to AC power supply for similarly applied voltage[197]. In addition to the applied voltage and frequency, for the pulsed power supply, pulse rise time, pulse-forming capacitance, and pulsed modes also affect the discharge characteristics. Jiang *et al.* reported that toluene conversion efficiency and energy efficiency reduce with an increase in the pulse forming capacitance[198]. This is due to the fact that the charge transfer efficiency is closely related to the pulse forming capacitance. The systematic study on the effect of the pulse mode on toluene degradation revealed that the removal efficiency and energy yield increase in the following order: – pulse < + pulse < ± pulse[199].

Packing material

Another interesting observation that has been made by researchers in the past few years is that higher specific surface area is not the only property of the packing material required for improving VOC removal efficiency and mineralization efficiency. Li *et al.* investigated the removal of toluene using ZSM-5 (S_{BET} = 306 m^2/g) and γ-Al_2O_3(S_{BET} = 175 m^2/g) and reported that the mineralization rate of γ-Al_2O_3 PBDBD reactor is higher[200]. This is due to the better discharge characteristics of γ-Al_2O_3 due to its higher dielectric constant. Wang *et al.* investigated different polymorphs of MnO_2 (such as α-MnO_2, β-MnO_2, γ-MnO_2, and δ-MnO_2) and reported that α-MnO_2 has better catalytic activity for toluene degradation, even though its specific surface area is lower than γ-MnO_2[201]. Among the four polymorphs under investigation, α-MnO_2 possesses a double-tunneled structure, the most stable crystal phase, the weakest Mn-O bond strength, and a larger content of surface-adsorbed oxygen. Thus, other surface and bulk properties of the packing material, such as dielectric constant and phase structure, are also important in addition to the large specific surface area for the plasma catalytic oxidation of VOCs.

Removal of VOC mixtures

Recently, Liu *et al.* investigated the simultaneous removal of co-existing VOCs in industrial exhaust (such as styrene and toluene) and reported that the presence of styrene inhibited the removal of toluene, whereas the removal of styrene was unaffected by the presence of toluene[202]. The effect of the co-existence on the removal efficiency was explained by the nature of the end group (single and double bond)[202]. Qin *et al.* investigated the mechanical mixing of two catalysts, Fe/13X and Mn/13X, for the simultaneous removal of toluene and ethyl acetate as the respective metal-loaded 13X has higher mineralization efficiency for the respective VOC[203]. As shown in Table 11, the number of works investigating the removal of a mixture of VOCs is limited.

Novel approaches

Recent works on double dielectric barrier discharge reactors (DDBD), where both electrodes are covered with the dielectric barrier, showed that the DDBD reactors have improved VOC removal efficiency and mineralization efficiency[204,206]. However, the research on the underlying mechanism which can explain the improved performance of the DDBD reactors is still in the nascent stage. Shang *et al.* investigated the decomposition of benzene using a novel approach by combining a DBD plasma catalysis reactor consisting of gas phase packed bed discharge (Mn-Cu/Al_2O_3 as the catalyst) and gas-liquid phase discharge chamber (Persulfate/H_2O)[207]. It has been reported that the benzene decomposition efficiency and mineralization rate were improved due to the presence of Mn-Cu/Al_2O_3 catalyst, the formation of by-products such as O_3 and NO_2 was suppressed due to the gas-liquid phase discharge and the addition of persulfate to H_2O further increased benzene removal efficiency (by the dissolution of O_3 in water, enhancing the formation of active species such as OH and H_2O_2).

Table 11. Overview of published work on IPC for the abatement of VOC mixture

Reactor	Catalyst	Carrier gas	Flow rate (L/min)	VOC_{in} (ppm)	VOC	η_r (%)	Sco_x (%)	By-products	Ref.
DDBD	Pt-Sn/Al_2O_3	Air	1	100	Toluene	85	-	Solid deposit	[204]
					TCE	71			
					Benzene	66			
DBD	10 wt% Mn/Al_2O_3	Air	0.2	-	Benzene	98	-	-	[205]
					Toluene	99			
					Xylene	74			

Adsorption plasma catalysis

Although plasma catalysis has been proven to be more efficient than the individual techniques for VOC abatement, the plasma discharge is continuously operating, resulting in reduced energy efficiency as most of the discharge energy will be utilized to excite the background gas (O_2 and N_2)[208]. Thus, for the treatment of the large volume of exhaust gas containing very low concentrations of VOCs (< 100 ppm), the alternate approach of adsorption plasma catalysis (APC), also known as cycled "storage-discharge", has been proposed and investigated[209,210]. Basically, APC involves two operating steps [Figure 14A]: (i) VOC in low concentration from exhaust or flue gas is trapped or adsorbed on the adsorbent and/or catalyst (storage stage-plasma off); and (ii) the trapped or adsorbed VOC is oxidized by NTP discharge (discharge stage-plasma on)[187]. Figure 14B shows the difference in the discharge power between continuous plasma catalysis and APC process. The energy cost (EC, in kWh/m^3) to remedy 1 m^3 of exhaust gas using continuous plasma catalysis and APC is as follows:

$$EC_{cont} = \frac{P_{discharge}^{cont}}{F_1} \quad (1)$$

$$EC_{APC} = \frac{P_{discharge}^{APC} t_2}{F_1 t_1} \quad (2)$$

where F_1 is the flow rate (in m^3/h) during the storage stage of APC/during the continuous plasma catalysis process, $P_{discharge}^{cont}$ is the discharge power of normal or continuous plasma catalysis (in kW), $P_{discharge}^{APC}$ is the discharge power during the discharge stage of APC (in kW), and t_1 and t_2 are the storage and discharge periods, respectively.

For this approach of APC, one of the key factors is to find a suitable adsorbent and/or catalyst which has the following properties: (i) high capability of VOC adsorption, which reduces the energy cost of the APC process by increasing the adsorption time [according to Equation (2)]; (ii) the ability to completely oxidize the adsorbed VOC to avoid the formation of toxic and unwanted toxic by-products, which improves the product selectivity and carbon balance; (iii) the ability to be regenerated by the NTP exposure, to avoid the extra step of calcination to regenerate the adsorbent and/or catalyst; and (iv) the stability in the NTP exposure, to reduce the material cost. Other advantages of APC over the continuous plasma catalysis process are the possibility to choose a different discharge gas (other than air) in order to improve the product selectivity[120] and promote the regeneration of the adsorbent/catalyst and the ability to adapt to change in the flow rate and VOC concentration in the exhaust gas[188].

Effect of process parameters: adsorption stage

Effect of surface and bulk properties of adsorbent/catalyst

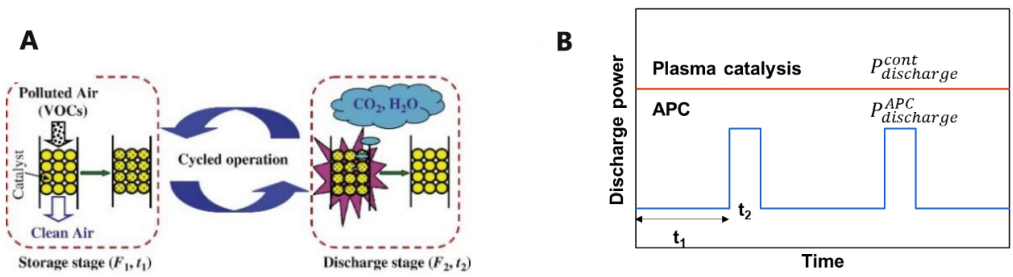

Figure 14. (A) The schematic representation of APC for VOC abatement and (B) the difference in discharge power for continuous plasma catalysis and APC. This figure is quoted with permission from Zhao *et al.*[120]. APC: Adsorption plasma catalysis; VOC: volatile organic compound.

The adsorption of VOCs on the adsorbent/catalyst plays an important role in determining the energy cost of APC process, and it depends on their surface and bulk properties, such as specific surface area, pore size, and pore volume. The choice of an adsorbent and/or catalyst with high S_{BET} and suitable pore size is crucial to enhance the adsorption time. Xu *et al.* investigated HZSM-5 with various S_{BET} (366-341 m^2/g) and pore size (0.53-0.52 nm) for APC removal of toluene and xylene and reported that the VOC adsorption capacity decreased with the decrease in S_{BET}[211]. Yi *et al.* reported that the toluene adoption capacity of MS-13X was far higher than MS-5A and Al_2O_3[212]. Their S_{BET}, pore volume, and pore size are shown in Table 12. Although MS-5A has similar S_{BET} to that of MS-13X and higher pore volume, the microporous size of MS-5A is 0.55 nm, which is smaller than the kinetic diameter of toluene (0.67 nm), resulting in poor adsorption capacity.

Effect of metal loading

Xu *et al.* investigated various metal-loaded SBA-15 (pure, Mn/SBA-15, Ag/SBA-15, and AgMn/SBA-15) for APC removal of toluene[213]. The breakthrough curve showed that the adsorption capacity of Mn-loaded SBA is lower than that of pure SBA-15, which is due to the decrease in the S_{BET} of SBA-15 after Mn loading [Table 13]. However, with Ag loading (Ag/SBA-15 and AgMn/SBA-15), the toluene adsorption capacity was remarkably increased. The S_{BET} of Ag-loaded SBA-15 was lower than the pure SBA-15, showing that the increase in toluene adsorption was not because of physical adsorption. It was reported that the presence of metal which possesses empty s-orbital and electrons available in d-orbital forms π-complexation bonding, resulting in increased toluene adsorption[214,215]. A similar observation was made by other researchers for the adsorption of toluene on various metal-loaded adsorbents/catalysts which form π-complexation bonding, such as Co[212].

The optimum amount of metal loading is crucial as this affects the S_{BET} and pore volume of the adsorbent. As shown in Figure 15, the toluene adsorption capacity increased with the increase in Co loading from 1% to 5% and then decreased with a further increase in Co loading. Yi *et al.* reported that, at the low value of Co loading, there was no formation of π-complexation bonding, whereas, at the higher value of Co loading, the pore volume and S_{BET} were decreased, resulting in reduced physical adsorption potential[212].

Effect of humidity

In real-world applications, the presence of humidity in exhaust gas is inevitable, and the presence of humidity affects both the adsorption stage (competitive adsorption) and NTP discharge stage (a major source of OH and HO_2 radicals) of the APC process. Researchers have reported that the presence of

Table 12. Surface area, pore volume, and pore diameter of various adsorbents

Catalyst	S_{BET} (m^2/g)	Pore volume (cm^3/g)	Pore size (nm)	
			Micro	Average
MS-13X	626.4	0.35	1.03	2.66
MS-5A	628.7	0.47	0.55	2.07
Al_2O_3	264.9	0.37	-	7.06

Table 13. Surface area, pore volume, and pore diameter of various metal-loaded SBA-15 catalysts[213]

Catalyst	S_{BET}(m^2/g)	Pore volume (cm^3/g)	Pore size (Å)
SBA-15	499	0.90	68.0
Mn/SBA-15	425	0.83	71.7
Ag/SBA-15	446	0.85	69.4
AgMn/SBA-15	465	0.82	69.3

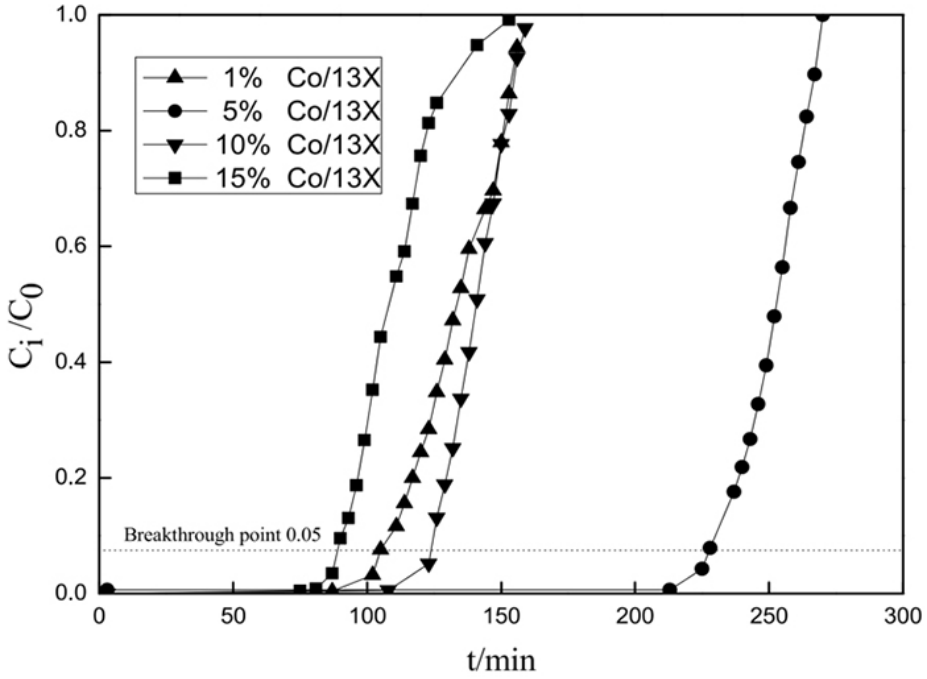

Figure 15. Adsorption breakthrough curves of toluene on different Co-loaded 13X (cobalt loading = 1%, 5%, 10%, and 15%), with toluene initial concentration = 150 ppm and total flow rate = 0.4 L/min. Re-printed with permission from Yi *et al.*[212].

humidity negatively impacts the removal of toluene[144,169].

In the APC process, the choice of adsorbent/catalyst suitable for a wide range of humidity avoids the competitive adsorption during the adsorption stage, and the independence to choose the difference discharge gas during the discharge stage avoids the quenching of electrons. Zhao *et al.* investigated the adsorption of formaldehyde on AgCu/HZ for a wide range of humidity (RH = 20%-93%) and reported that the HCHO breakthrough capacity in humid gas stream was reduced slightly when compared to dry gas stream[120]. However, the HCHO breakthrough capacity was kept constant through the wide range of humidity, which was explained by the excellent humidity tolerance of hydrophobic high silica zeolite. Fan *et*

al. reported that the breakthrough of water on HZSM-5 and Ag/HZSM-5 was just a few minutes due to the hydrophobic nature of HZSM-5; thus, the adsorption of toluene in the presence of humidity (RH = 50%) was not affected[216].

Effect of process parameters: Discharge stage

Effect of discharge gas

In the APC process, there is the possibility to choose a discharge gas other than the background exhaust gas. Although using O_2 as discharge gas avoids the formation of toxic by-products such as NO_x[217] and efficiently regenerates the adsorbent/catalyst, the use of O_2 increases the process cost and it is not readily available. On the other hand, air is readily available as a discharge gas. Zhao *et al.* compared the use of air and O_2 as discharge gas for APC removal of formaldehyde and reported that there was no difference in carbon balance and CO_2 selectivity[120]. However, while using air as discharge gas, the rate of CO_2 evolution was lower, resulting in extended "plasma on" time, which could negatively influence the energy cost of the APC process, and there was the formation of nitrogen oxides (such as N_2O and NO_2) as by-products. Dang *et al.* reported that the use of O_2 as discharge gas to oxidize toluene adsorbed on MnO_x/γ-Al_2O_3 and $AgO_x/\ \gamma$-Al_2O_3 effectively oxidized toluene to CO_2 within 60 min and suppressed the formation of N_2O[218].

Effect of gas flow

The gas flow rate plays an important role in determining the mineralization efficiency for plasma catalytic destruction of VOCs. When the gas flow rate increases, the residence time of VOCs in the plasma discharge region decreases and reduces the collision probability between the VOC molecules and plasma-generated active species[173]. In the APC process, the choice of discharge mode such as closed (inlet and outlet of the reactor are sealed), intermittent cycle (by alternating closed and ventilated discharge), or ventilated (with a flow of background gas such as N_2, O_2, or air) discharge depends mainly on the amount of adsorbed VOCs during the adsorption stage. Yi *et al.* investigated the closed and ventilated discharge for APC removal of toluene using MS-5A, MS-13X, and Al_2O_3 as packing material[219]. As shown in Figure 16, although the toluene removal efficiency was not affected by the discharge mode, the carbon balance (B_c) and CO_x selectivity were dependent on the amount of toluene adsorbed (Tol_{ads} for 13X, 5A, and Al_2O_3 were 0.57, 0.021, and 0.05 mmol, respectively). In the closed discharge mode, the amount of oxygen was limited, and the oxidation of toluene was mainly dependent on the amount of active oxygen species generated, resulting in deep toluene oxidation in the presence of less toluene due to increased residence time. On the other hand, for 13X, the B_c and CO_x selectivity were increased in ventilated discharge, as the loss of oxygen was replenished by the continuous flow, whereas, for the low concentration of toluene (5A and Al_2O_3), the utilization of NTP generated active species was poor and the toluene was desorbed and released to the gas stream unconverted. Dang *et al.* compared the intermittent (closed = 5 min and ventilated = 10 min) and ventilated discharge for APC removal of toluene using MnO_x/γ-Al_2O_3 and reported that the continuous mode exhibited better and deep toluene oxidation[218]. This was because the amount of toluene adsorbed was high (0.88 mmol), and the continuous flow replenished the reactive species generation and removed the oxidative products (CO and CO_2) produced, avoiding the active site blockage. The suitable gas flow rate during the discharge phase is dependent on the reactor configuration; thus, the optimization of the gas flow rate is important to obtain a better conversion, energy, and mineralization efficiency[220,221].

Effect of humidity

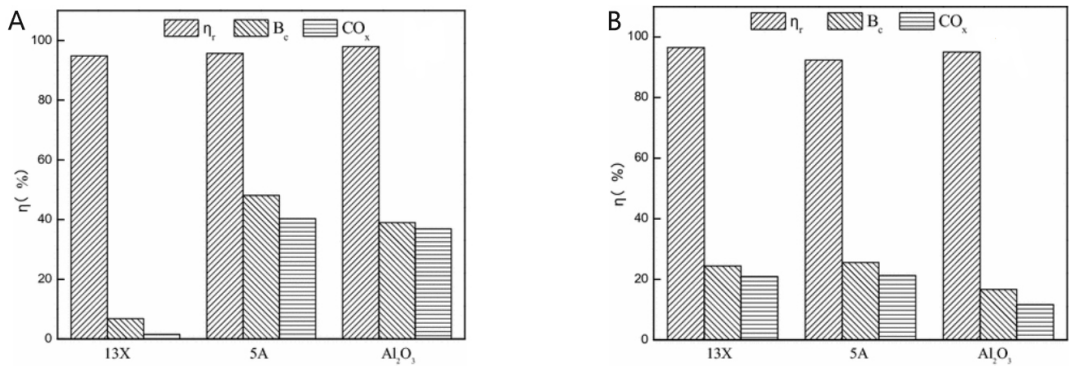

Figure 16. Degradation efficiency of toluene in APC process for (A) closed and (B) ventilated discharge mode. Re-printed with permission from Yi *et al.*[219]. APC: Adsorption plasma catalysis.

Xu *et al.* investigated APC removal of toluene using Ni-SBA in the presence of a wide range of humidity (RH = 20%-80%) and reported that the presence of humidity reduces the toluene mineralization rate[222]. This was explained by the quenching of energetic electrons due to the electronegative nature of water and the competitive adsorption of water vapor covers the active sites needed for O_3 adsorption and decomposition. On the other hand, it was reported that the presence of humidity reduces CO yield, which was explained by the influence of humidity on the formation of intermediates favorable for CO_2 formation.

Effect of metal loading

The mineralization efficiency and carbon balance of the APC process are important in order to reduce the formation of unwanted and more toxic by-products, and they depend on the catalytic activity of the adsorbent and/or catalyst. Noble metal-based catalysts such as Pt or Pd have been widely reported as highly active catalysts for VOC oxidation[223]. However, noble metal-based catalysts are expensive and susceptible to poisoning. Alternatively, transition metal oxide-based catalysts have been considered for the total oxidation of VOCs[224,225]. In the APC process, the decomposition of adsorbed VOC on adsorbent in NTP discharge proceeds via the reaction with the energetic electrons, ions, ozone, and atomic oxygen. It has been reported that the reaction rate of toluene with atomic oxygen ($k = 7.6\ 10^{-14}$ molecules·cm^{-3}s^{-1}) is higher than that with ozone ($k = 3.9\ 10^{-22}$ molecules·cm^{-3}s^{-1}), and the rate-determining step of toluene oxidation is the decomposition of ozone[213,226] according to Equations (3)- (5). Thus, to improve the CO_2 yield and selectivity, the choice of the packing material (catalyst) suitable for the decomposition of ozone to produce atomic oxygen, oxidation of CO, and, thus, total oxidation of adsorbed toluene is important.

$$O_3 + * \rightarrow O_2 + *O \quad (3)$$

$$O_3 + *O \rightarrow O_2 + *O_2 \quad (4)$$

$$*O_2 \rightarrow O_2 + * \quad (5)$$

where * represents the active catalyst site.

Xu *et al.* reported that loading SBA-15 with metals such as Ag and/or Mn showed improved CO_x yield and carbon balance when compared to pure SBA-15, which was mainly attributed to the ozone decomposition ability of the catalysts[213]. Yi *et al.* investigated various transition metal-loaded 13X (such as Cu/13X, Co/13X, Ce/13X, and Mg/13X) for the APC removal of toluene and reported that the CO and CO_2 yield,

CO_2 selectivity (S_{CO_2}), and carbon balance (B_c) were the highest when using Co/13X [Figure 17][212]. This is due to the presence of active sites (Co_3O_4 in Co/13X) which has large oxygen adsorption capacity and converts them to O^- and O^{2-}, which are stabilized on the catalyst surface resulting in enhanced reactivity. Wang *et al.* reported that the mineralization rate of various metal-loaded HZSM-5 for APC removal of toluene from humid air (RH = 40%) occurred in the following order: Ag-Mn/HZSM-5 (~94%) > Ce-Mn/HZSM-5 ~ Mn/ HZSM-5 (~70%) > Ag/ HZSM-5 > Ce/ HZSM-5[215]. The better catalytic activity of Ce-Mn- and Mn-loaded HZSM-5 was attributed to the strong oxygen storage/release ability of Mn and ozone decomposition ability of Mn, whereas the addition of Ag in Ag-Mn/HZSM-5 changed the toluene adsorption site to Ag (π-complexation), thereby leaving the Mn active sites for O_3 decomposition.

In addition to the kind of metal loading, the amount of metal loading affects the catalytic performance by altering the oxidation state, crystal structure, aggregation, and redistribution. Yi *et al.* studied the effect of Co loading on APC removal of toluene (1%, 5%, 10%, and 15%) and observed that the optimum Co loading was 5% for better catalytic performance[212]. When 1% Co was loaded, there was not enough formation of active species for the complete toluene oxidation, whereas increasing the Co loading beyond 5% resulted in agglomeration of the active sites (observed in SEM).

Stability of adsorbent/catalyst

The stability of adsorbent/catalyst over multiple cycles is crucial for its applications in cyclic processes such as adsorption plasma catalysis. The activity of the adsorbent and/or catalyst used as packing material in PBDBD reactor for VOC abatement shows time-dependent deterioration. Deactivation can be due to either the accumulation of organic intermediates on the surface of the catalyst[227] or changes in the surface and bulk properties after exposure to NTP discharge[228]. Xu *et al.* investigated the stability of AgMn/SBA-15 for the APC removal of toluene and reported that the toluene conversion and CO_x yield were not decreased during the five cycles of APC[213]. Zhao *et al.* investigated the stability of AgCu/HZ catalyst during APC removal of formaldehyde and reported that the carbon balance and CO_2 selectivity were maintained at ~100% for five cycles[120]. Fan *et al.* reported that the APC removal of benzene using Ag/HZSM-5 as a catalyst was very stable for five cycles[216]. Trinh *et al.* investigated the stability of Ag-loaded zeolite during APC removal of acetone for four cycles[229]. Although the catalytic performance was not degraded during these four cycles of APC, the temporal evolution curves of gaseous carbon-containing by-products (such as CO and CO_2) tended to be broader, probably due to the oxidation of the low volatile organic deposits on the catalyst.

The above-mentioned works investigated the stability of adsorbent/catalyst under NTP exposure in the APC process by comparing the VOC removal efficiency, carbon balance, and CO_2 selectivity for a very limited number of cycles (≤ 5). Wang *et al.* investigated the APC removal of toluene using Ag-Mn/HZSM-5 and reported that the toluene mineralization rate decreased from 93.5% to 68.6% during 10 cycles of APC[215]. They ascribed the deterioration of the catalyst performance to the accumulation of organic intermediates, and the catalytic activity was restored by calcination in air stream at 573 K for 2 h. It has also been reported that the surface and bulk properties of the adsorbent and/or catalyst can change, which leads to the deactivation of the catalysts[230]. Thus, it is crucial to investigate the bulk and surface properties of adsorbents and/or catalysts, such as phase, crystallinity, elemental composition, oxidation state of metal, morphology, *etc.*, which can be altered partially or completely by NTP exposure[187]. Qin *et al.* investigated the stability of γ-Al_2O_3-13X for APC removal of toluene by comparing both the mineralization rate (MR) and the physico-chemical properties of the fresh and used catalysts[231]. Although there was no significant change in the MR over the five cycles of APC, in FTIR spectra of the used catalysts, there were new peaks

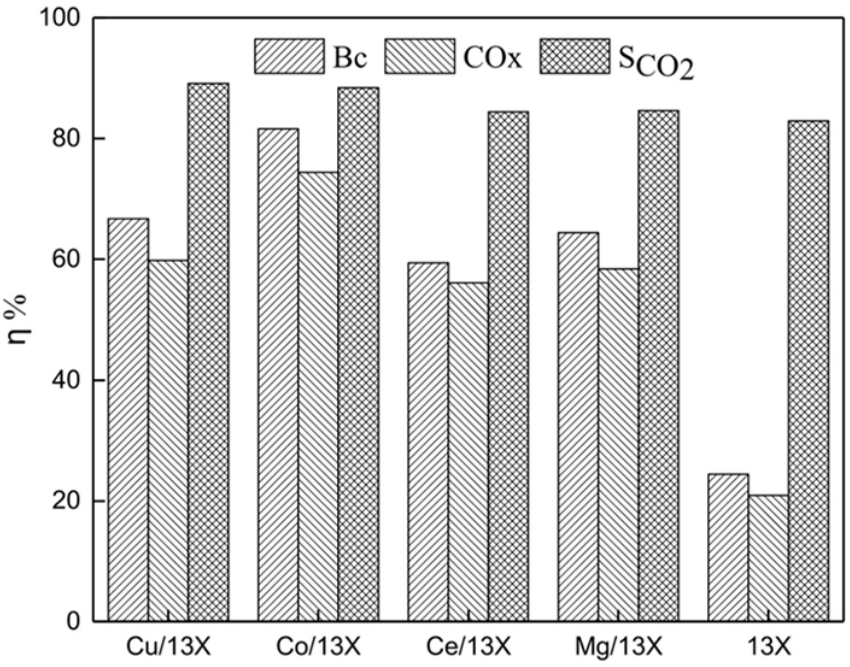

Figure 17. Carbon balance and CO_x and CO_2 selectivity for various metal-loaded 13X catalysts (total air flow rate = 0.1 L/min; discharge power = 20 W). Re-printed with permission from Yi *et al.*[212].

corresponding to C-O-H and methyl, indicating the presence of intermediate organic products on the surface of the catalyst. Other catalyst properties such as the crystal structure, S_{BET}, pore volume, and average pore size were not changed after the five cycles of APC. Although the deposition of organic products did not change the catalytic activity during five cycles of APC, the continuous accumulation of organic products might influence the catalytic activity and performance in the long run.

COUPLING ADSORPTION AND PHOTOCATALYSIS FOR VOC REMOVAL

Introduction

In addition to the above-discussed adsorption-catalysis coupling and plasma catalysis strategies for VOC removal, adsorption-photocatalysis coupling has also been exploited by researchers. Compared with the high temperature and pressure adopted during adsorption-catalysis and plasma catalysis processes, the adsorption-photocatalysis process gives rise to obvious advantages in VOC removal such as excellent elimination efficiency, low energy depletion, and environmentally friendliness[232-234]. As for the whole adsorption-photocatalysis process, the adsorption procedure ensures that the VOC molecules are transmitted from the gas phase to the solid phase to achieve the close contact between VOC molecules and photocatalysts. Moreover, the photocatalysis treatment is conducted at room temperature and decomposes VOCs into CO_2 and H_2O and therefore guarantees the regeneration of the adsorbent for constant VOC elimination[235]. The above merits indicate adsorption-photocatalysis coupling technology is an efficient and promising method for VOC removal.

Generally, photocatalytic oxidation has been carried out during the photocatalysis treatment process, which endows a facile and effective pathway for completely decomposing VOC molecules by utilizing photoinduced oxidizing species [Figure 18]. For instance, titanium dioxide, a typical photocatalyst, has frequently been used in adsorption-photocatalysis coupling for VOC removal. Under UV light irradiation, TiO_2 gives rise to the generation of highly oxidizing radicals, such as ·OH radicals (·OH/H_2O = +2.27 eV *vs.*

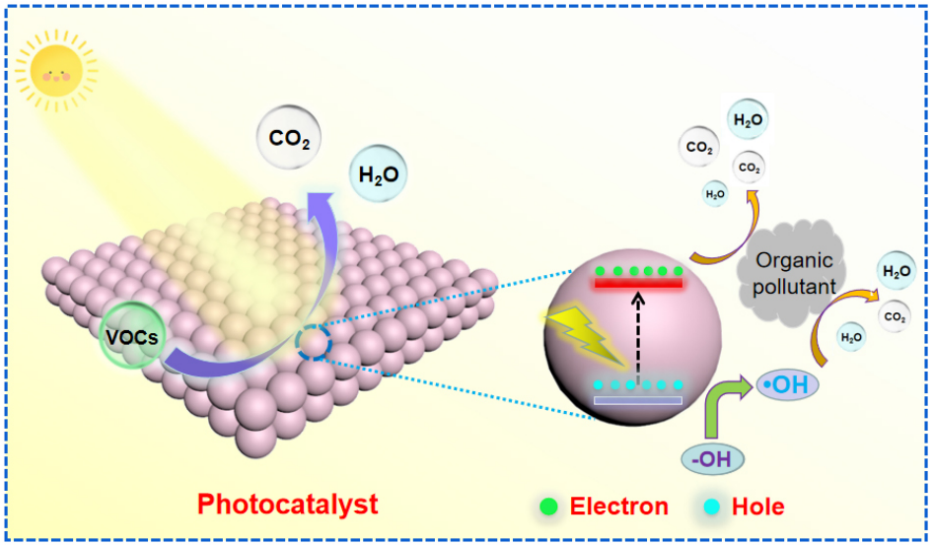

Figure 18. The schematic process of adsorption-photocatalysis coupling for VOC removal. VOC: Volatile organic compound.

SHE) and $\cdot O^{2-}$ (redox potential $O_2/\cdot O^{2-}$ = -0.28 eV *vs.* SHE), which lead to the decomposition of VOC molecules such as gaseous toluene and benzol in the atmosphere[232]. As for the strongly adsorbed VOC molecules on the surface of photocatalyst, they can be directly oxidized by the photogenerated hole on TiO_2 photocatalyst.

Mechanisms

Coupling adsorption and photocatalysis for VOC removal is composed of three predominant processes including mass transfer and transportation, surface photoredox reactions, and product desorption[236-240]. Here, we discuss the detailed mechanism of each process. (1) Mass transfer and transportation means that the VOC molecules are shifted from the gas phase to the surface of photocatalysts via an adsorption process due to the existence of interactions such as hydrogen bonds and van der Waals force between VOC molecules and photocatalysts. Thus, the modification of the surface chemistry of photocatalysts is of great importance for photocatalytic VOC elimination. (2) When the energy of excited light is greater than the band gap value of the photocatalyst, photogenerated electron-hole pairs are produced. The generated holes can directly oxidize organic molecules or oxidize water to produce hydroxyl radicals for the subsequent oxidation reaction. As to the electrons, they can combine with oxygen to create the oxidative superoxide radical to join in the oxidation degradation of organics. Finally, products such as CO_2, H_2O, or other intermediates are generated on the surface of photocatalyst. (3) Product desorption is also a crucial part of photocatalytic VOC elimination and sometimes will affect the activity and regeneration of photocatalyst. In particular, the undesired intermediates such as hydrocarbons and oxygen related species often adhere to the surface of photocatalyst, which may lead to the deactivation by the saturation and poison the catalyst surface, and thus bring out decreased catalytic performance[235]. Therefore, fast desorption of the produced products from the surface of the catalyst is significant for photocatalytic VOC elimination.

The state-of-art photocatalysts

Up to now, a series of semiconductors such as metal oxides and metal hydroxides have been developed for various photocatalytic applications[234-238]. Metal oxides are major candidates for VOC elimination via adsorption-photocatalysis coupling. Here, we present the state-of-the-art materials for VOC removal via adsorption-photocatalysis coupling technology. Meanwhile, the modification methods, operational parameters, and the mechanism for VOC removal are also thoroughly discussed.

TiO_2

As a well-studied photocatalyst, TiO_2 displays tremendous potential for photocatalytic VOC elimination under UV light illumination. Two forms of TiO_2, anatase and rutile, with band gaps of around 3.2 and 3.1 eV, respectively, are often obtained during chemical synthesis[241-243]. In comparison with rutile, anatase always gives rise to much higher photocatalytic VOC elimination activity because its conduction band level is more likely to produce stable surface ·OH radicals[241]. In practical applications, TiO_2 photocatalysts are prone to agglomeration and inactivation during a long-term reaction, which reduces their VOC elimination performance. Therefore, various strategies such as substrate fixing, ions doping, surface modification coupling with other metal oxides, and noble metal loading have been explored to enhance the VOC removal activity.

Structure and morphology modulation

The structure and morphology of TiO_2 have a great influence on its final photocatalytic performance. TiO_2 nanotubes have recently attracted much attention owing to their unique structure and morphology. For example, Xu *et al.* reported powder-type TiO_2 nanotubes for the enhanced photocatalytic gaseous acetaldehyde degradation ability in comparison with that of commercial P25 photocatalyst[241]. A TiO_2 nanotube array can be formed by loading uniform TiO_2 nanotubes on a titanium substrate, which shows an ordered structure and porous surface. Such a unique architecture favors reactant diffusion and transfer, thus being beneficial for the improved photocatalytic ability. Therefore, immobilization of TiO_2 nanotubes on a substrate is available from the view of practical air purification. Typically, highly ordered TiO_2 nanotube arrays on titanium foils with different lengths are fabricated by an electrochemical anodization strategy for photocatalytic degradation of gaseous acetaldehyde [Figure 19A and B][242]. It has been revealed that enhancing the lengths of nanotube arrays to a certain degree leads to increased photocatalytic acetaldehyde molecule elimination. Moreover, the as-fabricated TiO_2 nanotube arrays give rise to higher photocatalytic activity than that of a commercial P25-based film with the same thickness and geometric area. This enhancement can be attributed to the unique infrastructure and morphology of the nanotube array, which was profitable for the facile mass diffusion and the prohibited deactivation of TiO_2 nanotube during photocatalytic degradation.

Carbon substrate fixing

Carbon materials with abundant porous and large surface areas have been considered as promising substrates to support the distribution and fixation of TiO_2 photocatalysts[244,245,248-250]. Moreover, the stronger adsorption capacity, black color, and rapid electron shift on the interface of the carbon-TiO_2 hybrid can guarantee the adequate absorption of pollutant molecules on the active sites of photocatalyst, promote visible light harvesting, facilitate the production of active radicals, and prohibit the formation of by-products and the inactivation of photocatalysts.

For example, Li's team reported that TiO_2 particles are uniformly dispersed on activated carbon fibers (TiO_2-ACF) [Figure 19C] through an acid treatment method for efficient formaldehyde removal[244]. The C-Ti bond and surface hydroxyl groups are formed in the TiO_2-ACF composite. By changing the acid treatment time, the amounts of surface hydroxyl groups can be well tuned. Significantly, the created C-Ti bond on the interface between TiO_2 and ACF can promote the electron migration in the photocatalyst, and the abundant -OH species give rise to the increased adsorption of water and formaldehyde molecules, thus bringing out more ·OH radicals. Moreover, the rich pore structures in ACFs are also beneficial for reactant molecules' transfer and transportation. The synergistic effects of the enhanced light adsorption, facile mass diffusion,

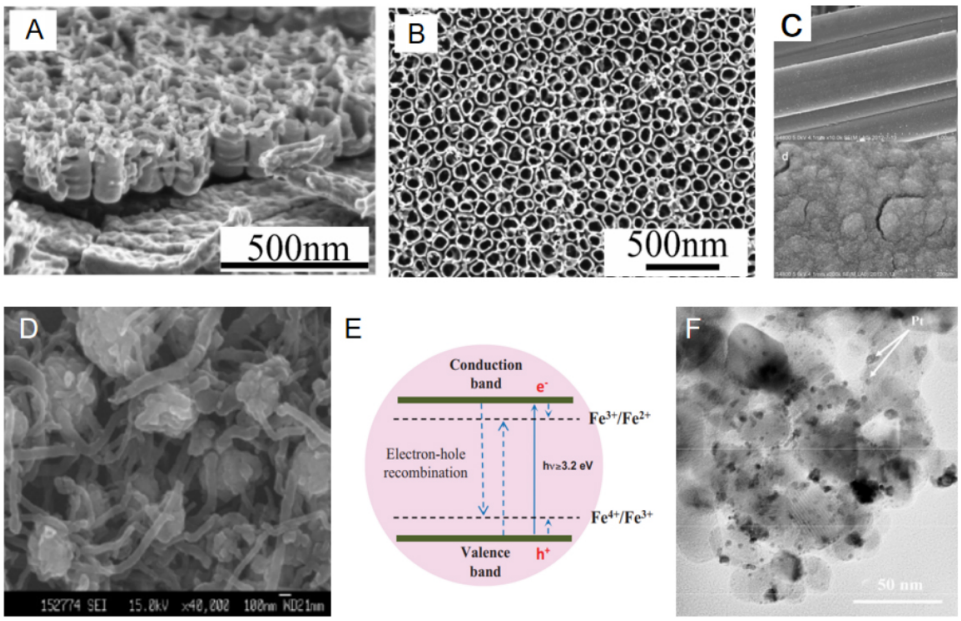

Figure 19. (A and B) SEM images of the TiO_2 nanotube arrays[242]. This figure is used with permission from the American Physical Society. (C) SEM image of the TiO_2-ACF photocatalyst[244]. This figure is used with permission from the Elsevier. (D) SEM image of the MWCNT-TiO_2 composite[245]. (E) Schematic Energy diagram of Fe^{3+} doped TiO_2[246]. This figure is used with permission from the Elsevier. (F) TEM image of the Pt-loaded TiO_2 photocatalyst[247].

and improved adsorption of water molecules result in increased photocatalytic formaldehyde elimination. Specifically, the TiO_2-ACF composite exhibited 20 times higher formaldehyde removal rate than that of pure TiO_2 powder.

Different from ACF discussed above, carbon nanotubes (CNTs) with a specific 1D cylinder configuration endow the unique hollow structure, which is profitable for better fixation of TiO_2 particles and prolongs the residence time of VOC molecules in photocatalysts, thus making CNTs an ideal co-adsorbent and matrix for photocatalytic VOC molecule removal[245,248]. TiO_2 nanosphere-loaded carbon nanotubes (MWCNT-TiO_2) were fabricated using a hydrothermal strategy by An *et al.*[245]. SEM images show that the TiO_2 nanospheres with tunable crystal facets are wrapped around CNTs with sphere sizes from 200 to 600 nm [Figure 19D]. As expected, the MWCNT-TiO_2 composite exhibited higher activity for the photocatalytic degradation of styrene gas than that of single anatase TiO_2. The improved styrene gas degradation performance for composite is attributed to the synergistic effects of nanostructured TiO_2 spheres and the positive function of CNTs. Specifically, by modulating the reaction conditions such as the ratios of CNTs/TiO_2 and temperature of hydrothermal preparation, TiO_2 spheres with various crystal facets can be obtained. Moreover, the merits of CNTs in promoting VOC molecule absorption and increasing contact between styrene and CNT-TiO_2 are involved. All the above facts are beneficial for the styrene molecule decomposition process.

Graphene possessing 2D layers of sp^2 hybridized carbon atoms displays a variety of merits such as good electronic conductivity and thermal conductivity and has been widely used in catalytic fields[249]. However, a single layer of graphene is prone to be aggregated because of its great van der Waals force. Moreover, the hydrophobic surface of graphene is not suitable to load and disperse oxides and attract VOC molecules. In this regard, some methods such as oxidation and acid treatment have been exploited to modify graphene. Up to today, graphene derivatives including graphene oxide (GO) and reduced graphene oxide (rGO),

endowed with abundant oxygen related groups such as hydroxyl, carboxylic, and carbonyl species on their surface, bring out both anchor dispersibility and favorable adsorption sites for oxide particles to facilitate VOC molecule removal.

For instance, Roso et al. synthesized a series of graphene-based TiO_2 hybrids and studied the effects of various co-catalysts (graphene, GO, and rGO) on the photocatalytic methanol vapor elimination ability[250]. They found that the morphologies of as-prepared composites depend on the type of graphene used. Graphene and GO are prone to be located inside the final composites, leaving TiO_2 on the outer surface of composites to contact with VOC molecules. As to the rGO/TiO_2 hybrid, the TiO_2 nanoparticles are uniformly dispersed between nanofibers due to the partial affinity of the composite with the polymer matrix. The configuration of rGO/TiO_2 is favorable for VOC molecule degradation because of the imitate contact with the photocatalyst and lower mass-transfer restrictions. Therefore, the functional groups on rGO surface exert significant function in affecting the adsorption–photocatalytic process during VOC molecule removal. Finally, the rGO/TiO_2 hybrid brings out the best activity for photocatalytic gas-phase methanol degradation.

As discussed above, TiO_2 immobilization on various carbon substrates is useful for improved adsorption-photocatalysis VOC removal. Adopting an available coating method and type of carbon substrate, two important facts in TiO_2 fixing should be considered. The used carbon substrate must have extraordinary physical and chemical stability in long-term photocatalysis VOC removal. Moreover, a carbon substrate with a large surface area or abundant porous structure for the TiO_2 fixing is necessary. Other fundamental characteristics of the carbon substrate are also required, such as strong attraction of TiO_2 nanoparticles, resistance against high calcination temperatures, and efficient absorbance ability for VOC molecules.

Metal ion doping

Transition metal ions are frequently doped into the lattice of TiO_2 for efficient photocatalysis VOC removal[246,251,252]. The new energy level can be created in the band gap of TiO_2, thus promoting visible light absorption. When the metal dopants substitute the sites of Ti^{4+}, the new energy level is formed near the CB of TiO_2, which can significantly promote photoinduced electron-hole pairs separation for the improved photocatalytic ability. In fact, the photocatalytic activity of metal ion-doped TiO_2 depends on several factors such as the amounts of dopants, the chemical properties of dopants, and the preparing conditions. Next, we outline several common metal ion dopants and discuss their photocatalytic VOC removal activity and limitations.

Transition metals such as Fe, Cu, and Ni can also be doped into TiO_2 for enhanced photocatalytic VOC removal activity due to the enhanced carrier separation and the reduced band gap[246,251-254]. More importantly, the lower cost of transition metals in comparison with noble metals is expected to lead to widespread utilization in large-scale industrial applications. Besides, the category and concentration of transition metal dopants are major factors in determining the photocatalytic VOC removal ability. The optimal amount of transition metal dopant is of great significance. When the amount is over the optimal value, the photocatalytic ability will decrease because more dopants will crash the lattice of TiO_2 and serve as a recombination site. Moreover, the change of chemical valence states (such as Fe^{3+}/Fe^{2+} and Ni^{2+}/Ni^{+}) of transition metal ions [Figure 19E] can also promote photoinduced electron-hole pair separation and facilitate photoelectrons transfer to oxygen to produce $\cdot O_2^-$ radicals[246]. Hence, many studies are dedicated to investigating the optimal category and amount of dopant for the best photocatalytic VOC removal activity. For example, Yang *et al.* reported that iron-doped TiO_2 was prepared on flexible glass fibers by a sol-gel

strategy for the improved photocatalytic elimination of benzene, toluene, ethylbenzene, and o-xylene[252]. Tieng *et al.* found that Fe^{3+} dopant in TiO_2 serving as trapping sites can effectively trap both photoinduced electrons and holes and maintain a long lifetime of photo-charges, thus giving rise to the higher photocatalytic ethylene degradation than that of pure TiO_2 photocatalyst.

Although metal ion doping leads to efficient photocatalytic VOC removal, some disadvantages still exist. For example, doping TiO_2 with Fe ions will lead to partial blockage on TiO_2 porous surface sites and cause the growth of particles, thus resulting in a reduced specific surface area and decreased photocatalytic activity. Therefore, the design of low-cost and efficient transition metals doped into TiO_2 is worthy of further study in the future.

Nonmetal ion doping

Nonmetal ion doping in TiO_2 materials has been considered an effective way to improve adsorption-photocatalysis VOC removal by enhancing the photo-response and modulating the energy configuration. Generally, the nonmetal ions replace the oxygen in the TiO_2 matrix and result in a reduced band gap for more visible light absorption. For TiO_2 photocatalyst, nonmetal ions such as C and N are frequently adopted into the TiO_2 lattice for enhanced photocatalytic VOC elimination[255-257].

C-doped TiO_2 with mesoporous structure was fabricated via a hydrothermal method with Ti $(SO_4)_2$ and glucose as precursors by Dong *et al.*[255]. A series of characterizations demonstrated that the oxygen atoms in the TiO_2 were replaced by carbon atoms, and a new O-Ti-C bond was created. Meanwhile, a new mid-gap state was produced in the band gap of TiO_2, thus promoting visible light absorption and prohibiting photoinduced carrier recombination. Based on these advantages, the as-synthesized C-doped TiO_2 photocatalyst showed higher activity in photocatalytic toluene vapor elimination than that of commercial P25 and C-doped TiO_2 synthesized by the solid-state route. Soon after, the post-thermal treatment of the obtained C-doped TiO_2 for further improved photocatalytic VOC elimination was also developed by this team[256]. The improvement of gaseous toluene elimination was found by the post-thermal treatment of the C-doped TiO_2 between 100 and 300 °C, and the optimal thermal treatment temperature was 200 °C. The enhancement can be attributed to the changes in the surface chemistry and optical properties of C-doped TiO_2. Specifically, thermal treatment repairs the surface defects and thus restricts the recombination of photoinduced carrier pairs. Moreover, the visible light absorption was further increased after post-thermal treatment.

Although nonmetal ion doping exerts an efficient function in promoting photocatalytic VOC elimination, some drawbacks still exist. For example, doping nonmetal ions into the TiO_2 lattice leads to the generation of oxygen vacancies, which may serve as an active site to facilitate photoinduced charge carrier recombination and thus are detrimental to the enhanced photocatalytic VOC removal. Thus, optimizing the synthesis route and preciously controlling the location and amount of oxygen vacancies in the TiO_2 lattice are of great importance for acquiring better photocatalytic VOC removal activity. Moreover, the synthesis route and cost for the photocatalyst should also be considered for large-scale VOC treatment. In general, the doping of nonmetal ions into the TiO_2 lattice needs high thermal treatment temperatures (> 500 °C) and a long synthesis time; hence, tremendous energy consumption is inevitable. Meanwhile, the utilization of detrimental, expensive, or unstable raw materials is often involved during the synthesis process. Therefore, finding a green, facile, low-cost, and sustainable preparation process is necessary for large-scale photocatalyst production.

Noble metal loading

Noble metals such as Pd, Pt, and Ag can expand the visible light absorption of TiO_2 photocatalysts[247,258,259]. Meanwhile, a Schottky barrier can be created at the noble metal-TiO_2 interface, which can retard the carrier recombination and thus increase photocatalysis activity. More importantly, noble metals possess extraordinary resistance to oxidation and corrosion in a humid atmosphere. For example, silver-doped TiO_2 photocatalysts with various silver amounts were prepared by Mogal *et al.*[258]. The obtained silver-doped TiO_2 photocatalysts presented improved photocatalytic phthalic acid degradation under UV light excitation due to the fast carrier separation and low-energy band gap. Similarly, enhanced ethanol partial oxidation degradation was also achieved over the Pt doped TiO_2 catalyst [Figure 19F][247].

Coupling with other metal oxides

Coupling with other metal oxides such as SiO_2 and WO_3 has been developed for enhanced photocatalytic VOC molecule removal[260-262]. Thus far, much research has focused on TiO_2/SiO_2 composites. Although SiO_2 is a total insulator and has no photocatalytic ability, the introduction of SiO_2 components in the composites can change the structure and surface functional group, such as pore volume and hydrophilic properties, thus influencing the final VOC molecule removal ability.

For example, Guan *et al.* found that the surface of TiO_2/SiO_2 shows stronger hydrophilic properties than that of pure TiO_2[260]. Specifically, the introduction of SiO_2 improves the acidity and leads to the enhancement of the hydroxyl amount in the composite films, thus favoring VOC molecules absorption and leading to promoted VOCs degradation (Figure 20A). Yu *et al.* confirmed that the grain size of TiO_2/SiO_2 hybrid was reduced when increasing the ratio of SiO_2[262]. Meanwhile, the rich hydroxyl species adhered to the surface of TiO_2/SiO_2 hybrid. The reduced size of TiO_2 may lead to a stronger driving force for photocarriers migration existing in quantum-sized TiO_2 in the TiO_2/SiO_2 hybrid. Meanwhile, the increased surface area brings out an enhanced adsorption ability of VOC molecules. More importantly, the abundant -OH species on the surface can trap photoinduced holes and thus restrict the recombination of electron-hole pairs. All these factors are favorable for the enhanced photocatalytic VOC elimination. As a result, hybrid TiO_2/SiO_2 photocatalytic activities of the composite thin films are still higher than that of pure TiO_2.

Zou *et al.* prepared the TiO_2-SiO_2 pellets using the sol-gel method[261]. The TiO_2-SiO_2 pellets presented high surface areas and abundant porous structure [Figure 20B], therefore giving rise to the strong adsorption capacity of VOCs. A series of characterizations suggested that the TiO_2-SiO_2 pellets exerted two functions as a photocatalyst and as an adsorbent in the adsorption-photocatalysis coupling system for gaseous toluene elimination. It is noteworthy that the catalyst can be self-regenerated by photocatalytic oxidation of the adsorbed toluene molecules. Thus, the TiO_2-SiO_2 pellets can be used for continuous VOC removal in a fixed-bed reactor under UV light illumination.

Surface modification

Surface modification has been developed to increase the photocatalytic activity of TiO_2[262,263]. Sumitsawan *et al.* adopted a plasma discharge method to treat TiO_2 nanoparticles adhering to a glass substrate[263]. It is found that the TiO_2 nanoparticles can be fluorinated (Ti-F) or covered with perfluorocarbon film (C-F) by controlling the plasma discharge conditions. Both modified TiO_2 photocatalysts showed higher photocatalytic m-xylene elimination than that of pristine TiO_2 nanoparticles. The water contact angle test suggested that plasma surface treatment can convert TiO_2 nanoparticles from hydrophilic to hydrophobic [Figure 20C and D]. Pristine TiO_2 presents as completely wettable at the contact angle of the water droplet.

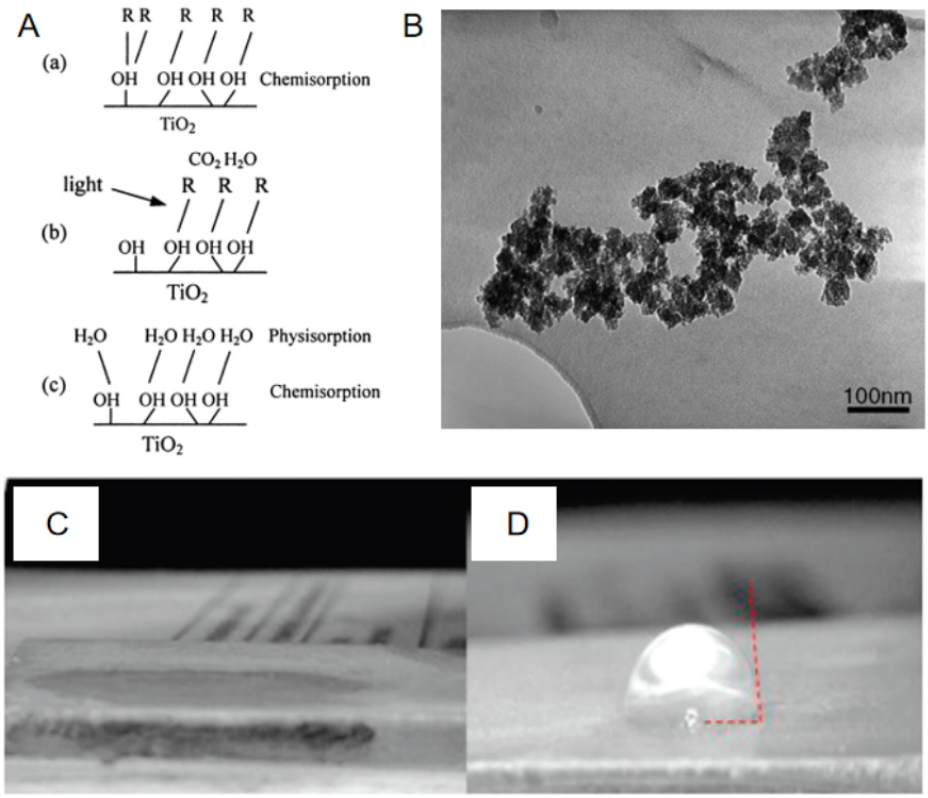

Figure 20. (A) Schematic VOC molecule absorption and degradation on the hydrophilic TiO_2-SiO_2 films[260]. (B) TEM image of the as-prepared TiO_2-SiO_2 photocatalyst[261]. Water contact angle of untreated TiO_2 (C) and plasma treated TiO_2[263]. (D) This figure is used with permission from the American Physical Society.

In contrast, the plasma-treated TiO_2 shows a contact angle and is thus considered hydrophobic. The hydrophobic character of modified TiO_2 could enhance the adsorption of the xylene from the flowing air to the surface of the photocatalyst and thus favor the improved photocatalytic activity.

Other metal oxides

In addition to TiO_2, other metal oxides such as WO_3 and Ga_2O_3 have also been explored for photocatalytic VOC elimination[264-267]. WO_3, as a typical semiconductor with a band gap value of about 2.5 eV, is widely used in photocatalytic oxidation reactions due to its positive VB potential (about 3.15 eV *vs.* NHE) and good chemical stability[264]. However, pure WO_3 photocatalyst usually displays insufficient photocatalysis oxidation ability because the lower CB edge (+ 0.3 - 0.5 eV *vs.* NHE) cannot afford enough reduction ability to reduce O_2 to produce strongly oxidizing radicals such as $\bullet O_2^-$ and $\bullet HO_2$. The inability for O_2 reduction by photoinduced electrons on the CB of WO_3 may also cause the undesired recombination of electron-hole pairs and thus result in poor photocatalytic oxidation ability. It has been revealed that platinum nanoparticles loading can promote the multi-electron reduction of dioxygen to produce active oxygen related species on the CB of WO_3 at a relatively positive reduction potential and thus are favorable for high photocatalytic oxidation ability. Kim *et al.* reported that the Pt/WO_3 composite gives rise to higher activity for photocatalytic VOC [dichloroacetate (DCA), 4-chlorophenol (4-CP), tetramethylammonium (TMA), and arsenite] removal than that of pure WO_3[267]. Specifically, the loading of platinum nanoparticles led to concurrent oxidative reactions on the surface of WO_3; meanwhile, the OH radicals were also produced by the reductive decomposition of H_2O_2, which was formed via the in situ reduction of O_2. It is noteworthy that Pt/WO_3 presented a higher rate of H_2O_2 generation than that of WO_3, thus favoring the OH radical

formation and leading to the promoted photocatalytic oxidation performance [Figure 21A and B].

Hou *et al.* fabricated porous Ga_2O_3 for efficient photocatalytic benzene decomposition[265]. Significantly, the photocatalytic elimination rate of gaseous benzene over Ga_2O_3 was about two times greater than that of commercial P25. This enhancement can be attributed to that Ga_2O_3 possesses stronger oxidative capability due to its more positive CB level [Figure 21C] and higher specific surface area in comparison with P25 photocatalyst.

Metal hydroxide

Apart from the above-mentioned metal oxides, metal hydroxide can also be used as a photocatalyst in adsorption-photocatalysis coupling for VOC removal[268-270]. For example, In $(OH)_3$ is a wide-gap semiconductor and can be used for UV light-driven photocatalytic reactions. Thus, using In $(OH)_3$ materials in adsorption-photocatalysis coupling has been conducted. Typically, In $(OH)_3$ nanocrystals with mesoporous structure have been fabricated by peptization of a colloidal precipitate with a post-heat treatment for acetone, benzene, and toluene degradation under UV light irradiation[268]. Specifically, the In $(OH)_3$ sample with a post-heat treatment temperature of 120 °C gives rise to the optimal photocatalytic performance for acetone degradation [Figure 21D], which can be ascribed to several major factors. Firstly, the In $(OH)_3$ sample post-treated at 120 °C exhibits the highest specific surface area. Therefore, more VOC molecules can be attracted on the surface of In $(OH)_3$, favoring enhanced photocatalytic ability. In addition to the surface area, the porous character of In $(OH)_3$ sample can also lead to its enhanced activity. Specifically, the existence of abundant mesopores in the In $(OH)_3$ nanoparticles brings out the fast diffusion and transfer of organic molecules during the photocatalytic process and increases the VOC removal rate. Finally, the crystal phase should be considered during the photocatalytic process. When the post-heat treatment temperature is over 120 °C, the new phase of In_2O_3 is formed due to the transformation from In $(OH)_3$. The reduced ratio of In $(OH)_3$ in the photocatalyst results in low photocatalytic performance. Thus, the post-heat treatment temperature of 120 °C is the optimal condition for obtaining the In $(OH)_3$ with the best photocatalytic activity.

Factors affecting PCO performance

Generally, several factors such as humidity, airflow rate, light source, and the initial VOC concentration significantly influence adsorption–photocatalysis coupling for VOC removal. These factors are thoroughly outlined in this section.

Humidity

The relative humidity plays a great role during the photocatalytic oxidation process. In fact, the humidity can be both profitable and detrimental to VOC degradation[232,233]. Particularly, water molecules can take part in the photocatalytic removal process by serving as competitive adsorbents and resources of ·OH radicals. For the competitive adsorbents, water molecules absorbing on the surface active sites of photocatalysts will decrease the adsorption ability of VOC molecules and restrict the subsequent photocatalytic reactions[268]. As to the resources of ·OH radicals, the produced ·OH radicals from water molecules can accelerate the photocatalytic oxidation reaction, thus favoring photocatalytic VOC removal[271]. Hence, carefully modulating the relative humidity for efficient photocatalytic VOC removal is of great significance.

Airflow rate

Increasing the airflow rate can present two distinct effects for photocatalytic VOC removal[234,265,266,272]. On the one hand, a fast airflow rate will lead to the reduced residence time for photocatalytic VOC oxidation and thus decrease VOC degradation ability. On the other hand, the promoted mass migration between the VOC

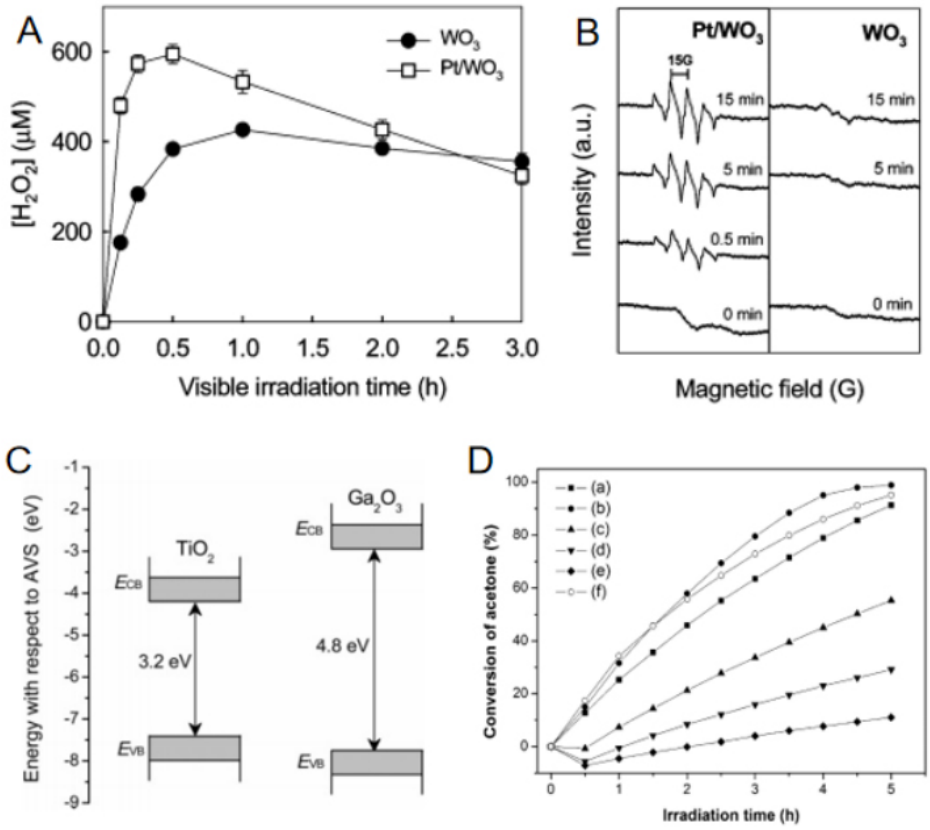

Figure 21. (A) Formation of H_2O_2 over WO_3 and Pt/WO_3 under visible-light excitation. (B) ESR spectra of DMPO-OH• adducts in an aqueous dispersion of Pt/WO_3 and WO_3[267]. (C) Bandgap structure of WO_3 and Ga_2O_3[265]. (D) The photocatalytic acetone oxidation over In $(OH)_3$s treated at various temperatures: (a) 60 °C; (b) 120 °C; (c) 160 °C; (d) 200 °C; and (e) 250 °C. (f) P25 was adopted as a reference[268]. This figure is used with permission from the American Physical Society.

molecules and photocatalysts under a high airflow rate can improve the pollutant removal efficiency[272,273]. Based on the above discussion, finding an optimum airflow rate to achieve maximum residence time of photocatalytic oxidation reaction and simultaneously optimal mass migration between the VOC molecules and photocatalysts is of significant importance to acquire the highest photocatalytic VOC molecule degradation efficiency.

Yang *et al.* studied the influence of various airflow rates on photocatalytic gaseous formaldehyde removal[273]. It was revealed that enhancing airflow rate brings out a fast mass transfer and a low concentration gradient between the bulk and the photocatalyst surface in laminar regimes. The influence of airflow rate on pollutant elimination falls under three distinct regimes. In low airflow rates, improving airflow rate favors VOC molecule elimination, which suggests that mass transfer on the surface of photocatalyst restricts VOC removal. In intermediate airflow rates, flow rate variation has no considerable effect on VOC removal. This means that surface reaction kinetics is the controlling stage. Finally, in high airflow rates, an increased airflow rate decreases the residence time for transferring VOCs contaminants from the gas phase to the catalyst surface, thereby decreasing the VOC removal rate.

Light source

Photogenerated electron-hole pairs are the key factor during the photocatalytic VOC pollutant oxidation process. Frequently used catalysts such as TiO_2 need a UV light equivalent energy source for the

illumination to produce photoinduced charge carriers. Among a series of reports, high-pressure mercury lamps, xenon lamps, and UV lights are major light sources for photocatalytic VOC removal[271-273]. Generally, the VOC elimination rate is proportional to the power of the light source. The photocatalytic VOC removal rate can be modulated by the first order of depletion rate of photogenerated carriers and a half order of their recombination speed. Therefore, the power of the light source has a direct influence on the removal rate. As UV light is deleterious to human beings and possibly results in forming secondary pollutants such as strong oxidizing species in the atmosphere[273], visible-light-driven VOC removal should be further researched in detail.

Deactivation and reactivation

The chemical and physical stability of photocatalysts is very important for long-term VOC removal. In fact, deactivation, regeneration, and reactivation often occur during the photocatalytic VOC treatment process[234]. For the adsorption-photocatalysis coupling system, the photocatalytic rate usually decreases with extending reaction time and the surface active sites simultaneously reduce due to the deactivation of the photocatalyst. The accumulation of reaction intermediates on the surface of photocatalyst leads to deactivation because these intermediates occupy active sites. For example, reaction intermediates such as formic acid are often adhered to the surface of TiO_2 photocatalyst due to its strong affinity during photocatalytic acetaldehyde elimination[235]. Although a certain amount of formic acid can be emitted into the atmosphere, the occupation of the surface active site results in the deactivation of TiO_2 photocatalyst. In practical application, the photocatalyst will be totally deactivated after 20 consecutive photocatalytic acetaldehyde degradation reactions because all the active sites capture reaction intermediates[274]. Therefore, the recovery of photocatalyst is put on the agenda. Typically, the absorbed reaction intermediates, including benzaldehyde and benzoic acid, could be totally removed with a heat treatment over 653 K. Hence, the reactivation of the photocatalysts by post calcination is often adopted.

Pollutant concentration

The pollutant concentration has a non-negligible effect on photocatalytic VOC removal[275]. Many studies have suggested that the appropriately lower concentrations of VOC lead to the increased elimination ability of VOCs, which is ascribed to the active sites of photocatalysts possessing limited adsorption capacity[275-277]. Moreover, the produced reaction intermediates will prohibit the adsorption of VOC molecules, especially when the pollutant concentration is high in the reaction system. As a result, the adsorption-photocatalysis coupling reaction system is more likely to treat VOCs at a relatively low concentration. As to the high concentration VOC removal, the surface of the photocatalyst will become saturated because of the shielding effect of the pollutant molecules and is thus detrimental to the efficient VOC treatment[277]. Moreover, the saturation and competition of photocatalyst between adsorbed pollutants are higher when inlet VOCs are at a high concentration.

CONCLUSION AND OUTLOOK

Human exposure to VOCs in the air is unavoidable in everyday life. Some VOCs are categorized as carcinogenic or reprotoxic by the European Union and the World Health Organization. Air-liquid interface exposure systems can be used to assess the toxicity of VOC emissions on respiratory symptoms. These techniques have the advantage of eliminating any direct interaction between the tested toxicants and the culture medium's components. Some experiments have used this technique to investigate the toxicity of single and mixed VOCs, as well as the compounds generated during the total catalytic oxidation of VOCs. By measuring the activation of XMEs, which are conventionally induced by polycyclic organic compounds, as well as the activation of AhR, in lung cells exposed to emissions from the catalytic degradation of toluene, the formation of high molecular weight compounds in total catalytic oxidation of VOCs can be deduced.

The toxicological study used to validate the system revealed the existence of by-products such as PAHs that were not discovered by the standard analytical method after the catalytic test. Therefore, adding an adsorption system seems to be a promising approach for thorough purification and validation of the catalytic processes. In this context, physico-chemical characterization of gaseous effluent is essential to implement an adapted and efficient VOC treatment technology. Data concerning the process, the chemicals used, and the effluent parameters (temperature, humidity, dust content, pressure, flow, *etc.*) must be collected first. Then, chemical analysis can be performed on a laboratory scale on the raw materials in order to prepare accurate on-site measurements. At last, continuous (e.g., THC analyzer) and semi-continuous (e.g., specific on-line analyzers, sampling on sorbent tubes, impingers, and containers) analytical techniques can be deployed on site for detailed evaluation. Continuous measurements give valuable information concerning the emission profile (cyclic or regular process) and the global concentration level, whereas semi-continuous techniques give detailed information about the specific VOCs involved. Depending on the industrial process studied, the VOC mixture to be treated can be quite complex and contain several chemical groups (e.g., aromatics, alcohol, esters, *etc.*), which may not react in the same way to the treatment technique.

In this review, three coupling techniques are presented, outlining their advantages and characteristics for effective removal of hazardous VOCs:

• Adsorption-catalytic oxidation:

Adsorption and catalytic oxidation are both efficient ways of environmental remediation of VOCs, whereas these techniques are sometimes not sufficient for some industrial applications, which produce low concentrated VOC emissions. Coupled, these systems become more adapted to treat diluted gaseous streams of VOCs (> 1%) since the adsorbent helps ensure a pre-concentration of VOCs before their elimination by catalytic oxidation. Adsorbents can act as solid catalysts, can be used as a support for a catalytic phase ensuring a high dispersion of the active species, and can be used prior to the catalytic set to eliminate organic or inorganic compounds (such as H_2S). The most used adsorbents cited in the literature are activated carbon (AC), biochar, zeolites, *etc.* Experimental conditions are important to surpass some of the drawbacks these materials can present. Hybrid adsorption–catalytic technology exhibiting high adsorption capacity, catalytic activity, and selectivity is provided as a new practical, efficient, and economical alternative to the conventional VOC removal treatments for controlling small concentrations of VOCs in industrial emissions.

• Adsorption-plasma catalysis:

Although NTP has been proposed as an end-of-pipe technology for the removal of VOCs, the formation of toxic by-products is still the major hindrance to the commercialization of this technique. The main strength of plasma catalysis lies in the synergetic effect of the two individual technologies, which enhances the mineralization efficiency and reduces the formation of unwanted by-products by catalysis. For in-plasma catalysis (IPC), the catalytic material is placed either within the plasma discharge or in the downstream of the plasma discharge (post-plasma catalysis). Several points are important for a catalyst suitable for NTP environment: its stability in plasma and in situ regeneration by NTP exposure. Although plasma catalysis has been proven more efficient than the individual techniques for VOC abatement, the treatment of a large volume of exhaust gas containing a very low concentration of VOCs needs an alternative approach: adsorption-plasma catalysis (APC).

• Adsorption-photocatalysis:

The adsorption-photocatalysis coupling technology is also one of the effective and promising methods for VOC removal. Compared with the high temperature and pressure adopted during adsorption-catalysis and plasma catalysis processes, the adsorption-photocatalysis process gives rise to obvious advantages in VOC removal such as excellent elimination efficiency, low energy depletion, and being environmentally friendly. Metal oxides are major candidates for VOC elimination via adsorption-photocatalysis coupling. Generally, several factors such as humidity, airflow rate, light source, and the initial VOC concentration significantly influence adsorption-photocatalysis coupling for VOC removal. As a result, the adsorption-photocatalysis coupling reaction system is more likely to treat VOCs at a relatively low concentration.

Therefore, for any industrial emission, one of these coupling techniques should provide complete, low-energy VOC removal. On-site characterization is essential to making the choice, and a toxicological validation is recommended to determine if an additional coupling adsorbent is needed for the complete removal of VOCs.

DECLARATIONS

Acknowledgement

The authors want to acknowledge Karen Leus (Univ. Ghent, Research Unit Plasma Technology) for her contribution in obtaining the copyrights permissions of the figures and tables of the adsorption/plasma catalysis part in this review.

Authors' contributions

This review is the result of a collaborative work between different teams and laboratories in the Interreg project:

• Toxicity of VOCs:

-Substantial contributions to conception, data curation and design of the study: Billet S, Landkocz Y, Méausoone C, Jaber N, Courcot D

-Writing-original draft preparation and review editing: Billet S

• Measurements of VOCs:

-Substantial contributions to conception, data curation and design of the study, writing-original draft preparation and review editing: Cazier F, Dewaele D, Genevray P

• Adsorption/catalysis of VOCs:

-Substantial contributions to conception, data curation and design of the study: El Khawaja R, Poupin C, Cousin R, Heymans N, De Weireld G, Siffert S

-Writing-original draft preparation and review editing: El Khawaja R, Siffert S

• Adsorption/plasma catalysis of VOCs:

-Substantial contributions to conception, data curation and design of the study: Veerapandian SKP, Bitar R, Abdallah G, Sonar S, Morent R, De Geyter N, Löfberg A, Lamonier JF, Giraudon JM

-Writing-original draft preparation: Veerapandian SKP, Bitar R

• Adsorption/photocatalysis of VOCs:

-Substantial contributions to conception, data curation and design of the study, writing-original draft preparation and review: Barakat T, Ding Y, Su BL

All authors contributed to the discussion and the revision of the paper. They have all read and agreed to the published version of the manuscript.

Availability of data and materials
Not applicable.

Financial support and sponsorship
The "DepollutAir" project (grant number 1.1.18) of the European Program INTERREG V France-Wallonie-Vlaanderen (FEDER), Région Wallone and Région Hauts-de-France are acknowledged for the funding and their support for this work.

Conflicts of interest
All authors declared that there are no conflicts of interest.

Ethical approval and consent to participate
Not applicable.

Consent for publication
Not applicable.

REFERENCES
1. World Health Organization. Ambient air pollution: a global assessment of exposure and burden of disease; 2016. Available from: https://apps.who.int/iris/handle/10665/250141 [Last accessed on 28 Jun 2022].
2. Dehghani M, Fazlzadeh M, Sorooshian A, et al. Characteristics and health effects of BTEX in a hot spot for urban pollution. *Ecotoxicol Environ Saf* 2018;155:133-43. DOI PubMed
3. Billionnet C, Gay E, Kirchner S, Leynaert B, Annesi-Maesano I. Quantitative assessments of indoor air pollution and respiratory health in a population-based sample of French dwellings. *Environ Res* 2011;111:425-34. DOI PubMed
4. Lim SK, Shin HS, Yoon KS, et al. Risk assessment of volatile organic compounds benzene, toluene, ethylbenzene, and xylene (BTEX) in consumer products. *J Toxicol Environ Health A* 2014;77:1502-21. DOI PubMed
5. Parra M, Elustondo D, Bermejo R, Santamaría J. Quantification of indoor and outdoor volatile organic compounds (VOCs) in pubs and cafés in Pamplona, Spain. *Atmospheric Environment* 2008;42:6647-54. DOI
6. Waring MS, Siegel JA. An evaluation of the indoor air quality in bars before and after a smoking ban in Austin, Texas. *J Expo Sci Environ Epidemiol* 2007;17:260-8. DOI PubMed
7. Lan Q, Zhang L, Li G, et al. Hematotoxicity in workers exposed to low levels of benzene. *Science* 2004;306:1774-6. DOI PubMed PMC
8. Baan R, Grosse Y, Straif K, et al. A review of human carcinogens - part F: chemical agents and related occupations. *The Lancet Oncology* 2009;10:1143-4. DOI PubMed
9. Guha N, Loomis D, Grosse Y, et al. Carcinogenicity of trichloroethylene, tetrachloroethylene, some other chlorinated solvents, and their metabolites. *The Lancet Oncology* 2012;13:1192-3. DOI PubMed
10. Marques MM, Beland FA, Lachenmeier DW, et al. Carcinogenicity of acrolein, crotonaldehyde, and arecoline. *The Lancet Oncology* 2021;22:19-20. DOI PubMed
11. Plenge-Bönig A, Karmaus W. Exposure to toluene in the printing industry is associated with subfecundity in women but not in men. *Occup Environ Med* 1999;56:443-8. DOI
12. Svensson BG, Nise G, Erfurth EM, Nilsson A, Skerfving S. Hormone status in occupational toluene exposure. *Am J Ind Med* 1992;22:99-107. DOI PubMed
13. Paterson CA, Sharpe RA, Taylor T, Morrissey K. Indoor PM2.5, VOCs and asthma outcomes: a systematic review in adults and their home environments. *Environ Res* 2021;202:111631. DOI PubMed
14. Monteil C. Acrolein toxicity: comparative in vitro study with lung slices and pneumocytes type II cell line from rats. *Toxicology* 1999;133:129-38. DOI PubMed
15. Win-Shwe TT, Fujimaki H. Neurotoxicity of toluene. *Toxicol Lett* 2010;198:93-9. DOI PubMed
16. Bolden AL, Kwiatkowski CF, Colborn T. New look at BTEX: are ambient levels a problem? *Environ Sci Technol* 2015;49:5261-76. DOI PubMed
17. Hirsch T, Weiland SK, von Mutius E, et al. Inner city air pollution and respiratory health and atopy in children. *Eur Respir J* 1999;14:669-77. DOI PubMed
18. Rumchev K, Spickett J, Bulsara M, Phillips M, Stick S. Association of domestic exposure to volatile organic compounds with asthma

in young children. *Thorax* 2004;59:746-51. DOI PubMed PMC
19. Hulin M, Caillaud D, Annesi-Maesano I. Indoor air pollution and childhood asthma: variations between urban and rural areas. *Indoor Air* 2010;20:502-14. DOI PubMed
20. Ortega C, Hernandez-trujillo V. Exposure to indoor endocrine-disrupting chemicals and childhood asthma and obesity. *Pediatrics* 2019;144:S42-S42. DOI PubMed
21. Billionnet C, Sherrill D, Annesi-Maesano I; GERIE Study. Estimating the health effects of exposure to multi-pollutant mixture. *Ann Epidemiol* 2012;22:126-41. DOI PubMed
22. Arif AA, Shah SM. Association between personal exposure to volatile organic compounds and asthma among US adult population. *Int Arch Occup Environ Health* 2007;80:711-9. DOI PubMed
23. Ware JH, Spengler JD, Neas LM, et al. Respiratory and irritant health effects of ambient volatile organic compounds. The Kanawha County Health Study. *Am J Epidemiol* 1993;137:1287-301. DOI PubMed
24. Duong A, Steinmaus C, McHale CM, Vaughan CP, Zhang L. Reproductive and developmental toxicity of formaldehyde: a systematic review. *Mutat Res* 2011;728:118-38. DOI PubMed PMC
25. Huff JE, Eastin W, Roycroft J, Eustis SL, Haseman JK. Carcinogenesis studies of benzene, methyl benzene, and dimethyl benzenes. *Ann N Y Acad Sci* 1988;534:427-40. DOI PubMed
26. Kodavanti PR, Royland JE, Moore-Smith DA, et al. Acute and subchronic toxicity of inhaled toluene in male Long-Evans rats: oxidative stress markers in brain. *Neurotoxicology* 2015;51:10-9. DOI PubMed
27. Lash LH, Chiu WA, Guyton KZ, Rusyn I. Trichloroethylene biotransformation and its role in mutagenicity, carcinogenicity and target organ toxicity. *Mutat Res Rev Mutat Res* 2014;762:22-36. DOI PubMed PMC
28. Muralidhara S, Ramanathan R, Mehta SM, Lash LH, Acosta D, Bruckner JV. Acute, subacute, and subchronic oral toxicity studies of 1,1-dichloroethane in rats: application to risk evaluation. *Toxicol Sci* 2001;64:135-45. DOI PubMed
29. Zhang Y, Yang Y, He X, et al. The cellular function and molecular mechanism of formaldehyde in cardiovascular disease and heart development. *J Cell Mol Med* 2021;25:5358-71. DOI PubMed PMC
30. Toxicology Program. NTP toxicology and carcinogenesis studies of benzene (CAS No. 71-43-2) in F344/N rats and B6C3F1 mice (Gavage Studies). *Natl Toxicol Program Tech Rep Ser* 1986;289:1-277. DOI
31. Gałęzowska G, Chraniuk M, Wolska L. In vitro assays as a tool for determination of VOCs toxic effect on respiratory system: a critical review. *TrAC Trends in Analytical Chemistry* 2016;77:14-22. DOI
32. Norbäck D, Björnsson E, Janson C, Widström J, Boman G. Asthmatic symptoms and volatile organic compounds, formaldehyde, and carbon dioxide in dwellings. *Occup Environ Med* 1995;52:388-95. DOI PubMed PMC
33. Rasmussen RE. In vitro systems for exposure of lung cells to NO2 and O3. *J Toxicol Environ Health* 1984;13:397-411. DOI PubMed
34. Aufderheide M, Knebel J, Ritter D. Novel approaches for studying pulmonary toxicity in vitro. *Toxicology Letters* 2003;140-141:205-11. DOI PubMed
35. Kim HR, Cho HS, Shin DY, Chung KH. Novel approach to study the cardiovascular effects and mechanism of action of urban particulate matter using lung epithelial-endothelial tetra-culture system. *Toxicol In Vitro* 2017;38:33-40. DOI PubMed
36. Thorne D, Kilford J, Payne R, et al. Development of a BALB/c 3T3 neutral red uptake cytotoxicity test using a mainstream cigarette smoke exposure system. *BMC Res Notes* 2014;7:367. DOI PubMed PMC
37. Al Zallouha M, Landkocz Y, Brunet J, et al. Usefulness of toxicological validation of VOCs catalytic degradation by air-liquid interface exposure system. *Environ Res* 2017;152:328-35. DOI PubMed
38. Brunet J, Genty E, Landkocz Y, et al. Identification of by-products issued from the catalytic oxidation of toluene by chemical and biological methods. *Comptes Rendus Chimie* 2015;18:1084-93. DOI
39. Livak KJ, Schmittgen TD. Analysis of relative gene expression data using real-time quantitative PCR and the 2 (-Delta Delta C (T)) Method. *Methods* 2001;25:402-8. DOI PubMed
40. Méausoone C, Landkocz Y, Cazier F, Seigneur M, Courcot D, Billet S. Toxicological responses of BEAS-2B cells to repeated exposures to benzene, toluene, m-xylene, and mesitylene using air-liquid interface method. *J Appl Toxicol* 2021;41:1262-74. DOI PubMed
41. Billet S, Garçon G, Dagher Z, et al. Ambient particulate matter (PM2.5): physicochemical characterization and metabolic activation of the organic fraction in human lung epithelial cells (A549). *Environ Res* 2007;105:212-23. DOI PubMed
42. Kim S, Lan Q, Waidyanatha S, et al. Genetic polymorphisms and benzene metabolism in humans exposed to a wide range of air concentrations. *Pharmacogenet Genomics* 2007;17:789-801. DOI PubMed
43. Gutierrez-Ruiz MC, Gomez Quiroz LE, Hernandez E, et al. Cytokine response and oxidative stress produced by ethanol, acetaldehyde and endotoxin treatment in HepG2 cells. *Isr Med Assoc J* 2001;3:131-6. PubMed
44. Méausoone C, El Khawaja R, Tremolet G, et al. In vitro toxicological evaluation of emissions from catalytic oxidation removal of industrial VOCs by air/liquid interface (ALI) exposure system in repeated mode. *Toxicol In Vitro* 2019;58:110-7. DOI PubMed
45. Cazier F, Dewaele D, Nouali H, Vasseur A. Improvement of the on site VOC measurement in industrial emissions, CEM 2006, Ademe 7ème Conférence Int. Sur La Mes. Polluants à l'émission, 31 Janvier - 2 Février 2006, Paris;2006.
46. Brown R, Purnell C. Collection and analysis of trace organic vapour pollutants in ambient atmospheres. *Journal of Chromatography A* 1979;178:79-90. DOI
47. Bishop RW, Valis RJ. A laboratory evaluation of sorbent tubes for use with a thermal desorption gas chromatography-mass selective

detection technique. *Journal of Chromatographic Science* 1990;28:589-93. DOI

48. Bruner F, Crescentini G, Mangani F. Graphitized carbon black: a unique adsorbent for gas chromatography and related techniques. *Chromatographia* 1990;30:565-72. DOI
49. Mccaffrey CA, Maclachlan J, Brookes BI. Adsorbent tube evaluation for the preconcentration of volatile organic compounds in air for analysis by gas chromatography-mass spectrometry. *Analyst* 1994;119:897-902. DOI
50. No CBPECCAS. Sampling method for volatile organic compounds (SMVOC); 1996. Available from: https://swap.stanford.edu/20140413191218/http://www.epa.gov/epawaste/hazard/testmethods/sw846/pdfs/0031.pdf [Last accessed on 28 Jun 2022].
51. British HSE method MDHS104: volatile organic compounds in air.
52. Thomas R, Marotta L, Provost R. A single-method approach for the analysis of volatile and semivolatile organic compounds in air using thermal desorption coupled with GC-MS. *LCGC Europe* 2014. Available from: https://www.chromatographyonline.com/view/single[Last accessed on 28 Jun 2022]
53. Kamal MS, Razzak SA, Hossain MM. Catalytic oxidation of volatile organic compounds (VOCs) - a review. *Atmospheric Environment* 2016;140:117-34. DOI PubMed
54. Liotta L. Catalytic oxidation of volatile organic compounds on supported noble metals. *Applied Catalysis B: Environmental* 2010;100:403-12. DOI
55. Jabłońska M, Król A, Kukulska-zając E, et al. Zeolites Y modified with palladium as effective catalysts for low-temperature methanol incineration. *Applied Catalysis B: Environmental* 2015;166-167:353-65. DOI
56. Tidahy H, Siffert S, Wyrwalski F, Lamonier J, Aboukaïs A. Catalytic activity of copper and palladium based catalysts for toluene total oxidation. *Catalysis Today* 2007;119:317-20. DOI
57. Cecilia J, Arango-díaz A, Marrero-jerez J, et al. Catalytic behaviour of CuO-CeO2 systems prepared by different synthetic methodologies in the CO-PROX reaction under CO2-H2O feed stream. *Catalysts* 2017;7:160. DOI
58. Romero D, Chlala D, Labaki M, et al. Removal of toluene over NaX zeolite exchanged with Cu2+. *Catalysts* 2015;5:1479-97. DOI
59. Castaño MH, Molina R, Moreno S. Mn-Co-Al-Mg mixed oxides by auto-combustion method and their use as catalysts in the total oxidation of toluene. *Journal of Molecular Catalysis A: Chemical* 2013;370:167-74. DOI
60. Zhang W, Qu Z, Li X, Wang Y, Ma D, Wu J. Comparison of dynamic adsorption/desorption characteristics of toluene on different porous materials. *Journal of Environmental Sciences* 2012;24:520-8. DOI PubMed
61. Wang Y, Su X, Xu Z, et al. Preparation of surface-functionalized porous clay heterostructures via carbonization of soft-template and their adsorption performance for toluene. *Applied Surface Science* 2016;363:113-21. DOI
62. Yang X, Yi H, Tang X, et al. Behaviors and kinetics of toluene adsorption-desorption on activated carbons with varying pore structure. *J Environ Sci (China)* 2018;67:104-14. DOI PubMed
63. Lillo-ródenas M, Cazorla-amorós D, Linares-solano A. Behaviour of activated carbons with different pore size distributions and surface oxygen groups for benzene and toluene adsorption at low concentrations. *Carbon* 2005;43:1758-67. DOI
64. Xie H, Shen Y, Zhou G, Chen S, Song Y, Ren J. Effect of preparation conditions on the hydrogen storage capacity of activated carbon adsorbents with super-high specific surface areas. *Materials Chemistry and Physics* 2013;141:203-7. DOI
65. Jain A, Balasubramanian R, Srinivasan M. Production of high surface area mesoporous activated carbons from waste biomass using hydrogen peroxide-mediated hydrothermal treatment for adsorption applications. *Chemical Engineering Journal* 2015;273:622-9. DOI
66. Zhang Z, Jiang C, Li D, et al. Micro-mesoporous activated carbon simultaneously possessing large surface area and ultra-high pore volume for efficiently adsorbing various VOCs. *Carbon* 2020;170:567-79. DOI
67. Srivastava I, Singh PK, Gupta T, Sankararamakrishnan N. Preparation of mesoporous carbon composites and its highly enhanced removal capacity of toxic pollutants from air. *Journal of Environmental Chemical Engineering* 2019;7:103271. DOI
68. Nasrullah A, Saad B, Bhat A, et al. Mangosteen peel waste as a sustainable precursor for high surface area mesoporous activated carbon: characterization and application for methylene blue removal. *Journal of Cleaner Production* 2019;211:1190-200. DOI
69. Wang J, Wu Z, Niu Q, et al. Highly efficient adsorptive removal of toluene using silicon-modified activated carbon with improved fire resistance. *J Hazard Mater* 2021;415:125753. DOI PubMed
70. Monneyron P, Manero M-, Manero S. A combined selective adsorption and ozonation process for VOCs removal from air. *Can J Chem Eng* 2007;85:326-32. DOI
71. Bläker C, Pasel C, Luckas M, Dreisbach F, Bathen D. Investigation of load-dependent heat of adsorption of alkanes and alkenes on zeolites and activated carbon. *Microporous and Mesoporous Materials* 2017;241:1-10. DOI
72. Zhang X, Gao B, Zheng Y, et al. Biochar for volatile organic compound (VOC) removal: Sorption performance and governing mechanisms. *Bioresour Technol* 2017;245:606-14. DOI PubMed
73. Kupryianchyk D, Hale S, Zimmerman AR, et al. Sorption of hydrophobic organic compounds to a diverse suite of carbonaceous materials with emphasis on biochar. *Chemosphere* 2016;144:879-87. DOI PubMed
74. Mohamed AR, Mohammadi M, Darzi GN. Preparation of carbon molecular sieve from lignocellulosic biomass: A review. *Renewable and Sustainable Energy Reviews* 2010;14:1591-9. DOI
75. Molina-sabio M, Gonzalez M, Rodriguez-reinoso F, Sepúlveda-escribano A. Effect of steam and carbon dioxide activation in the micropore size distribution of activated carbon. *Carbon* 1996;34:505-9. DOI
76. Feng D, Guo D, Zhang Y, et al. Functionalized construction of biochar with hierarchical pore structures and surface O-/N-containing

groups for phenol adsorption. *Chemical Engineering Journal* 2021;410:127707. DOI
77. Han Y, Boateng AA, Qi PX, Lima IM, Chang J. Heavy metal and phenol adsorptive properties of biochars from pyrolyzed switchgrass and woody biomass in correlation with surface properties. *J Environ Manage* 2013;118:196-204. DOI PubMed
78. Dehkhoda AM, Gyenge E, Ellis N. A novel method to tailor the porous structure of KOH-activated biochar and its application in capacitive deionization and energy storage. *Biomass and Bioenergy* 2016;87:107-21. DOI
79. Lonappan L, Liu Y, Rouissi T, Brar SK, Surampalli RY. Development of biochar-based green functional materials using organic acids for environmental applications. *Journal of Cleaner Production* 2020;244:118841. DOI
80. Kumar A, Singh E, Khapre A, Bordoloi N, Kumar S. Sorption of volatile organic compounds on non-activated biochar. *Bioresour Technol* 2020;297:122469. DOI PubMed
81. Vikrant K, Na C, Younis SA, Kim K, Kumar S. Evidence for superiority of conventional adsorbents in the sorptive removal of gaseous benzene under real-world conditions: test of activated carbon against novel metal-organic frameworks. *Journal of Cleaner Production* 2019;235:1090-102. DOI
82. Rawal A, Joseph SD, Hook JM, et al. Mineral-biochar composites: molecular structure and porosity. *Environ Sci Technol* 2016;50:7706-14. DOI PubMed
83. Yang G, Chen H, Qin H, Feng Y. Amination of activated carbon for enhancing phenol adsorption: Effect of nitrogen-containing functional groups. *Applied Surface Science* 2014;293:299-305. DOI
84. Soscún H, Castellano O, Hernández J, Hinchliffe A. Acidity of the Brönsted acid sites of zeolites. *Int J Quantum Chem* 2001;82:143-50. DOI
85. Guisnet M, Pinard L. Zéolithes - De la synthèse aux applications. *Tech l'ingénieur* 2018. DOI
86. Brodu N, Sochard S, Andriantsiferana C, Pic JS, Manero MH. Fixed-bed adsorption of toluene on high silica zeolites: experiments and mathematical modelling using LDF approximation and a multisite model. *Environ Technol* 2015;36:1807-18. DOI PubMed
87. Kim K, Ahn H. The effect of pore structure of zeolite on the adsorption of VOCs and their desorption properties by microwave heating. *Microporous and Mesoporous Materials* 2012;152:78-83. DOI
88. Li X, Wang J, Guo Y, Zhu T, Xu W. Adsorption and desorption characteristics of hydrophobic hierarchical zeolites for the removal of volatile organic compounds. *Chemical Engineering Journal* 2021;411:128558. DOI
89. Yin T, Meng X, Jin L, Yang C, Liu N, Shi L. Prepared hydrophobic Y zeolite for adsorbing toluene in humid environment. *Microporous and Mesoporous Materials* 2020;305:110327. DOI
90. Lv Y, Sun J, Yu G, et al. Hydrophobic design of adsorbent for VOC removal in humid environment and quick regeneration by microwave. *Microporous and Mesoporous Materials* 2020;294:109869. DOI
91. Yang R. Gas separation by adsorption processes. *Chemical Engineering Science* 1988;43:985. DOI
92. Meier M, Turner M, Vallee S, Conner WC, Lee KH, Yngvesson KS. Microwave regeneration of zeolites in a 1 meter column. *AIChE Journal* 2009;55:1906-13. DOI
93. Cherbański R, Komorowska-durka M, Stefanidis GD, Stankiewicz AI. Microwave swing regeneration vs. temperature swing regeneration - comparison of desorption kinetics. *Ind Eng Chem Res* 2011;50:8632-44. DOI
94. Guillemot M, Mijoin J, Mignard S, Magnoux P. Volatile organic compounds (VOCs) removal over dual functional adsorbent/catalyst system. *Applied Catalysis B: Environmental* 2007;75:249-55. DOI
95. Urbutis A, Kitrys S. Dual function adsorbent-catalyst CuO-CeO2/NaX for temperature swing oxidation of benzene, toluene and xylene. *Open Chemistry* 2014;12:492-501. DOI
96. Wang Y, Yang D, Li S, Chen M, Guo L, Zhou J. Ru/hierarchical HZSM-5 zeolite as efficient bi-functional adsorbent/catalyst for bulky aromatic VOCs elimination. *Microporous and Mesoporous Materials* 2018;258:17-25. DOI
97. Nigar H, Julián I, Mallada R, Santamaría J. Microwave-assisted catalytic combustion for the efficient continuous cleaning of VOC-containing air streams. *Environ Sci Technol* 2018;52:5892-901. DOI PubMed
98. Roland U, Kraus M, Holzer F, Trommler U, Kopinke F. Selective dielectric heating for efficient adsorptive-catalytic cleaning of contaminated gas streams. *Applied Catalysis A: General* 2014;474:244-9. DOI
99. Joung H, Kim J, Oh J, You D, Park H, Jung K. Catalytic oxidation of VOCs over CNT-supported platinum nanoparticles. *Applied Surface Science* 2014;290:267-73. DOI
100. Kim K, Kang C, You Y, et al. Adsorption-desorption characteristics of VOCs over impregnated activated carbons. *Catalysis Today* 2006;111:223-8. DOI
101. Minh NT, Thanh LD, Trung BC, An NT, Long NQ. Dual functional adsorbent/catalyst of nano-gold/metal oxides supported on carbon grain for low-temperature removal of toluene in the presence of water vapor. *Clean Techn Environ Policy* 2018;20:1861-73. DOI
102. Zhang J, Rao C, Peng H, et al. Enhanced toluene combustion performance over Pt loaded hierarchical porous MOR zeolite. *Chemical Engineering Journal* 2018;334:10-8. DOI
103. Yao S, Fang W, Wang B, et al. Rh1Cu3/ZSM-5 as an efficient bifunctional catalyst/adsorbent for VOCs abatement. *Catal Lett* 2022;152:771-80. DOI
104. Aziz A, Sajjad M, Kim M, Kim KS. An efficient Co-ZSM-5 catalyst for the abatement of volatile organics in air: effect of the synthesis protocol. *Int J Environ Sci Technol* 2018;15:707-18. DOI
105. Beauchet R. Oxydation catalytique de divers composes organiques volatils (COV) à l'aide de catalyseurs zeolithiques; 2008. DOI
106. Baek S, Kim J, Ihm S. Design of dual functional adsorbent/catalyst system for the control of VOC's by using metal-loaded

hydrophobic Y-zeolites. *Catalysis Today* 2004;93-95:575-81. DOI

107. Wu SM, Yang XY, Janiak C. Confinement effects in zeolite-confined noble metals. *Angew Chem Int Ed Engl* 2019;58:12340-54. DOI PubMed
108. Liu G, Tian Y, Zhang B, Wang L, Zhang X. Catalytic combustion of VOC on sandwich-structured Pt@ZSM-5 nanosheets prepared by controllable intercalation. *J Hazard Mater* 2019;367:568-76. DOI PubMed
109. Chai Y, Shang W, Li W, et al. Noble metal particles confined in zeolites: synthesis, characterization, and applications. *Adv Sci (Weinh)* 2019;6:1900299. DOI PubMed PMC
110. Chen C, Chen F, Zhang L, et al. Importance of platinum particle size for complete oxidation of toluene over Pt/ZSM-5 catalysts. *Chem Commun (Camb)* 2015;51:5936-8. DOI PubMed
111. Dong T, Liu W, Ma M, et al. Hierarchical zeolite enveloping Pd-CeO2 nanowires: an efficient adsorption/catalysis bifunctional catalyst for low temperature propane total degradation. *Chemical Engineering Journal* 2020;393:124717. DOI
112. Soares OSGP, Fonseca AM, Parpot P, Órfão JJM, Pereira MFR, Neves IC. Oxidation of volatile organic compounds by highly efficient metal zeolite catalysts. *ChemCatChem* 2018;10:3754-60. DOI
113. Shi C, Chen B, Li X, Crocker M, Wang Y, Zhu A. Catalytic formaldehyde removal by "storage-oxidation" cycling process over supported silver catalysts. *Chemical Engineering Journal* 2012;200-202:729-37. DOI
114. Adebayo BO, Krishnamurthy A, Rownaghi AA, Rezaei F. Toluene abatement by simultaneous adsorption and oxidation over mixed-metal oxides. *Ind Eng Chem Res* 2020;59:13762-72. DOI
115. Kim H. Nonthermal plasma processing for air-pollution control: a historical review, current issues, and future prospects. *Plasma Process Polym* 2004;1:91-110. DOI
116. Fridman A. Plasma chemistry. New york: Cambridge University press; 2008. DOI
117. Vandenbroucke AM, Morent R, De Geyter N, Leys C. Non-thermal plasmas for non-catalytic and catalytic VOC abatement. *J Hazard Mater* 2011;195:30-54. DOI PubMed
118. An HT, Pham Huu T, Le Van T, Cormier J, Khacef A. Application of atmospheric non thermal plasma-catalysis hybrid system for air pollution control: toluene removal. *Catalysis Today* 2011;176:474-7. DOI
119. Holzer F, Kopinke FD, Roland U. Influence of ferroelectric materials and catalysts on the performance of non-thermal plasma (NTP) for the removal of air pollutants. *Plasma Chem Plasma Process* 2005;25:595-611. DOI
120. Zhao D, Li X, Shi C, Fan H, Zhu A. Low-concentration formaldehyde removal from air using a cycled storage-discharge (CSD) plasma catalytic process. *Chemical Engineering Science* 2011;66:3922-9. DOI
121. Urashima K, Jen-shih Chang. Removal of volatile organic compounds from air streams and industrial flue gases by non-thermal plasma technology. *IEEE Trans Dielect Electr Insul* 2000;7:602-14. DOI
122. Chen HL, Lee HM, Chen SH, Chang MB, Yu SJ, Li SN. Removal of volatile organic compounds by single-stage and two-stage plasma catalysis systems: a review of the performance enhancement mechanisms, current status, and suitable applications. *Environ Sci Technol* 2009;43:2216-27. DOI PubMed
123. Ollegott K, Wirth P, Oberste□beulmann C, Awakowicz P, Muhler M. Fundamental properties and applications of dielectric barrier discharges in plasma-catalytic processes at atmospheric pressure. *Chemie Ingenieur Technik* 2020;92:1542-58. DOI
124. Chang T, Shen Z, Huang Y, et al. Post-plasma-catalytic removal of toluene using MnO2-Co3O4 catalysts and their synergistic mechanism. *Chemical Engineering Journal* 2018;348:15-25. DOI
125. Karuppiah J, Sivachandiran L, Karvembu R, Subrahmanyam C. Catalytic nonthermal plasma reactor for the abatement of low concentrations of isopropanol. *Chemical Engineering Journal* 2010;165:194-9. DOI
126. Tang X, Feng F, Ye L, et al. Removal of dilute VOCs in air by post-plasma catalysis over Ag-based composite oxide catalysts. *Catalysis Today* 2013;211:39-43. DOI
127. Sultana S, Vandenbroucke A, Mora M, et al. Post plasma-catalysis for trichloroethylene decomposition over CeO2 catalyst: Synergistic effect and stability test. *Applied Catalysis B: Environmental* 2019;253:49-59. DOI
128. Yang S, Yang H, Yang J, et al. Three-dimensional hollow urchin α-MnO2 for enhanced catalytic activity towards toluene decomposition in post-plasma catalysis. *Chemical Engineering Journal* 2020;402:126154. DOI
129. Neyts EC, Bogaerts A. Understanding plasma catalysis through modelling and simulation - a review. *J Phys D: Appl Phys* 2014;47:224010. DOI
130. Mirzaei A, Kim J, Kim HW, Kim SS. Resistive-based gas sensors for detection of benzene, toluene and xylene (BTX) gases: a review. *J Mater Chem C* 2018;6:4342-70. DOI
131. Magureanu M, Mandache NB, Eloy P, Gaigneaux EM, Parvulescu VI. Plasma-assisted catalysis for volatile organic compounds abatement. *Applied Catalysis B: Environmental* 2005;61:12-20. DOI
132. Huang HB, Ye DQ, Leung DYC. Removal of toluene using UV-irradiated and nonthermal plasma-driven photocatalyst system. *J Environ Eng* 2010;136:1231-6. DOI
133. Subrahmanyam C, Renken A, Kiwi-minsker L. Catalytic non-thermal plasma reactor for abatement of toluene. *Chemical Engineering Journal* 2010;160:677-82. DOI
134. Durme J, Dewulf J, Demeestere K, Leys C, Van Langenhove H. Post-plasma catalytic technology for the removal of toluene from indoor air: effect of humidity. *Applied Catalysis B: Environmental* 2009;87:78-83. DOI
135. Hayashi K, Yasui H, Tanaka M, Futamura S, Kurita S, Aoyagi K. Temperature dependence of toluene decomposition behavior in the discharge-catalyst hybrid reactor. *IEEE Trans on Ind Applicat* 2009;45:1553-8. DOI

136. Ban J, Son Y, Kang M, Choung S. Highly concentrated toluene decomposition on the dielectric barrier discharge (DBD) plasma-photocatalytic hybrid system with Mn-Ti-incorporated mesoporous silicate photocatalyst (Mn-Ti-MPS). *Applied Surface Science* 2006;253:535-42. DOI
137. Huang H, Ye D. Combination of photocatalysis downstream the non-thermal plasma reactor for oxidation of gas-phase toluene. *J Hazard Mater* 2009;171:535-41. DOI PubMed
138. Harling AM, Glover DJ, Whitehead JC, Zhang K. The role of ozone in the plasma-catalytic destruction of environmental pollutants. *Applied Catalysis B: Environmental* 2009;90:157-61. DOI
139. Delagrange S, Pinard L, Tatibouet J. Combination of a non-thermal plasma and a catalyst for toluene removal from air: Manganese based oxide catalysts. *Applied Catalysis B: Environmental* 2006;68:92-8. DOI
140. Demidyuk V, Whitehead JC. Influence of temperature on gas-phase toluene decomposition in plasma-catalytic system. *Plasma Chem Plasma Process* 2007;27:85-94. DOI
141. Harling AM, Demidyuk V, Fischer SJ, Whitehead JC. Plasma-catalysis destruction of aromatics for environmental clean-up: effect of temperature and configuration. *Applied Catalysis B: Environmental* 2008;82:180-9. DOI
142. Demidiouk V, Jae Ou Chae. Decomposition of volatile organic compounds in plasma-catalytic system. *IEEE Trans Plasma Sci* 2005;33:157-61. DOI
143. Li D, Yakushiji D, Kanazawa S, Ohkubo T, Nomoto Y. Decomposition of toluene by streamer corona discharge with catalyst. *Journal of Electrostatics* 2002;55:311-9. DOI
144. Durme J, Dewulf J, Sysmans W, Leys C, Van Langenhove H. Efficient toluene abatement in indoor air by a plasma catalytic hybrid system. *Applied Catalysis B: Environmental* 2007;74:161-9. DOI
145. Ge H, Hu D, Li X, Tian Y, Chen Z, Zhu Y. Removal of low-concentration benzene in indoor air with plasma-MnO 2 catalysis system. *Journal of Electrostatics* 2015;76:216-21. DOI
146. Jiang N, Qiu C, Guo L, et al. Post plasma-catalysis of low concentration VOC over alumina-supported silver catalysts in a surface/packed-bed hybrid discharge reactor. *Water Air Soil Pollut* 2017:228. DOI
147. Hu J, Jiang N, Li J, Shang K, Lu N, Wu Y. Degradation of benzene by bipolar pulsed series surface/packed-bed discharge reactor over MnO_2-TiO_2/zeolite catalyst. *Chemical Engineering Journal* 2016;293:216-24. DOI
148. Zhang S, Shen X, Liang J. Atmospheric pressure oxidation of dilute xylene using plasma-assisted MnOX catalysis system with different precursors. *Molecular Catalysis* 2019;467:87-94. DOI
149. Wang L, He H, Zhang C, Wang Y, Zhang B. Effects of precursors for manganese-loaded γ-Al2O3 catalysts on plasma-catalytic removal of o-xylene. *Chemical Engineering Journal* 2016;288:406-13. DOI
150. Piroi D, Magureanu M, Mandache NB, Parvulescu VI. The decomposition of p-xylene in air by plasma-assisted catalysis. 2008 17th International Conference on Gas Discharges and Their Applications; 2008. p. 473-6. Available from: https://ieeexplore.ieee.org/abstract/document/5379364 [Last accessed on 28 Jun 2022].
151. Fan X, Zhu TL, Wang MY, Li XM. Removal of low-concentration BTX in air using a combined plasma catalysis system. *Chemosphere* 2009;75:1301-6. DOI PubMed
152. Oda T, Takahashi T, Yamaji K. TCE decomposition by the nonthermal plasma process concerning ozone effect. *IEEE Trans on Ind Applicat* 2004;40:1249-56. DOI
153. Han S, Oda T, Ono R. Improvement of the energy efficiency in the decomposition of dilute trichloroethylene by the barrier discharge plasma process. *IEEE Trans on Ind Applicat* 2005;41:1343-9. DOI
154. Magureanu M, Mandache NB, Hu J, Richards R, Florea M, Parvulescu VI. Plasma-assisted catalysis total oxidation of trichloroethylene over gold nano-particles embedded in SBA-15 catalysts. *Appl Catal B* 2007;76:275-81. DOI
155. Vandenbroucke A, Morent R, De Geyter N, et al. Plasma-catalytic decomposition of TCE. *Int J Plasma Environ Sci Technol* 2010;4:135-8. Available from: http://ijpest.com/Contents/04/2/PDF/04[Last accessed on 28 Jun 2022]
156. Han S, Oda T. Decomposition mechanism of trichloroethylene based on by-product distribution in the hybrid barrier discharge plasma process. *Plasma Sources Sci Technol* 2007;16:413-21. DOI
157. Vandenbroucke A, Mora M, Jiménez-sanchidrián C, et al. TCE abatement with a plasma-catalytic combined system using MnO_2 as catalyst. *Appl Catal B* 2014;156-157:94-100. DOI
158. Dinh MN, Giraudon J, Lamonier J, et al. Plasma-catalysis of low TCE concentration in air using $LaMnO_3$+δ as catalyst. *Appl Catal B* 2014;147:904-11. DOI
159. Li Y, Fan Z, Shi J, Liu Z, Shangguan W. Post plasma-catalysis for VOCs degradation over different phase structure MnO_2 catalysts. *Chem Eng J* 2014;241:251-8. DOI
160. Li Y, Fan Z, Shi J, Liu Z, Zhou J, Shangguan W. Modified manganese oxide octahedral molecular sieves M'-OMS-2 (M' = Co,Ce,Cu) as catalysts in post plasma-catalysis for acetaldehyde degradation. *Catal Today* 2015;256:178-85. DOI
161. Chang T, Shen Z, Ma C, et al. Process optimization of plasma-catalytic formaldehyde removal using MnOx–Fe_2O_3 catalysts by response surface methodology. *J. Environ Chem Eng* 2021;9:105773. DOI
162. Zhu X, Liu S, Cai Y, et al. Post-plasma catalytic removal of methanol over Mn-Ce catalysts in an atmospheric dielectric barrier discharge. *Appl Catal B* 2016;183:124-32. DOI
163. Norsic C, Tatibouët J, Batiot-dupeyrat C, Fourré E. Non thermal plasma assisted catalysis of methanol oxidation on Mn, Ce and Cu oxides supported on γ-Al_2O_3. *Chem Eng J* 2016;304:563-72. DOI
164. Karuppiah J, Linga Reddy E, Manoj Kumar Reddy P, Ramaraju B, Subrahmanyam C. Catalytic nonthermal plasma reactor for the

abatement of low concentrations of benzene. *Int J Environ Sci Technol* 2014;11:311-8. DOI

165. Guo H, Liu X, Hojo H, Yao X, Einaga H, Shangguan W. Removal of benzene by non-thermal plasma catalysis over manganese oxides through a facile synthesis method. *Environ Sci Pollut Res Int* 2019;26:8237-47. DOI PubMed
166. Xu N, Fu W, He C, et al. Benzene removal using non-thermal plasma with CuO/AC catalyst: reaction condition optimization and decomposition mechanism. *Plasma Chem Plasma Process* 2014;34:1387-402. DOI
167. Jiang N, Hu J, Li J, Shang K, Lu N, Wu Y. Plasma-catalytic degradation of benzene over Ag-Ce bimetallic oxide catalysts using hybrid surface/packed-bed discharge plasmas. *Appl Catal B* 2016;184:355-63. DOI
168. Zhu B, Zhang L, Li M, Yan Y, Zhang X, Zhu Y. High-performance of plasma-catalysis hybrid system for toluene removal in air using supported Au nanocatalysts. *Chem Eng J* 2020;381:122599. DOI
169. Wu J, Xia Q, Wang H, Li Z. Catalytic performance of plasma catalysis system with nickel oxide catalysts on different supports for toluene removal: effect of water vapor. *Appl Catal B* 2014;156-157:265-72. DOI
170. Xu W, Chen B, Jiang X, et al. Effect of calcium addition in plasma catalysis for toluene removal by Ni/ZSM-5 : acidity/basicity, catalytic activity and reaction mechanism. *J Hazard Mater* 2020;387:122004. DOI PubMed
171. Yao S, Chen Z, Xie H, et al. Highly efficient decomposition of toluene using a high-temperature plasma-catalysis reactor. *Chemosphere* 2020;247:125863. DOI PubMed
172. Wu J, Huang Y, Xia Q, Li Z. Decomposition of toluene in a plasma catalysis system with NiO, MnO_2, CeO_2, Fe_2O_3, and CuO catalysts. *Plasma Chem Plasma Process* 2013;33:1073-82. DOI
173. Wang B, Chi C, Xu M, Wang C, Meng D. Plasma-catalytic removal of toluene over CeO_2 -MnO x catalysts in an atmosphere dielectric barrier discharge. *Chem Eng J* 2017;322:679-92. DOI
174. Yu X, Dang X, Li S, Zhang J, Zhang Q, Cao L. A comparison of in- and post-plasma catalysis for toluene abatement through continuous and sequential processes in dielectric barrier discharge reactors. *J Clean Prod* 2020;276:124251. DOI
175. Xu X, Wu J, Xu W, et al. High-efficiency non-thermal plasma-catalysis of cobalt incorporated mesoporous MCM-41 for toluene removal. *Catal Today* 2017;281:527-33. DOI
176. Sudhakaran MSP, Trinh HQ, Karuppiah J, Hossian MM, Mok YS. Plasma catalytic removal of p-Xylene from air stream using γ-Al2O3 supported manganese catalyst. *Top Catal* 2017;60:944-54. DOI
177. Wang L, Zhang C, He H, Liu F, Wang C. Effect of doping metals on OMS-2/γ-Al_2O_3 catalysts for plasma-catalytic removal of. *o* ;120:6136-44. DOI
178. Wu Z, Zhou W, Zhu Z, Hao X, Zhang X. Enhanced oxidation of xylene using plasma activation of an Mn/Al_2O_3 catalyst. *IEEE Trans Plasma Sci* 2020;48:163-72. DOI
179. Zhu X, Gao X, Qin R, et al. Plasma-catalytic removal of formaldehyde over Cu-Ce catalysts in a dielectric barrier discharge reactor. *Appl Catal B* 2015;170-171:293-300. DOI
180. Liang WJ, Li J, Li JX, Zhu T, Jin YQ. Formaldehyde removal from gas streams by means of $NaNO_2$ dielectric barrier discharge plasma. *J Hazard Mater* 2010;175:1090-5. DOI PubMed
181. Ding H, Zhu A, Lu F, Xu Y, Zhang J, Yang X. Low-temperature plasma-catalytic oxidation of formaldehyde in atmospheric pressure gas streams. *J Phys D: Appl Phys* 2006;39:3603-8. DOI
182. Jia Z, Ben Amar M, Yang D, et al. Plasma catalysis application of gold nanoparticles for acetaldehyde decomposition. *Chem Eng J* 2018;347:913-22. DOI
183. Vega-gonzález A, Duten X, Sauce S. Plasma-catalysis for volatile organic compounds decomposition: complexity of the reaction pathways during acetaldehyde removal. *Catalysts* 2020;10:1146. DOI
184. Kostov K, Honda RY, Alves L, Kayama M. Characteristics of dielectric barrier discharge reactor for material treatment. *Braz J Phys* 2009;39:2. DOI
185. Chen HL, Lee HM, Chen SH, Chang MB. Review of packed-bed plasma reactor for ozone generation and air pollution control. *Ind Eng Chem Res* 2008;47:2122-30. DOI
186. Ye Z, Veerapandian SKP, Onyshchenko I, et al. An in-depth investigation of toluene decomposition with a glass beads-packed bed dielectric barrier discharge reactor. *Ind Eng Chem Res* 2017;56:10215-26. DOI
187. Kaliya Perumal Veerapandian S, Giraudon JM, De Geyter N, et al. Regeneration of hopcalite used for the adsorption plasma catalytic removal of toluene by non-thermal plasma. *J Hazard Mater* 2021;402:123877. DOI PubMed
188. Veerapandian S, Leys C, De Geyter N, Morent R. Abatement of VOCs Using packed bed non-thermal plasma reactors: a review. *Catalysts* 2017;7:113. DOI
189. Vandenbroucke AM, Morent R, Geyter ND, Leys C. Decomposition of toluene with plasma-catalysis: a review. *J Adv Oxid Technol* 2012;15:232-41. DOI
190. Feng X, Liu H, He C, Shen Z, Wang T. Synergistic effects and mechanism of a non-thermal plasma catalysis system in volatile organic compound removal: a review. *Catal Sci Technol* 2018;8:936-54. DOI
191. Durme J, Dewulf J, Leys C, Van Langenhove H. Combining non-thermal plasma with heterogeneous catalysis in waste gas treatment: a review. *Appl Catal B* 2008;78:324-33. DOI
192. Whitehead JC. Plasma–catalysis: the known knowns, the known unknowns and the unknown unknowns. *J Phys D: Appl Phys* 2016;49:243001. DOI
193. Neyts EC, Ostrikov KK, Sunkara MK, Bogaerts A. Plasma catalysis: synergistic effects at the nanoscale. *Chem Rev* 2015;115:13408-46. DOI PubMed

194. Li S, Dang X, Yu X, Abbas G, Zhang Q, Cao L. The application of dielectric barrier discharge non-thermal plasma in VOCs abatement: a review. *Chem Eng J* 2020;388:124275. DOI
195. Zhang Y, Nie J, Yuan C, et al. CuO@Cu/Ag/MWNTs/sponge electrode-enhanced pollutant removal in dielectric barrier discharge (DBD) reactor. *Chemosphere* 2019;229:273-83. DOI PubMed
196. Mei D, Tu X. Conversion of CO_2 in a cylindrical dielectric barrier discharge reactor: effects of plasma processing parameters and reactor design. *Journal of CO2 Utilization* 2017;19:68-78. DOI
197. Yuan D, Tang S, Qi J, Li N, Gu J, Huang H. Comparison of hydroxyl radicals generation during granular activated carbon regeneration in DBD reactor driven by bipolar pulse power and alternating current power. *Vacuum* 2017;143:87-94. DOI
198. Jiang N, Qiu C, Guo L, et al. Improved performance for toluene abatement in a continuous-flow pulsed sliding discharge reactor based on three-electrode configuration. *Plasma Chem Plasma Process* 2019;39:227-40. DOI
199. Jiang N, Guo L, Qiu C, et al. Reactive species distribution characteristics and toluene destruction in the three-electrode DBD reactor energized by different pulsed modes. *Chem Eng J* 2018;350:12-9. DOI
200. Li S, Yu X, Dang X, Guo H, Liu P, Qin C. Using non-thermal plasma for decomposition of toluene adsorbed on γ-Al_2O_3 and ZSM-5: Configuration and optimization of a double dielectric barrier discharge reactor. *Chem Eng J* 2019;375:122027. DOI
201. Wang T, Chen S, Wang H, Liu Z, Wu Z. In-plasma catalytic degradation of toluene over different MnO_2 polymorphs and study of reaction mechanism. *Chinese J Catal* 2017;38:793-803. DOI
202. Liu R, Song H, Li B, Li X, Zhu T. Simultaneous removal of toluene and styrene by non-thermal plasma-catalysis: effect of VOCs interaction and system configuration. *Chemosphere* 2021;263:127893. DOI PubMed
203. Qin C, Guo M, Jiang C, et al. Simultaneous oxidation of toluene and ethyl acetate by dielectric barrier discharge combined with Fe, Mn and Mo catalysts. *SSci Total Environ* 2021;782:146931. DOI
204. Mustafa MF, Fu X, Liu Y, Abbas Y, Wang H, Lu W. Volatile organic compounds (VOCs) removal in non-thermal plasma double dielectric barrier discharge reactor. *J Hazard Mater* 2018;347:317-24. DOI PubMed
205. Hoseini S, Rahemi N, Allahyari S, Tasbihi M. Application of plasma technology in the removal of volatile organic compounds (BTX) using manganese oxide nano-catalysts synthesized from spent batteries. *J Clean Prod* 2019;232:1134-47. DOI
206. Mustafa MF, Fu X, Lu W, et al. Application of non-thermal plasma technology on fugitive methane destruction: configuration and optimization of double dielectric barrier discharge reactor. *J Clean Prod* 2018;174:670-7. DOI
207. Shang K, Ren J, Zhang Q, Lu N, Jiang N, Li J. Successive treatment of benzene and derived byproducts by a novel plasma catalysis-adsorption process. *J Environ Chem Eng* 2021;9:105767. DOI
208. Yamagata Y, Niho K, Inoue K, Okano H, Muraoka K. Decomposition of volatile organic compounds at low concentrations using combination of densification by zeolite adsorption and dielectric barrier discharge. *Jpn J Appl Phys* 2006;45:8251-4. DOI
209. Sivachandiran L, Thevenet F, Rousseau A. Non-thermal plasma assisted regeneration of acetone adsorbed TiO_2 surface. *Plasma Chem Plasma Process* 2013;33:855-71. DOI
210. Sultana S, Vandenbroucke A, Leys C, De Geyter N, Morent R. Abatement of VOCs with alternate adsorption and plasma-assisted regeneration: a review. *Catalysts* 2015;5:718-46. DOI
211. Xu W, Lin K, Ye D, Jiang X, Liu J, Chen Y. Performance of toluene removal in a nonthermal plasma catalysis system over flake-like HZSM-5 zeolite with tunable pore size and evaluation of its byproducts. *Nanomaterials (Basel)* 2019;9:290. DOI PubMed PMC
212. Yi H, Yang X, Tang X, et al. Removal of toluene from industrial gas over 13X zeolite supported catalysts by adsorption-plasma catalytic process: removal of toluene by adsorption plasma catalytic process. *J Chem Technol Biotechnol* 2017;92:2276-86. DOI
213. Xu X, Wang P, Xu W, et al. Plasma-catalysis of metal loaded SBA-15 for toluene removal: comparison of continuously introduced and adsorption-discharge plasma system. *Chem Eng J* 2016;283:276-84. DOI
214. Trinh QH, Lee SB, Mok YS. Removal of ethylene from air stream by adsorption and plasma-catalytic oxidation using silver-based bimetallic catalysts supported on zeolite. *J Hazard Mater* 2015;285:525-34. DOI PubMed
215. Wang W, Wang H, Zhu T, Fan X. Removal of gas phase low-concentration toluene over Mn, Ag and Ce modified HZSM-5 catalysts by periodical operation of adsorption and non-thermal plasma regeneration. *J Hazard Mater* 2015;292:70-8. DOI PubMed
216. Fan H, Shi C, Li X, Zhao D, Xu Y, Zhu A. High-efficiency plasma catalytic removal of dilute benzene from air. *J Phys D: Appl Phys* 2009;42:225105. DOI
217. Kim H, Ogata A, Futamura S. Oxygen partial pressure-dependent behavior of various catalysts for the total oxidation of VOCs using cycled system of adsorption and oxygen plasma. *Appl Catal B* 2008;79:356-67. DOI
218. Dang X, Huang J, Cao L, Zhou Y. Plasma-catalytic oxidation of adsorbed toluene with gas circulation. *Catal Commun* 2013;40:116-9. DOI
219. Yi H, Yang X, Tang X, et al. Removal of toluene from industrial gas by adsorption–plasma catalytic process: comparison of closed discharge and ventilated discharge. *Plasma Chem Plasma Process* 2018;38:331-45. DOI
220. Hosseini MS, Asilian Mahabadi H, Yarahmadi R. Removal of toluene from air using a Cycled Storage-Discharge (CSD) plasma catalytic process. *Plasma Chem Plasma Process* 2019;39:125-42. DOI
221. Youn JS, Bae J, Park S, Park YK. Plasma-assisted oxidation of toluene over Fe/zeolite catalyst in DBD reactor using adsorption/desorption system. *Catal Commun* 2018;113:36-40. DOI
222. Xu W, Jiang X, Chen H, et al. Adsorption-discharge plasma system for toluene decomposition over Ni-SBA catalyst: in situ observation and humidity influence study. *Chem Eng J* 2020;382:122950. DOI
223. Abdelouahab-reddam Z, Mail RE, Coloma F, Sepúlveda-escribano A. Platinum supported on highly-dispersed ceria on activated

carbon for the total oxidation of VOCs. *APPL CATAL A-GEN* 2015;494:87-94. DOI

224. Chen H, Yan Y, Shao Y, Zhang H. Catalytic activity and stability of porous Co–Cu–Mn mixed oxide modified microfibrous-structured ZSM-5 membrane/PSSF catalyst for VOCs oxidation. *RSC Adv* 2014;4:55202-9. DOI
225. Liao Y, Zhang X, Peng R, Zhao M, Ye D. Catalytic properties of manganese oxide polyhedra with hollow and solid morphologies in toluene removal. *Appl Surf Sci* 2017;405:20-8. DOI
226. Durme J, Dewulf J, Sysmans W, Leys C, Van Langenhove H. Abatement and degradation pathways of toluene in indoor air by positive corona discharge. *Chemosphere* 2007;68:1821-9. DOI PubMed
227. Chao CY, Kwong CW, Hui KS. Potential use of a combined ozone and zeolite system for gaseous toluene elimination. *J Hazard Mater* 2007;143:118-27. DOI PubMed
228. Qin C, Huang X, Zhao J, Huang J, Kang Z, Dang X. Removal of toluene by sequential adsorption-plasma oxidation: mixed support and catalyst deactivation. *J Hazard Mater* 2017;334:29-38. DOI PubMed
229. Trinh QH, Gandhi MS, Mok YS. Adsorption and plasma-catalytic oxidation of acetone over zeolite-supported silver catalyst. *Jpn J Appl Phys* 2015;54:01AG04. DOI
230. Vepek S. Mechanism of the deactivation of Hopcalite catalysts studied by XPS, ISS, and other techniques. *J Catal* 1986;100:250-63. DOI
231. Qin C, Guo H, Bai W, et al. Kinetics study on non-thermal plasma mineralization of adsorbed toluene over γ-Al_2O_3 hybrid with zeolite. *J Hazard Mater* 2019;369:430-8. DOI PubMed
232. Shayegan Z, Lee C, Haghighat F. TiO_2 photocatalyst for removal of volatile organic compounds in gas phase – a review. *Chem Eng J* 2018;334:2408-39. DOI
233. Tseng TK, Lin YS, Chen YJ, Chu H. A review of photocatalysts prepared by sol-gel method for VOCs removal. *Int J Mol Sci* 2010;11:2336-61. DOI PubMed PMC
234. Zou W, Gao B, Ok YS, Dong L. Integrated adsorption and photocatalytic degradation of volatile organic compounds (VOCs) using carbon-based nanocomposites: a critical review. *Chemosphere* 2019;218:845-59. DOI PubMed
235. Huang Y, Ho SS, Lu Y, et al. Removal of indoor volatile organic compounds via photocatalytic oxidation: a short review and prospect. *Molecules* 2016;21:56. DOI PubMed PMC
236. Li H, Jiang F, Drdova S, Shang H, Zhang L, Wang J. Dual-function surface hydrogen bonds enable robust O_2 activation for deep photocatalytic toluene oxidation. *Catal Sci Technol* 2021;11:319-31. DOI
237. Wang L, Xu X, Wu S, Cao F. Nonstoichiometric tungsten oxide residing in a 3D nitrogen doped carbon matrix, a composite photocatalyst for oxygen vacancy induced VOC degradation and H_2 production. *Catal Sci Technol* 2018;8:1366-74. DOI
238. Weon S, He F, Choi W. Status and challenges in photocatalytic nanotechnology for cleaning air polluted with volatile organic compounds: visible light utilization and catalyst deactivation. *Environ Sci : Nano* 2019;6:3185-214. DOI
239. Zhang W, Li G, Yin H, Zhao K, Zhao H, An T. Adsorption and desorption mechanism of aromatic VOCs onto porous carbon adsorbents for emission control and resource recovery: recent progress and challenges. *Environ Sci : Nano* 2022;9:81-104. DOI
240. Chen R, Li J, Wang H, et al. Photocatalytic reaction mechanisms at a gas–solid interface for typical air pollutant decomposition. *J Mater Chem A* 2021;9:20184-210. DOI
241. Xu H, Vanamu G, Nie Z, et al. Photocatalytic oxidation of a volatile organic component of acetaldehyde using titanium oxide nanotubes. *J Nanomater* 2006;2006:1-8. DOI
242. Liu Z, Zhang X, Nishimoto S, Murakami T, Fujishima A. Efficient photocatalytic degradation of gaseous acetaldehyde by highly ordered TiO_2 nanotube arrays. *Environ Sci Technol* 2008;42:8547-51. DOI PubMed
243. Wang M, Ioccozia J, Sun L, Lin C, Lin Z. Inorganic-modified semiconductor TiO_2 nanotube arrays for photocatalysis. *Energy Environ Sci* 2014;7:2182. DOI
244. Liu R, Li W, Peng A. A facile preparation of TiO_2/ACF with C Ti bond and abundant hydroxyls and its enhanced photocatalytic activity for formaldehyde removal. *Appl Surf Sci* 2018;427:608-16. DOI
245. An T, Chen J, Nie X, et al. Synthesis of carbon nanotube-anatase TiO_2 sub-micrometer-sized sphere composite photocatalyst for synergistic degradation of gaseous styrene. *ACS Appl Mater Interfaces* 2012;4:5988-96. DOI PubMed
246. Tieng S, Kanaev A, Chhor K. New homogeneously doped Fe (III)–TiO_2 photocatalyst for gaseous pollutant degradation. *APPL CATAL A-GEN* 2011;399:191-7. DOI
247. Murcia J, Hidalgo M, Navío J, Vaiano V, Ciambelli P, Sannino D. Ethanol partial photoxidation on Pt/TiO_2 catalysts as green route for acetaldehyde synthesis. *Catal Today* 2012;196:101-9. DOI
248. Shaban M, Ashraf AM, Abukhadra MR. TiO_2 nanoribbons/carbon nanotubes composite with enhanced photocatalytic activity; fabrication, characterization, and application. *Sci Rep* 2018;8:781. DOI PubMed PMC
249. Khan ME, Khan MM, Cho MH. Recent progress of metal-graphene nanostructures in photocatalysis. *Nanoscale* 2018;10:9427-40. DOI PubMed
250. Roso M, Boaretti C, Bonora R, Modesti M, Lorenzetti A. Nanostructured active media for volatile organic compounds abatement: the synergy of graphene oxide and semiconductor coupling. *Ind Eng Chem Res* 2018;57:16635-44. DOI
251. Colón G, Maicu M, Hidalgo M, Navío J. Cu-doped TiO_2 systems with improved photocatalytic activity. *Appl Catal B* 2006;67:41-51. DOI
252. Yang SB, Chun HH, Tayade RJ, Jo WK. Iron-functionalized titanium dioxide on flexible glass fibers for photocatalysis of benzene, toluene, ethylbenzene, and o-xylene (BTEX) under visible- or ultraviolet-light irradiation. *J Air Waste Manag Assoc* 2015;65:365-73.

DOI PubMed

253. Bensouici F, Bououdina M, Dakhel A, et al. Optical, structural and photocatalysis properties of Cu-doped TiO_2 thin films. *Appl Surf Sci* 2017;395:110-6. DOI
254. Shaban M, Ahmed AM, Shehata N, Betiha MA, Rabie AM. Ni-doped and Ni/Cr co-doped TiO_2 nanotubes for enhancement of photocatalytic degradation of methylene blue. *J Colloid Interface Sci* 2019;555:31-41. DOI PubMed
255. Dong F, Wang H, Wu Z. One-step "Green" synthetic approach for mesoporous C-doped titanium dioxide with efficient visible light photocatalytic activity. *J Phys Chem C* 2009;113:16717-23. DOI
256. Dong F, Guo S, Wang H, Li X, Wu Z. Enhancement of the visible light photocatalytic activity of c-doped TiO_2 nanomaterials prepared by a green synthetic approach. *J Phys Chem C* 2011;115:13285-92. DOI
257. Higashimoto S, Tanihata W, Nakagawa Y, Azuma M, Ohue H, Sakata Y. Effective photocatalytic decomposition of VOC under visible-light irradiation on N-doped TiO_2 modified by vanadium species. *APPL CATAL A-GEN* 2008;340:98-104. DOI
258. Mogal SI, Gandhi VG, Mishra M, et al. Single-step synthesis of silver-doped titanium dioxide: influence of silver on structural, textural, and photocatalytic properties. *Ind Eng Chem Res* 2014;53:5749-58. DOI
259. Nie L, Duan B, Lu A, Zhang L. Pd/TiO_2 @ carbon microspheres derived from chitin for highly efficient photocatalytic degradation of volatile organic compounds. *ACS Sustainable Chem Eng* 2019;7:1658-66. DOI
260. Guan K. Relationship between photocatalytic activity, hydrophilicity and self-cleaning effect of TiO_2/SiO_2 films. *Surf Coat Technol* 2005;191:155-60. DOI
261. Zou L, Luo Y, Hooper M, Hu E. Removal of VOCs by photocatalysis process using adsorption enhanced TiO_2–SiO_2 catalyst. *Chem Eng Process* 2006;45:959-64. DOI
262. Yu J, Yu JC, Zhao X. The effect of SiO_2 addition on the grain size and photocatalytic activity of TiO_2 thin films. *J Sol-Gel Sci Technol* 2002;24:95-103. DOI
263. Sumitsawan S, Cho J, Sattler ML, Timmons RB. Plasma surface modified TiO_2 nanoparticles: improved photocatalytic oxidation of gaseous m-xylene. *Environ Sci Technol* 2011;45:6970-7. DOI PubMed
264. Arai T, Horiguchi M, Yanagida M, Gunji T, Sugihara H, Sayama K. Complete oxidation of acetaldehyde and toluene over a Pd/WO (3) photocatalyst under fluorescent- or visible-light irradiation. *Chem Commun (Camb)* 2008;43:5565-7. DOI PubMed
265. Hou Y, Wang X, Wu L, Ding Z, Fu X. Efficient decomposition of benzene over a beta-Ga_2O_3 photocatalyst under ambient conditions. *Environ Sci Technol* 2006;40:5799-803. DOI PubMed
266. Chen LC, Pan GT, Yang TC, Chung TW, Huang CM. In situ DRIFT and kinetic studies of photocatalytic degradation on benzene vapor with visible-light-driven silver vanadates. *J Hazard Mater* 2010;178:644-51. DOI PubMed
267. Kim J, Choi W. Response to comment on "Platinized WO_3 as an environmental photocatalyst that generates OH radicals under visible light". *Environ Sci Technol* 2011;45:3183-4. DOI
268. Yan T, Long J, Shi X, Wang D, Li Z, Wang X. Efficient photocatalytic degradation of volatile organic compounds by porous indium hydroxide nanocrystals. *Environ Sci Technol* 2010;44:1380-5. DOI PubMed
269. Zhang W, Yang Z, Wang H, et al. Crystal facet-dependent frustrated Lewis pairs on dual-metal hydroxide for photocatalytic CO_2 reduction. *Appl Catal B Environ* 2022;300:120748. DOI
270. Lu KQ, Li YH, Zhang F, et al. Rationally designed transition metal hydroxide nanosheet arrays on graphene for artificial CO_2 reduction. *Nat Commun* 2020;11:5181. DOI PubMed PMC
271. Fresno F, Hernández-alonso MD, Tudela D, Coronado JM, Soria J. Photocatalytic degradation of toluene over doped and coupled (Ti,M)O_2 (M=Sn or Zr) nanocrystalline oxides: Influence of the heteroatom distribution on deactivation. *Appl Catal B* 2008;84:598-606. DOI
272. Han Z, Chang V, Wang X, Lim T, Hildemann L. Experimental study on visible-light induced photocatalytic oxidation of gaseous formaldehyde by polyester fiber supported photocatalysts. *Chem Eng J* 2013;218:9-18. DOI
273. Yang L, Liu Z, Shi J, Zhang Y, Hu H, Shangguan W. Degradation of indoor gaseous formaldehyde by hybrid VUV and TiO_2/UV processes. *Sep Purif Technol* 2007;54:204-11. DOI
274. Ameen M, Raupp GB. Reversible catalyst deactivation in the photocatalytic oxidation of diluteo-xylene in air. *J Catal* 1999;184:112-22. DOI
275. Mamaghani AH, Haghighat F, Lee C. Photocatalytic oxidation of MEK over hierarchical TiO_2 catalysts: effect of photocatalyst features and operating conditions. *Appl Catal B* 2019;251:1-16. DOI
276. Shayegan Z, Haghighat F, Lee C. Photocatalytic oxidation of volatile organic compounds for indoor environment applications: three different scaled setups. *Chem Eng J* 2019;357:533-46. DOI
277. Héquet V, Raillard C, Debono O, Thévenet F, Locoge N, Le Coq L. Photocatalytic oxidation of VOCs at ppb level using a closed-loop reactor: the mixture effect. *Appl Catal B* 2018;226:473-86. DOI

Rebecca El Khawaja

Rebecca El Khawaja obtained her M.Sc. in physical chemistry of materials from the Lebanese University in 2017. She worked with the Rennes School of Chemistry on her final project to study the hydrogenation of aromatic compounds in the presence of ordered mesoporous catalysts using various alumina precursors and organic surfactants. During her PhD at the University of the Littoral Opal Coast, Rebecca worked on the development of hybrid systems based on adsorption/catalysis coupling for the catalytic oxidation of oxygenated and cyclic VOCs from industrial sources. Her interests include hybrid material, catalysis, depollution and recently waste valorization as she joined EPIC research team at Polytechnique Montreal as a postdoctoral fellow.

Savita Kaliya Perumal Veerapandian

Savita Kaliya Perumal Veerapandian received her PhD degree in Engineering Physics from Ghent University, Belgium in 2021. She was working on the Sequential adsorption plasma catalysis for the abatement of toluene under the supervision of Prof. Rino Morent. Her research work was carried out within the framework of INTERREG project DepollutAir. The main aspects of her research include reducing process cost by sequential treatment, reducing material cost by plasma assisted regeneration of the catalysts and improving the product selectivity and yield. During her research career, she published 14 articles in peer-reviewed journals and she actively participated in 12 International conferences and workshops.

Rino Morent

Rino Morent obtained in 2004 his PhD in Engineering: Applied Physics at Ghent University. In 2012 he was appointed as professor in plasma technology at Ghent University, thanks to obtaining the ERC Starting Grant PLASMAPOR. At the moment he is Full Professor and leading the experimental Research Unit Plasma Technology (RUPT). RUPT focuses on the development of different atmospheric pressure plasma sources (including pulsed discharges, plasma jets & dielectric barrier discharges) and their applications in gas conversion, materials science, air cleaning, energy solutions, biomedical applications and plasma medicine.

Guy De Weireld

Guy De Weireld is full professor in chemical thermodynamics, environment, industrial processes, and sustainable development at the Faculty of Engineering, University of Mons (Belgium). His main research field is adsorption in porous materials and catalysis. He has experience in CO_2 capture, gas separation, gas purification (removing of acid compounds from natural gas, VOC from exhaust air) and CO_2 conversion to fuel as well as techno-economic and environmental assessments in carbon capture, utilization, and storage. Since 2019, he is the coordinator of the H2020-MOF4AIR project: Metal Organic Frameworks for carbon dioxide Adsorption processes in power production and energy Intensive industRies.

Yang Ding

Yang Ding received his M.Sc. degree from College of Chemistry and Materials Science at Shanghai Normal University in 2018. He is currently a PhD student in the Laboratory of Inorganic Materials Chemistry (CMI) of University of Namur under the supervision of Prof. Bao-Lian Su. His research interests include porous materials synthesis and characterization, photocatalytic pollutants elimination and sustainable energy production.

Renaud Cousin

Renaud Cousin received his PhD degree in Spectroscopy and Chemistry from Littoral Côte d'Opale University in Dunkirk, France, in 2000 on the topic “Soot Oxidation”. After a postdoctoral position at the University of Strasbourg sponsored by Daimler, he worked as Assistant Professor at the Littoral Côte d'Opale University, France, from 2003 to 2016. In 2014 he obtained the accreditation to Supervise Research (Habilitation Thesis). Since 2016 he was promoted to Full Professor. Currently his research focuses on the development and characterization of heterogeneous catalysts for application to the elimination of environmental pollutants (Soot, CO, VOCs, …). He has co-authored over 80 peer reviewed scientific papers and 1 patent.

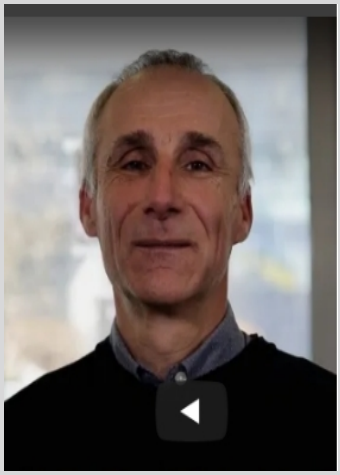

Fabrice Cazier

Fabrice Cazier obtained his PhD in Chemical Sciences at Lille University (France) in 1990 with works dealing with "Development of analytical methods for organic and nitrated pollutants in the atmosphere". He worked then as a searcher for the Air Quality monitoring network on VOC and nitrogen oxides monitoring. In 1993, he managed the creation of an analytical laboratory dedicated to risk evaluation and environmental analysis. He became the Director of this unit in 1995. Since then, as Director of the Common Centre of Measurements (CCM) of the Université du Littoral Côte d'Opale (ULCO), he has developed a large expertise in chemical analysis applied to the environment and manages a highly equipped laboratory available as well for research teams as for industrial partners. He is notably specialized in gaseous compounds and particulate matter measurements.

Sylvain Billet

Sylvain Billet has been an associate professor in industrial and environmental toxicology at the Environmental Chemistry and Interactions with the Living Organisms at the University of the Opal Coast (UCEIV, ULCO), France since 2009. He is general secretary of the French Cellular and Molecular Toxicology Society (STCM). His PhD in toxicology focused on the biotransformation and genotoxicity of organic pollutants adsorbed on the surface of fine atmospheric particles. He has since set up a method of exposure of complex cultures of human respiratory cells in order to characterize the toxicity of gaseous air pollutants alone or in mixtures.

Jean-François Lamonier

Jean-François Lamonier is a full Professor in Department of Chemistry and Deputy Director of the Chevreul Institute, Lille University (France). Jean-François Lamonier leads the team "Catalytic Remediation" of the « Unité de Catalyse et Chimie du Solide » laboratory. His research addresses the catalytic oxidation technologies for Volatile Organic Compounds emissions removal and the catalytic pyrolysis of plastic waste. His research comprises (i) the development of transition metal oxide nanomaterials with emphasis in the elucidation of the structure-chemical properties and catalytic activity relationship and (ii) the coupling of abatement technologies such as non-thermal plasma and heterogeneous catalysis. For this last-mentioned topic Jean-François Lamonier heads the International Associated Laboratory "Plasma & Catalysis" between Lille University and Ghent University (Belgium).

Bao-Lian Su

Bao-Lian Su created the Laboratory of Inorganic Materials Chemistry (CMI) at the University of Namur, Belgium in 1995. He is Full Professor, Member of the European Academy of Sciences, Member of the Royal Academy of Belgium, Fellow of the Royal of Society of Chemistry, UK and Life Member of Clare Hall College, University of Cambridge. He is also a strategy scientist at Wuhan University of Technology, China. His research fields include the synthesis, the property study and the molecular engineering of organized, hierarchically porous and bio-organisms for artificial photosynthesis, (photo) Catalysis, Energy Conversion and Storage, Biotechnology, Cell therapy and Biomedical applications.

Stéphane Siffert

Stéphane Siffert is a full Professor in Department of Chemistry and Director of Unit of Environmental Chemistry and Interactions with leaving organisms (UCEIV, UR 4492, FR CNRS 3417), Dunkerque (France). He was coordinator of three European Interreg projects till 2022 on Volatile Organic Compounds (VOC) removal. His mean research is on catalytic treatment of pollutants, especially the oxidation of VOC, and also purification and valorisation of CO_2. He works on oxides synthesized by "classic" and "hydrotalcite" way, zeolites and highly structured meso and macroporous compounds and noble metals catalysts.

AUTHOR INSTRUCTIONS

1. Submission Overview

Before you decide to publish with *Chemical Synthesis*, please read the following items carefully and make sure that you are well aware of Editorial Policies and the following requirements.

1.1 Topic Suitability

The topic of the manuscript must fit the scope of the journal. Please refer to Aims and Scope for more information.

1.2 Open Access and Copyright

The journal adopts Gold Open Access publishing model and distributes content under the Creative Commons Attribution 4.0 International License. Copyright is retained by authors. Please make sure that you are well aware of these policies.

1.3 Publication Fees

Chemical Synthesis is an open access journal. When a paper is accepted for publication, authors are required to pay Article Processing Charges (APCs) to cover its editorial and production costs. The APC for each submission is $600. There are no additional charges based on color, length, figures, or other elements. For more details, please refer to OAE Publication Fees.

1.4 Language Editing

All submissions are required to be presented clearly and cohesively in good English. Authors whose first language is not English are advised to have their manuscripts checked or edited by a native English speaker before submission to ensure the high quality of expression. A well-organized manuscript in good English would make the peer review even the whole editorial handling more smoothly and efficiently.
If needed, authors are recommended to consider the language editing services provided by Charlesworth to ensure that the manuscript is written in correct scientific English before submission. Authors who publish with OAE journals enjoy a special discount for the services of Charlesworth via the following two ways.

Submit your manuscripts directly at http://www.charlesworthauthorservices.com/~OAE;
Open the link http://www.charlesworthauthorservices.com/, and enter Promotion Code “OAE” when you submit.

1.5 Work Funded by the National Institutes of Health

If an accepted manuscript was funded by National Institutes of Health (NIH), the authors may inform Editors of the NIH funding number. The Editors are able to deposit the paper to the NIH Manuscript Submission System on behalf of the authors.

2. Submission Preparation

2.1 Cover Letter

A cover letter is required to be submitted accompanying each manuscript. It should be concise and explain why the study is significant, why it fits the scope of the journal, and why it would be attractive to readers, etc.
Here is a guideline of a cover letter for authors’ consideration:
In the first paragraph: include the title and type (e.g., Original Article, Review, Case Report, etc.) of the manuscript, a brief on the background of the study, the question the author sought out to answer and why;
In the second paragraph: concisely explain what was done, the main findings and why they are significant;
In the third paragraph: indicate why the manuscript fits the Aims and Scope of the journal, and why it would be attractive to readers;
In the fourth paragraph: confirm that the manuscript has not been published elsewhere and not under consideration of any other journal. All authors have approved the manuscript and agreed on its submission to the journal. Journal’s specific requirements have been met if any.
If the manuscript is contributed to a Special Issue, please also mention it in the cover letter.
If the manuscript was presented partly or entirely in a conference, the author should clearly state the background information of the event, including the conference name, time and place in the cover letter.

2.2 Types of Manuscripts

The journal publishes Research Article, Review Article, Short Communication, Feature Article, Commentary, Editorial, News, Research Highlight, Perspective, *etc*. For more details about paper type, please refer to the following table.

Manuscript Type	Definition	Abstract	Keywords	Main Text Structure
Research Article	A Research Article is a seminal and insightful research study and showcases that often involves modern techniques or methodologies. Authors should justify that their work are of novel findings.	The abstract should state briefly the purpose of the research, the principal results and major conclusions. No more than 250 words.	3-6 keywords.	The main content should include four sections: Introduction, Experimental, Results and discussion, and Conclusions.
Review Article	A Review Article should be an authoritative, well balanced and critical survey of recent progresses in an attractive or a fundamental chemical research field.	Unstructured abstract. No more than 250 words.	3-6 keywords.	The main text may consist of several sections with unfixed section titles. We suggest that the author include an "Introduction" section at the beginning, several sections with unfixed titles in the middle part, and a "Conclusion and outlook" section in the end. Corresponding authors are requested to provide a short biography (up to 200 words) and headshot for inclusion at the end of the published article.
Short Communication	Short Communications are for the urgent publication of a research which is of outstanding significance and interest to experts in the field and also to general chemistry readership. Authors should write in a clear and concise way to demonstrate the necessity of an urgent publication.	Unstructured abstract. No more than 150 words.	3-6 keywords.	The short Communication is a one body text with maximum 4 items (figures and tables) and 12 references.
Feature Article	A Feature Article is not a typical review. Feature article should highlight the author's contribution to a key field with a balanced discussion of related work from the field. A Feature Article should not, in principle, contain original research.	Unstructured abstract. No more than 250 words.	3-6 keywords.	The main text may consist of several sections with unfixed section titles. We suggest that the author include an "Introduction" section at the beginning, several sections with unfixed titles in the middle part, and a "Conclusion and outlook" section in the end.
Commentary	A Commentary is to provide comments on a newly published article or an alternative viewpoint on a certain topic.	Unstructured abstract. No more than 250 words.	3-6 keywords.	/
Editorial	An Editorial can be a comment about an important event in the world related or not to chemistry or a particular discovery in chemistry, needing a particular attention of chemistry community.	None required.	None required	/
News	A News comments an important event in the world related or not to chemistry, or a particular discovery in chemistry, needing a particular attention of chemistry community.	None required.	None required	/
Research Highlight	A Research Highlight article is peer-reviewed paper and highlights work recently published in the journal or in a recent issue of another journal.	None required.	3-6 keywords.	/
Perspective	A Perspective provides personal points of view on the state-of-the-art of a specific area of knowledge and its future prospects.	Unstructured abstract. No more than 150 words.	3-6 keywords.	/

2.3 Manuscript Structure

2.3.1 Front Matter

2.3.1.1 Title

The title of the manuscript should be concise, specific and relevant, with no more than 16 words if possible. When gene or protein names are included, the abbreviated name rather than full name should be used.

2.3.1.2 Authors and Affiliations

Authors' full names should be listed. The initials of middle names can be provided. Institutional addresses and email addresses for all authors should be listed. At least one author should be designated as corresponding author. In addition, corresponding authors are suggested to provide their Open Researcher and Contributor ID upon submission. Please note that any change to authorship is not allowed after manuscript acceptance.

2.3.1.3 Highlights

Highlights are mandatory because they can help increase the discoverability of your article through search engines. They consist of a short collection of bullet points that capture the novel results of your research as well as new methods that were used during the study (if any). They should be submitted in a separate editable file in the online submission system. Please use 'Highlights' in the file name and include 3 to 5 bullet points (maximum 85 characters per bullet point, including spaces).

2.3.1.4 Abstract

The abstract should be a single paragraph with word limitation and specific structure requirements (for more details please refer to Types of Manuscripts). It usually describes the main objective(s) of the study, explains how the study was done, including any model organisms used, without methodological detail, and summarizes the most important results and their significance. The abstract must be an objective representation of the study: it is not allowed to contain results which are not presented and substantiated in the manuscript, or exaggerate the main conclusions. Citations should not be included in the abstract.

2.3.1.5 Graphical Abstract

The graphical abstract is essential as this can catch first view of your publication by readers. We recommend you to submit an eye-catching figure. It should summarize the content of the article in a concise graphical form. It is recommended to use it because this can make online articles get more attention. The graphic abstract should be submitted as a separate document in the online submission system. Please provide an image with a minimum of 531 × 1,328 pixels (h × w) or proportionally more. The image should be readable at a size of 5 × 13 cm using a regular screen resolution of 96 dpi. Preferred file types: tiff, psd, AI, jpeg and eps files.

2.3.1.6 Keywords

Three to six keywords should be provided, which are specific to the article, yet reasonably common within the subject discipline.

2.3.2 Main Text

Manuscripts of different types are structured with different sections of content. Please refer to Types of Manuscripts to make sure which sections should be included in the manuscripts.

2.3.2.1 Introduction

The introduction should contain background that puts the manuscript into context, allow readers to understand why the study is important, include a brief review of key literature, and conclude with a brief statement of the overall aim of the work and a comment about whether that aim was achieved. Relevant controversies or disagreements in the field should be introduced as well.

2.3.2.2 Experimental

Experimental should contain sufficient details to allow others to fully replicate the study. New methods and protocols should be described in detail while well-established methods can be briefly described or appropriately cited. Experimental participants selected, the drugs and chemicals used, the statistical methods taken, and the computer software used should be identified precisely. Statistical terms, abbreviations, and all symbols used should be defined clearly. Protocol documents for clinical trials, observational studies, and other non-laboratory investigations may be uploaded as supplementary materials.

2.3.2.3 Results and Discussion

This section should contain the findings of the study and discuss the implications of the findings in context of existing research and highlight limitations of the study. Future research directions may also be mentioned. Results of statistical analysis should also be included either as text or as tables or figures if appropriate. Authors should emphasize and summarize only the most important observations. Data on all primary and secondary outcomes identified in the section Methods should also be provided. Extra or supplementary materials and technical details can be placed in supplementary documents.

2.3.2.4 Conclusions

It should state clearly the main conclusions and include the explanation of their relevance or importance to the field.

2.3.3 Back Matter

2.3.3.1 Acknowledgments

Anyone who contributed towards the article but does not meet the criteria for authorship, including those who provided professional writing services or materials, should be acknowledged. Authors should obtain permission to acknowledge from all those mentioned in the Acknowledgments section. This section is not added if the author does not have anyone to acknowledge.

2.3.3.2 Authors' Contributions

Each author is expected to have made substantial contributions to the conception or design of the work, or the acquisition, analysis, or interpretation of data, or the creation of new software used in the work, or have drafted the work or substantively revised it.

Please use Surname and Initial of Forename to refer to an author's contribution. For example: made substantial contributions to conception and design of the study and performed data analysis and interpretation: Salas H, Castaneda WV; performed data acquisition, as well as provided administrative, technical, and material support: Castillo N, Young V.

If an article is single-authored, please include "The author contributed solely to the article." in this section.

2.3.3.3 Availability of Data and Materials

In order to maintain the integrity, transparency and reproducibility of research records, authors should include this section in their manuscripts, detailing where the data supporting their findings can be found. Data can be deposited into data repositories or published as supplementary information in the journal. Authors who cannot share their data should state that the data will not be shared and explain it. If a manuscript does not involve such issue, please state "Not applicable." in this section.

2.3.3.4 Financial Support and Sponsorship

All sources of funding for the study reported should be declared. The role of the funding body in the experiment design, collection, analysis and interpretation of data, and writing of the manuscript should be declared. Any relevant grant numbers and the link of funder's website should be provided if any. If the study is not involved with this issue, state "None." in this section.

2.3.3.5 Conflicts of Interest

Authors must declare any potential conflicts of interest that may be perceived as inappropriately influencing the representation or interpretation of reported research results. If there are no conflicts of interest, please state "All authors declared that there are no conflicts of interest." in this section. Some authors may be bound by confidentiality agreements. In such cases, in place of itemized disclosures, we will require authors to state "All authors declare that they are bound by confidentiality agreements that prevent them from disclosing their conflicts of interest in this work.". If authors are unsure whether conflicts of interest exist, please refer to the "Conflicts of Interest" of *Chemical Synthesis* Editorial Policies for a full explanation.

2.3.3.6 Ethical Approval and Consent to Participate

Research involving human subjects, human material or human data must be performed in accordance with the Declaration of Helsinki and approved by an appropriate ethics committee. An informed consent to participate in the study should also be obtained from participants, or their parents or legal guardians for children under 16. A statement detailing the name of the ethics committee (including the reference number where appropriate) and the informed consent obtained must appear in the manuscripts reporting such research.

Studies involving animals and cell lines must include a statement on ethical approval. More information is available at Editorial Policies.

If the manuscript does not involve such issue, please state "Not applicable." in this section.

2.3.3.7 Consent for Publication

Manuscripts containing individual details, images or videos, must obtain consent for publication from that person, or in the case of children, their parents or legal guardians. If the person has died, consent for publication must be obtained from the next of kin of the participant. Manuscripts must include a statement that a written informed consent for publication was obtained. Authors do not have to submit such content accompanying the manuscript. However, these documents must be available if requested. If the manuscript does not involve this issue, state "Not applicable." in this section.

2.3.3.8 Copyright

Authors retain copyright of their works through a Creative Commons Attribution 4.0 International License that clearly states how readers can copy, distribute, and use their attributed research, free of charge. A declaration "© The Author(s)

2022." will be added to each article. Authors are required to sign License to Publish before formal publication.

2.3.3.9 References

References should be numbered in order of appearance at the end of manuscripts. In the text, reference numbers should be placed in square brackets and the corresponding references are cited thereafter. If the number of authors is less than or equal to six, we require to list all authors' names. If the number of authors is more than six, only the first three authors' names are required to be listed in the references, other authors' names should be omitted and replaced with "et al.". Abbreviations of the journals should be provided on the basis of Index Medicus. Information from manuscripts accepted but not published should be cited in the text as "Unpublished material" with written permission from the source.

References should be described as follows, depending on the types of works:

Types	Examples
Journal articles by individual authors	Weaver DL, Ashikaga T, Krag DN, et al. Effect of occult metastases on survival in node-negative breast cancer. *N Engl J Med* 2011;364:412-21. [PMID: 21247310 DOI: 10.1056/NEJMoa1008108]
Organization as author	Diabetes Prevention Program Research Group. Hypertension, insulin, and proinsulin in participants with impaired glucose tolerance. *Hypertension* 2002;40:679-86. [PMID: 12411462]
Both personal authors and organization as author	Vallancien G, Emberton M, Harving N, van Moorselaar RJ; Alf-One Study Group. Sexual dysfunction in 1,274 European men suffering from lower urinary tract symptoms. *J Urol* 2003;169:2257-61. [PMID: 12771764 DOI: 10.1097/01.ju.0000067940.76090.73]
Journal articles not in English	Zhang X, Xiong H, Ji TY, Zhang YH, Wang Y. Case report of anti-N-methyl-D-aspartate receptor encephalitis in child. *J Appl Clin Pediatr* 2012;27:1903-7. (in Chinese)
Journal articles ahead of print	Odibo AO. Falling stillbirth and neonatal mortality rates in twin gestation: not a reason for complacency. BJOG 2018; Epub ahead of print [PMID: 30461178 DOI: 10.1111/1471-0528.15541]
Books	Sherlock S, Dooley J. Diseases of the liver and billiary system. 9th ed. Oxford: Blackwell Sci Pub; 1993. pp. 258-96.
Book chapters	Meltzer PS, Kallioniemi A, Trent JM. Chromosome alterations in human solid tumors. In: Vogelstein B, Kinzler KW, editors. The genetic basis of human cancer. New York: McGraw-Hill; 2002. pp. 93-113.
Online resource	FDA News Release. FDA approval brings first gene therapy to the United States. Available from: https://www.fda.gov/NewsEvents/Newsroom/PressAnnouncements/ucm574058.htm. [Last accessed on 30 Oct 2017]
Conference proceedings	Harnden P, Joffe JK, Jones WG, editors. Germ cell tumours V. Proceedings of the 5th Germ Cell Tumour Conference; 2001 Sep 13-15; Leeds, UK. New York: Springer; 2002.
Conference paper	Christensen S, Oppacher F. An analysis of Koza's computational effort statistic for genetic programming. In: Foster JA, Lutton E, Miller J, Ryan C, Tettamanzi AG, editors. Genetic programming. EuroGP 2002: Proceedings of the 5th European Conference on Genetic Programming; 2002 Apr 3-5; Kinsdale, Ireland. Berlin: Springer; 2002. pp. 182-91.
Unpublished material	Tian D, Araki H, Stahl E, Bergelson J, Kreitman M. Signature of balancing selection in Arabidopsis. *Proc Natl Acad Sci U S A*. Forthcoming 2002.

For other types of references, please refer to U.S. National Library of Medicine.
The journal also recommends that authors prepare references with a bibliography software package, such as EndNote to avoid typing mistakes and duplicated references.

2.3.3.10 Supplementary Materials

Additional data and information can be uploaded as Supplementary Materials to accompany the manuscripts. The supplementary materials will also be available to the referees as part of the peer-review process. Any file format is acceptable, such as data sheet (word, excel, csv, cdx, fasta, pdf or zip files), presentation (PowerPoint, pdf or zip files), image (cdx, eps, jpeg, pdf, png or tiff), table (word, excel, csv or pdf), audio (mp3, wav or wma) or video (avi, divx, flv, mov, mp4, mpeg, mpg or wmv). All information should be clearly presented. Supplementary materials should be cited in the main text in numeric order (e.g., Supplementary Figure 1, Supplementary Figure 2, Supplementary Table 1, Supplementary Table 2, etc.). The style of supplementary figures or tables complies with the same requirements on figures or tables in main text. Videos and audios should be prepared in English, and limited to a size of 500 MB or a duration of 3 minutes.

2.4 Manuscript Format

2.4.1 File Format

Manuscript files can be in DOC and DOCX formats and should not be locked or protected.

2.4.2 Length

There are no restrictions on paper length, number of figures, or amount of supporting documents. Authors are encouraged to present and discuss their findings concisely.

2.4.3 Language

Manuscripts must be written in English.

2.4.4 Multimedia Files

The journal supports manuscripts with multimedia files. The requirements are listed as follows:
Videos or audio files are only acceptable in English. The presentation and introduction should be easy to understand. The frames should be clear, and the speech speed should be moderate.
A brief overview of the video or audio files should be given in the manuscript text.
The video or audio files should be limited to a size of up to 500 MB.
Please use professional software to produce high-quality video files, to facilitate acceptance and publication along with the submitted article. Upload the videos in mp4, wmv, or rm format (preferably mp4) and audio files in mp3 or wav format.

2.4.5 Figures

Figures should be cited in numeric order (e.g., Figure 1, Figure 2) and placed after the paragraph where it is first cited;
Figures can be submitted in format of tiff, psd, AI or jpeg, with resolution of 300-600 dpi;
Figure caption is placed under the Figure;
Diagrams with describing words (including, flow chart, coordinate diagram, bar chart, line chart, and scatter diagram, *etc.*) should be editable in word, excel or powerpoint format. Non-English information should be avoided;
Labels, numbers, letters, arrows, and symbols in figure should be clear, of uniform size, and contrast with the background;
Symbols, arrows, numbers, or letters used to identify parts of the illustrations must be identified and explained in the legend;
Internal scale (magnification) should be explained and the staining method in photomicrographs should be identified;
All non-standard abbreviations should be explained in the legend;
Permission for use of copyrighted materials from other sources, including re-published, adapted, modified, or partial figures and images from the internet, must be obtained. It is authors' responsibility to acquire the licenses, to follow any citation instruction requested by third-party rights holders, and cover any supplementary charges.

2.4.6 Tables

Tables should be cited in numeric order and placed after the paragraph where it is first cited;
The table caption should be placed above the table and labeled sequentially (e.g., Table 1, Table 2);
Tables should be provided in editable form like DOC or DOCX format (picture is not allowed);
Abbreviations and symbols used in table should be explained in footnote;
Explanatory matter should also be placed in footnotes;
Permission for use of copyrighted materials from other sources, including re-published, adapted, modified, or partial tables from the internet, must be obtained. It is authors' responsibility to acquire the licenses, to follow any citation instruction requested by third-party rights holders, and cover any supplementary charges.

2.4.7 Abbreviations

Abbreviations should be defined upon first appearance in the abstract, main text, and in figure or table captions and used consistently thereafter. Non-standard abbreviations are not allowed unless they appear at least three times in the text. Commonly-used abbreviations, such as DNA, RNA, ATP, *etc*., can be used directly without definition. Abbreviations in titles and keywords should be avoided, except for the ones which are widely used.

2.4.8 Italics

General italic words like *vs*., *et al., etc*., *in vivo*, *in vitro*; *t* test, *F* test, *U* test; related coefficient as *r*, sample number as *n*, and probability as *P*; names of genes; names of bacteria and biology species in Latin.

2.4.9 Units

SI Units should be used. Imperial, US customary and other units should be converted to SI units whenever possible. There is a space between the number and the unit (i.e., 23 mL). Hour, minute, second should be written as h, min, s.

2.4.10 Numbers

Numbers appearing at the beginning of sentences should be expressed in English. When there are two or more numbers in a paragraph, they should be expressed as Arabic numerals; when there is only one number in a paragraph, number < 10 should be expressed in English and number > 10 should be expressed as Arabic numerals. 12345678 should be written as 12,345,678.

2.4.11 Equations

Equations should be editable and not appear in a picture format. Authors are advised to use either the Microsoft Equation Editor or the MathType for display and inline equations.

2.5 Submission Link

Submit an article via https://oaemesas.com/login?JournalId=cs.

www.oaepublish.com

Chemical Synthesis
(*CS*)
Los Angeles Office
245 E Main Street ste122, Alhambra,
CA 91801, USA
E-mail: editorialoffice@chesynjournal.com
Website: www.chesynjournal.com